Title

Coupled Stiffness-Permeability Analysis of a Single Rough Surfaced Fracture by the Three-Dimensional Boundary Element Method

Author

Chen, D.-W.

Publication Date

1990-05-01

LBL-29203

Lawrence Berkeley Laboratory
UNIVERSITY OF CALIFORNIA

EARTH SCIENCES DIVISION

Coupled Stiffness-Permeability Analysis of a Single Rough Surfaced Fracture by the Three-Dimensional Boundary Element Method

D.-W. Chen
(Ph.D. Thesis)

May 1990

Prepared for the U.S. Department of Energy under Contract Number DE-AC03-76SF00098.

DISCLAIMER

LBL-29203

Coupled Stiffness-Permeability Analysis of a Single Rough Surfaced Fracture by the Three-Dimensional Boundary Element Method

Di-Wen Chen

(Ph.D. Thesis)

Department of Materials Science and Mineral Engineering
University of California

and

Earth Sciences Division
Lawrence Berkeley Laboratory
University of California
Berkeley, California 94720

May 1990

This work was supported by the Manager, Chicago Operations, Repository Technology Program, Repository Technology and Transportation Division, of the U.S. Department of Energy under Contract No. DE-AC03-76SF00098.

COUPLED STIFFNESS-PERMEABILITY ANALYSIS OF A SINGLE ROUGH SURFACED FRACTURE BY THE THREE-DIMENSIONAL BOUNDARY ELEMENT METHOD

Di-Wen Chen

Department of Materials Science and Mineral Engineering
University of California, Berkeley
Berkeley, California 94720

ABSTRACT

An understanding of the mechanical and hydraulic properties of fractures has become increasingly important in various problems, particularly those involving underground waste isolation and production from fractured oil reservoirs.

A typical fracture consists of asperity regions where the two rock surfaces are in contact, surrounded by regions where the two surfaces are separated by an aperture that may vary from point to point. When fluid flow through such a fracture, it not only must flow around the contact areas, but also has a tendency to preferentially flow through the channels with the largest apertures, since hydraulic conductance is locally proportional to the aperture cubed (*Brown*, 1987). The permeability therefore depends on the amount of contact area, the spatial distribution of the contact areas, as well as the aperture (*Chen, Zimmerman, and Cook*, 1989). All of these parameters are, in turn, functions of the stress to which the fracture is subjected.

There are two aspects of my analysis using a boundary element technique. The first part is an attempt to compute separately the tortuosity and the stiffness induced by the contact area. The second part has to do with hydromechanical coupling between stress, stiffness, and hydraulic conductivity of fractures.

For the hydromechanical coupling, I start by generating fractures with random aperture distributions, and which have a certain of statistical correlation between the

aperture at different locations. The hydraulic conductivity of the fracture is then computed. An increment of normal stress is then applied to the fracture, and its deformation is calculated. In some locations, the aperture decreases, while at other points the deformation may be large enough to create new contact area. After the new fracture geometry is found, the permeability is recalculated. Thus I determine the relationship between normal stress, average aperture, joint stiffness, and permeability.

These simulations should provide insight into the coupled hydromechanical behavior of fractures. For example, one interesting result is that the relationship between permeability and average aperture does not follow the "cubic law". If realistic aperture distributions can be found, this procedure could be used to predict permeability and stiffness.

Neville G. W. Cook

N. G. W. Cook

Thesis Committee Chairman

Table of Contents

LIST OF TABLES

LIST OF FIGURES

Acknowledgements

I wish to acknowledgement my enormous debt of gratitude to all those who made it possible for me to complete this dissertation:

To Professor N. G. W. Cook, my research advisor, for his keen insights, patience, and concern for me.

To Dr. Jane Long, without whose consistent support I could not have finished my academic work at the University of California.

To Professor P. Witherspoon, who helped me get my first appointment as a graduate research assistant at the Lawrence Berkeley Laboratory, and to whom I could always turn no matter what the problem.

To Dr. R. W. Zimmerman, whose suggestions have been stimulating and invaluable, and who has provided me with much help along the way.

To Professor S. Berger for his encouragement during all of this work.

And finally my gratitude to my friends, Debby Hopkins, Joyce Williams, Herb Williams, Chen-Wuing Lui, Chao Shan, Daniel Maloney, Wendy Rice, and others too numerous to list, for their moral support and help enabling me to express myself in English.

This work was supported by the Manager, Chicago Operations, Repository Technology Program, Repository Technology and Transportation Division, DOE. The support is gratefully acknowledged.

CHAPTER 1

INTRODUCTION

1.1. MOTIVATION AND PURPOSE

It is a common phenomenon that low permeability rock masses contain countless fractures and joints on all dimensional scales. Investigators (Louis 1976) divide rock masses into the following groups (Fig. 1-1) with respect to their hydraulic properties:

(1) homogenous porous media containing small pores; this group comprises jointed rock masses that have been laid down at great depths;

(2) porous jointed media in which the joints determine the hydraulic properties of the rock mass;

(3) porous media containing impermeable barriers, in which joints are filled with a fine impervious material (e.g. clay); fluid can flow through such media only through rock bridges which provide hydraulic connections;

(4) porous media containing small channels found in large joints filled with an impervious material through which water can flow;

(5) karstic media containing wide passages and caverns of various geometrical forms, created by the solution and removal of the rock by underground water flowing through it.

Rock masses most often occur as jointed porous media (Fig. 1-1b). The remaining types are rarely encountered; karstic media must be considered separately. Fracture-dominated flow in many jointed media with low matrix permiability has become increasingly important in various problems of geotechnical interest, particularly those

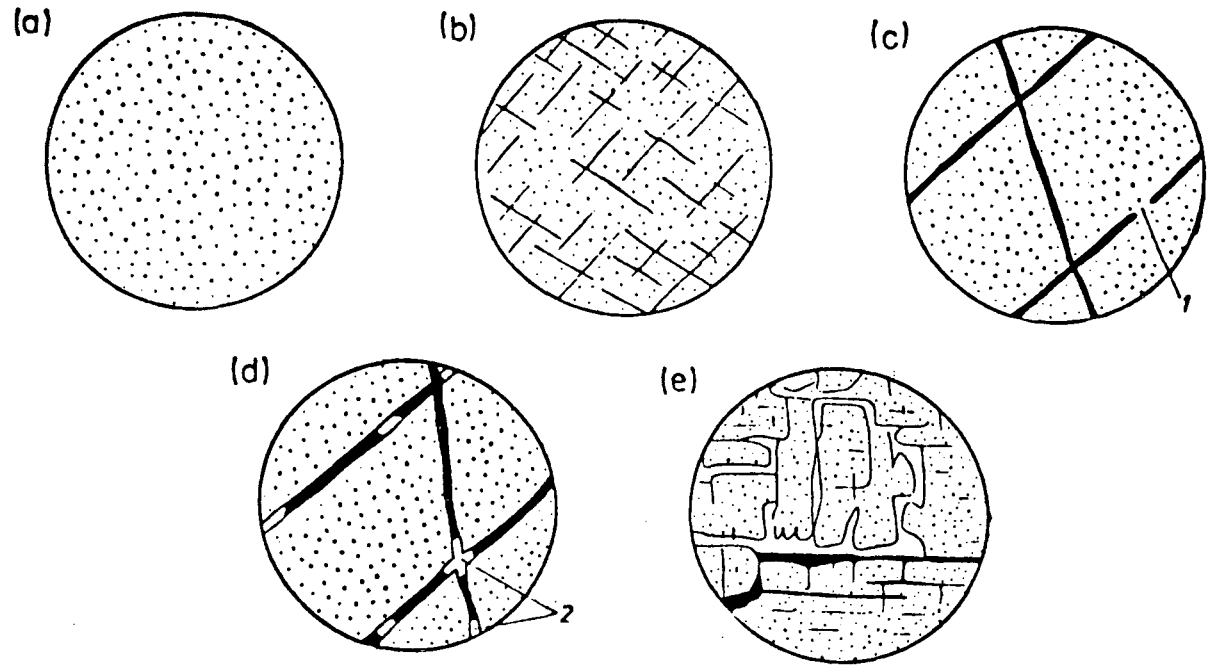

Fig. (1-1) Kind of media occurring in rock masses (after Louis, 1976): (a) porous medium, (b) porous jointed medium, (c) porous medium with impervious barriers (1-rock bridge), (d) porous medium containing channels (2-channel) (e) karstic medium.

involving underground waste isolation. For example, it is crucial to the assessment of the risks of underground disposal of nuclear waste. If rock masses were truly solid, burying waste underground would be risk free. But, because there are discontinuities (joints, faults, cleavage, bedding etc.) in rock, nuclear wastes might escape from a underground repository by traveling through discontinuities in the rock. If the waste travels far enough, aquifers or rivers and lakes could be contaminated. The risk of underground disposal depends on how far wastes travel, and how economical the engineering of underground disposal is. To assess the risk, we have to predict the amount of fluid flow through a network of fractures, or calculate the flow through a particular complex fracture or fault. In either case, an understanding of the mechanical and hydraulic properties of single fracture is required because the hydraulic and mechanical properties of a jointed rock mass depend on the hydraulic conductivity of a single joint.

To predict flow through a fracture, engineers often use the familiar cubic law:

$$Q = h^3 \, |\nabla P| \, / \, 12\mu \qquad (1\text{-}1)$$

where h is fracture aperture, $|\nabla P|$ is the magnitude of the fluid pressure gradient, and μ is the viscosity of the fluid. The cubic law is derived from the Navier-Stokes equation for incompressible flow, in which the fracture is assumed to be a planar channel with parallel sides; flow within this channel is considered to be viscous laminar flow with no-slip boundary conditions. From the derivation of equation 1-1, we know that the velocity profile for this flow is parabolic, with zero velocity at the upper and lower surfaces in order to satisfy the no-slip boundary condition. The total fluid flux Q, which is found by integrating the velocity across the thickness of the channel, varies as

the cube of the separation h between the plates.

The cubic law has been widely used, but experiments show it is not sufficient to describe flow through most fractures in rock. Raven and Gale (1985) performed experiments on flow in tension fractures using homogeneous samples of granite, basalt and marble, and found that their results did not follow the cubic law. In analysis of fracture displacement and fluid flow data from the comprehensive lab experiments, Pyrak-Nolte et al. (1987) suggested a power-law relationship between flow and displacement, but the power differed greatly from a cubic law representation.

Deviations from the cubic law are expected, and the reasons that the cubic law breaks down can be explained. The deviation comes from the hypothesis that assumes the planar surfaces remain parallel. In another words, in the hypothesis fracture apertures are constant, surfaces are smooth, and the top and the bottom surfaces are not in contact at any point of the fracture. On the contrary, in reality apertures change along the fracture, surfaces are rough, and a fracture has contact points or areas. When a fracture is stressed, the void space of a fracture deforms and a change in contact area takes place; the change in void geometry and increase in contact area then causes a change in the hydraulic and mechanical properties of the fracture.

We can understand why the cubic law is not sufficient; however, to better describe flow through a fracture, we have to do more investigation to account for the effect of fracture roughness. This work is devoted to relating the mechanical properties of the fractured rock to the geometrical characterization of the rough-walled fracture. Then the equation describing flow through a fracture with smooth parallel walls can be modified to include the effect of the contact areas of the fracture surfaces. If realistic

aperture distributions can be found, the numerical simulation procedure could be used to predict the flow rate as a function of normal stress and roughness parameters.

1.2. APPROACH

There are two approaches in scientific and engineering research. Experiments in the field and in the lab are the most important and fundamental type of research. The second approach is to develop analytical solutions for problems. However, analytical solutions are only easily derived when the mathematical region is homogeneous, when the geometry is simple, when the boundary conditions are relatively straightforward, and when the governing partial differential equations are linear. In recent years, the numerical technique has now reached such a stage of development and popularity that one might well doubt whether there is any other approach which can offer comparable power, versatility and simplicity. The latter techniques permit us to work on quantitative aspects of realistic problems in engineering and applied science where the boundary geometry of the region of interest is far too complex for analytical solutions to be feasible. Since there are investigators working on *in situ* and laboratory experiments, and analytical solutions are precluded due to the complex geometry of fracture void space and irregular boundary conditions, an approximate solution using a numerical method becomes the only feasible way to solve complex problems that account for diverse fracture hydromechanical properties, with the precision and resolution needed for this study.

Numerical methods can be divided into two distinct classes: those that require approximations to be made throughout the region of interest, and those that require

approximations to be made only on the boundary of the region. Finite difference and finite element methods fall in the first class. Boundary element methods constitute the second class. Up to now no one has used the boundary element method in three dimensions to study the hydraulic and mechanical properties of fractures. I have developed two computer programs using the boundary element method to numerically simulate fracture deformation and flow through the fracture. I chose the boundary element method as the numerical solution technique because the method has these advantages:

(1) Only the surface or boundary, rather than whole body or region, is required to be discretized for the boundary element method. Therefore, preparing and checking the input data is simplified. This is a very important point in practice. The advantage is obvious for my coupled computer programs because the fracture deformation program and the flow program share the same very complex rough-walled fracture boundary. The output of the fracture deformation program provides the input to the flow program directly.

(2) Boundary element method reduces the dimensionality of the basic process by one, i.e. only two-dimensional surface-integral equations arise for three dimension problems. It means that boundary element methods lead to a much smaller system of algebraic equations than a finite element solution for the same problem. From the computational point of view, much less computer storage and computer time will be required by the boundary element method. This advantage is particularly important for the three-dimensional problem where we take into account the effect of randomly distributed

contact areas on fracture stiffness and flow tortuosity.

(3) Boundary element methods are particularly attractive for simulating the fracture deformation problem, which may be expressed as an exterior boundary value problem, where the fracture rough-walled surfaces define the boundary of a fracture in an infinite space. Boundary element methods do not impose restrictions on the size of the solution region (i.e., the region may be extended out to infinity.).

I focus the content of my thesis on the results obtained from the numerical simulations, even though I spent more than 60% my research time on developing and validating the boundary element method computer programs. Results are presented in chapters 4, and 5. Two computer programs are listed in the Appendix, with instructions for their use.

CHAPTER 2

REVIEW OF PREVIOUS WORK

The effect of fracture geometry on mechanical and hydraulical properties of many rock masses has been studied experimentally and theoretically by many researchers and engineers. Fracture mechanical properties can be characterised by a specific stiffness, which is defined as the slope of a tangent to the curve relating the average closure between the two surfaces of a fracture to the stress across the fracture, at a given stress.

2.1. MECHANICAL DEFORMATION

The deformation of the asperities of contact and apertures between two rough surfaces of a fracture in response to normal stress across the fracture is a matter of great practical and theoretical significance.

Goodman (1976) has done experiments of measuring fracture closure as a function of normal stress on artificially induced tensile fracture. Two types of measurements were made. In one case, ''mated'' fractures were used, in which the two halves of the core were placed in the same relative position that they occupied before fracturing the core, so that the hills and valleys of the two fracture surfaces were complements of one another. In the other case, the experiments were done with ''unmated'' fractures, in which the two surfaces were rotated from their original position relative to one another, and removed uncorrelated for all wavelengths. As would be expected, he found that unmated surfaces showed much greater fracture closure, and resulted in much lower fracture stiffness, than did the mated surfaces. He also proposed an

empirical relationship between the fracture closure and the normal stress in the following dimensionless form:

$$\frac{\sigma - \zeta}{\zeta} = C\left[\frac{d}{d_m - d}\right]^t \tag{2-1}$$

where

σ = *the* normal effective stress,

ζ = *an* initial, low "seating" stress,

d = *the* joint closure,

d_m = *the* maximum joint closure,

t = *an* exponent.

C = *a* constant

Mated and unmated fractures follow the same relationship but with different constants c and t.

Swan (1983) measured normal stiffness in slate joints. Essentially, his method follows that used by Goodman (1976) in that a correction is made to the stiffness data obtained from an inclusively defined joints. The experiments in which joints have been deformed under normal stress exhibited a logarithmic load-deformation behaviour, as found by Goodman (1976), in all but a few cases within the range $0 < \sigma < 20$ MPa. He indicated that a simple linear relationship between stiffness and stress is appropriate, even taking into account aperture effects.

Bandis at al. (1983) collected fresh and weathered joint samples from exposures of five rock types in the United Kindom, namely slate, dolerite, limestone, siltstone and sandstone. They conducted laboratory investigations of the deformation

characteristics of the natural, unfilled rock joints under normal loading. The following hyperbolic function fit their data well for mated surfaces

$$\sigma = \frac{d}{\alpha - \beta d} = \frac{1}{\frac{\alpha}{d} - \beta} \tag{2-2}$$

where σ and d are as defined in equation 2-1 and α and β are constants. Equation 2-2 implies that for very large values of σ ($\rightarrow\infty$), d must tend to the limiting value α/β, hence the maximum fracture closure d_m defines the asymptote α/β. Also, the specific stiffness of the joint, κ, at any level of σ was found from the derivative of equation 2-2

$$\kappa = \frac{\partial\sigma}{\partial d} = \frac{1}{\alpha(1-\frac{\beta}{\alpha}d)^2} \tag{2-3}$$

from which the initial normal stiffness κ_o (as σ=0) is given by the inverse of α, so that the specific stiffness at any stress becomes

$$\kappa = \frac{\kappa_o}{(1 - \frac{d}{d_m})^2}. \tag{2-4}$$

For unmated joints, they established the following exponential empirical relationship between joint stiffness and closure.

$$\ln\sigma = C + Jd \tag{2-5}$$

from which the specific stiffness becomes

$$\kappa = \frac{\partial\sigma}{\partial d} = J\sigma \tag{2-6}$$

so that unmated joints with uncorrelated upper and lower surfaces exhibited

proportionality between normal stress and stiffness.

Raven and Gale (1985) collected five granite core samples (0.100, 0.150, 0.193, 0.245, and 0.294 m dia) with the natural fracture plane located halfway along the core length. These cores were collected using a rock bolting, overcoring technique to ensure minimal disturbance of the fracture plane during sampling. In the process of the uniaxial compression testing, fracture and rock deformation across the fracture plane and the applied load were measured. The maximum axial stress is 30 MPa. They indicated that the most notable feature of the fracture closure-stress curves during loading and unloading is the highly non-linear behaviour with pronounced hysteresis and permanent deformation and that non-linear behaviour is compatible with the mechanics of fracture deformation. As load is applied across the fracture plane, the fracture closes, rapidly increasing the number of contact points which distributes load, and decreases closure rate. They calculated the normal fracture stiffness by differentiating the normal stress-deformation curves, and indicated that the normal stiffness-stress relations were approximately linear, particularly at normal stress less than 15-20 MPa. However with increasing load cycle the change in normal stiffness-stress relation decreases with increasing sample size, and the stiffnesses are not linear functions of stress except for the smallest sample.

Pyrak-Nolte et al. (1987) summarized and analyzed results of a comprehensive laboratory study of the mechanical displacement, permeability, and void geometry of single rock fractures in a quartz monzonite. Though typically very non-linear, their closure-stress curves show very little hysteresis. It means that the rock, including the asperities of contact between the fracture surfaces and the voids adjacent to these

asperities, deforms reversibly, that is, elastically. They found that specific stiffness is not proportional to stress as it would be expected by equation 2-6 and that even at a stress of 85 MPa, the joints continued to close and the stiffness remained finite. The finite stiffness at the highest values of stress is explained by the fact that there still are open voids between the surfaces of the fractures at these stresses.

Pyrak-Nolte et al. (1987) developed a metal-injection technique that provided quantitative data on the precise geometry of the void spaces between the fracture surfaces and the areas of contact at different stresses. The metal casts of the void geometry corresponding to the normal stress were examined using both a scanning electron microscope and photographic techniques. Images of each of the two fracture surfaces were superimposed to form a composite image of the contact area and void geometry. Percent contact area - stress curves were obtained for two samples from the composite images. They noticed that contact areas are of the same order of magnitude as found by Goodman (1976) and Bandis et al. (1983) and that the increase in contact area with stress for one of the samples correlated well with observed increases in stiffness with stress.

Some reseachers explored a theoretical approach to predict fracture closure and fluid conductivity as function of stress. Greenwood and Williamson (1966) presented a theory of elastic contact between a random nominally rough surface and a perfectly smooth surface. They assumed that the rough surface was covered by a large number of identical, spherically shaped asperities all having the same radius of curvature, $\tilde{R}$, with heights described by a specified statistical distribution. Each asperity deforms as a Hertzian contact (Timoshenko and Goodier 1951) for a rough surface pressed against

another flat surface. The total behavior was calculated by the sum of all contacting asperities. They showed that for a peak height distribution $\Phi(Z^*)$, elastic Hertzian contact theory will result in n contacts, given by

$$n = \eta A \int_{\bar{d}}^{\infty} \Phi(Z^*) dZ^* \tag{2-7}$$

where the true contact area, A' is:

$$A' = \pi \tilde{R} \eta A \int_{\bar{d}}^{\infty} (Z^* - \tilde{d}) \Phi(Z^*) dZ^* \tag{2-8}$$

and the relationship between fracture closure d and far field normal stress σ is:

$$\sigma = \frac{4}{3} \eta \tilde{R}^{1/2} E' \int_{\bar{d}}^{\infty} (Z^* - \bar{d})^{3/2} \Phi(Z^*) dZ^* \tag{2-9}$$

where

$$\frac{1}{E'} = \frac{1 - \nu_1^2}{E_1} + \frac{1 - \nu_2^2}{E_2} \tag{2-10}$$

and E and ν are the Young's modulus and Poisson's ratio of the two elastic surfaces,

A = nominal contact area,

Z^* = height of local maximum on the composite topography,

η = the number of asperity peaks per unit area,

$\bar{d}$ = the separation between reference planes in the two surfaces at any stress, so that $\bar{d} = d_o - d$. d_o is initial separation at zero stress and d is the closure of the two surfaces.

Using equations 2-8 and 2-9 and assuming an exponential distribution of peak asperity heights, given by

$$\Phi(Z^*) = \frac{1}{s}\, e^{-Z^*/s}, \tag{2-11}$$

Greenwood and Williamson (1966) and Swan (1983) derived the following expressions for the normal displacement, $\bar{d}$, contact area of the asperities, A', and the specific stiffness, κ,

$$\bar{d} = \left\{ d_o - s \ln [\pi^{1/2}(\eta \tilde{R} s) E'(s/\tilde{R})^{1/2}] \right\} + s \ln\sigma = \alpha + s \ln\sigma , \tag{2-12}$$

$$A' = (\pi \tilde{R}/s)^{1/2} \sigma A / E' , \tag{2-13}$$

$$\kappa = \frac{\partial \sigma}{\partial \bar{d}} = \frac{\sigma}{s} . \tag{2-14}$$

Note that α is a constant and equations 2-12 and 2-14 are of the same form as equations 2-5 and 2-6 found by Bandis et al. (1983).

Greenwood and Williamson concluded that although height distributions tend to be Gaussian rather than exponential, the exponential distribution is nevertheless a fair approximation to the uppermost 25% of the asperities of most surfaces, and that fracture deformation depends as much on the details of the surface topography as on the elastic constants of the fracture.

Instead of probability density functions for the asperity heights, Swan (1983) used digital profiles from the actual surfaces to calculate the deformation of the fracture. Swan measured topography of ten different joint surfaces of Offerdale slate with a simple profilemeter, and showed that these particular joints exhibited a Gaussian-type height distribution. For certain conditions and assumptions, he observed that hydraulic conductivity, normal stiffness, and the true contact area are simple function of pressure and initial aperture, and that the surface roughness properties appear to be irrelevant.

Brown and Scholz (1985a and 1986) developed a more general version of the Greenwood and Williamson elastic contact theory. This theory is valid for the contact of two rough surfaces (both mated and unmated) and is entirely consistent with the Greenwood and Williamson (1966) theory if one surface is assumed to be flat. Superpositioning the heights at each point along the surfaces, they obtained a continuous function of two dimensions which they termed the composite topography that contained only the uncorrelated part of the two surface profiles. Describing the contact of two rough surface by the heights of the local maxima of the composite topography, they overcome the difficulty of the Greenwood and Williamson analysis. The difficulty is that Greenwood and Williamson theory deals with one rough surface in contact with another flat surface, whereas each of the two surfaces of a rock fracture is rough. Brown and Scholz (1985a and 1986) also included a term in their theory to account for tangential stress causing from the oblique contact of spheres so that the stresses at the contacts are not restricted to be normal. The results of their more general theory of elastic contact is as follows:

$$\sigma = \frac{4}{3}\eta<\psi><E'><R^{1/2}> \int_{\bar{d}}^{\infty} (Z^* - d_o + d)^{3/2}\, \Phi(Z^*)dZ^* \ , \qquad (2\text{-}15)$$

where

Z^* = random variable representing the height of the peaks,

η = total number of maxima per unit area,

$<\psi>$ = mean value of the tangential stress correction factor,

$<E'>$ = mean value of elastic constant,

$<R^{1/2}>$ = mean value of square root of curvature of the contacts,

d = joint closure,

σ = normal stress,

d_o = the distance between the reference planes at $\sigma = 0$,

$\bar{d}$ = $d_o - d$,

$\Phi(Z^*)$ = probability density function.

The derivation of equation 2-15 required the curvature term $\tilde{R}$ and the tangential stress correction ψ to be statistically independent of the heights of local maxima on the composite topography, and implicit in the derivation of equation 2-15 is the assumption that the contacts do not interact elastically and that the half spaces on each side of the surfaces do not deform elastically, only the contacts deform.

Brown and Scholz (1985a and 1986) measured both joint closure and surface topography and used the techniques, developed by Nayak (1971) and Adler and Firman (1981), for mapping power spectra to probability density functions for the height of three dimensional peaks, as well as for finding the density of peaks and their curvature for Gaussian and inverted chi-square distributions, respectively. They indicated that the advantages of the inverted chi-square distribution is that it contains a parameter controlling its skewness, and therefore fits the topography data better than the symmetric Gaussian. Another property of the inverted chi-square distribution is that it has a finite maximum height, as does a real surface. This is in contrast to the Gaussian distribution, which has finite probability at heights approaching infinity.

They undertook a power spectra study of topographic measurements on natural joints in crystalline and sedimentary rocks, a bedding plane surface, and a frictional wear surfaces with wavelengths from 1 m to 20 μm. Their results of power spectra

showed that on each surface studied, although the slope of the power spectra on a log-log plot usually lies in the fractal range, it is not a constant and tends to decrease gradually as one moves from high to low frequency. The slope was interpreted as a fractal dimension which is a "jaggedness" parameter, indicating the propertion of high-to low frequency roughness. Steep spectral slopes, or small fractal dimensions, result in high correlation of the height of nearby points on the surface. Conversely, surfaces with shallow spectral slopes, or large fractal dimensions, appear rough on a fine scale since heights of near by points become more independent. Since the slope of the power spectra was not constant for a given surface, a simple relationship between roughness and surface size did not exist and it was suggested that extrapolation of rms roughness to larger surface sizes from limited bandwidth measurements must be done with care. However, the power spectrum showed that a strong correlation exists between the heights and wavelengths of the surface roughness, and also provided an idea of the expected variation in mechanical and hydraulical properties for natural discontinuities in rock.

Brown and Scholz eventually tested their elastic contact theory between two rough surfaces quantitatively by comparing fracture closures from experiment with fracture closures predicted by the theory. Good agreement between equation 2-15 and experimental joint closure measurements on ground surfaces of fused-silica glass samples and rock samples with uncertainties in some parameters implies that the theory still contains the essential physics of the joint closure process.

None of the asperity models discussed above takes account of the interaction between asperities or of the related deformation of each elastic half space bounded by

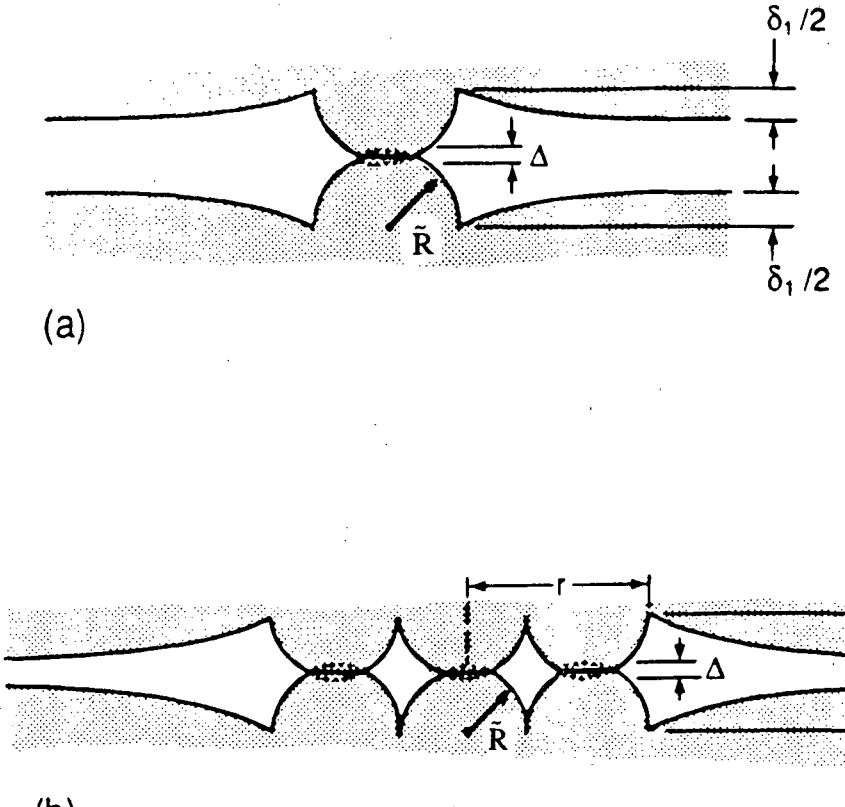

Fig. (2-1) (a) Sketch showing the deformations due to the contact between a simple pair of hemispherical asperities of radius $\tilde{R}$ and the indentation of the adjacent half spaces. (b) The deformations due to the contacts between several, contiguous pairs of hemispherical asperities contained within a radius r and the indentation of the adjacent half spaces (after Cook, 1988).

the joint surfaces. To account for the deformation of the half spaces defining the fracture in addition to the deformation of the asperities, Cook (1988) considered two simplified models; one of a single pair of hemispherical asperities in contact between two elastic half spaces of the same material, and another of a group of proximate hemispherical asperities, Figure 2-1. Both of these deformations were calculated from Hertzian contact theory (Timoshenko and Goodier 1951). The displacement, Δ, between the bases of the pair of hemispherical asperities of radius, $\tilde{R}$, under a load, T, was given by

$$\Delta = 2\left[\frac{3T}{4E'\tilde{R}^{1/2}}\right]^{2/3} = 2\left[\frac{3\pi p}{4E'}\right]^{2/3}\tilde{R}\ , \tag{2-16}$$

where $p = T/\pi\tilde{R}^2$ = the equivalent uniform stress on the circular contact between the base of the hemisphere and the half space. The maximum indentation δ_1, of the two half spaces by a uniform stress applied over the circular contact between the hemisphere and the surface of the half space is

$$\delta_1 = \left[\frac{4p}{E'}\right]\tilde{R}\ , \tag{2-17}$$

where $E' = (1 - \nu^2)/E$. The ratio of δ_1/Δ for an isolated pair of hemispherical asperities is

$$\frac{\delta_1}{\Delta} = \left[\frac{8\sqrt{2}}{3\pi}\right]^{2/3}\left[\frac{p}{E'}\right]^{1/3}, \tag{2-18}$$

so that $\delta < \Delta$, especially at relatively low stresses. For n asperities, the displacement due to the spherical contacts remains the same, Δ, but the maximum indentation of the two half spaces becomes

$$\delta_n = \left[\frac{4p}{E'}\right] \sqrt{n}\tilde{R} \ . \tag{2-19}$$

The ratio between the indentation of the half spaces by multiple asperities, δ_n, and the deformation at their spherical contacts, Δ, becomes

$$\frac{\delta_n}{\Delta} = \left[\frac{8\sqrt{2}}{3\pi}\right]^{2/3} (\frac{p}{E'})^{1/3}\sqrt{n} \ , \tag{2-20}$$

so that $\delta_n > \Delta$ for $n > [p/E']^{-2/3}$.

Cook's theory demonstrated that the deformation of the half spaces adjacent to a joint is important. Further, the fact that the specific stiffness of multiple contacts with different spacing on a flat, elastic surface is significantly less than it would be for widely separated contacts without any interaction may explain, to some extent, the non-linear increase in stiffness with stress as observed by Raven and Gale (1985) and Pyrak-Nolte at al. (1987).

2.2. FLUID FLOW

Because of recognition of the importance of flow through fractures in a number of natural flow systems, a considerable amount of experimental and theoretical research has been carried out on fluid flow between parallel surfaces with varying degrees of roughness.

Lomize (1951) was the first to study comprehensively the influence of roughness of fracture surfaces on flow rate. In terms of the Reynolds number Re and the friction factor Ψ he reduced the so-called cubic law for laminar flow in an open fracture with smooth walls to the simple relationship

$$\Psi = 96/\mathrm{Re}. \tag{2-21}$$

Changing the fracture walls from smooth to rough, he developed an empirical equation which included fracture roughness ε

$$\Psi = \frac{96}{\mathrm{Re}}\left[1 + 6.0\left[\frac{\varepsilon}{2h}\right]^{1.5}\right], \tag{2-22}$$

and is valid for $\frac{\varepsilon}{h} > 0.065$.

In general, laminar flow between parallel plates is given by an equation of the form

$$\Psi = \frac{96}{\mathrm{Re}} f \tag{2-23}$$

or

$$Q = \frac{1}{f}\,\frac{h^3}{12\mu}\,\frac{dP}{dx} \tag{2-24}$$

where $f = 1$ for smooth parallel plates, and $f > 1$ for rough parallel plates,

Q = the flux per unit length normal to the direction of the flow,

h = the aperture between the plates,

μ = the viscosity of the fluid,

$\frac{dP}{dx}$ = the pressure gradient in the direction of the flow.

Lomize demostrated the validity of equation 2-24 as long as the flow was laminar. The onset of turbulence was found to occur at Re ≈ 2300.

Witherspoon et al. (1980) did flow tests from a so-called ''closed'' condition, while a number of other workers (Louis 1969, Baker 1955, Huitt 1956, Maini 1971, Parrish 1963, Rayneau 1972, Rissler 1978) have investigated the effects of roughness

on flow in open fractures (Witherspoon 1980). Witherspoon et al. undertook laboratory investigations on tension fractures that were artificially induced in homogeneous samples of granite, basalt, and marble, which showed that the cubic law for a fluid flow in a fracture was valid. The investigations included radial and straight flow geometries and covered apertures ranging from 250 down to 4 μm and normal stress up to 20 MPa. Most of their results were found to follow the cubic law whether the fractures were open or closed. They reported that the effect of deviations from the ideal parallel plate concept only caused an apparent reduction in flow and were taken care of by the factor f, when it varied from 1.04 to 1.65. However, one of their data, for a joint in marble, exhibited marked deviations from the cubic law, as apertures decreased below 10μm. The specific flow became more or less independent, as the aperture further reduced below 6μm with increasing stress.

Engelder and Scholz (1981) measured flow rates and thus permeability within ground joints of Cheshire quartzite covered with particles of #80 grit at effective pressures up to 200 MPa. They observed the same puzzling phenomena that at high flow rates and wider apertures the flow-aperture curves appeared to parallel a cubic law, but at low flow rates and narrower apertures flow rates per hydraulic head $Q/\Delta P$ were independent of apertures. They concluded that at low effective pressures and wide apertures the cubic law was confirmed, but cubic law at high effective pressure was inadequate. A modification was then presented for the cubic law, by considering the theory of random surfaces of Greenwood and Williamson (1966) :

$$Q = \left[\frac{W_n - [W_o + (E' A \sigma_o)^{1/2} \exp((d_o - d)/2s)]}{2}\right] \frac{\rho g d^3}{12\mu} \frac{dP}{dx} . \qquad (2\text{-}25)$$

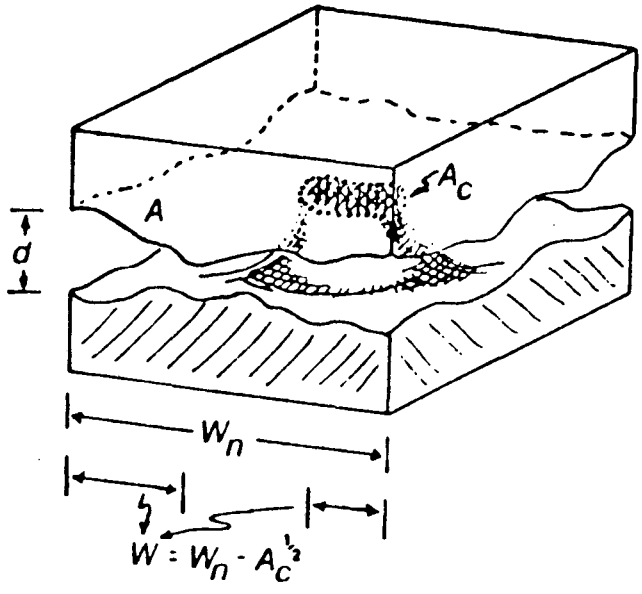

Fig. (2-2) Schematic of a joint where A is the nominal surface area, A_c is the real area of contact, d is mean aperture, W_n is nominal width of joint, and W is the effective cross-sectional width (after Engelder and Scholz, 1981).

As Figure 2-2 shows, where

W_n = nominal width of the fracture ,

W_o = contact cross section at zero effective pressure,

s = standard deviation of the topography of fracture surfaces,

σ_o = a normal effective reference pressure,

E' = the mean value of the elastic constants pertinent to Hertzian contact,

d = the aperture between two surfaces of fracture,

d_o = the aperture at σ_o,

ρ = the density of the fluid,

g = the gravitational constant,

μ = the viscosity of the fluid,

$\frac{dP}{dx}$ = the pressure gradient in the direction of the flow.

The contact area at σ_o, A_{oc}, can be expressed as follows:

$$A_{oc} = E' \sigma_o A \ . \tag{2-26}$$

Equation 2-25 then is rewritten as

$$Q = \left[\frac{W_n - [W_o + A_{oc}{}^{1/2} \exp((d_o - d)/2s)]}{2} \right] \frac{\rho g d^3}{12\mu} = \frac{C d^3}{f} \frac{dP}{dx}, \tag{2-27}$$

where

$$C = \frac{\rho g}{12\mu} \ , \quad \text{and} \quad \frac{1}{f} = \frac{W_n - [W_o + A_{oc}{}^{1/2} \exp((d_o - d)/2s)]}{2} \ .$$

Notice that equation 2-27 has two problems. One is that it does not consider the effect of new contacts, produced as stress increases on the flow, and another is the assumption that stiffness-stress relationship is linear.

Raven and Gale (1985) conducted steady-state radial-flow tests at different stresses on the same natural joint in samples of granite with diameters from 0.1 m to 0.294 m. Their flow rate-aperture curves departured from the cubic law plotted as a straight line on a log-log plot with a slope equal to one third. At low to intermediate normal stress, the fracture aperture and flow rate were characterized by slope less than one third, suggesting a reduction in flow rate greater than that attributable simply to fracture closure. They interpreted that this additional flow-rate reduction was probably due to increasing contact area and flow-path tortuosity with increases in normal stress. At high normal stress the fracture aperture and flow rate showed a slope that was greater than one third and approached unity. They stated that this increased slope suggested the calculated residual fracture aperture at maximum normal stress might be too

small and thus the parallel plate model might not be valid for rough fractures at high normal stress.

Pyrak-Nolte et al. (1987) measured hydraulic conductivity with a linear flow technique for three natural joints on which they had made measurement of joint closure and contact areas as a function of normal stress. They found that at large joint aperture, corresponding to high stress, specific flow decreased much more rapidly than the aperture to the third power, and that at effective stresses higher than 20 MPa, the mean fracture aperture continued to diminish with increasing stress, but this had little effect on flow because the small tortuous flow channels deformed little with increasing stress. Thus their results showed departures from the cubic law, and non-stress related changes in permeability at high stress similar to those noted above. Inlight of the value of the irreducible, aperture-independent limit at the highest stresses and smallest apertures, they proposed that the specific flow through natural joints is given by an equation of the form

$$Q = Q_{\infty} + C(d_m - d)^t \ , \tag{2-28}$$

where

Q_{∞} = the irreducible flow at high stress,

C = an empirical constant depending upon the viscosity of the fluid, the head gradient and the topography of the two joint surfaces,

d = the joint closure,

d_m = the joint aperture at zero stress,

t = an empirical exponent that depends upon the topographies of the two joint surfaces.

As described in the discussion on mechanical deformation, Pyrak-Nolte et al. (1987) have developed a metal-casting technique of the void spaces between natural joint surfaces at different effective stresses and a computer enhanced composite image of these void spaces at a stress of 35 MPa. This image showed relatively large void spaces (oceans) connected by tortuosity paths through regions of high contact density (archipelagoes). This enabled them to explain the finite joint stiffness and the stress-independent flow or the irreducible flow at high stresses. They indicated that at the highest stresses and smallest apertures, the principal impediments to fluid flow through the space between joint surfaces in partial contact were to be found in the tortuous channels through the archipelagoes of asperity contact between the relatively large oceanic voids, and that if these channels comprise conduits of roughly equant cross sectional dimensions, the conduits would deform relatively little as the stress increased, leading to a constant resistance to flow, so that the deformation of the large voids gave the joint finite stiffness at high stresses but had virtually no effect on fluid flow, though it did effect the storativity of the joint.

Brown (1987) generated numerically realistic rough surfaces using a fractal model of surface topography. Pairs of these surfaces were places together at some fixed distance and were held parallel to form a ''joint'' with a random aperture distribution. He further examined the deviation of fluid flow through rock joints from the parallel plate model using a two dimensional finite-difference method. He did a total of 300 simulations. Three fractal dimensions were used to generate model surfaces. Ignoring the deformation of the surfaces and setting the points with local aperture $D(x,y)=0$ as ''contacts'', he separated pairs of surfaces at 10 different mechanical apertures, D_m,

which were the separations between the mean joint surfaces. Finally, 10 different pairs of surfaces were considered at each fractal dimension and mechanical aperture. The solution of the simulation was the local volume flow rate through the joint. This solution was used directly in the cubic law to get so-called "hydraulic aperture", D_h

$$D_h = \left[\frac{12Q\mu}{\Delta P/L_x}\right]^{1/3}, \tag{2-29}$$

where Q was the average flux per unit width of the joint obtained from the simulations, and $\Delta P/L_x$ was the average pressure gradient across the whole joint. Quantitative measures of the validity of the cubic law were then obtained by comparing the hydraulic aperture to the mechanical aperture D_m and the mean aperture $<D>$. A mean aperture was defined by

$$<D> = \frac{1}{L_x L_y}\int_0^{L_x}\int_0^{L_y} D(x,y)\,dx\,dy \tag{2-30}$$

where $D(x,y)$ was the local aperture and and L_x and L_y were the dimension of the joint plane.

He plotted the parameter $[D_h/<D>]^3$ for different mechanical apertures or separations and showed that the parameter is always less than unity, particularly for small values of the mechanical aperture. In other words, the results showed that at large separations the surface topography has little effect and at small separations the flow is tortuous, tending to be channeled through high-aperture region. However, the actual flow rate between rough surfaces was about 70-90% of that predicted by the parallel plate model. As Cook (1988) commented, the discrepancy was quite insufficient to explain the major departures from the cubic law for flow through joints

as observed by Witherspoon et al. (1980), Engelder and Scholz (1981), Raven and Gale (1985) and Pyrak-Nolte et al. (1987).

With two first-order approximations, Cook (1988) derived the equation (2-31) for flow through a joint as follows:

$$Q = \frac{D_h^3}{12\mu}\frac{dP}{dx}\frac{1}{\tau}\frac{1-\bar{a}}{1+\bar{a}} = \frac{\rho g}{12\mu}\frac{dP}{dx}D_o^3[1+\ln\bar{D}]^3\frac{\bar{D}^2}{2-\bar{D}}, \qquad (2\text{-}31)$$

where the fraction of the joint area in contact, $\bar{a}$, at any stress is assumed by the ratio of the closure at this stress, d, to the mean aperture at zero stress, D_o, the tortuosity, τ, at any stress is assumed by the ration of the mean joint aperture at zero stress to the mean joint aperture at that stress, D^*, i.e. $\tau = D_o/D^*$, and $\bar{D} = D^*/D_o = (d-D_o)/D_o$. Equation 2-31 can be written as

$$\ln\left[\frac{12\mu Q}{\rho g\frac{dP}{dx}D_o^3}\right] = \ln\left[[1+\ln\bar{D}]\frac{\bar{D}^2}{2-\bar{D}}\right], \qquad (2\text{-}32)$$

which is plotted in Figure 2-3. From Figure 2-3 it can be seen that the slope of the line relating the logarithms of specific flow and aperture is not 3, as given by the cubic law, but is always greater than about 6. It means that, even to a first order approximation, specific flow for joint in partial contact should not be proportional to the cube of the joint aperture but rather to a higher and variable power, as can be seen in the data from Witherspoon et al. (1980). As suggested by Pyrak-Nolta et al., equations 2-31 and 2-32 were also modified by adding to them the stress-independent component of flow, Q_∞, to yield

$$Q = \frac{D_h^3}{12\mu}\frac{dP}{dx}\frac{1}{\tau}\frac{1-\bar{a}}{1+\bar{a}} = \frac{\rho g}{12\mu}\frac{dP}{dx}D_o^3[1+\ln\bar{D}]^3\frac{\bar{D}^2}{2-\bar{D}} + Q_\infty, \qquad (2\text{-}33)$$

and

$$\ln\left[\frac{12\mu Q}{\rho g \frac{dP}{dx} D_o^3}\right] = \ln\left[[1 + \ln\bar{D}]\frac{\bar{D}^2}{2-\bar{D}}\right] + Q_\infty . \qquad (2\text{-}34)$$

Equation 2-34 was also plotted in Figure 2-3 from which it could be seen that this equation represents the stress-independent flow at high stresses quite well.

Coakley (1989) generated fracture patterns of voids and contact areas, with complexity typical of experimental data, by clipping a correlated Gaussian process defined on a N by N pixel square region. As Brown (1987) did, he assumed that local flow was proportional to local aperture cubed times local pressure gradient, and solved the flow through a pattern of voids and contact areas using a finite-difference method. After solving for the flow through simulated 10 by 10 and 30 by 30 pixel patterns of voids and contact areas, he developed a model to predict equivalent permeability in terms of spatial statistics computed from the arrangement of voids and contact areas within the fracture.

Walsh (1981) analyzed the effect of increasing contact areas and decreasing apertures of a fracture under increasing compression on the flow through the fracture. Making use of a analogy between the two-dimensional heat flow in a medium with constant conductivity and the laminar flow of an incompressible fluid, he found that the effective macroscopic permeability k^* was

$$\frac{k^*}{k_o} = \frac{1-c}{1+c}, \qquad (2\text{-}35)$$

where k_o is permeability of the fracture with no asperities and c is the ratio of the contact area to the total area of the fracture. The effective macroscopic permeability,

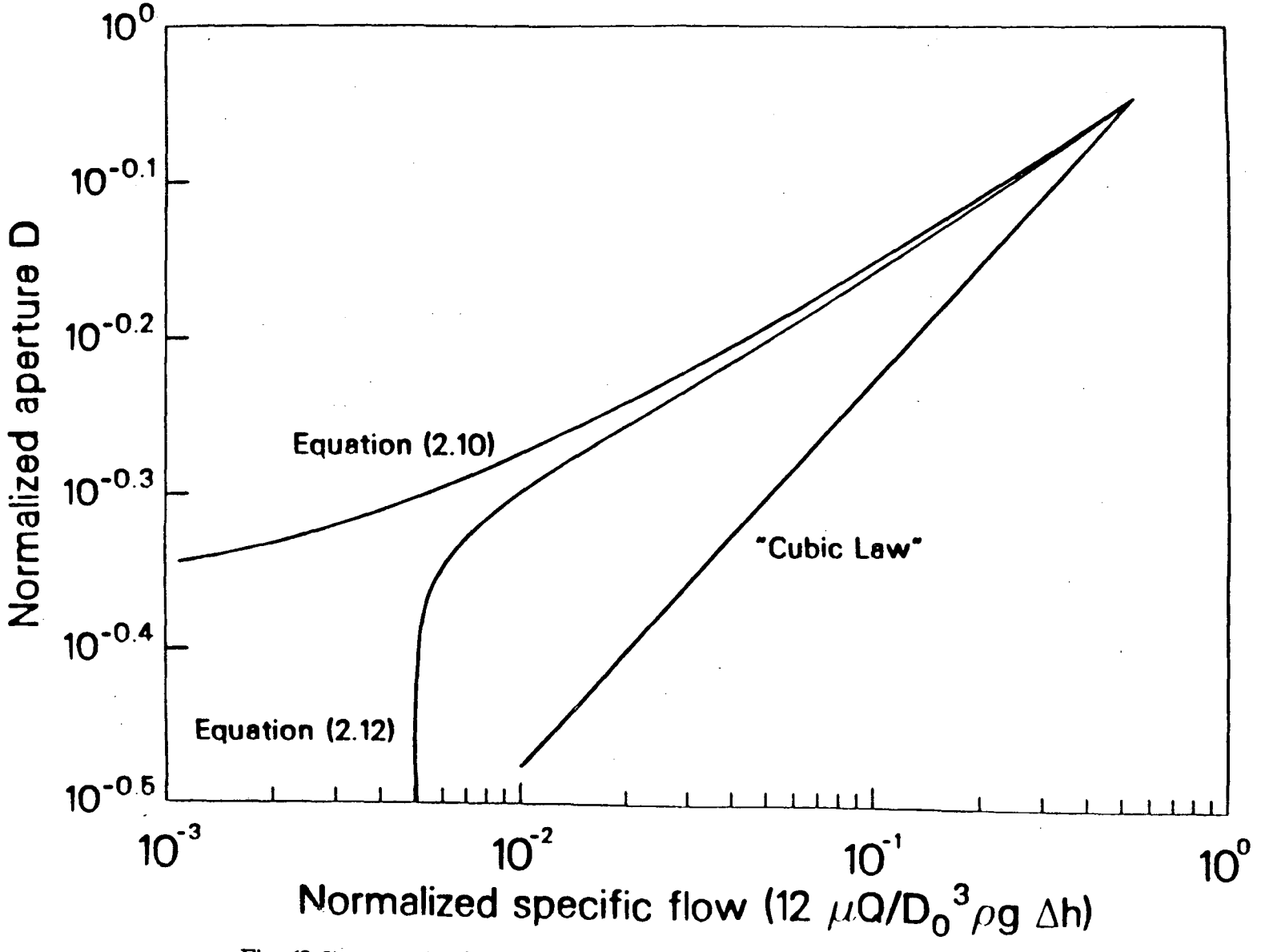

Fig. (2-3) A plot of the logarithm of normalized joint aperture against the logarithm of normalized specific flow according to equation (2-32 and 2-34), analytical solutions that account for the effects of tortuosity, and contact area, and irreducible flow, respectively (after Cook, 1988).

k^*, can represent flow through the fracture on a length scale large enough to cover many asperities.

Chen et al. (1989) used numerical analogues and analytical methods to investigate the effect of contact area geometry on the permeability of a fracture. They verified equation 2-35, derived by Walsh (1981) using a Maxwell-type effective medium approximation, for contact areas up to at least 25%. Considering that equation 2-35 might be a good approximation for flow only when contact areas are uniformly spaced and had nearly circular shape. They extended the Walsh-Maxwell approach to randomly oriented obstacles of elliptical shape with the results verified numerically for certain values of the aspect ratio and percentage contact area. The expression for elliptical obstructions was only slightly different in form from equation 2-35 for circular obstructions:

$$\frac{k^*}{k_o} = \frac{1 - \beta c}{1 + \beta c}, \tag{2-36}$$

where

$$\beta = \frac{(1 + \alpha)^2}{4\alpha}, \tag{2-37}$$

and the aspect ratio α (≤ 1) was defined as the ratio of the minor to major axis.

They also studied fractures with more irregular contact area geometries using the boundary-element method. They found that such fractures had permeabilities that were lower (by as much as 30%) than would be predicted by Walsh's expression, but which could be fit very well by the effective medium approximation if an equivatent aspect ratio is used.

2.3. SUMMARY

Using a wide variety of rocks, fluids, joints, flow geometries, measuring techniques, and analysis method, different investigators noted similar phenomena, such as the nonlinear stress-deformation relationship, and the effect of aperture variation on the flow through a single fracture. However, this review points out several significant inconsistencies, such as stress-stiffness relationship, applicability of the cubic law, and the effect of contact area or tortuosity on flow. Existence of inconsistencies leads us to do further research on this project. Witherspoon et al. (1980) pointed out that "Much more work is needed in understanding the mechanical and hydraulic behavior of a fracture that is deforming under stress".

CHAPTER 3

MATHEMATICAL FORMULATION

3.1. GENERAL

Many important engineering problems can be reduced to mathematical models classified as "boundary value problems". These are characterized by a region of interest R enclosed within a boundary S. The physics of the problem in R is modeled by a partial differential equation. If sufficient constraints or conditions are specified on the boundary, the solution to the problem then is assured uniquely. Two boundary value problems need to be solved for studying hydro-mechanical properties of a single rough-walled fracture. One is fracture elastic deformation subject to uniform normal stress. Another is the viscous steady flow of an ircompressible fluid flow through the fracture void space under a uniform pressure gradient. In Figure 3-1, the fracture is represented by a very thin and very wide channel bounded by surfaces. The inner side is rough, and consists of regions where the top surface and bottom surface are in contact (asperities), surrounded by regions where the two surfaces are separated by a distance (known as the aperture, h) that varies spatially. A normal distributed load T is applied in the direction perpendicular to the fracture plane.

The fracture deformation problem is a so-called exterior problem in which the region of interest R is the infinite region outside the boundary S. The object of solving the fracture problem is to find the distributions of stresses and displacements in the infinite body and on the fracture boundary. The flow problem is called an interior problem in which R, the region of interest, is the finite region inside the fracture. The object of solving the flow problem is to find the distributions of fluid pressures and

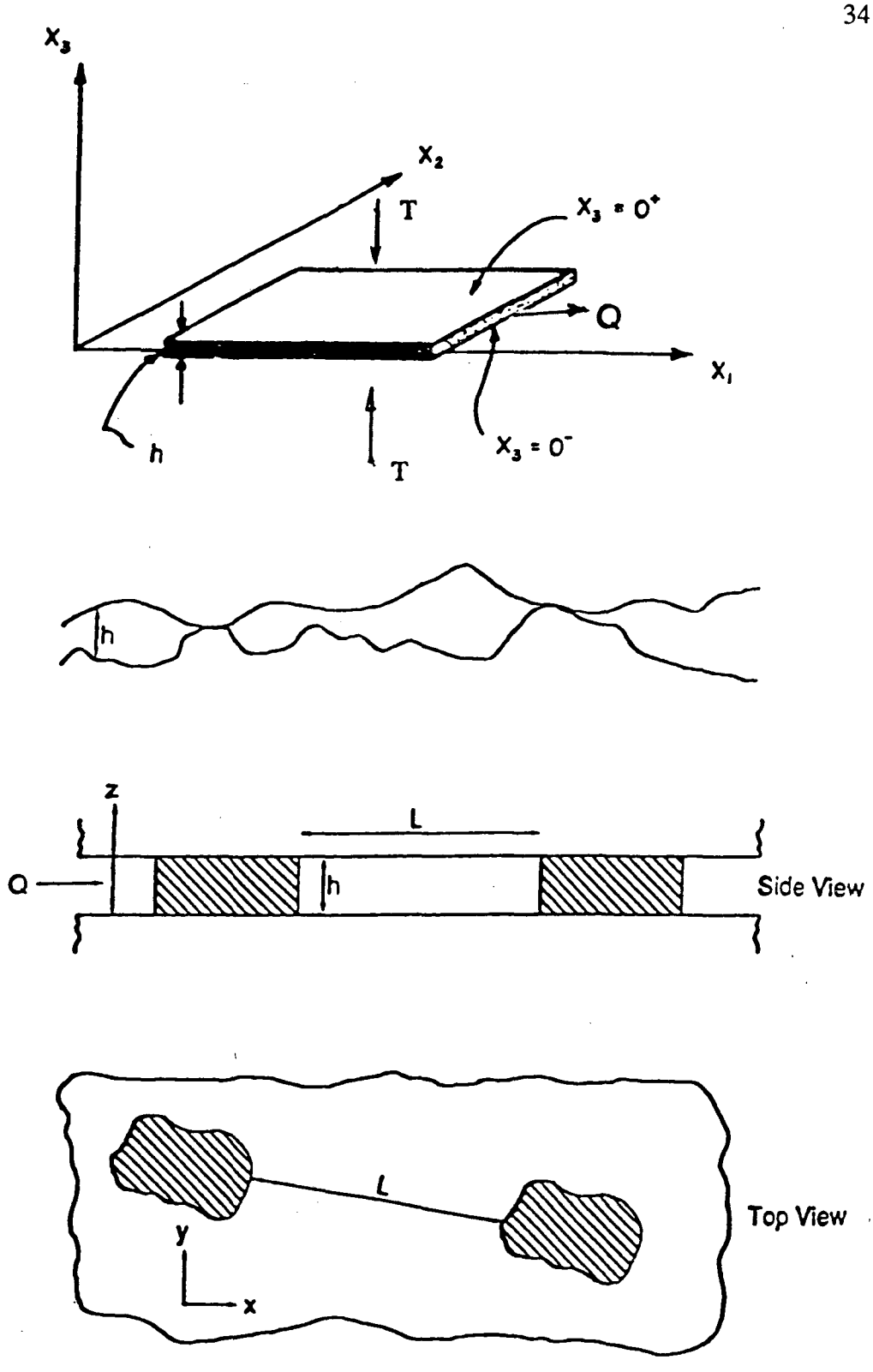

Fig. (3-1) (a) Representation of a horizontal fracture in an infinite space.
(b) Side view of a rock fracture.
(c) & (d) Idealized fracture with parallel walls and isolated asperities.

fluxes in the fracture void space and on the fracture boundary.

The specified boundary conditions differ when we solve two problems separately. Components of traction and components of displacements are specified at the external boundary (the periphery of fracture) and the internal boundaries (the peripheries of contact areas) in three dimensions for solving the fracture deformation problem, while components of fluid pressure and flux are defined at the boundaries only in the fracture plane (two dimensions) for solving the flow problem.

As mentioned before, an exact analytical solution is almost impossible to find for problems with complex boundary conditions, and the boundary element method becomes the best alternative approach.

The following section briefly describes the boundary element method that utilizes "point-source" type solutions to the governing partial differential equation, and superimposes them to satisfy the boundary conditions in some average or approximate sense. Detail of the method can be found in Brebbia (1978) and Crouch (1983). The emphasis is on understanding the simple physical idea underlying the use of boundary element method in terms of introducing numerical procedures of the boundary element method.

3.2. FRACTURE ELASTIC DEFORMATION PROBLEM

The boundary element technique to solve fracture elastic deformation problem can be explained more fully with reference to Figure 3-2. The fracture is assumed to be so thin that we can consider it as a horizontal plane in the mathematical sense. The co-ordinates (x, y, z) or (x_1, x_2, x_3) are chosen such that the z axis is vertical and

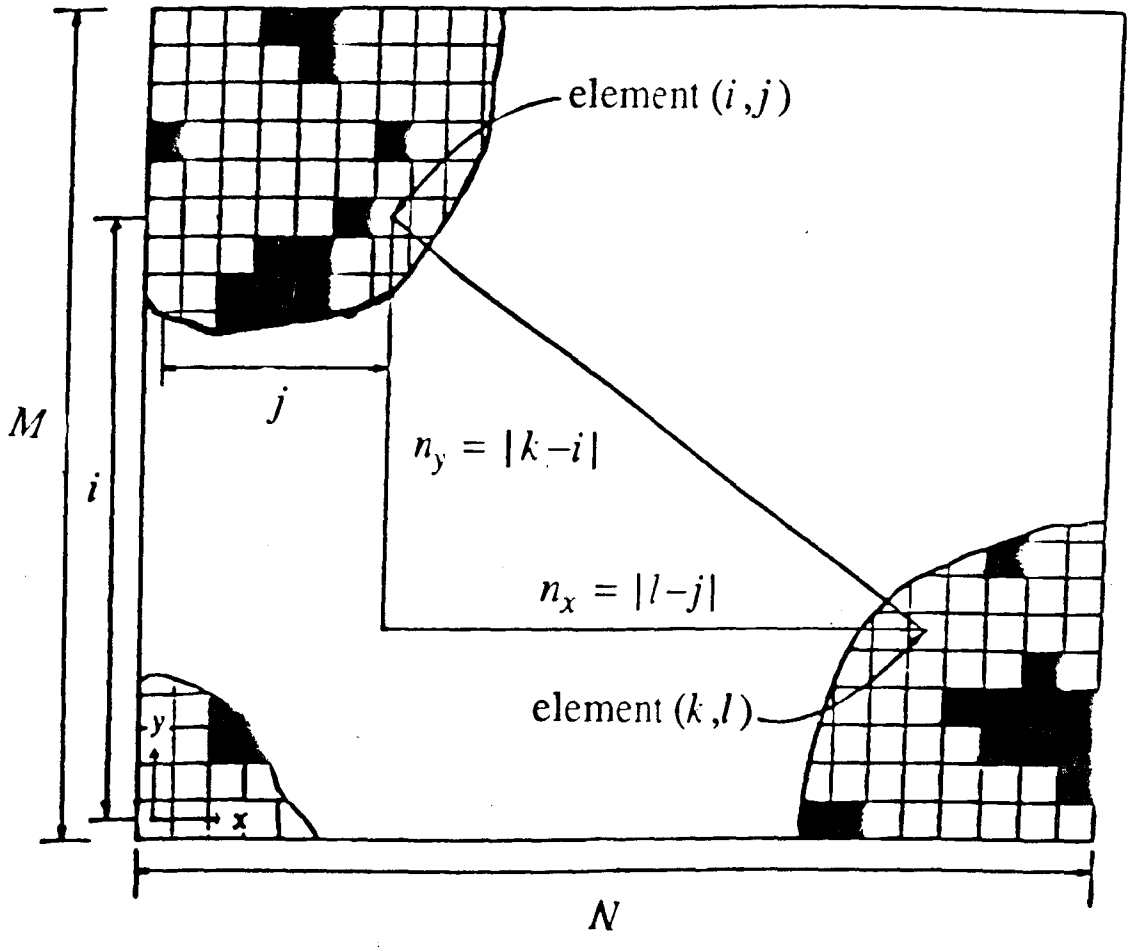

Figure 3-2 Definition of grid for the fracture plane z = 0. Elements in black represent contact areas.

positive upwards. The fracture then is defined as the plane $z=0$. The top of this plane, $z=0_+$, represents the hangingwall and the bottom, $z=0_-$, represents the footwall. The displacements and stresses are denoted as u_i and σ_{ij}. A solution to a boundary value problem in elastostatics implies a solution to the displacement equations of equilibrium, subject to a set of specific boundary conditions. It means that the displacement equations of equilibrium are the governing partial differential equations for the fracture deformation problem. The displacement equations of equilibrium are given by (Love 1944)

$$u_{i,jj} + \frac{1}{1-2\nu} u_{j,ij} = \beta_i \tag{3-1}$$

where the plane $z=0$ is the fracture plane, β_i are body forces, and ν is Poisson's ratio. The stresses and displacements are assumed to vanish as $x^2 + y^2 \rightarrow \infty$. Along the $z=0$ boundary, the proper boundary conditions depend on whether or not the point $(x,y,0)$ is a region of contact between the two faces of the fracture. If the faces are in contact, we use the conditions that

$$\sigma_{xz} = \sigma_{yz} = 0, \quad u_z = 0.$$

The no-shear boundary conditions assume that the rock faces are frictionless; the calculations can also be carried out under the ''opposite'' assumption, which is that no shear displacements are allowed, i.e., $u_x = u_y = 0$. At points where the faces are not in contact, the boundary conditions are

$$\sigma_{xz} = \sigma_{yz} = 0, \quad \sigma_{zz} = -T_{zz},$$

where T_{zz} is the normal traction.

It may be helpful to summarize the numerical procedure of boundary element method in a few simple steps:

(1) The boundary of interest in the fracture plane now is divided into a grid of $M \times N$ squares called boundary elements. We will suppose that the boundary elements are small enough so that the normal stress σ_{zz} acting on each one can be taken as a constant. The side length of each square is 2a, and the elements are numbered such that they can be identified by a matrix location with respect to the low left-hand corner of the grid. Square (i,j) for example, denotes the (row, column) location of a particular grid element, i in the x direction and j in the y direction.

(2) We will imagine that a "point-source" with components is associated with each element. i.e., place one "point-source" at the midpoint of each element. This point source could represent a heat source or sink in a heat flow problem, for example, or it could represent a point force applied within an elastic solid for a problem in solid mechanics. Here we make the "point-source" represent a displacement discontinuity with components D_x, D_y, and D_z. The displacement discontinuity components define as relative displacements between the hangwall ($z=0_+$) and the footwall ($z=0_-$) of the fracture:

$$D_i = u_i(x_1, x_2, 0_-) - u_i(x_1, x_2, 0_+) \tag{3-2}$$

Each element (i,j) of the grid has associated with it a constant displacement discontinuity with components D_x, D_y, D_z.

(3) Then we seek analytical solutions corresponding to the "point-source" in an infinite homogeneous region, which satisfy the displacement equilibrium equation without body forces, i.e. $\beta_i = 0$. These solutions have been found in many disciplines,

and are usually called singular solutions because, mathematical speaking, they are well behaved everywhere in the region of interest except at the point of the ''point-source'', where there is a mathematical anomaly or ''singularity''. The singular solution to the problem of a constant displacement discontinuity over a square element of the fracture plane is given by Rongved (1957):

$$
\begin{aligned}
u_1 &= 2(1-\nu)\phi_{1,3} - (1-2\nu)\phi_{3,1} - x_3\phi_{k,k1} \\
u_2 &= 2(1-\nu)\phi_{2,3} - (1-2\nu)\phi_{3,2} - x_3\phi_{k,k2} \\
u_3 &= 2(1-\nu)\phi_{3,3} - (1-2\nu)(\phi_{1,1} + \phi_{2,2}) - x_3\phi_{k,k3}
\end{aligned}
\tag{3-3}
$$

$$
\begin{aligned}
\sigma_{11} &= -2G\,[2\phi_{1,13} + 2\nu\phi_{2,23} + 2\nu\phi_{3,33} - (1-2\,\nu)\phi_{3,11} - x_3\phi_{k,k11}] \\
\sigma_{22} &= -2G\,[2\phi_{2,23} + 2\nu\phi_{1,13} + 2\nu\phi_{3,33} - (1-2\,\nu)\phi_{3,22} - x_3\phi_{k,k22}] \\
\sigma_{33} &= -2G\,[2\phi_{3,33} - x_3\phi_{k,k33}] \\
\sigma_{12} &= -2G\,[(1-\nu)(\phi_{1,23} + \phi_{2,13}) - (1-2\nu)\phi_{3,12} - x_3\phi_{k,k12}] \\
\sigma_{13} &= -2G\,[2\phi_{1,33} + \nu(\phi_{1,22} - \phi_{2,12}) - x_3\phi_{k,k13}] \\
\sigma_{23} &= -2G\,[2\phi_{2,33} + \nu(\phi_{2,11} - \phi_{1,12}) - x_3\phi_{k,k23}]
\end{aligned}
\tag{3-4}
$$

In these equations, functions ϕ_i (i = 1 to 3) are

$$\phi_i = \frac{1}{8\pi(1-\nu)} D_i I(x_1, x_2, x_3) \tag{3-5}$$

in which

$$I(x_1, x_2, x_3) = \int_{-a}^{a}\int_{-a}^{a} [(x_1 - \xi_1)^2 + (x_2 - \xi_2)^2 + x^2_3]^{-1}\, d\xi_1\, d\xi_2 \tag{3-6}$$

where the integration is performed for ξ_1, ξ_2 in the square element $|x_1| \le a$, $|x_2| \ge a$, x_3=0. 2a is the side length of the square element. We can rewrite equations 3-3 and

3-4 in explicit form as follows:

$$u_1 = \frac{1}{8\pi(1-\nu)}\Big[[2(1-\nu)I_{,3}-x_3I_{,11}]D_1 - x_3I_{,12}D_2 - [(1-2\nu)I_{,2}+x_3I_{,13}]D_3\Big]$$

$$u_2 = \frac{1}{8\pi(1-\nu)}\Big[x_3I_{,12}D_1 + [2(1-\nu)I_{,3}-x_3I_{,22}]D_2 - [(1-2\nu)I_{,2}+x_3I_{,23}]D_3\Big]$$

$$u_3 = \frac{1}{8\pi(1-\nu)}\Big[[2(1-\nu)I_{,1}-x_3I_{,13}]D_1 + [(1-2\nu)I_{,2}-x_3I_{,23}]D_2 + [2(1-\nu)I_{,3}-x_3I_{,33}]D_3\Big] \qquad (3\text{-}7)$$

$$\sigma_{11}=-A\Big[[2I_{,13}-x_3I_{,111}]D_1 + [2\nu I_{,23}-x_3I_{,112}]D_2 + [2\nu I_{,33}-(1-2\nu)I_{,11}-x_3I_{,113}]D_3\Big]$$

$$\sigma_{22}=-A\Big[[2\nu I_{,13}-x_3I_{,122}]D_1 + [2\nu I_{,23}-x_3I_{,222}]D_2 + [2\nu I_{,33}-(1-2\nu)I_{,22}-x_3I_{,223}]D_3\Big]$$

$$\sigma_{33}=-A\Big[x_3I_{,133}D_1 + x_3I_{,233}D_2 + [I_{,33}-x_3I_{,333}]D_3\Big]$$

$$\sigma_{12}=-A\Big[[(1-\nu)I_{,23}-x_3I_{,112}]D_1 + [(1-\nu)I_{,13}-x_3I_{,122}]D_2 + [(1-2\nu)I_{,12}-x_3I_{,123}]D_3\Big]$$

$$\sigma_{13}=-A\Big[[(1-\nu)I_{,33}-\nu I_{,11}-x_3I_{,113}]D_1 + [\nu I_{,12}+x_3I_{,123}]D_2 - x_3I_{,133}D_3\Big]$$

$$\sigma_{23}=-A\Big[[\nu I_{,12}+x_3I_{,123}]D_1 - [(1-\nu)I_{,33}-\nu I_{,22}+x_3I_{,233}]D_2 - x_3I_{,333}D_3\Big]$$

$$A = \frac{G}{4\pi(1-\nu)}, \qquad \text{and} \qquad G = \frac{E}{2(1+\nu)} \qquad (3\text{-}8)$$

Using equation 3-6, it can be shown that the functions $I_{,123}$, etc., in equations 3-7 and 3-8 have the following values:

$$I_{,12} = \frac{1}{R_1} + \frac{1}{R_2} - \frac{1}{R_3} - \frac{1}{R_4}$$

$$I_{,13} = \frac{z(y+a)}{[R_3^2-(y+a)^2]R_3} + \frac{z(y-a)}{[R_4^2-(y-a)^2]R_4} - \frac{z(y-a)}{[R_1^2-(y-a)^2]R_1} - \frac{z(y+a)}{[R_2^2-(y+a)^2]R_2}$$

$$I_{,22} = \frac{(x-a)(y+a)}{[R_{32}-(x-a)^2]R_3} + \frac{(x+a)(y-a)}{[R_4^2-(x+a)^2]R_4} - \frac{(x-a)(y-a)}{[R_1^2-(x-a)^2]R_1} - \frac{(x+a)(y+a)}{[R_2^2-(x+a)^2]R_2}$$

$$I_{,23} = \frac{z(x-a)}{[R_3{}^2-(x-a)^2]R_3} + \frac{z(x+a)}{[R_4{}^2-(x+a)^2]R_4} - \frac{z(x-a)}{[R_1{}^2-(x-a)^2]R_1} - \frac{z(x+a)}{[R_2{}^2-(x+a)^2]R_2}$$

$$I_{,33} = -\frac{(x-a)(y+a)}{R_3}\left[\frac{1}{R_3{}^2-(y+a)^2} + \frac{1}{R_3{}^2-(x-a)^2}\right] \tag{3-9}$$

$$I_{,113} = \frac{z(x-a)(y-a)[3R_1{}^2-(y-a)^2]}{[(x-a)^2+z^2]^2R_1{}^3} + \frac{z(x+a)(y+a)[3R_2{}^2-(y+a)^2]}{[(x+a)^2+z^2]^2R_2{}^3} -$$

$$-\frac{z(x-a)(y+a)[3R_3{}^2-(y+a)^2]}{[(x-a)^2+z^2]^2R_3{}^3} - \frac{z(x+a)(y-a)[3R_4{}^2-(y-a)^2]}{[(x+a)^2+z^2]^2R_4{}^3}$$

$$I_{,123} = z\left[\frac{1}{R_3{}^3} + \frac{1}{R_4{}^3} - \frac{1}{R_1{}^3} - \frac{1}{R_2{}^3}\right]$$

$$I_{,223} = \frac{z(x-a)(y-a)[3R_1{}^2-(x-a)^2]}{[(y-a)^2+z^2]^2R_1{}^3} + \frac{z(x+a)(y+a)[3R_2{}^2-(x+a)^2]}{[(y+a)^2+z^2]^2R_2{}^3} -$$

$$-\frac{z(x-a)(y+a)[3R_3{}^2-(x-a)^2]}{[(y+a)^2+z^2]^2R_3{}^3} - \frac{z(x+a)(y-a)[3R_4{}^2-(x+a)^2]}{[(y-a)^2+z^2]^2R_4{}^3}$$

$$I_{,333} = -I_{,113} - I_{,223}$$

$$I_{,133} = -PP1 - PP2 - PP3 - PP4 - PP5$$

$$I_{,233} = -QQ1 - QQ2 - QQ3 - QQ4 - QQ5 \tag{3-10}$$

$$PP1 = \frac{(y-a)\left[(x-a)^2[R_1{}^2+(x-a)^2] - z^2[R_1{}^2-(x-a)^2]\right]}{[(x-a)^2+z^2]^2R_1{}^3}$$

$$PP2 = \frac{(y+a)\left[(x+a)^2[R_2{}^2+(x+a)^2] - z^2[R_2{}^2-(x+a)^2]\right]}{[(x+a)^2+z^2]^2R_2{}^3}$$

$$PP3 = -\frac{(y+a)\left[(x-a)^2[R_3{}^2+(x-a)^2] - z^2[R_3{}^2-(x-a)^2]\right]}{[(x-a)^2+z^2]^2R_3{}^3} \tag{3-11}$$

$$PP4 = -\frac{(y-a)\left[(x+a)^2[R_4{}^2 + (x+a)^2] - z^2[R_4{}^2 - (x+a)^2]\right]}{[(x+a)^2 + z^2]^2 R_4{}^3}$$

$$PP5 = \frac{y+a}{R_3{}^3} + \frac{y-a}{R_4{}^3} - \frac{y-a}{R_1{}^3} - \frac{y+a}{R_2{}^3}$$

$$QQ1 = \frac{(x-a)\left[(y-a)^2[R_1{}^2 + (y-a)^2] - z^2[R_1{}^2 - (y-a)^2]\right]}{[(y-a)^2 + z^2]^2 R_1{}^3}$$

$$QQ2 = \frac{(x+a)\left[(y+a)^2[R_2{}^2 + (y+a)^2] - z^2[R_2{}^2 - (y+a)^2]\right]}{[(y+a)^2 + z^2]^2 R_2{}^3}$$

$$QQ3 = -\frac{(x-a)\left[(y+a)^2[R_3{}^2 + (y-a)^2] - z^2[R_3{}^2 - (y+a)^2]\right]}{[(y+a)^2 + z^2]^2 R_3{}^3} \qquad (3\text{-}11)$$

$$QQ4 = -\frac{(x+a)\left[(y-a)^2[R_4{}^2 + (y-a)^2] - z^2[R_4{}^2 - (y-a)^2]\right]}{[(y-a)^2 + z^2]^2 R_4{}^3}$$

$$QQ5 = \frac{x-a}{R_3{}^3} + \frac{x+a}{R_4{}^3} - \frac{x-a}{R_1{}^3} - \frac{x+a}{R_2{}^3}$$

$$R_1{}^2 = (x-a)^2 + (y-a)^2 + z^2$$

$$R_2{}^2 = (x+a)^2 + (y+a)^2 + z^2 \qquad (3\text{-}12)$$

$$R_3{}^2 = (x-a)^2 + (y+a)^2 + z^2$$

$$R_4{}^2 = (x+a)^2 + (y-a)^2 + z^2$$

the stresses σ_{13}, σ_{23} and σ_{33} represent the tractions on the fracture plane. These quantites can be written in unabridged notation as

$$\sigma_{xz} = -A\left\{\left[(1-\nu)\frac{\partial^2 I}{\partial z^2} - \nu\frac{\partial^2 I}{\partial x^2} - x_3\frac{\partial I^2 \partial I}{\partial x^2 \partial z}\right]D_x - \left[\nu\frac{\partial I\,\partial I}{\partial x\,\partial y} + x_3\frac{\partial I\,\partial I\,\partial I}{\partial x\,\partial y\,\partial z}\right]D_y - x_3\frac{\partial I\,\partial^2 I}{\partial x\,\partial z^2}D_z\right\}$$

$$\sigma_{yz} = -A\left\{\left[\nu\frac{\partial I\,\partial I}{\partial x\,\partial y} + x_3\frac{\partial I\,\partial I\,\partial I}{\partial x\,\partial y\,\partial z}\right]D_x + \left[(1-\nu)\frac{\partial^2 I}{\partial z^2} - \nu\frac{\partial^2 I}{\partial y^2} - x_3\frac{\partial I^2 \partial I}{\partial y^2 \partial z}\right]D_y - x_3\frac{\partial I\,\partial^2 I}{\partial y\,\partial z^2}D_z\right\}$$

$$\sigma_{xz}=-A\left\{-x_3\frac{\partial I\,\partial^2 I}{\partial x\,\partial z^2}D_x-x_3\frac{\partial I\,\partial^2 I}{\partial y\,\partial z^2}D_y+\left[\frac{\partial^2 I}{\partial z^2}-x_3\frac{\partial^3 I}{\partial z^3}\right]D_z\right\} \tag{3-13}$$

The effects of a single elemental displacement discontinuity on the displacements and stresses at an arbitrary point in the infinite solid can be computed from the above singular solutions.

(4) We now set up a system of $3\times M\times N$ linear algebraic equations to express the combined effects of all $M\times N$ singularities or ''point-source'' at any one element in term of the strengths of the singularities, i.e. D_x, D_y, and D_z. The system of algebraic equations is formed by considering the boundary conditions for each element. If stresses $\overset{ij}{\sigma}_{xz}=(\overset{ij}{\sigma}_{xz})_o$, $\overset{ij}{\sigma}_{yz}=(\overset{ij}{\sigma}_{yz})_o$, and $\overset{ij}{\sigma}_{zz}=(\overset{ij}{\sigma}_{zz})_o$ are prescribed at the (i, j) boundary element, it then follows from equation 3-11 that the induced tractions at the midpoint of element (i, j) are related to the displacement discontinuity components at all elements (k, l) of the grid by equations of the form:

$$\begin{aligned}
(\overset{ij}{\sigma}_{xz})_o&=\sum_{k=1}^{m}\sum_{l=1}^{n}\overset{ijkl}{A}_{xx}\overset{kl}{D}_x+\overset{ijkl}{A}_{xy}\overset{kl}{D}_y+\overset{ijkl}{A}_{xz}\overset{kl}{D}_z\\
(\overset{ij}{\sigma}_{yz})_o&=\sum_{k=1}^{m}\sum_{l=1}^{n}\overset{ijkl}{A}_{xy}\overset{kl}{D}_x+\overset{ijkl}{A}_{yy}\overset{kl}{D}_y+\overset{ijkl}{A}_{yz}\overset{kl}{D}_z\\
(\overset{ij}{\sigma}_{zz})_o&=\sum_{k=1}^{m}\sum_{l=1}^{n}\overset{ijkl}{A}_{xz}\overset{kl}{D}_x+\overset{ijkl}{A}_{yz}\overset{kl}{D}_y+\overset{ijkl}{A}_{zz}\overset{kl}{D}_z
\end{aligned} \tag{3-14}$$

where $\overset{ijkl}{A}_{xx}$, etc., are matrices of influence coefficients for the fracture plane. For example, $\overset{ijkl}{A}_{yz}$ gives a induced stress $\overset{ij}{\sigma}_{zz}$ along the axis z at the center of an element (i, j) due to a unit displacement discontinuity D_y over the element (k, l). The influence coefficients depend upon the elastic properties of the rock mass, the size of the grid elements and the distances from element (k, l) to element (i, j) (see Fig. 3-2).

Simularly, if displacements $\overset{ij}{u}_{xz}=(\overset{ij}{u}_{xz})_o$, $\overset{ij}{u}_{yz}=(\overset{ij}{u}_{yz})_o$, and $\overset{ij}{u}_{zz}=(\overset{ij}{u}_{zz})_o$ are prescribed, then the (i, j) th equations are

$$
\begin{aligned}
(\overset{ij}{u}_{xz})_o &= \sum_{k=1}^{m}\sum_{l=1}^{n} \overset{ijkl}{B}_{xx}\overset{kl}{D}_x + \overset{ijkl}{B}_{xy}\overset{kl}{D}_y + \overset{ijkl}{B}_{xz}\overset{kl}{D}_z \\
(\overset{ij}{u}_{yz})_o &= \sum_{k=1}^{m}\sum_{l=1}^{n} \overset{ijkl}{B}_{xy}\overset{kl}{D}_x + \overset{ijkl}{B}_{yy}\overset{kl}{D}_y + \overset{ijkl}{B}_{yz}\overset{kl}{D}_z \qquad (3\text{-}15) \\
(\overset{ij}{u}_{zz})_o &= \sum_{k=1}^{m}\sum_{l=1}^{n} \overset{ijkl}{B}_{xz}\overset{kl}{D}_x + \overset{ijkl}{B}_{yz}\overset{kl}{D}_y + \overset{ijkl}{B}_{zz}\overset{kl}{D}_z
\end{aligned}
$$

Mixed formulations in which, for example, $\overset{ij}{u}_{zz}$, $\overset{ij}{\sigma}_{xz}$ and $\overset{ij}{\sigma}_{yz}$ are prescribed are handled by selecting the appropriate ones of equations 3-14 and 3-15. Proceeding in this way for i=1 to M, and j=1 to N, we obtain a system of $3MN$ algebraic equations in $3MN$ unknown displacement discontinuity components.

(5) Then we solve the equations equations 3-14 and 3-15 for the unknown displacement discontinuity components by iteration.

(6) The last step is to back substitute the displacement discontinuity components into equations 3-7 and 3-8 to obtain the value of displacement u_i and stresses σ_{ij} at any point in the infinite body and the fracture surface.

3.3. FLOW PROBLEM

The flow of a Newtonian fluid (such as water) through a fracture is governed by the Navier-Stokes equations:

$$\rho_f \frac{\partial \vec{u}}{\partial t} = -\rho_f (\vec{u}\bullet\nabla)\vec{u} - \nabla P + \mu\nabla^2\vec{u} \qquad (3\text{-}16)$$

where $\vec{u} = (u, v, w)$ is the velocity vector, ρ_f is fluid density, μ is fluid viscosity, t is

time, and P is the fluid pressure. If a uniform pressure gradient

$$\nabla P = (\frac{\partial P}{\partial x}, 0, 0) \tag{3-17}$$

forces fluid between the plates of the fracture, and fluid velocity is assumed to vanish at the plates, the Navier-Stokes equations solution is

$$\nabla P = \mu \nabla^2 \vec{u} . \tag{3-18}$$

The exact solution for flow between two parallel plates under a uniform pressure gradient is known (Schlichting 1968); This solution gives the familiar cubic law $Q=h^3|\nabla P|/12\mu$, where $|\nabla P|$ is the magnitude of the pressure gradient, and μ is the viscosity of the fluid. However, exact solutions for other specific geometries are extremely difficult to obtain. For a fracture that is modeled as two parallel plates propped open by discrete areas of contact (Fig. 3-1), the flow cannot be everywhere parallel to the overall pressure gradient, since the fluid must follow a tortuous path as it circumvents the obstacles. If the flow rates are suitably low, and if the aperture h is small relative to the characteristic distance L between the contact areas (Fig. 3-1), the flow can be well approximated by ''Hele-Shaw'' flow (Schlichting 1968, p. 114). The precise constraint on the velocity is that

$$Re^* = \rho U h^2/\mu L << 1, \tag{3-19}$$

where Re^* is the reduced Reynolds' number, and U is the mean velocity magnitude. In Hele-Shaw flow, the fluid still has a parabolic velocity profile, and the velocity vector $\vec{u}$ at each point is still in the direction of decreasing pressure, but the local pressure gradient is not necessarily the same as the overall macroscopic pressure gradient. The velocity profile for this type of flow is given by

$$\vec{u} = \frac{-\nabla P}{2\mu} z\ (z - h\ ), \tag{3-20}$$

where z is the transverse coordinate measured from the bottom wall. The pressure is found by solving the two dimensional Laplace equation in the region of the x-y plane exterior to the obstacles, i.e.

$$\nabla^2 P(x,y) = 0. \tag{3-21}$$

Equations 3-20 and 3-21 can be proved easily:

when $\dfrac{\partial P}{\partial z} = 0,$ and $\dfrac{\partial^2 u}{\partial x^2} << \dfrac{\partial^2 u}{\partial z^2}$.

Navier-Stokes equations reduce to

$$\text{a)}\ \frac{\partial P}{\partial x} = \mu \frac{\partial^2 u}{\partial z^2} \qquad \text{b)}\ \frac{\partial P}{\partial y} = \mu \frac{\partial^2 v}{\partial z^2} \qquad \text{c)}\ \frac{\partial P}{\partial y} = 0 \tag{3-22}$$

from equation 3-22-c, $P = P(x,y)$ only,

from equation 3-22-a,
$$\frac{\partial u}{\partial z} = \frac{1}{\mu}\frac{\partial P}{\partial x} z + c_1,$$

$$u = \frac{1}{2\mu}\frac{\partial P}{\partial x} z^2 + c_1 z + c_2.$$

Use no slip boundary conditions, i.e. u=0 at z=0, z=h, we then obtain:

$$u = \frac{1}{2\mu}\frac{\partial P}{\partial x}\ (z^2 - zh\ ),$$

from equation 3-22-b,
$$v = \frac{1}{2\mu}\frac{\partial P}{\partial x}\ (z^2 - zh\ ).$$

Invoke conservation of mass:

$$\frac{\partial u}{\partial x} + \frac{\partial v}{\partial y} + \frac{\partial w}{\partial z}$$

$$\frac{\partial u}{\partial x} + \frac{\partial v}{\partial y} + 0 = \frac{z(z-h)}{2\mu}\left[\frac{\partial^2 P}{\partial x^2} + \frac{\partial^2 P}{\partial y^2}\right] = 0$$

therefore, $$\frac{\partial^2 P}{\partial x^2} + \frac{\partial^2 P}{\partial y^2} = 0 .$$

Since there can be no flow into or out of the obstacles, the pressure field must satisfy $\partial P / \partial n = 0$ along the obstacle boundaries, where n is the outward unit normal vector. The external boundaries are typically either no-flow or constant-pressure boundaries (Fig. 3-3). Note that while the obstacles are correctly treated as being impermeable, it is not possible to impose the no-slip boundary condition along these surfaces, since the Laplace equation is of lower order than the Navier-Stokes equations. This incorrect boundary condition introduces an error which is on the order of (h/L), and which therefore should be negligible for many applications. For example, typical values of h for fractures in crystalline rock are on the order of 10-100 μm, while asperity separations L are usually on the order of millimeters (Pyrak-Nolte et al. 1987).

The flow problem which we are to solve can be posed as follows (Fig. 3-3). A two-dimensional homogeneous flow region containing contact areas of various shapes is bounded by four edges of the square (or rectangle). Fixed pressures $P(x_o)$ are maintained on two opposing edges of the region, while the other two sides are taken to be no-flow boundary (normal velocity component $u(x_o)$=0. The Laplace quation has to be satisfied by the pressure (or potential) $P(x)$ at any point (x, y, z) or (x_1, x_2, x_3). We are to determine the flow velocity and potential existing at any specified point within the flow region or on the boundary using boundary element method.

We know that, in any boundary value problem, some of the boundary parameters are specified as constraints while the rest emerge from the solution to the problem as a whole. In the foregoing description of the boundary element technique for the deformation problem, we first solve for the singularities (displacement discontinuities) that

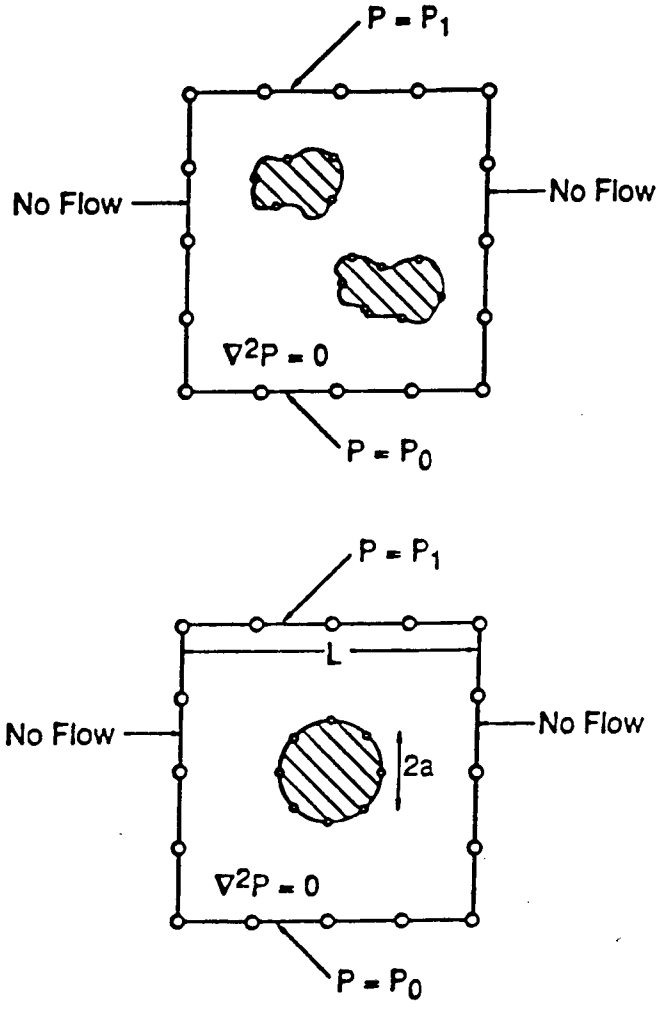

Fig. (3-3) Schematic diagram of the basic computational problem, showing two asperities, the no-flow and constant-pressure boundaries, and the discrete nodal points used in the boundary-element calculations.

satisfy the specified boundary conditions, and then compute the rest of the boundary parameters in terms of these displacement discontinuities. The boundary element technique that we use to solve the flow problem is a more mathematical treatment based on concepts of classical potential theory and is called direct boundary element method because the unspecified boundary parameters are obtained directly.

Now we start from the governing differential equation 3-21 for the basic development of a direct boundary element solution

$$\frac{\partial^2 P(x)}{\partial x_i \partial x_i} = \frac{\partial^2 P(x)}{\partial x_1 \partial x_1} + \frac{\partial^2 P(x)}{\partial x_2 \partial x_2} = 0 . \tag{3-21}$$

In order to investigate the possibility of actually integrating equation 3-21, over the domain R, we introduce a function $G(x, \xi)$ which is, as yet, undefined except that it is sufficiently continuous to be differentiable as often as required.

We then multiply both sides of equation 3-21 by $G(x, \xi)$, integrate solely the term $\frac{\partial^2 P(x)}{\partial x_1 \partial x_1}$ by parts twice, and use the limits defined in Figure 3-4. These operations generate the following series of equation 3-22:

$$\int_R \left[G \frac{\partial^2 P}{\partial x_1 \partial x_1} \right] dR(x) = \int_{x_2^1}^{x_2^2} \int_{x_1^1}^{x_1^2} \left[G \frac{\partial^2 P}{\partial x_1 \partial x_1} \right] dx_1 dx_2$$

$$= \int_{x_2^1}^{x_2^2} \left[\left[G \frac{\partial P}{\partial x_1} \right]_{x_1^1}^{x_1^2} - \int_{x_1^1}^{x_1^2} \left[\frac{\partial G}{\partial x_1} \frac{\partial P}{\partial x_1} \right] dx_1 \right] dx_2$$

$$= \int_R \left[\left[G \frac{\partial P}{\partial x_1} - \frac{\partial G}{\partial x_1} P \right]_{x_1^1}^{x_1^2} + \int_{x_1^1}^{x_1^2} \left[P \frac{\partial^2 G}{\partial x_1 \partial x_1} \right] dx_1 \right] dx_2 \tag{3-23}$$

The first integral on the right in equation 3-23 can be interpreted as a boundary integral over S by noting that at (x_1^1, x_1^2) on S, $dx_2 = n_1 dS$ (Fig. 3-4). Equation 3-23 can therefore be written as

$$\int_R \left[G \frac{\partial^2 P}{\partial x_1 \partial x_1} \right] dR(x) = \int_S \left[G \frac{\partial P}{\partial x_1} - P \frac{\partial G}{\partial x_1} \right] n_1 dS + \int_R \left[P \frac{\partial^2 G}{\partial x_1 \partial_1} \right] dR$$

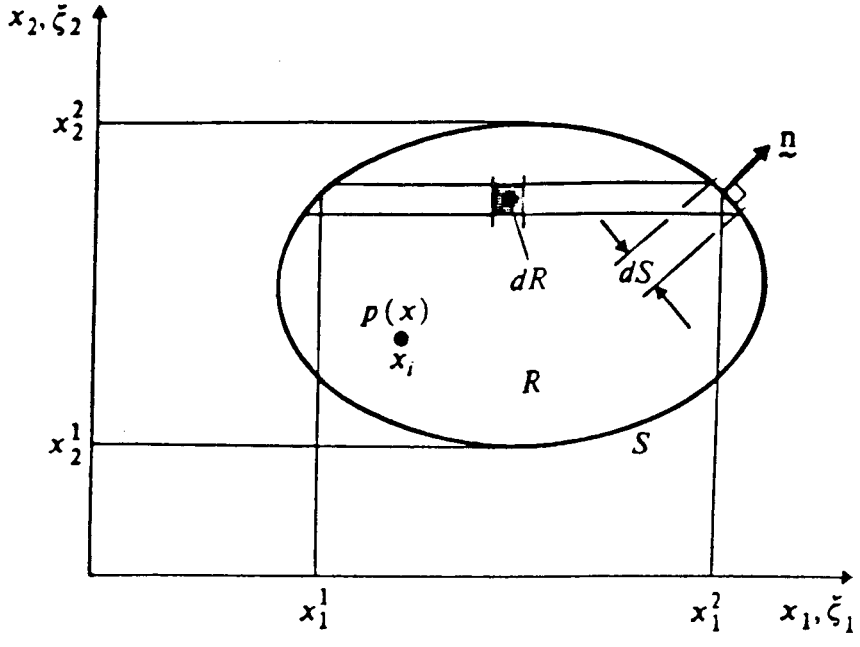

Figure 3-4 Definition of integral limits (after Banerjee and Butterfield, 1981).

If we perform exactly similar operations on the $(\partial^2 G / \partial x_2 \partial_2)$ term and add the results, we obtain

$$\int_R \left[G \frac{\partial^2 P}{\partial x_i \partial x_i} \right] dR(x) = \int_S \left[G \frac{\partial P}{\partial x_i} - P \frac{\partial G}{\partial x_i} \right] n_i dS + \int_R \left[P \frac{\partial^2 G}{\partial x_i \partial_i} \right] dR \quad . \qquad (3\text{-}24)$$

We now specify G to be a solution of

$$\frac{\partial^2 G(x, \xi)}{\partial x_i \partial x_i} + \Delta(x, \xi) = 0 \qquad (3\text{-}25)$$

where $n_1 = \partial x_2/\partial S$, $n_2 = \partial x_1/\partial S$, and $\Delta(x, \xi)$ is the two-dimensional Dirac delta function, which is mathematically equivalent to the effect of a unit concentrated charge applied at the point ξ. The key property of the delta function is that it is zero unless all corresponding components of x_i and ξ_i are identical, where it becomes infinitely large in such a way that

$$\int_{-\infty}^{\infty}\int_{-\infty}^{\infty} \Delta(x, \xi)\, dx\, dy = \int_R \Delta(x, \xi) dR = 1 \tag{3-26}$$

When $x_i \equiv \xi_i$, $\Delta(x, \xi)$ has a shifting property such that, for example,

$$\int_R P(x)\Delta(x, \xi) dR(x) = P(\xi) \qquad \xi_i \in R \tag{3-27}$$

i.e., when the left-hand-side product in the equation 3-26 is integrated over R, the value of $P(\sigma)$ at the specific point $x_i = \xi_i$ is shifted out as the only non-zero resultant.

The fundamental solution $G(x, \xi)$ of equation 3-25, which is a basic component of all the subsequent analysis, relates the $P(x)$ generated at a "field point" (x_i) by a unit source $e(\xi)$, say, applied at a "load point" (ξ_i) in an infinite two-dimensional body. Although the origin for the coordinates (ξ_i) is identical to that for (x_i), it is absolutely essential that each set be reserved for a specific purpose. Thus the classical singular solution can be written as

$$P(x) = G(x, \xi)e(\xi) \tag{3-28}$$

where

$$G(x, \xi) = -\frac{1}{2\pi}\ln\left[\frac{1}{r}\right] \tag{3-29}$$

and

$$r^2 = (x_1 - \xi_1)^2 + (x_2 - \xi_2)^2 = (x - \xi)_i (x - \xi)_i \tag{3-30}$$

The last term of equation 3-24 reduces to $-P(\xi)$ from equations 3-25, 3-27, and the left side of equation 3-24 is equal to zero from equations 3-21 and 3-26. Thus we can rewrite equation 3-24 as

$$P(\xi) = \int_S \left[G(x, \xi) \frac{\partial P(x)}{\partial x_i} - P(x) \frac{\partial G(x, \xi)}{\partial \xi} \right] n_i(x) dS(x) \, . \tag{3-31}$$

If we define

$$h(x, \xi) = -[\partial G(x, \xi)/\partial x_i] n_i(x)$$

and specify that the flux or velocity in the n_i direction is

$$u(x) = -[\partial P(x)/\partial x_i] \, n_i(x)$$

then equation 3-31 can be written more concisely as

$$P(\xi) = \int_S [P(x) h(x, \xi) - u(x) G(x, \xi)] dS(x) \, . \tag{3-32}$$

This equation enables us to calculate the flow potential at any point ξ from a knowledge of both the potential and the flux at all points around the boundary S. For developing a boundary element technique, it is best considered as determining $P(\xi)$ at any point (ξ) by a summation of effects from other points (x) over S.

Equation 3-32 is valid for any point in the domain, but in order to formulate the problem as a boundary technique we need to take it to the boundary. This has been done by C.A. Brebbia (1978, P.51). He has the following equation for a point on the boundary,

$$\tfrac{1}{2}P(\xi_o) = \int_S [P(x)h(x, \xi_o) - u(x)G(x, \xi_o)]dS(x) \,. \tag{3-33}$$

Equation 3-33 will now be applied on the boundary S of the domain R under consideration. In a ''well-posed'' problem, one of either $P(x_o)$ or $u(x_o)$ will be known at every point of the boundary. The key problem is the solution of equation 3-33 using the specified boundary conditions to calculate the remaining, initially unknown, boundary values of the flow potential P and velocity u.

For simplicity, we consider only a linear boundary element discretization scheme with a constant distributions of variables over the elements. If we divide the boundaries into N straight line segments or elements (Fig. 3-3), of which the mth and nth respectively are typical members, because the values of P and u are assumed to be constant on each element and equal to the value at the mid-node of the element, then the equation 3-34 can be written for the mth element on the boundary as

$$\tfrac{1}{2}P(\xi_o^m) = \sum_{n=1}^{N} P(x)^n \int_{S_n} h(x^n, \xi_o^m)dS(x^n) - \sum_{n=1}^{N} u(x)^n \int_{S_n} G(x^n, \xi_o^m)dS(x^n) \tag{3-34}$$

The terms $\int_{S_n} h(x^n, \xi_o^m)dS(x^n)$ relate the ''m'' node with the segment ''n'' over which the integral is carried out. We shall call these integrals $\mathbf{H}_{mn}$. The integral $\int_{S_n} G(x^n, \xi_o^m)dS(x^n)$ will be called $\mathbf{G}_{mn}$. Hence we have

$$\tfrac{1}{2}P^m = \sum_{n=1}^{N} P(x)^n \mathbf{H}_{mn} - \sum_{n=1}^{N} u(x)^n \, \mathbf{G}_{mn} \tag{3-35}$$

if the $\frac{1}{2}P^m$ term is absorbed into the $m = n$ position of the $\mathbf{H}_{mn}$ matrix. By allowing P to range over 1, ..., N we obtain

$$\sum_{n=1}^{N} P(x)^n \mathbf{H}_{mn} = \sum_{n=1}^{N} u(x)^n \mathbf{G}_{mn} \ . \tag{3-36}$$

The matrix equivalent of equation 3-36, a set of equations for the nodes, can then be expressed as

$$\mathbf{PH} = \mathbf{UG} \tag{3-37}$$

where **P** and **U** are $N \times 1$ columns, and **H** and **U** are compatible row vectors.

The simplest boundary-value problems will have either the flow potentials specified at all boundary points (hence P is known) or the fluxes specified similarly (in which case u is known). In either case the unspecified boundary information, P or u respectively, can be calculated directly from equation 3-37. In the general, mixed boundary-value problem, N_1 values of P will be specified on S_1 of S and N_2 values of the flux u over S_2 of S, where , in a well-posed problem, $(S_1 + S_2) = S$ always.

Note that $N_1 + N_2$ boundary-values are known, hence there is a set of N unknowns in equation 3-37. If we rearrange the equation 3-37 in such a way that all the unknowns on the left hand side, we can write:

$$\mathbf{A\,X} = \mathbf{Y} \tag{3-38}$$

where **X** is the vector of unknowns P and u.

Solving equation 3-38 for **X** with the result that all P and u components (i.e. both P and u at every boundary element) are now known around the boundary S. Once the values of P and u on the whole boundary are known we can calculate the value of P at any interior point using equation 3-32 or 3-35. We can also calculate internal velocities or fluxes $u(\xi)$ by differentiating the ξ dependent terms in equation 3-32 under the integral sign

$$u(\xi) = \int_S [P(x)\hat{h}(x,\xi) - u(x)h(x,\xi)]dS(x) \tag{3-39}$$

where a new expresson $\hat{h}(x,\xi)$ is shown as follows:

$$\hat{h}(x,\xi) = -\frac{\partial h(x,\xi)}{\partial \xi_j} n_j(\xi) = \frac{\partial^2 G(x,\xi_j)}{\partial x_i \partial \xi_j} n_i(x) n_j(\xi) \tag{3-40}$$

3.4. SUMMARY

The principal idea behind the boundary element method is that the solution throughout the fracture region can be written in terms of point sources of variable magnitude, distributed along the boundary of the fracture region. If the boundary is discretized into a finite number of elements, and the specific boundary condition is assumed to be constant over each element, this leads to a finite number of algebraic equations for the magnitudes of the point sources. After solving for the equations, the stress and displacement distributions, or the potential and flux distributions throughout the fracture region, including the boundaries, can be found.

Based on the above formulations, two computer programs have been developed in FORTRAN to simulate the elastic deformation and the flow through a fracture with variable apertures and contact areas. The program for the elastic problem is named ROUGH, and FLOW is the name of the program for flow. Note that while elasticity equations were solved in the three-dimensional region bounded by the fracture "plane", the flow equations are solved in the two-dimensional region of the fracture plane; hence different discretizations must be used for the two problems.

CHAPTER 4

SIMULATING THE EFFECT OF CONTACT AREA ON COMPRESSIBILITY AND FLOW.

For a fractured medium, the percentage of contact area between the surfaces of the fracture is a key parameter which controls fracture stiffness and flow. Pronounced changes in the area of contact between asperities with increasing stress give rise to a non-linear stress-strain relationship. Fluid flow through a fracture whose flow path is partially blocked by areas of contact between the two surfaces may differ significantly from that through a pair of parallel plates, as described by the cubic law.

Because direct measurement of fracture void space and contact area at different levels of normal stress is not easy, studies of the effect of contact area on fracture stiffness and flow through the fracture have been limited. Recently, Pyrak et al. (1987) have made concurrent measurements of contact area and void space geometry, and fluid flow (1987) across three different natural joints in specimens of quart monzonite 0.05 m in diameter, at room temperature and at 100°C. To study contact areas and void spaces between the fracture surfaces, they injected molten Wood's metal into single fractures of granite specimens at different levels of applied normal stress. After the samples were cooled to solidify the alloy, precise metal casts of the void spaces resulted. The plan areas of the casts adhering to each surface were photographed and the casts were examined both optically and in a scanning electron microscope. They showed the areas of contact at different effective stresses, and found that the contact area of the stiffest specimen had asymptoted to a value of about 40 percent at a stress of 85 MPa. An asymptotic contact area (< 100%) at high stresses may be a basic

reason to interpret the experimental phenomenon that fracture stiffness tend to a finite value at high stresses, and that the specific flow becomes more or less independent of further reduction in aperture. However, I would like to use the computer to generate fracture void spaces and contact areas, and to study fracture stiffness and fluid conductivity as functions of percent contact area.

4.1. FRACTURE APERTURE GENERATION

In order to study the mechanical stiffness and hydraulic conductivity of fractures as a function of normal stress, I start my simulations by first developing a statistical model to generate an aperture distribution, which represents the fracture under zero normal load. A fracture is defined by upper and lower surfaces which either are separated by a distance (known as the aperture) that may vary from point to point, or touch each other (aperture=0, known as "contact area"). For simplicity, the upper and lower surfaces are assumed to be mirror reflections of each other about the fracture plane. Simulated fractures are created by discretizing the fracture plane into a square array that is (30×30) for the present study, and randomly assigning a independent log-normally distributed variable, X_{ij}, to each square element (i, j). A moving average filter then is convolved with the independent random aperture X_{ij} to get a correlated lognormally distributed value, Y_{ij}:

$$Y_{ij} = \sum_{k=-D}^{D} \sum_{l=-D}^{D} X_{i-k\ j-l} H_{kl} \tag{4-1}$$

where H_{kl}, the filter weights, are radially symmetric and decay exponentially,

$$H_{kl} = \begin{cases} C \exp(-\lambda\sqrt{k^2 + l^2}) & \text{for } \sqrt{k^2 + l^2} \le D \\ 0 & \text{otherwise} \end{cases} \tag{4-2}$$

D = determines the size of the filter,

λ = the exponential damping factor, which determines how fast the weights in the filter fall off zero,

C = the normalization factor, which is adjusted so that each of Y_{ij} has mean zero and fixed standard deviation.

By ordering the correlated variables from smallest to largest, and using fixed fractional contact area, the clipping level, Y_o, can be found. After clipping with the clipping level, a fixed fractional contact area is reached. The clipping process can be expressed as

$$I_{ij} = \begin{cases} 1 & Y_{ij} \geq Y_o \quad \text{void} \\ 0 & Y_{ij} < Y_o \quad \text{contact} \end{cases} \tag{4-3}$$

The final step is to set the fixed mean of the random variables.

To generate a fracture realization with variable aperture and contact area, filter radius, D, exponential damping factor, λ, normalization factor, C, the seed for generating the random Gaussians, fixed fractional contact area, c, and fixed mean of apertures, $\bar{h}$, must be specified. In my simulation, the filter radius D is of 7.5 element length, and the exponential damping factor, λ, is a variable ranging from 0.25 to 3.0. λ measures the correlation between contact area and open area. Larger values of λ correspond to contact areas that are more "dispersed", while smaller values of λ correspond to contact areas that are more "compact". All procedures for generating fractures with correlated variable apertures and contact areas are performed by a computer program developed by Coakley (1989).

In this chapter, attention will be focused on the stiffness and the tortuosity induced by the percentage and the spacial arrangement of contact areas. I therefore consider idealized fractures consisting of two parallel surfaces, with isolated contact areas. Variable apertures of the fracture generated by the computer program are set to a constant which is large enough to ensure that no new contact area will be created as normal load applies.

4.2. EFFECT OF FRACTIONAL CONTACT AREA ON COMPRESSIBILITY

Zimmerman (1984) studied the effect of pore shape on crack compressibility based on classical elasticity and indicated that the information obtained from his analysis was extremely useful in correlating compressibility data on porous rocks to other rock properties such as thermal conductivity, electrical resistivity, permeability, and velocities of sonic or seismic wave, each of which is highly dependent on the pore geometry.

It is envisioned that compressibility is a important mechanical property which relates reciprocally with specific stiffness. Specific stiffness of the fracture is defined as the inverse of the tangent slopes to the displacement *vs.* stress curve. Compressibility, C_o, expresses the effect of normal stress variations on the volume of fracture void space, V_v and is defined here as follows:

$$C_o = -\frac{1}{V_v}\left[\frac{\partial V_v}{\partial T}\right], \tag{4-4}$$

where T is the normal effective load applied uniformly to the fracture. Note that the definition of the compressibility as the slope of the volume of fracture void space *vs.*

normal stress curve contains a minus sign, to ensure that the numerical value of the compressibility will be positive.

The compressibility of the fracture is modeled in terms of the deformation of a half-space that is subjected to normal load across the "contact areas", so that the computer program ROUGH is used, which solves the full three-dimensional equations of elasticity for the infinite half-space. As a uniform constant normal stress $T = 10$ is applied to the fracture and the two surfaces of the fracture move closer together (Fig. 3-1-a), change of the volume of the void space, δV_v, can be calculated comparing to the initial volume V_v. Initial stress is also known, $T = 0$, so that compressibility of a fracture with fixed fractional contact area and fixed value of λ will be figured out easily by equation 4-4. In the computer simulation, numerical values have to be chosen for all parameters. All fractures have the same Young's modulus, E=6×10^4 MPa, and same Poisson's ratio, ν=0.25, in order to obtain case-by-case comparable results. It is to be expected that the stiffness of a fracture will increase (or the compressibility of a fracture will decreases) as the area of contact increases, since a fracture without any contact regions would posses no stiffness whatsoever (Zimmerman et al. 1990). It is also true, although it is perhaps not obvious, that the stiffness will depend on the size and shape of the contact areas, aside from its dependence on the amount of contact area (Hopkins et al. 1987). I therefore change fraction of contact area c and the exponential damping factor λ, which represents the distribution of a fracture, for each fracture or case. Fractional contact areas considered range from 5% to 30%, with an increment of 5%. The eight values of λ considered are 0.25, 0.75, 1.00, 1.25, 1.50, 1.75, 2.00, and 3.00. A total of 48 cases have done for simulating the fracture

compressibity as a function of the contact area distribution, as well as a function of fractional contact area.

The results are shown in Tables 4-1 and 4-2. The plots in Figures 4-1 and 4-2 correspond to the compressibilities of the fractures with contact area variations and with λ values as shown in Tables 4-1 and 4-2, respectively.

The plots show that fracture compressibility decreases non-linearly with increasing contact area. Similar to the experimental results obtained by Pyrak et al. (1987) in the laboratory for a granite core sample with a fracture oriented perpendicular to the axis of the core, the values of fracture stiffnesses tend to asymptote to a constant, finite value at high fraction of contact area. Figure 4-2 and Table 4-2 also suggest that correlation of contact areas with voids, which represents spatial arrangment of contact areas, is a important parameter in determining fracture compressibility. Fracture compressibility decreases as a non-linear function of the exponential damping factor, λ. The curves in Figure 4-2 imply that the more compact the contact area, the more compressible the fracture. However, fracture compressibility tends to be independent of λ if λ is greater than 2.00.

4.3. EFFECT OF FRACTIONAL CONTACT AREA ON FLOW

The flow through a fracture occluded by contact areas also strongly depends on the contact areas, which introduce longer flow path and tortuosity. Despite the recognition of the effect of contact area on flow considerable, controversy exists about the tortuosity when using the cubic law. The experiments conducted by Iwai (1976) suggested that flow-aperture curve is consistent with the cubic law for rough-walled

Table. 4-1 Compressibility dependence on fractional contact area for constant aperture fracture.

contact	λ=0.25	λ=0.75	λ=1.00	λ=1.25	λ=1.50	λ=1.75	λ=2.00	λ=3.00
area	C_o	C_o	C_o	C_o	C_o	C_o	C_o	C_o
5%	0.04130	0.03186	0.03014	0.02968	0.02890	0.02864	0.02838	0.02777
10%	0.03485	0.02704	0.02497	0.02341	0.02217	0.02161	0.02114	0.02013
15%	0.03246	0.02381	0.02185	0.02004	0.01826	0.01775	0.01727	0.01636
20%	0.03048	0.02109	0.01922	0.01722	0.01598	0.01535	0.01478	0.01381
25%	0.02832	0.01929	0.01707	0.01506	0.01396	0.01343	0.01309	0.01174
30%	0.02668	0.01813	0.01458	0.01351	0.01269	0.01203	0.01163	0.01062

† The unit of compressibility C_o is 1/MPa.

Table. 4-2 Compressibility dependence on exponential damping factor λ for constant aperture fracture.

λ	c = 5%	c = 10%	c = 15%	c = 20%	c = 25%	c = 30%
	C_o	C_o	C_o	C_o	C_o	C_o
0.25	0.04130	0.03485	0.03246	0.03048	0.02832	0.02668
0.75	0.03186	0.02704	0.02381	0.02109	0.01929	0.01813
1.00	0.03014	0.02497	0.02185	0.01922	0.01707	0.01458
1.25	0.02968	0.02341	0.02004	0.01722	0.01506	0.01351
1.50	0.02890	0.02217	0.01826	0.01598	0.01396	0.01296
1.75	0.02864	0.02161	0.01775	0.01535	0.01343	0.01203
2.00	0.02838	0.02114	0.01727	0.01478	0.01309	0.01163
3.00	0.02777	0.02013	0.01636	0.01381	0.01174	0.01062

† The unit of compressibility C_o is 1/MPa.

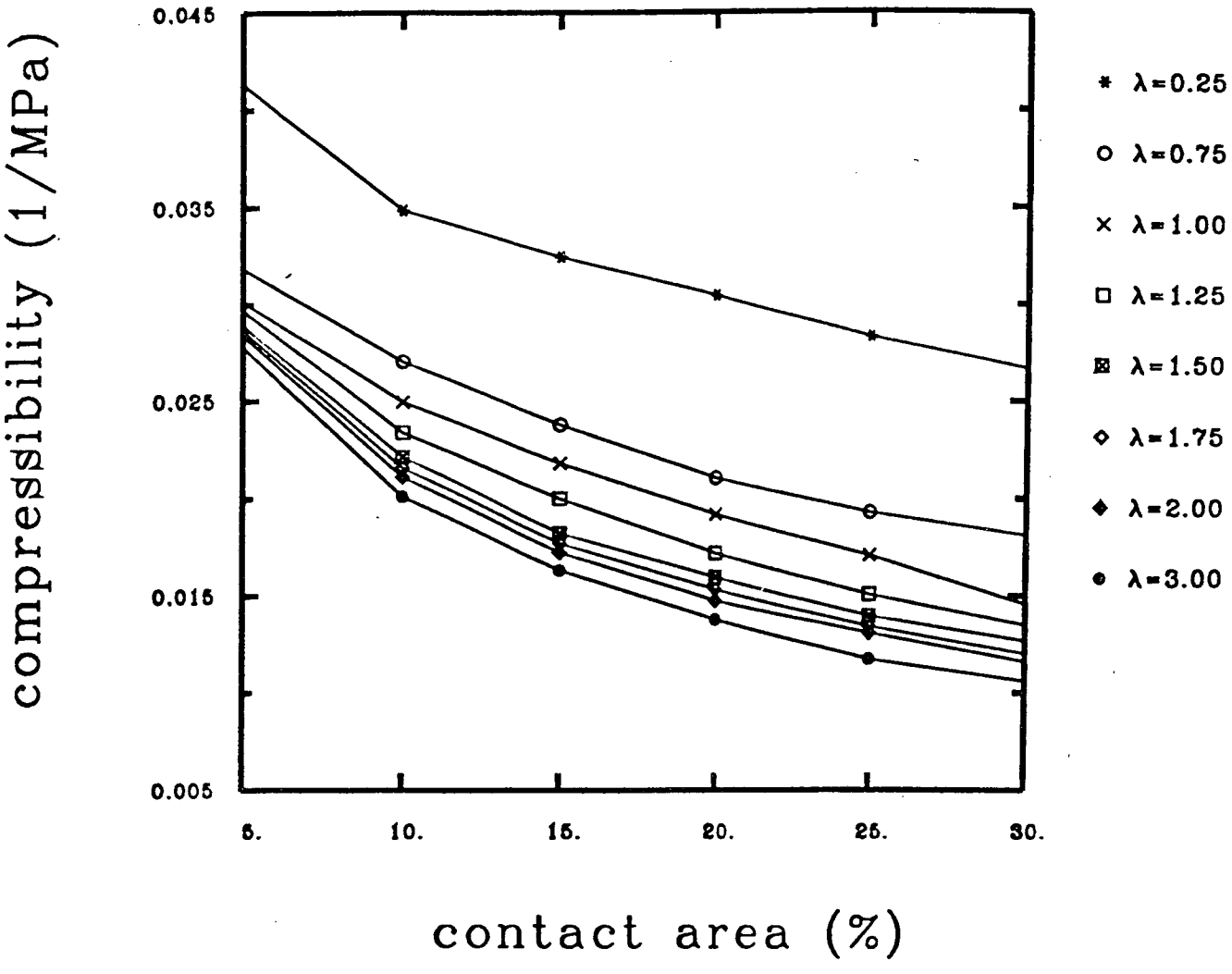

Fig. 4-1 Compressibility dependence on fractional contact area for constant aperture fracture.

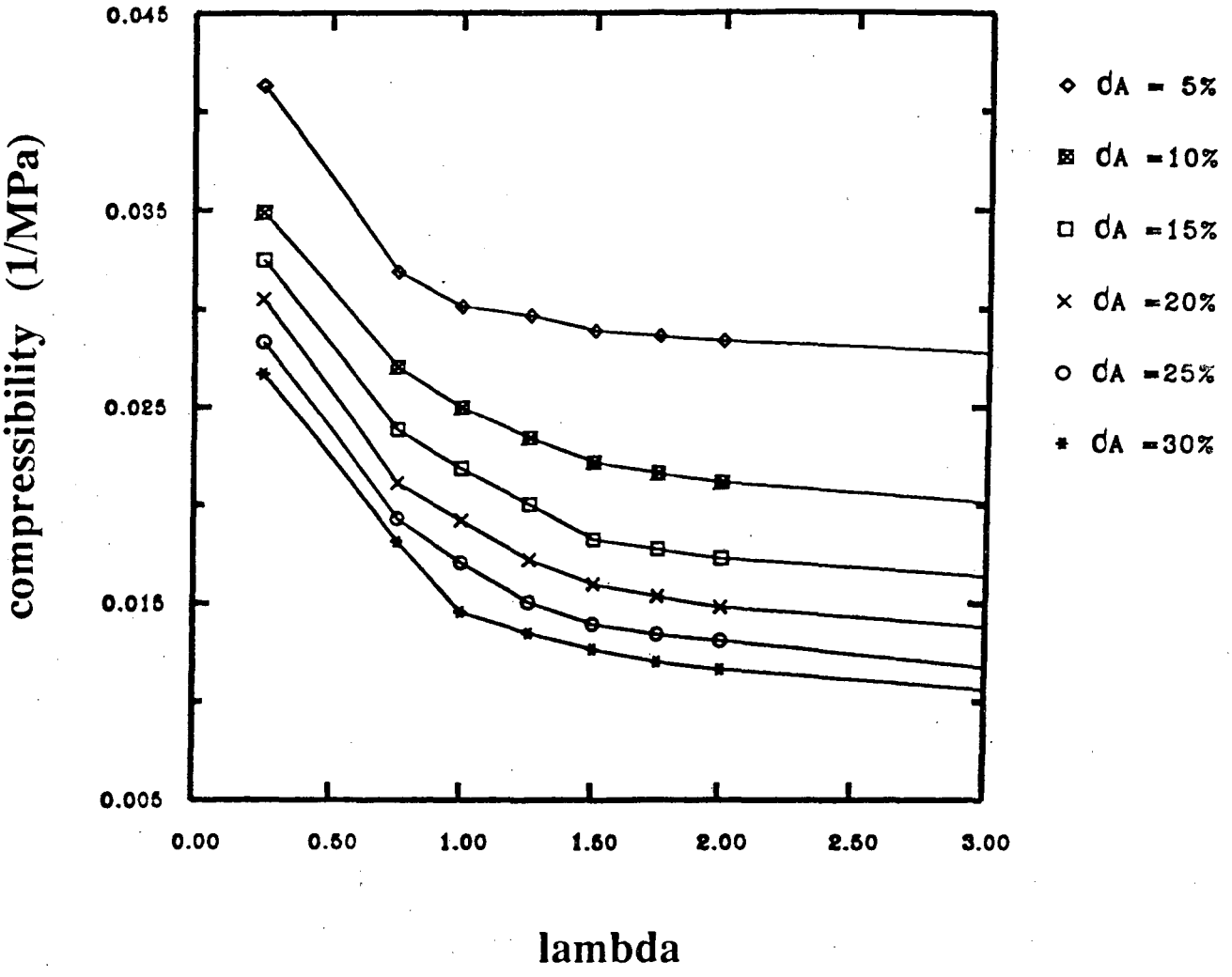

Fig. 4-2 Compressibility dependence on exponential damping factor λ for constant aperture fracture.

fractures under low normal stress. Validity of the cubic law implies that a fracture is modeled by a pair of parallel plates, and that the effect of contact area on flow is ignored. However, according to the results provided by an electrical resistance analog, Tsang (1984) suggested that a 1-2 order of magnitude error should result from neglecting the tortuosity when using the cubic law. More recent studies (Raven and Gale 1985., Pyrak et al. 1987) indicate significant deviations from the cubic law even at low stress or at a low fraction of contact area. Walsh (1981) adapt Maxwell's effective medium approach, along with the solutions for the potential fields surrounding circular inclusions (Carlaw & Jaeger 1959, p.426), to drive an expression, equation 2-35, for the effective permeability as a function of fractional contact area of the fracture.

In order to better understand the effect of contact areas on flow at low fraction of contact area, boundary element calculations (computer program FLOW), analogue electrical conductivity measurements, and an effective medium approximation are used to study the permeability of fractures with circular, elliptical and irregular asperity shapes.

As mentioned in Chapter 3, numerical solution of the full three-dimensional Navier-Stokes equations is far from trivial. In order to circumvent this difficulty, I have only performed flow simulations under the assumption that the aperture, in those regions not obstructed by asperities, is equal to a constant, h. I therefore sacrifice some of the effect of aperture variation, while still accounting for the effect of contact area and of the effect of the mean aperture. For this model, subject to a few other conditions, the Navier-Stokes equations can be reduced to a two-dimensional Laplace equation.

Fractures in these simulations are also generated with fixed percentage of contact area and constant apertures. Contact areas of a fracture are correlated with voids by a exponential damping coefficient λ.

A schematic diagram of a typical flow region, containing two contact regions, is shown in Figure 3-3. Both the external and internal boundaries are discretized. In my calculation, I take the fracture to occupy a square region in the x-y plane, with two opposing faces being boundaries of constant pressure. The pressure difference between these two faces can be taken as being of unit magnitude. The two other opposing faces are taken to be no-flow boundaries. After solving for the pressure field throughout the flow region, the flux out of the flow region is found by calculating $\partial P / \partial n$ along one of the constant-pressure boundaries, and summing the contribution from each element.

In general, the effective fracture permeability will depend on both the shape of the obstructions, and their location and orientation. Thus the permeability of fractures with circular, elliptical, and irregular obstruction shapes have been studied.

4.3.1. Circular obstructions

The case of circular obstructions to consider is the simplest one, for which the issue of orientation is not relevant; this also the only case for which analytical estimates of the permeability have been derived as equation 2-35 (Walsh 1981). Equation 2-35 is as follows:

$$\frac{k^*}{k_o} = \frac{1-c}{1+c}, \tag{4-5}$$

where k_o is permeability of the fracture with no asperities and c is the ratio of the

contact area to the total area of the fracture. The effective macroscopic permeability, k^*, can represent flow through the fracture on a length scale large enough to cover many asperities. Walsh interpreted this result as applying to "randomly located" obstructions. However, the Maxwell formalism cannot account for correlations in the locations of the asperities. Furthermore, any deviation from randomness would introduce a second order effect that is probably not felt at the low values of c found in naturally occurring fractures, which are usually less than 25% (Tsang & Witherspoon 1981).

Boundary element calculations were carried out for fractures with circular obstructions arranged in both hexagonal (Fig. 4-3) and square arrays (Table 4-3), for values of c ranging from 0 to 0.25. When the obstructions have the sort of symmetry exhibited by these arrangements, it suffices to perform the calculations in a "unit cell" formed by the imaginary grid of intersecting no-flow and constant pressure lines. perhaps surprisingly, in light of its approximate nature, Walsh's expression was found to be extremely accurate. The effect of asperity location was less than 1% at these values of c, and so it seems that the asumption of randomness can be relaxed when applying Walsh's expression.

As an additional check on the accuracy of the boundary-element calculations, analogue measurements were also carried out. Since the fluid flow is described by Laplace's equation, with the contact areas serving as impermeable boundaries, this problem is analogous to the flow of electrical current in a thin sheet with holes punched in it. Since the holes obstruct the flow of electrical current, they play the role of the asperity obstacles. Experiments were therefore carried out on such sheets to

measure the overall electrical conductivity (which is the analogue of the fracture permeability), in order to validate the numerical code. For these experiments, a thin sheet of conductive paper is cut into a square, and a strip of metallic paint is applied to two opposing edges. Since the conductivity of the paint is much higher than that of the paper, these edges will therefore be lines of constant potential. Holes which have the desired shapes, sizes and locations are cut out of the sheet, and the overall conductance is measured with an ohmmeter. Since resistance measurements can be made very accurately, this method is limited only by the precision with which the holes can be cut. As Figure 4-3 and Table 4-3 show, the measured electrical conductivities also agreed very closely with equation 4-5.

4.3.2. Elliptical obstructions

Since the Walsh-Maxwell effective medium approach works very well for circular obstructions, it is worthwhile to extend it to more general shapes.

Effective-medium theory was introduced by Maxwell (Carlaw & Jaeger 1959, p.426) to predict the overall electrical conductivity of composite media. The flow problem outlined above is a typical one in the area of effective properties of heterogeneous media. The unobstructed areas between the obstacles are regions of permeability k_o (say), while the obstacles are regions of zero permeability, and it is desired to determine the effective macroscopic permeability k^* that can represent flow through the fracture on a length scale large enough to cover many asperities. Since this problem is governed by Laplace's equation, Maxwell's method is applicable to this problem. In the terminology of the present problem, this method considers the decrease in flow due

to a single obstacle of known size and shape, averages this effect over all shapes and orientations of the obstacles, and then equates the resulting decrease in flux to that which would be caused by a single circular "obstruction" which has some effective permeability k^*. Walsh (1981) applied this method to a fracture with "randomly" located circular obstructions; we extend this method to cases where the obstacles are elliptical in shape, with random orientations (Chen et al. 1989).

One general shape that is often used in modeling various physical properties of rocks is the ellipse (Zimmerman 1984). Although it could be said that the ellipse, as well as the circle, are both too idealized to represent real asperities, the ellipse has the advantage that by varying the aspect ratio, one can achieve different values of the perimeter-to-area ratio.

The basic problem that must be solved in order to apply this approach to elliptical obstructions is Laplace's equation in the region exterior to an ellipse, with a uniform potential gradient at infinity, and no flow across the boundary of the ellipse. The ellipse has an arbitrary angular orientation with respect to the imposed potential; the effect on the flow is then averaged over all (equally likely) orientations. The solution to this problem can be found in Batchelor (1967), where it was derived in the context of inviscid flow across an ellipse. Note that this is mathematically equivalent to our problem, although the physical analogy is not so direct, since in the inviscid problem the velocity potential which satisfies equation 3-21 is not equal to the pressure. While the intermediate algebraic steps are somwhat complicated, the final expression for the effective permeability is only slightly different in form from equation 4-5 for circular obstructions:

$$\frac{k^*}{k_o} = \frac{1 - \beta c}{1 + \beta c}, \quad \text{where} \quad \beta = \frac{(1+\alpha)^2}{4\alpha}, \tag{4-6}$$

and the aspect ratio α (≤ 1) is defined as the ratio of the minor to major axis. Note that for circular obstructions, $\alpha = 1$, and $\beta = 1$, so that expression 4-6 for elliptical obstructions reduces to Walsh's expression for circular obstructions.

The beta factor defined in equation 4-6 is always greater than 1, and monotonically increases as the ellipse becomes more elongated. Hence the $k^*(c)/k_o$ curves for elliptical obstructions will always lie below Walsh's curve. (In face, since circular ''inclusion'' usually lead to upper or lower bounds in effective medium problems, it is reasonable to expect that Walsh's result is an upper bound with respect to all possible geometries). The predictions of the effective medium theory for α=0.2 are shown in Figure 4-4, where they are compared to boundary element calculations. The elliptical obstacles were generated by placing them on an hexagonal array (as in Figure 4-4), and then assigning to each ellipse a randomly chosen angular orientation. Over the range of contact areas shown in the figure, the effective medium estimates are very accurate. (Note that a contact area of 4% consisting of ellipses with α=0.2 corresponds to the same number of obstacles per unit area as a 20% concentration of circular obstacles). Due to the extremely laborious and painstaking procedure required to cut out the holes in conductive sheet, only one analogue measurement was made; this value (Fig. 4-4) was also in relatively close agreement with the predictions of equation 4-6.

4.3.3. Irregular obstructions

The shapes of asperity obstructions found in real rock fractures are of course more irregular than circles or ellipses. We have therefore used our boundary element code to study flow around irregularly shaped obstacles such as that shown in Figure 4-5 and Table 4-5. These patterns are generated by breaking up the square into a 64x64 rectangular grid, and assigning each grid block to be either an obstruction zone or a flow zone. The parameter that can be altered when generating these patterns is the correlation parameter, exponential damping factor λ (see Coakley 1989). As expected, the calculated permeabilities lie below equation 4-5. These permeabilities can be fit fairly well by using the elliptical obstruction model (equation 4-6) and a value of α=0.25. It can be conjectured that this value of α is somehow related to the perimeter-to-area ratio of the irregular obstruction pattern; this possibility is currently being investigated.

4.4. Summary

Numerical, analogue and analytical methods have been used to investigate the effect of contact area geometry on the permeability of a fracture. To isolate the effect of contact area, the fracture aperture has been assumed constant in the region between the asperities. For obstacles that are circular in the plane of the fracture, the expression derived by Walsh (1981) using a Maxwell-type effective medium approximation (equation 4-5) was found to be very accurate for contact area up to at least 25%. The Walsh-Maxwell approach was extended to randomly oriented obstacles of elliptical shape (equation 4-6), with the results verified numerically for certain values of the

aspect ratio and precentage contact area. Fractures with more irregular contact area geometries were also studies using boundary-element approarch. Such fractures had premeabilities that were lower (by as much as 30%) than would be predicted by Walsh's expression, but which could be fit very well by the effective medium approximation if an equivalent aspect ratio is used.

Table. 4-3 Normalized permeability of a fracture with circular asperities.

circular obstructions					
contact area %	$\frac{1-c}{1+c}$	checkerboard		uniform layout	
		flux f/f_o	asperity geometry	flux f/f_o	asperity geometry
			flow out		flow out
5	0.9048	0.8673	↑ ↑ ↑ ↑ ↑	0.8688	↑ ↑ ↑ ↑ ↑
10	0.8181	0.7496		0.7543	
15	0.7391	0.6433		0.6572	
20	0.6666	0.5461		0.5745	
25	0.6000	0.4588	↑ ↑ ↑ ↑ ↑	0.5051	↑ ↑ ↑ ↑ ↑
			flow in		flow in

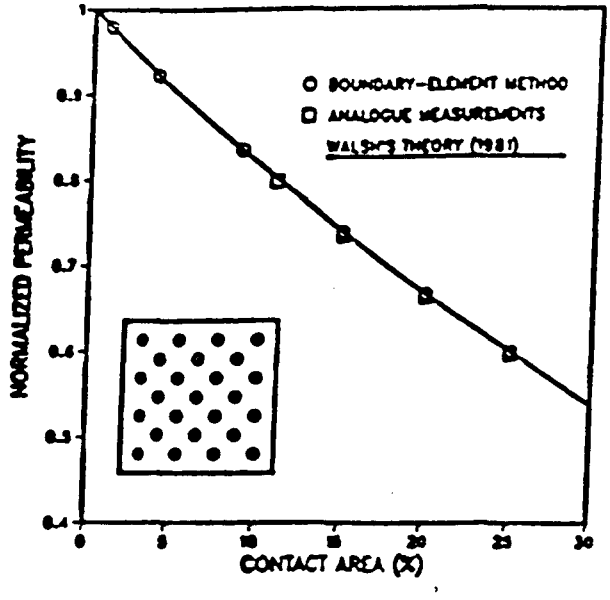

Fig. 4-3 Normalized permeability of a fracture with circular asperities; asperity geometry shown in inset.

Table. 4-4 Normalized permeability of a fracture with elliptical asperities.

elliptical obstructions					
contact area %	$\frac{1-\beta c}{1+\beta c}$	checkerboard		irregular	
		flux f/f_o	asperity geometry	flux f/f_o	asperity geometry
			flow out		flow out
5	0.9750	0.9736	↑ ↑ ↑ ↑ ↑	0.9753	↑ ↑ ↑ ↑ ↑
10	0.9500	0.9479		0.9466	
15	0.9250	0.9228		0.9238	
20	0.9000	0.8983		0.9040	
25	0.8750	0.8757	↑ ↑ ↑ ↑ ↑	0.5051	↑ ↑ ↑ ↑ ↑
			flow in		flow in

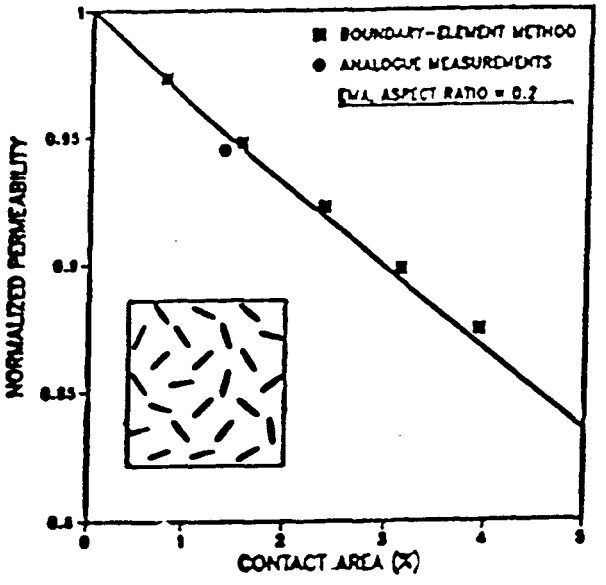

Fig. 4-4 Normalized permeability of a fracture with elliptical asperities; asperity geometry shown in inset.

Table. 4-5 Normalized permeability of a fracture with irregular asperities.

irregular obstructions					
contact area %	$\lambda = 0.75$		$\lambda = 1.50$		remark
	seed	flux f/f_o	seed	flux f/f_o	
5		0.8456		0.8534	
10		0.7213		0.7196	
15	90105030	0.6166	10011001	0.5890	flow out ↑ ↑ ↑ ↑ ↑
20		0.5195		0.4575	
25		0.4576		0.4129	
5		0.8686		0.8578	
10		0.7794		0.7240	
15	90100109	0.6761	37533573	0.6000	
20		0.5075		0.5002	↑ ↑ ↑ ↑ ↑
25		0.4474		0.4314	flow in
5		0.8635		0.8499	f_o = 3.3359000
10		0.7118		0.7431	■ contact area
15	43211234	0.5918	11111111	0.6405	
20		0.5251		0.5427	
25		0.4244		0.4174	
5		0.8790		0.8735	
10		0.7336		0.7486	
15	25522552	0.6403	99111199	0.5886	
20		0.5066		0.5018	
25		0.4492		0.4375	
5		0.8488		0.8624	
10		0.7096		0.7302	
15	12345678	0.5469	28766782	0.6188	
20		0.5359		0.5331	
25		0.3981		0.4919	

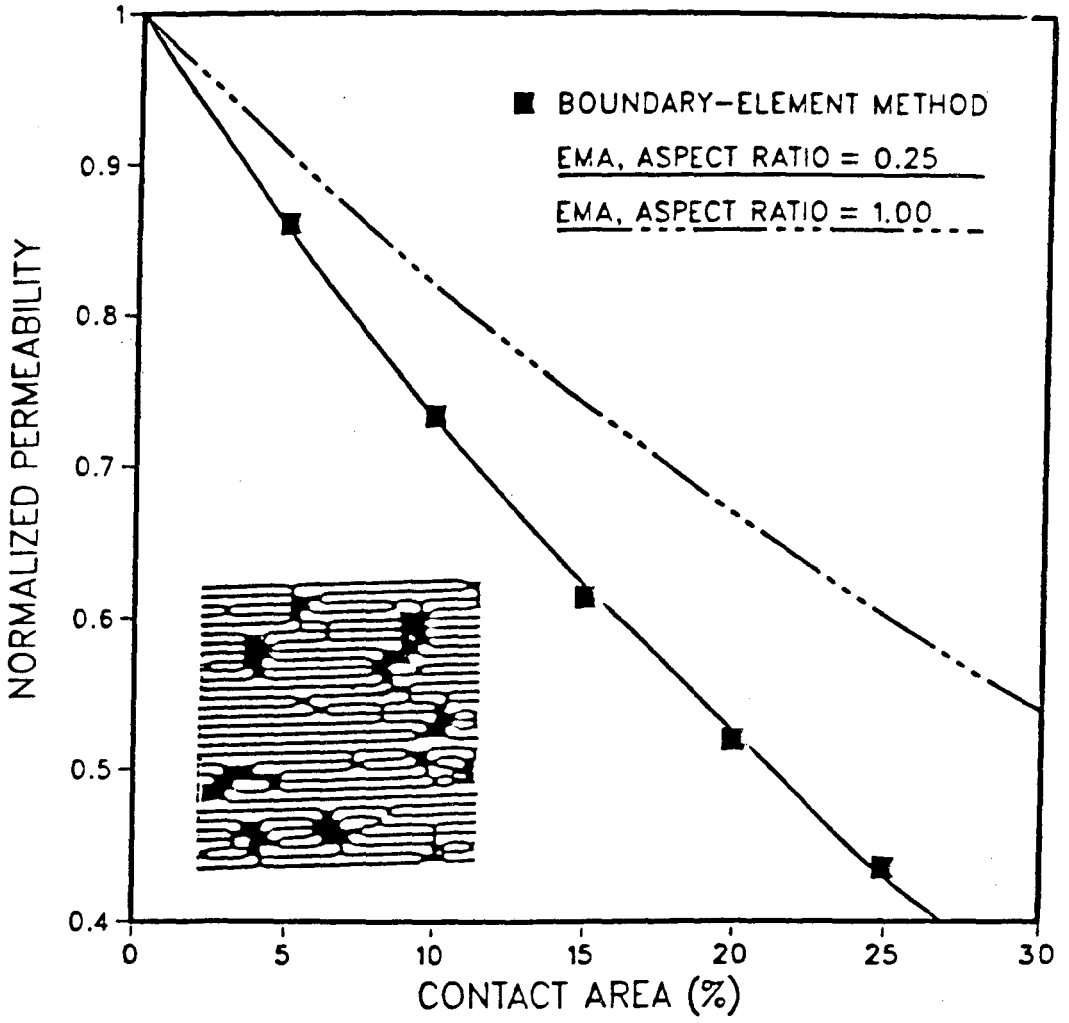

Fig. 4-5 Normalized permeability of a fracture with irregular asperities; example of asperity geometry is shown in the inset.

CHAPTER 5

COUPLED STIFFNESS-PERMEABILITY ANALYSIS

5.1. GENERAL

The hydraulic and mechanical behavior of a rock fracture or joint is strongly dependent on the geometry of the void space. When fluid flows through a fracture composed of two irregular surfaces in partial contact, it flows through those channels that have the largest apertures, and around the contact areas. Hydraulic conductance is locally proportional to the cube of the aperture (Brown 1987), so the permeability depends on the amount of contact area and the spatial distribution of the contact areas, as well as the aperture height (Chen et al. 1989). All of these parameters are, in turn, functions of the stress to which the fracture is subjected (Zimmerman et al. 1990). As the normal stress acting on a fracture increases, the apertures will decrease. In some parts of the fracture, this deformation will be large enough that new contact areas are created (Tsang & Witherspoon 1981). Both of these effects, the decrease of the aperture and the creation of new contact area, will cause the permeability to decrease.

The mechanical stiffness of a fracture also depends on the geometry of the fracture, as well as on the mechanical properties of the intact rock. It is to be expected that the stiffness will increase as the area of contact increases, since a fracture without any contact regions would possess no stiffness whatsoever. It is also true, although it is perhaps not obvious, that the stiffness will depend on the size and shape of the contact areas, aside from its dependence on the amount of contact area (Hopkins et al. 1987). For any given distribution of contact areas, the stiffness does not depend explicitly on the aperture; this is analogous to the fact that, to a very high approximation, the

increase in the compressibility of a rock due to a penny-shaped crack is independent of the aperture of the crack (Zimmerman et al. 1986). However, the aperture does determine the rate at which new contact area is created under the application of a normal load. Hence, the stress-dependence of stiffness will be strongly influenced by the distribution of apertures.

I have attempted to model the phenomena described above, using the boundary element methods. As mentioned above, the advantage of my approach is that both the mechanical deformation and permeability of a fracture can be studied using the same fracture geometry for both problems. In this way I am able to study the effect of the aperture distribution, and the distribution of contact areas, on both stiffness and permeability (cf., Barton et al. 1985; Pyrak-Nolte et al. 1987).

I start this analysis by also generating a log-normal aperture distribution, which represents the fracture under zero normal load, on 30x30 grids. These distributions can be quantified by the contact area percentage, c, the mean aperture, $\bar{h}$, the standard deviation of the distributions of apertures, s, and an exponential damping factor (correlation factor), λ, which measures the correlation between contact area and open area (Coakley 1989). The hydraulic conductivity of the fracture is computed by the boundary element method, FLOW, assuming that the aperture is everywhere equal to $\bar{h}$. An increment of normal stress is then applied to the fracture, and its deformation is calculated by the elastostatic boundary element method ROUGH. In those regions where the fracture is open, the two faces of fracture move closer together; in some locations the aperture merely decreases, while at other points the deformation may be large enough to create new contact area. After this deformation is found, the contact area

and the average aperture are recalculated. The permeability of the new fracture geometry is then calculated, and the process is continued. I thereby generate a relationship between normal stress, the amount of contact area, the average aperture, the normal stiffness, and the permeability. Since each calculation with specified statistical parameters represents one realization of a stochastic orecess, the precedure is repeated for 10 realizations, in order to arrive at statistically meaningful properties.

After studying the general hydromechanical properties of a fracture with variable apertures, I carried out parameter sensitivity studies by varying the standard deviation s of the lognormal aperture density distribution, and the correlation factor λ. The flow calculations are carried out using the simplification that the aperture is everywhere equal to its average value, $\bar{h}$. In another words, only the effect of the fracture contact area on flow is considered, and the effect of fracture surfaces roughness on flow is still not exactly included in the flow modeling. This assumption creates an error whose magnitude is difficult to estimate. However, tests to perceive the effect of the roughness on flow have been tried by closing up the apertures, whose magnitude is less than one fifth of average aperture and by simulating the flow through the contact-increased and mean aperture-decreased fracture at each stress level. Comparisons between distributions of fracture contact areas resulted by deformed and undeformed cases were also performed in order to note the importance of considering fracture deformation.

5.2. GENERAL BEHAVIOR OF FRACTURE DEFORMATION AND FLOW

Considering statistically meaningful properties, ten realizations have been generated for analysis of general behavior of fracture deformation and flow. The initial contact area of each realization at zero load is 5%, its mean aperture is 10 μm, and the standard deviation of its apertures is 4.576 μm. The λ parameter is taken to be 0.75. The results of these ten realizations are listed and plotted in Figure 5-1 to 5-10. To illustrate the sort of results, I will examine in detail the stiffness and permeability found for two particular realizations of a simulated fracture. Two such sets of results will be sufficient to illustrate which properties display a strong "sample-to-sample" variance, and which do not.

At zero stress, the contact area for one of the realizations appears at upper left corner in Figs. 5-1 to 5-10, which is to say as a few isolated, slightly irregular patches. As the normal load on the fracture is increased, the percentage of contact area increases at a nearly linear rate (see Figs. 5-1 to 5-11 and Table 5-1). We can note the lack of a connected (bottom to top) flow path at T=40 MPa in the Figure 5-4 (seed=129921), while a connected flow path still exists at T=70 MPa in the Figure 5-3 (seed=999).

As is typical of a real fracture, the average joint closure increases with stress, but at a continually decreasing rate (Fig. 5-12 & Table 5-2). In other words, the fracture becomes stiffer as the stress increases. This is shown in Figure 5-13 and Table 5-3, where the fracture stiffness which is non-linear is plotted and listed as a function of the normal stress. Notice also that the fracture stiffness may be tending to asymptote to some constant value at the highest stresses.

The hydromechanical coupled simulation between the stress applied to the fracture and the flow through the fracture shows very good agreement with the experimental results obtained by Pyrak et al (1987). Since the flow rate, under a fixed pressure gradient, is proportional to the cube of average aperture $\bar{h}$, and since average aperture decreases rapidly with stress (Fig. 5-12), I expect that the flow rate will drop off rapidly with stress. This is verified in Figure 5-14, which shows the flow rate initially dropping off at a rate roughly proportional to the 3rd power of the stress, and then dropping off more rapidly after the stress reaches some "critical" value. This rapid falloff may correspond to the percolation limit, at which a connected open pathway for fruid flow no longer exists. Another instructive way to look at the results is as in Figure 5-15, which shows the logarithm of flow rate, normalized to its zero-stress and no-contact value, plotted as a function of the logarithm of average aperture. Note that as the stress increases, the flowrate falls below that which would be predicted by the cubic law. This reflects the "tortuosity" effect, in which the fluid is forced to flow around the closed-off asperity regions. As described by the models of Walsh (1981) and Chen et al. (1989), the tortuosity is an increasing function of contact area, hence it is to be expected that the tortuosity will increase as the stress increases.

For the same set of statistical parameters, there is of course some variation in the calculated properties of the fracture, between different realizations. Fractures with different initial aperture distributions, but the same mean, standard deviation, and initial contact area, tend to have very nearly the same mechanical behavior (see Figs. 5-16, 5-17, 5-18, and Table 5-11, 5-12, 5-13). The hydraulic properties, on the other hand, show much more variability (Figs. 5-14, 5-15 and Tables 5-14, 5-15). At stresses below about 30 MPa, the permeability-pressure curves for the different realizations lie

close together. However, the pressure above which the permeability drops off rapidly to zero varies from about 40 MPa to 70 MPa between the different fracture realizations.

5.3. PARAMETER SENSITIVITY STUDIES

Based on the ten realizations governed by a particular set of aperture parameters, I have discussed the general behavior of fracture deformation and flow through a fracture with variable apertures. The effect of percent contact area on fracture stiffness and permeability has also been discussed in the chapter 4. I now turn to study the effect of the variation of aperture parameters, except the parameter of percent contact area which I have discussed in Chapter 4, on the fracture deformation and flow through a fracture. The parameter sensitivity studies have been carried out by coupling simulation between fracture deformation and fluid flow by varying (1) the standard deviation s in the lognormal aperture density distribution, (2) the correlation factor λ, which measures the correlation between contact area and open area, and (3) the average aperture $\bar{h}$.

5.3.1. Dependence on the standard deviation s and the correlation factor λ:

Fractures at stress T=0 with variable apertures were generated with a specified set of aperture parameters ($\bar{h}$,c,s,λ), then simulations for fracture deformation and flow through the fracture were carried out. Three values of the standard deviation s (2.926, 4.576, 7.089), and two values of correlation factor λ (0.75, 1.50) were used. Throughout the sensitivity studies, the average aperture $\bar{h}$=10 μm and the percent

contact area c=5% at stress σ=0 were maintained. The six sets of $(\bar{h}, c, s, \lambda)$ values chosen therefore were set 1: s=2.926, λ=0.75; set 2: s=4.576, λ=0.75; set 3: s=7.089, λ=0.75; set 4: s=2.926, λ=1.50; set 5: s=4.576, λ=1.50; and set 6: s=7.089, λ=1.50. Stress applied to the fracture changes from 0 MPa to 70 MPa with increments of 10 MPa. The results of standard deviation s and correlation factor λ sensitivity studies are summarized in Table 5-6 and plotted from Figure 5-19 to 5-24.

When the normal load on the fracture is less than 20 MPa, the fractures with the larger standard deviation display a more rapid increase in the percentage of contact area, while when the normal load is greater than 20 MPa, a more rapid increase in the area of contact is taken by the fracture with smaller standard deviation. The total increase of the contact area for smaller standard deviation is more than that for larger standard deviation (Fig. 5-19, 5-20). It is found that for a larger s, the percent contact area vs stress curve will asymptote to a constant (i.e. there is no increase in contact area with increasing stress) more rapidly. These trends may be explained by the fact that a larger standard deviation means a greater number of small apertures (Moreno et al. 1988) and large apertures, while a smaller standard deviation means a greater number of medium apertures. Since contact area is a sensitive parameter which strongly affects the hydromechanical behavior of fractures, and it depends on s, fracture hydromechanical behavior must be a function of s. Figure 5-21 shows that for a given value of normal stress, the closure is decreasing functions of s.

Contact area as a function of the normal stress also depends on the statistical parameter λ. Recall that the larger values of λ correspond to contact areas that are more dispersed, while smaller values of λ correspond to more compact regions of

contact. As also discussed in Chapter 4, for a given amount of contact area, the stiffness is an increasing function of λ, reflecting the fact that, for example, two separate contact areas of 1 mm^2 will be "stiffer" than one contact region of 2 mm^2, which is certainly plausible (Zimmerman et al. 1990). It is therefore understandable that for stress greater than 20 MPa, and for a larger λ, the closure and the percent contact area of the fracture are less than those for a smaller λ (see Figs. 5-20c, 5-21c), and that fracture stiffness vs normal stress curves have exact reciprocal relationships with corresponding percent contact area vs stress curves (compare between Figs. 5-20 and 5-22). I prove once more that fracture stiffness depends strongly on the percentage and the distribution of contact areas which is a function of λ and s when stress increases.

The effect of standard deviation s on the flow properties is shown in Figs. 5-23 and 5-24. As stress increases, for a larger standard deviation s=7.089, the flow is increased (Fig. 5-23) and the relationship between the logarithm of specific flow and the logarithm of aperture is linear with a larger exponent of 5.7, while for a smaller standard deviation s=2.926, the flow is decreased and the relationship is a linear with a smaller exponent of 4.6 (Fig. 5-24). For a larger standard deviation s=7.089, the percolation limit, at which a connected open pathway for fluid flow no longer exists, is reached at a lower critical stress of 50 MPa, while a smaller standard deviation s=2.926, the connected open pathway for fluid flow still exists at the stress of 50 MPa (Figs. 5-19, 5-24). These trends may be explained by the fact that the mean aperture of the fracture with larger s is larger due to less closure even if a larger standard deviation means a greater number of small apertures and a larger percent contact area at low stress level.

The effect of λ on flow properties is more complicated, and implicit, since the distribution of aperture directly affects the mechanical closure of the fracture, which in turn explicitly determines the permeability (Zimmerman et al. 1990). The effect of λ on the flow properties increases with increasing standard deviation. With stress less than 40 MPa and standard deviation s=2.926, the slope of the straight line plotting the logarithm of the fracture mean aperture against the logarithm of specific flow is the same when λ changes from 0.75 to 1.50. For a higher standard deviation s=7.089, the slope increases from 5 to 5.7 when λ changes from 0.75 to 1.50. When the same standard deviation s=7.089 is maintained, the percolation limit is reached at a critical stress of 50 MPa for a larger correlation factor λ=1.5, while it is reached at a higher critical stress of 60 MPa for λ=0.75 (Fig. 5-24c). The effect of λ on the critical stress implies that new contact areas produced by applied normal stress always occur in the middle of "oceanic" voids separated by "archipelagoes" of contact areas. It means that for a fracture with larger λ or more dispersed contact area distribution, a connected open pathway for fluid flow is blocked up more easily by the new created contact areas with increasing stress.

5.3.2. Sensitivity studies for mean aperture of fracture:

In the usual parallel plate model of a fracture, the flow is proportional to the cube of the mean aperture $\bar{h}$. In the real world, surfaces of a fracture are rough and a fracture has areas of contact. We know that roughness along the fracture walls plays a definite role in controlling the flow; however, it is difficult to estimate the effect of fracture roughness. The purpose of the following sensitivity studies for the fracture mean aperture that I have been carried out is to give some qualitative impressions

about the roughness effect.

In order to study the effect of the variation of $\bar{h}$, simulations in the begining were the same as the above case studies for general behaviors of fracture deformation and flow. Fractures are generated by different fracture geometry parameters ($\bar{h}$, s, λ), and deformed by an increment of normal stress applied to the fracture. Afterwards, at each stress level, the local apertures $h(x,y)$, if less than $0.2\bar{h}$, were set to zero, mean aperture and percent contact area were calculated to obtain a new distribution of contact areas (see Fig. 5-25), and the simulations of flow through the fracture with decreased mean aperture $\bar{h}_c$, and increased and redistributed contact area were carried out. Four fractures with geometry parameters ($\bar{h}$, s, λ) were chosen for the mean aperture sensitivity studies. The four sets of ($\bar{h}$, s, λ) values were set 1: s=2.934, λ=1.5; set 2: s=4.576, λ=1.5; set 3: s=7.090, λ=1.5; set 4: s=4.576, λ=0.75. The fracture mean apertures at T=0 were set to $\bar{h}$=10 μm.

Results of mean aperture sensitivity studies are summarized in Tables 5-7 and 5-8. The results show that mean apertures $\bar{h}_c$ decrease (Tables 5-7, 5-8), distributions of contact areas change (Fig. 5-25), and, consequently, flow rates drop off(Fig. 5-26) as local apertures less than $0.2\bar{h}$ are closed up at different stress levels. The maximum drop of flow rates has the value 72.22% when the variation of the mean aperture is 6.2%. Since variation of mean aperture, $\Delta\bar{h}$, is a function of the aperture density distribution function $n(\bar{h})$ (Fig. 5-28), both $\Delta\bar{h}$ and $n(\bar{h})$ vary with increasing normal stress, and $\Delta\bar{h}$ is therefore not a linear function of either the mean aperture or the normal stress. The curves of Δh vs normal stress (Table 5-8) show a "saddle" relations. As expected, since flow rate is related to a cube of mean aperture, decrement of flow

rate with increasing normal stress exhibits two peaks (Fig. 5-26b). For the fracture with smaller standard deviation s=2.934, only the first peak of flow rate appears (Fig. 5-26a). For the fracture with larger standard deviation s=7.090, the first peak shifts to a lower normal stress, and the flow rate falls off before the second peak shows up. The latter may reflect the fact that the permeability of a ''tight'' fracture is dominated by the critical neck after stress or percent contact area reaches some ''critical'' value. The critical neck is defined as the smallest aperture along the path of highest aperture through the fracture. The results also show that the effect of correlation factor λ on the flow is important (compare Fig.5-26b with Fig.5-26d). Smaller λ causes more decrement of the flow.

Through the mean aperture sensitivity studies, I find that a cubic law using mean aperture as the variable is inadequate for estimating the joint flow (Fig. 5-27). Flow along a fracture depends on the actual local aperture at the microscopic level, and while the most important parameter to affect the flowpath topology is s, the standard deviation in the lognormal aperture distribution, the effect of λ on the flowpath topology should not be neglected. Normal stress across the fracture changes the flowpath topology by diminishing the apertures and increasing the areas of contact (Pyrak-Nolte et al. 1988). Once the normal stress reaches a ''critical value'', the flow is dominated by the critical neck which is also affected by the standard deviation s.

5.3.3. Sensitivity studies for the effect of contact deformations on the flow:

Brown (1987) has done a computer simulation of laminar flow between rough surfaces using the finite-difference method. In his simulations, he ignored the deformation of the fracture surfaces at contacts, and the local aperture $h(x,y)$ was set to zero as if the material at the contacts had been dissolved away. Results of his flow simulations show that the flow rate is not particularly sensitive to the slope of the power spectrum, and that the actual flow rate between rough surfaces is about 70-90% of that predicted by the parallel plate model. However, his results are quite insufficient to explain the major departures from the cubic law for flow through fractures as observed by Witherspoon et al.(1980), Engelder and Scholz (1981), Raven and Gale (1985), pyrak-nolte et al. (1987), and Zimmerman et al. (1990). The disagreement between Brown (1987) and other investigators may be result from neglecting the fracture deformation. It is difficult to estimate the effect of neglecting fracture deformation on the flow along the fracture. What I will do is to roughly show that consideration of the fracture deformation is necessary.

Two fractures with different geometry parameters ($\bar{h}$, s, λ) were generated. With $\bar{h}$=10 μm and s=4.576 for both fractures, λ is changed from 0.75 for first fracture to 1.50 for the second fracture. In order to obtain the percent contact area, $c(\%)$, and the distribution of contact area at each stress level for deformed cases, an increment of normal stress was applied to the fracture, and its deformation calculated. After fracture deformation was found, the contact area and the average aperture were recalculated. Since the percent contact area $c(\%)$ at each stress level could be found for deformed cases, and initial aperture density distribution functions were characterized by a given

s and $\bar{h}$=10 μm (Fig. 5-28), the amount of contact areas and the distribution of contact areas at each stress level for undeformed cases are obtained by clipping the initial aperture density distribution function with the known corresponding percent contact area of deformed cases. Figure 5-29 shows the comparison of the contact area distributions at each stress level between deformed and undeformed cases. It is clear that while new contact areas created by the increment of the normal stress for undeformed cases are likely to surround the pre-existing contact areas, and the new contact areas produced by deformation are likely to occur in the middle of the large void spaces (oceans) between the regions of high contact density (archipelagoes). The more dispersed distribution of the contact area caused by the fracture deformation implies that the fracture is ''stiffer'', flow along the fracture is proportional to a larger exponent (at least greater than 5.0) of the mean aperture, and the flow falls off at a lower stress level.

5.4. SUMMARY

Boundary element methods have been used to study the deformation and permeability of simulated fractures as a function of normal stress. Statistically equivalent fractures are characterized by their initial mean aperture, aperture standard deviation, and a parameter that quantifies the compactness of the contact regions called correlation factor. Many of the observed features of real rock fracture behavior are reproduced by these simulations. The stiffness of the fractures drops off asymptotically as the stress is increased, while the contact area increases at a nearly linear rate. At low stresses, the permeability drops off at a rate proportional to the third power of the normal stress (cf., Walsh 1981). At some critical stress, typically on the order of 30-70 MPa, the

percolation limit, the point of smallest aperture along the path of highest aperture, is reached, and the permeability drops precipitously. For different statistically equivalent realizations, the critical stress is the only property that exhibits a strong sample-to-sample variation. Results of the parameter sensitivity studies show that while the fracture permeability may be stress history dependent, it is uniquely defined by the local aperture at the microscopic level. The stress history determines the fracture aperture density distribution function and, consequently, its local aperture for a given stress. However, the initial fracture aperture density distribution function strongly depends on the standard deviation s and the correlation factor λ. s and λ are important parameters for stiffness, flow and percolation limit. Finally, it is roughly verified that ignoring the fracture deformation will create an error whose magnitude is difficult to estimate but necessary to consider.

Table 5-1 percent contact area as a function of normal stress, for ten different realizations.

standard deviation=4.576, filter coefficient λ= 0.75											
normal stress	contact area (%)										
	seed for generating different realizations										
MPa	333	666	999	129921	169961	159	747	36963	471118	992431	mean
0	5.00	5.00	5.00	5.00	5.00	5.00	5.00	5.00	5.00	5.00	5.00
10	5.00	5.33	5.00	5.00	5.00	5.00	5.00	5.00	5.00	5.00	5.03
20	10.00	15.22	12.00	13.89	12.67	12.44	12.67	10.44	17.22	15.78	13.23
30	29.89	31.22	30.67	29.67	30.33	30.33	29.33	27.00	31.00	32.89	30.23
40	43.56	44.00	47.22	45.67	45.89	43.67	43.11	42.78	44.67	46.78	44.74
50	55.11	53.78	59.44	55.00	57.00	53.89	55.11	53.22	55.78	57.00	55.53
60	62.22	64.33	69.00	64.33	64.44	60.89	64.00	62.00	65.44	66.11	64.28

Table 5-2 Joint closure as a function of normal stress, for ten different realizations.

standard deviation=4.576, filter coefficient λ= 0.75											
normal stress	closure (μm)										
	seed for generating different realizations										
MPa	333	666	999	129921	169961	159	747	36963	471118	992431	mean
0	0.000	0.000	0.000	0.000	0.000	0.000	0.000	0.000	0.000	0.000	0.000
10	2.950	3.431	3.290	3.291	3.284	3.070	3.109	2.954	3.592	3.466	3.244
20	5.629	5.937	6.112	5.823	6.011	5.623	5.707	5.595	6.044	5.982	5.846
30	7.048	7.279	7.452	7.153	7.472	6.922	7.152	7.133	7.307	7.274	7.219
40	7.872	8.070	8.195	7.913	8.267	7.692	7.972	7.968	8.110	8.001	8.006
50	8.404	8.572	8.636	8.384	8.750	8.221	8.494	8.498	8.618	8.488	8.506
60	8.780	8.904	8.929	8.725	9.075	8.610	8.844	8.869	8.962	8.821	8.852

Table 5-3 Stiffness as a function of normal stress, for ten different realizations.

standard deviation=4.576, filter coefficient λ= 0.75											
normal stress	stiffness ($Mpa/\mu m$)										
	sced for generating different realizations										
MPa	333	666	999	129921	169961	159	747	36963	471118	992431	mean
5	3.390	2.915	3.040	3.038	3.045	3.257	3.216	3.385	2.784	2.885	3.096
15	3.733	3.990	3.544	3.949	3.667	3.917	3.849	3.786	4.078	3.974	3.849
25	7.047	7.452	7.463	7.519	6.845	7.698	6.920	6.502	7.918	7.740	7.310
35	12.136	12.642	13.459	13.158	12.579	12.987	12.195	11.976	12.453	13.755	12.734
45	18.797	19.920	22.676	21.231	20.704	18.904	19.157	18.868	19.685	20.534	20.048
55	26.596	30.120	34.130	29.326	30.769	25.707	28.571	26.954	29.070	30.030	29.127

Table 5-4 Flow rate under a unit pressure gradient, as a function of normal stress for ten realizations.

standard deviation=4.576, filter coefficient λ= 0.75											
normal stress	normalized flow rate (Q/Q_o)										
	seed for generating different realizations										
MPa	333	666	999	129921	169961	159	747	36963	471118	992431	mean
0	0.8602	0.8517	0.8539	0.8539	0.8447	0.8496	0.8694	0.9877	0.8193	0.8566	0.8647
10	0.3014	0.2396	0.2579	0.2578	0.2559	0.2828	0.2845	0.3455	0.2156	0.2390	0.2680
20	0.05428	0.04299	0.03750	0.04158	0.04073	0.04874	0.04719	0.06261	0.03230	0.03242	0.03775
30	0.007987	0.006493	0.003370	0.006104	0.004432	0.004450	0.006357	0.004407	0.004722	0.003286	0.004457
40	0.001784	0.000492	0.000392	0.000000	0.000000	0.001110	0.001394	0.000436	0.000504	0.000850	0.000696
50	0.000277	0.000000	0.000155			0.000444	0.000000	0.000000	0.000000	0.000250	0.000011
60	0.000000		0.000061			0.000000				0.000097	0.0000016

Table 5-5 Permeability as a function of mean aperture for ten realizations.

standard deviation=4.576, filter coefficient λ= 0.75									
seed for generating different realizations									
333		666		999		129921		169961	
$\bar{h}$	Q/Q_o	$\bar{h}$	Q/Q_o	$\bar{h}$	Q/Q_o	$\bar{h}$	Q/Q_o	$\bar{h}$	Q/Q_o
10.000	0.8602	10.000	0.8517	10.000	0.8539	10.000	0.8539	10.000	0.8447
7.052	0.8602	6.569	0.8453	6.710	0.8539	6.709	0.8539	6.716	0.8447
4.371	0.6500	4.063	0.6409	3.888	0.6381	4.177	0.5706	3.989	0.6417
2.952	0.3105	2.721	0.3223	2.548	0.2040	2.847	0.2645	2.528	0.2743
2.128	0.1851	1.930	0.0684	1.805	0.0666	2.087	0.0000	1.733	0.0000
1.596	0.0682	1.428	0.0000	1.364	0.0611	1.616		1.250	
1.220	0.0000	1.096		1.071	0.0494	1.275		0.925	
seed for generating different realizations									
159		747		36963		471118		992431	
$\bar{h}$	Q/Q_o	$\bar{h}$	Q/Q_o	$\bar{h}$	Q/Q_o	$\bar{h}$	Q/Q_o	$\bar{h}$	Q/Q_o
10.000	0.8496	10.000	0.8694	10.000	0.9877	10.000	0.8193	10.000	0.8566
6.930	0.8496	6.891	0.8694	7.046	0.9877	6.408	0.8193	6.534	0.8566
4.377	0.5812	4.293	0.5964	4.405	0.7325	3.956	0.5217	4.018	0.4998
3.078	0.1526	2.848	0.2752	2.867	0.1870	2.693	0.2418	2.726	0.1622
2.308	0.0903	2.028	0.1672	2.032	0.0520	1.890	0.0746	1.990	0.1078
1.779	0.0788	1.506	0.0000	1.502	0.0000	1.382	0.0000	1.512	0.0723
1.390		1.156		1.131		1.038		1.179	0.0590

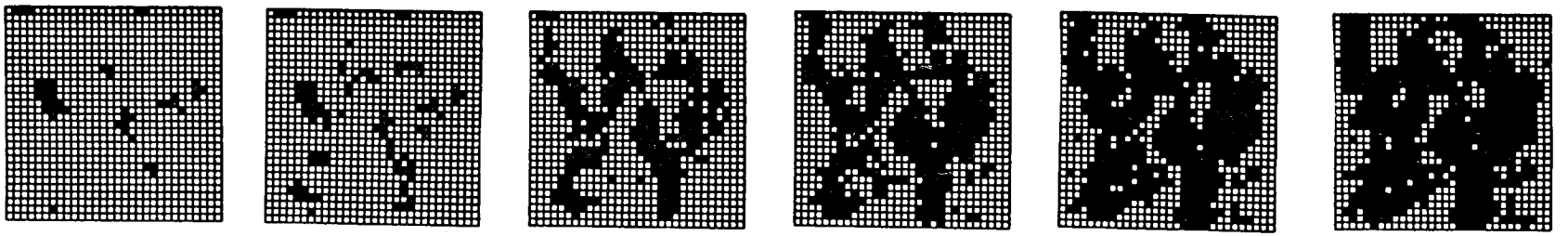

T=10 T=20 T=30 T=40 T=50 T=60

seed=333, standard deviation=4.576, filter coefficient λ=0.75						
normal stress *MPa*	contact area %	ave. aperture μm	closure μm	stiffness *MPa* /μm	normalized flux f/f_o	flow rate Q/Q_o
0	5.00	10.000	0.000	3.390	0.8602	0.8602
10	5.00	7.050	2.950	3.733	0.8602	0.3014
20	10.00	4.371	5.629	7.047	0.6500	0.05428
30	29.89	2.952	7.048	12.136	0.3105	0.007987
40	43.56	2.128	7.872	18.797	0.1851	0.001784
50	55.11	1.596	8.404	26.596	0.0682	0.0002772
60	62.22	1.220	8.780		0.0000	0.0000000

Figure 5-1 Contact area (in black) as a function of normal stress T. Note the lack of a connected flow path at 60 MPa (top); average aperture, stiffness, contact area percentage, and flow rate etc. as a function of normal stress (bottom) for the realization generated by seed 333.

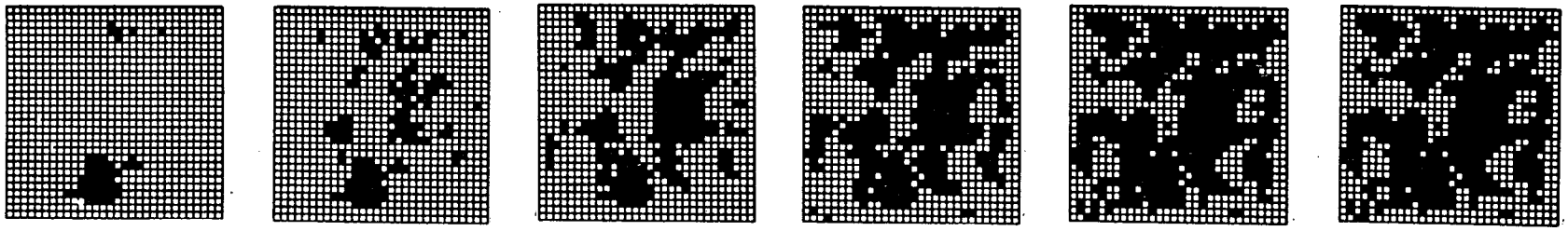

seed=666, standard deviation=4.576, filter coefficient λ=0.75						
normal stress	contact area	ave. aperture	closure	stiffness	normalized flux	flow rate
MPa	%	μm	μm	*MPa* /μm	f/f_o	Q/Q_o
0	5.00	10.000	0.000		0.8517	0.8517
10	5.33	6.569	3.431	2.915	0.8453	0.2396
20	15.22	4.063	5.937	3.990	0.6409	0.04299
30	31.22	2.721	7.279	7.452	0.3223	0.006493
40	44.00	1.930	8.070	12.642	0.0684	0.000492
50	53.78	1.428	8.572	19.920		
60	64.33	1.096	8.904	30.120		

Figure 5-2 contact area (in black) as a function of normal stress T. Note the lack of a connected flow path at 50 MPa (top); average aperture, stiffness, contact area percentage, and flow rate etc. as a function of normal stress (bottom) for the realization generated by seed 666.

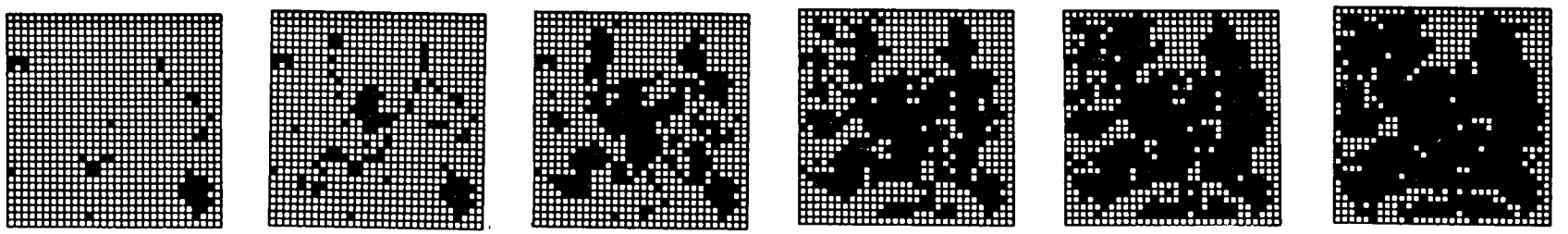

seed=999, standard deviation=4.576, filter coefficient λ=0.75						
normal stress	contact area	ave. aperture	closure	stiffness	normalized flux	flow rate
MPa	%	μm	μm	*MPa* /μm	f/f_o	Q/Q_o
0	5.00	10.000	0.000		0.8539	0.8539
10	5.00	6.710	3.290	3.040	0.8539	0.2579
20	12.00	3.888	6.112	3.544	0.6381	0.0375
30	30.67	2.548	7.452	7.463	0.2040	0.00337
40	47.22	1.805	8.195	13.459	0.0666	0.000392
50	59.44	1.364	8.636	22.676	0.0611	0.000155
60	69.00	1.071	8.929	34.130	0.0494	0.000061

Figure 5-3 contact area (in black) as a function of normal stress T; average aperture, stiffness, contact area percentage, and flow rate etc. as a function of normal stress (bottom) for the realization generated by seed 999.

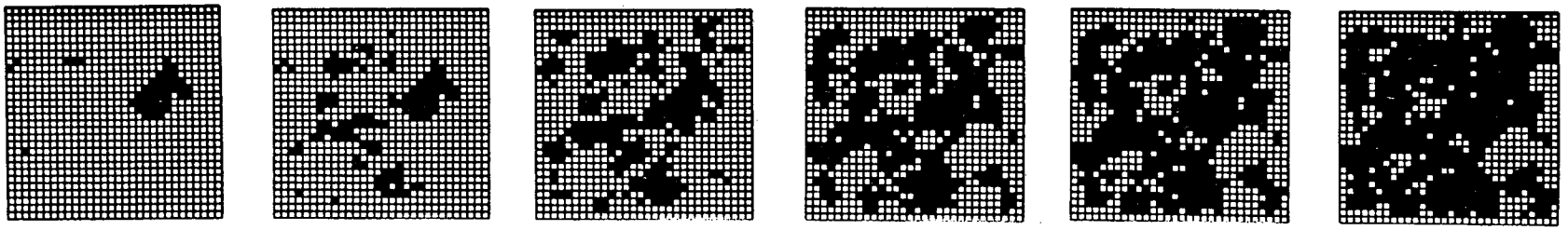

seed=129921, standard deviation=4.576, filter coefficient λ=0.75						
normal stress	contact area	ave. aperture	closure	stiffness	normalized flux	flow rate
MPa	%	μm	μm	*MPa* /μm	f/f_o	Q/Q_o
0	5.00	10.000	0.000	3.038	0.8539	0.8539
10	5.00	6.709	3.291	3.949	0.8539	0.2578
20	13.89	4.177	5.823	7.519	0.5706	0.04158
30	29.67	2.847	7.153	13.158	0.2645	0.006104
40	45.67	2.087	7.913	21.231	0.0000	0.000000
50	55.00	1.616	8.384	29.326		
60	64.33	1.275	8.725			

Figure 5-4 contact area (in black) as a function of normal stress T. Note the lack of a connected flow path at 40 MPa (top); average aperture, stiffness, contact area percentage, and flow rate etc. as a function of normal stress (bottom) for the realization generated by seed 129921.

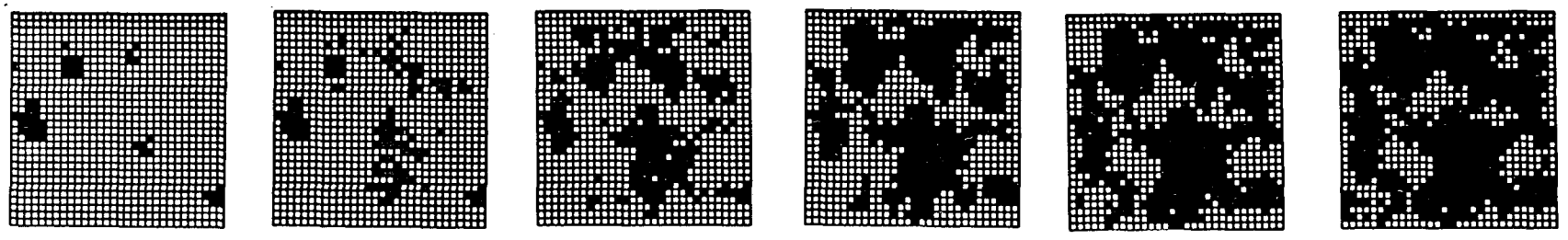

seed=169961, standard deviation=4.576, filter coefficient λ=0.75						
normal stress	contact area	ave. aperture	closure	stiffness	normalized flux	flow rate
MPa	%	μm	μm	$MPa/\mu m$	f/f_o	Q/Q_o
0	5.00	10.000	0.000	3.045	0.8447	0.8447
10	5.00	6.716	3.284	3.667	0.8447	0.2559
20	12.67	3.989	6.011	6.845	0.6417	0.04073
30	30.33	2.528	7.472	12.579	0.2743	0.004432
40	45.89	1.733	8.267	20.704	0.0000	
50	57.00	1.250	8.750	30.769		
60	64.44	0.925	9.075			

Figure 5-5 contact area (in black) as a function of normal stress T. Note the lack of a connected flow path at 50 MPa (top); average aperture, stiffness, contact area percentage, and flow rate etc. as a function of normal stress (bottom) for the realization generated by seed 169961.

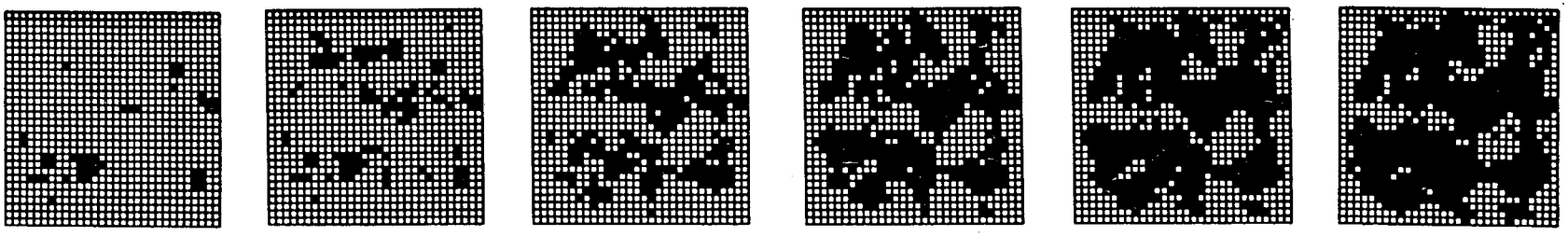

T=10 T=20 T=30 T=40 T=50 T=60

seed=159, standard deviation=4.576, filter coefficient λ=0.75						
normal stress	contact area	ave. aperture	closure	stiffness	normalized flux	flow rate
MPa	%	μm	μm	*MPa* /μm	f/f_o	Q/Q_o
0	5.00	10.000	0.000	3.257	0.8496	0.8496
10	5.00	6.930	3.070	3.917	0.8496	0.2828
20	12.44	4.377	5.623	7.698	0.5812	0.04874
30	30.33	3.078	6.922	12.987	0.1526	0.004450
40	43.67	2.308	7.692	18.904	0.0903	0.001110
50	53.89	1.779	8.221	25.707	0.0788	0.0004437
60	60.89	1.390	8.610		0.0000	0.0000000

Figure 5-6 contact area (in black) as a function of normal stress T; average aperture, stiffness, contact area percentage, and flow rate etc. as a function of normal stress (bottom) for the realization generated by seed 159.

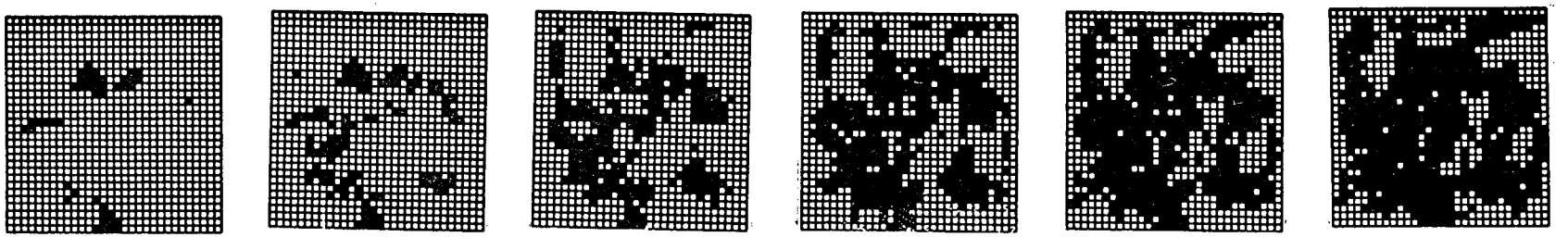

seed=747, standard deviation=4.576, filter coefficient λ=0.75						
normal stress	contact area	ave. aperture	closure	stiffness	normalized flux	flow rate
MPa	%	μm	μm	*MPa* /μm	f/f_o	Q/Q_o
0	5.00	10.000	0.000		0.8694	0.8694
10	5.00	6.891	3.109	3.216	0.8694	0.2845
20	12.67	4.293	5.707	3.849	0.5964	0.04719
30	29.33	2.848	7.152	6.920	0.2752	0.006357
40	43.11	2.028	7.972	12.195	0.1672	0.001394
50	55.11	1.506	8.494	19.157	0.0000	0.000000
60	64.00	1.156	8.844	28.571		

Figure 5-7 contact area (in black) as a function of normal stress T. Note the lack of a connected flow path at 50 MPa (top); average aperture, stiffness, contact area percentage, and flow rate etc. as a function of normal stress (bottom) for the realization generated by seed 747.

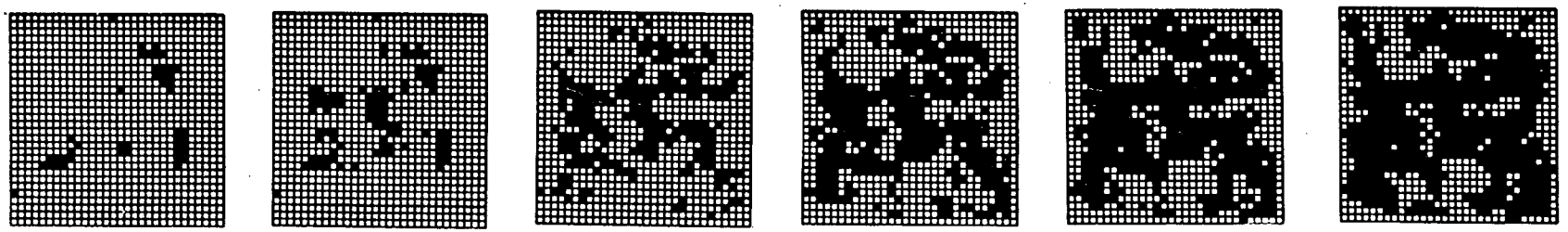

seed=36963, standard deviation=4.576, filter coefficient λ=0.75						
normal stress	contact area	ave. aperture	closure	stiffness	normalized flux	flow rate
MPa	%	μm	μm	*MPa* /μm	f/f_o	Q/Q_o
0	5.00	10.000	0.000		0.9877	0.9877
10	5.00	7.046	2.954	3.385	0.9877	0.3455
20	10.44	4.405	5.595	3.786	0.7325	0.06261
30	27.00	2.867	7.133	6.502	0.1870	0.004407
40	42.78	2.032	7.968	11.976	0.0520	0.0004363
50	53.22	1.502	8.498	18.868	0.0000	0.0000000
60	62.00	1.131	8.869	26.954		

Figure 5-8 contact area (in black) as a function of normal stress T. Note the lack of a connected flow path at 60 MPa (top); average aperture, stiffness, contact area percentage, and flow rate etc. as a function of normal stress (bottom) for the realization generated by seed 36963.

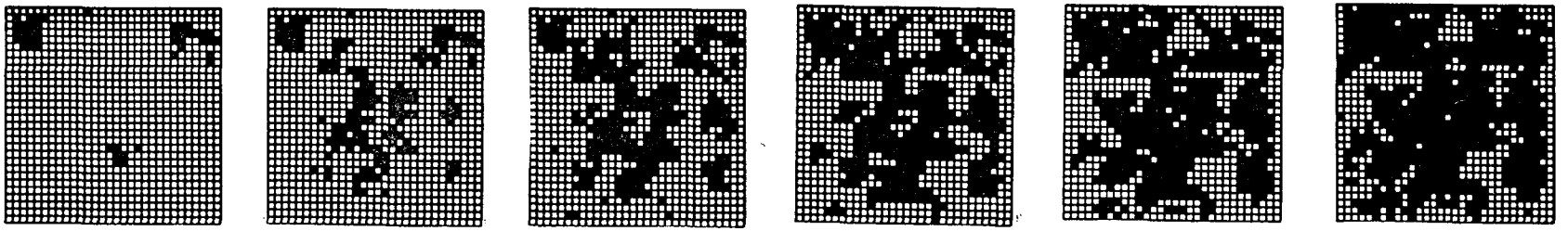

T=10 T=20 T=30 T=40 T=50 T=60

seed=471118, standard deviation=4.576, filter coefficient λ=0.75						
normal stress	contact area	ave. aperture	closure	stiffness	normalized flux	flow rate
MPa	%	μm	μm	*MPa* /μm	f/f_o	Q/Q_o
0	5.00	10.000	0.000		0.8193	0.8193
10	5.00	6.408	3.592	2.784	0.8193	0.2156
20	17.22	3.956	6.044	4.078	0.5217	0.0323
30	31.00	2.693	7.307	7.918	0.2418	0.004722
40	44.67	1.890	8.110	12.453	0.0746	0.0005036
50	55.78	1.382	8.618	19.685	0.0000	0.0000000
60	65.44	1.038	8.962	29.070		

Figure 5-9 contact area (in black) as a function of normal stress T. Note the lack of a connected flow path at 50 MPa (top); average aperture, stiffness, contact area percentage, and flow rate etc. as a function of normal stress (bottom) for the realization generated by seed 471118.

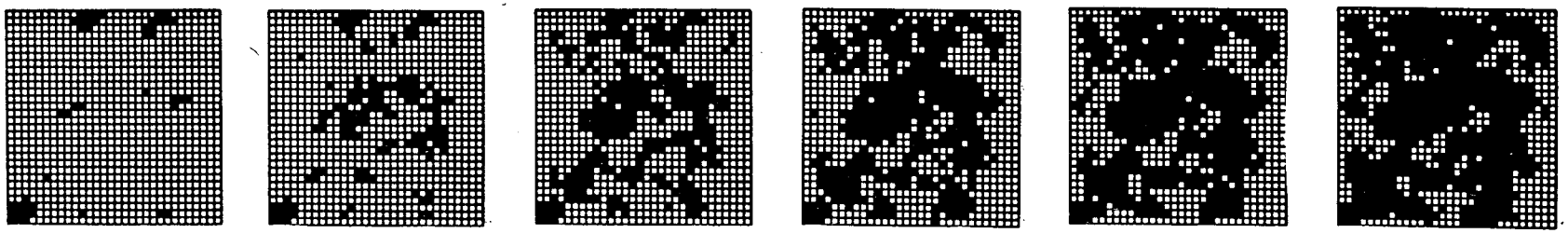

seed=992431, standard deviation=4.576, filter coefficient λ=0.75						
normal stress	contact area	ave. aperture	closure	stiffness	normalized flux	flow rate
MPa	%	μm	μm	*MPa* /μm	f/f_o	Q/Q_o
0	5.00	10.000	0.000	2.885	0.8566	0.8566
10	5.00	6.534	3.466	3.974	0.8566	0.2390
20	15.78	4.018	5.982	7.740	0.4998	0.03242
30	32.89	2.726	7.274	13.755	0.1622	0.003286
40	46.78	1.990	8.001	20.534	0.1078	0.0008495
50	57.00	1.512	8.488	30.030	0.0723	0.0002499
60	66.11	1.179	8.821		0.0590	0.00009669

Figure 5-10 contact area (in black) as a function of normal stress T. Note the lack of a connected flow path at 40 MPa (top); average aperture, stiffness, contact area percentage, and flow rate etc. as a function of normal stress (bottom) for the realization generated by seed 992431.

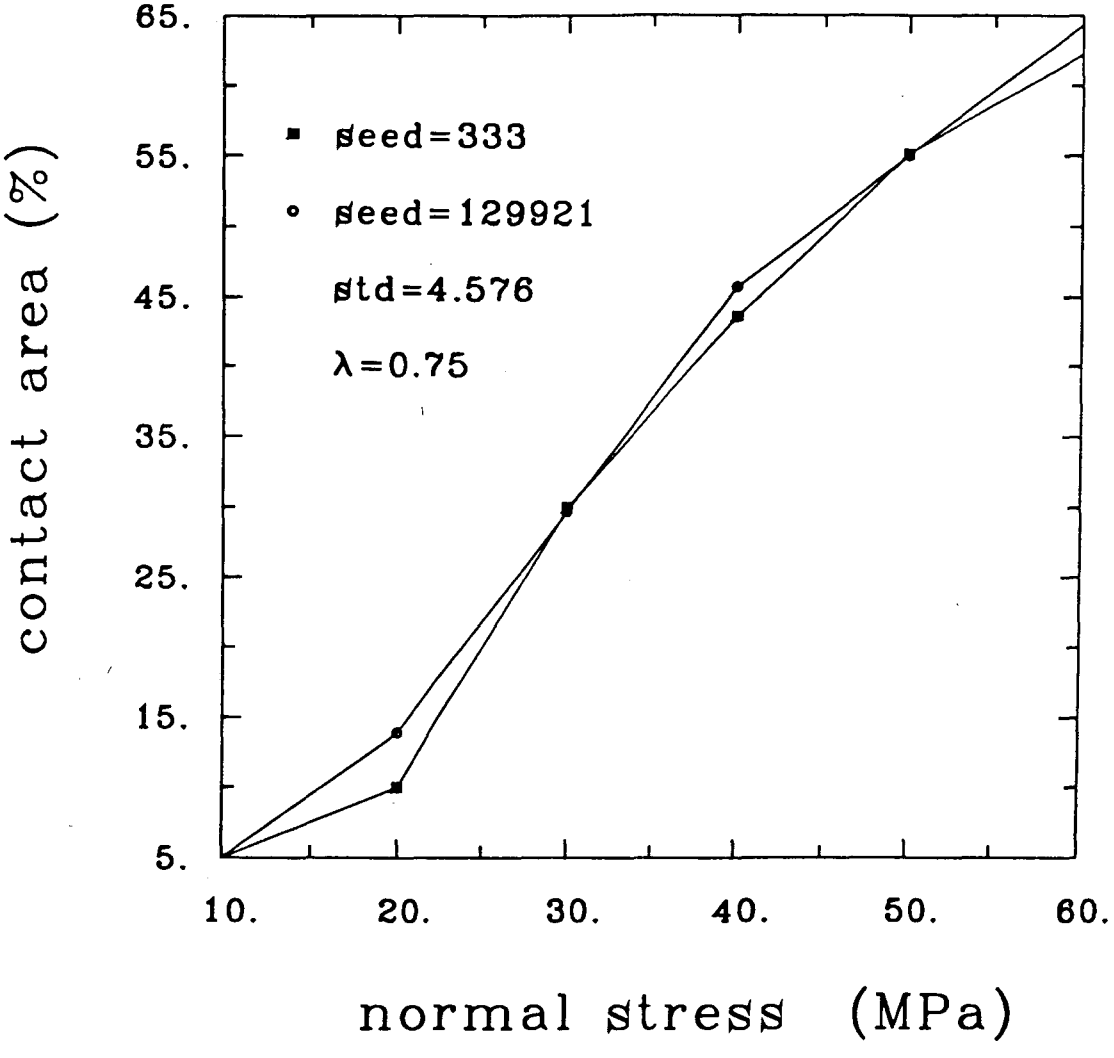

Figure 5-11 Percent contact area as a function of normal stress, for two different realizations.

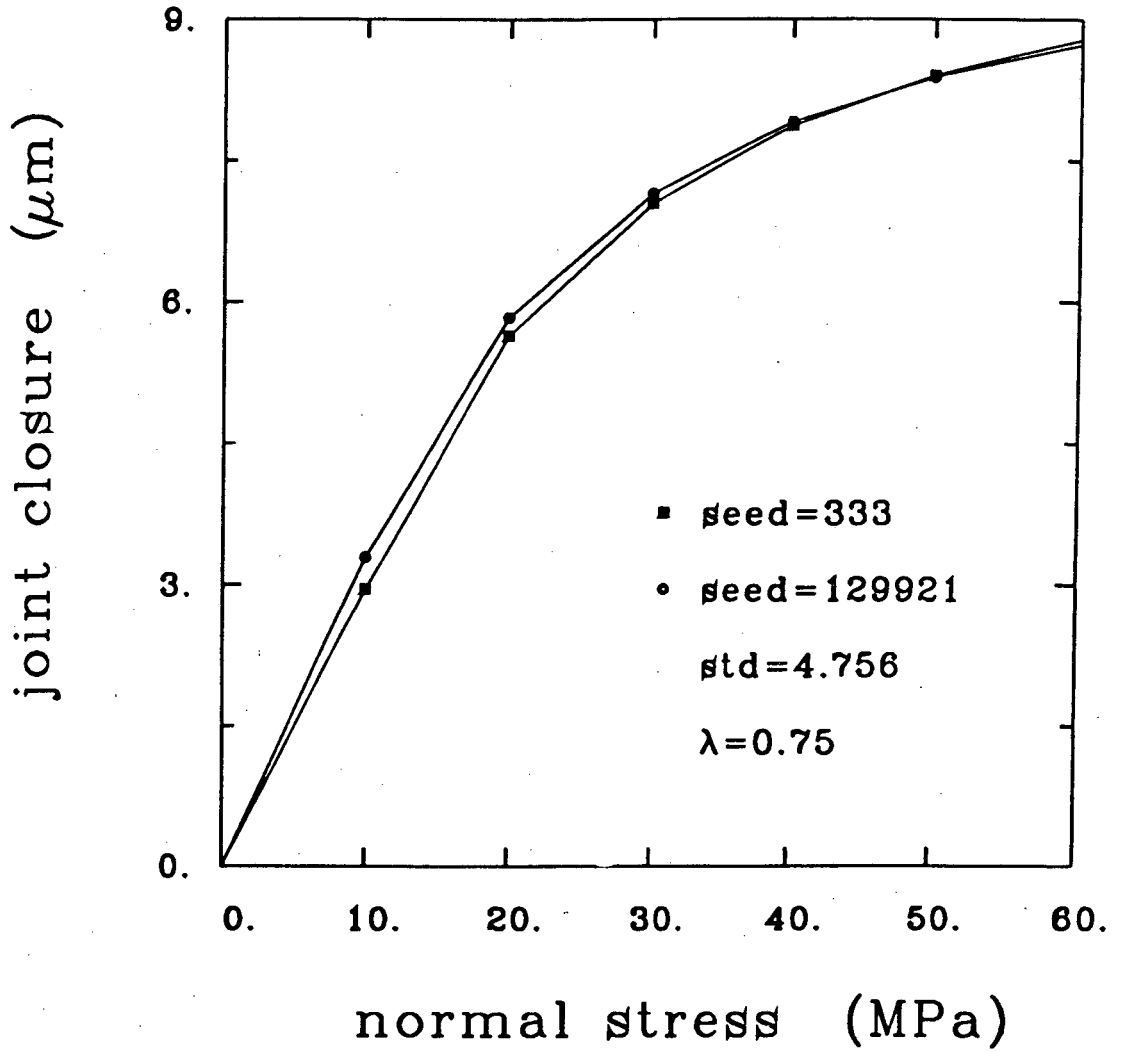

Figure 5-12 Joint closure as a function of normal stress, for two different realizations.

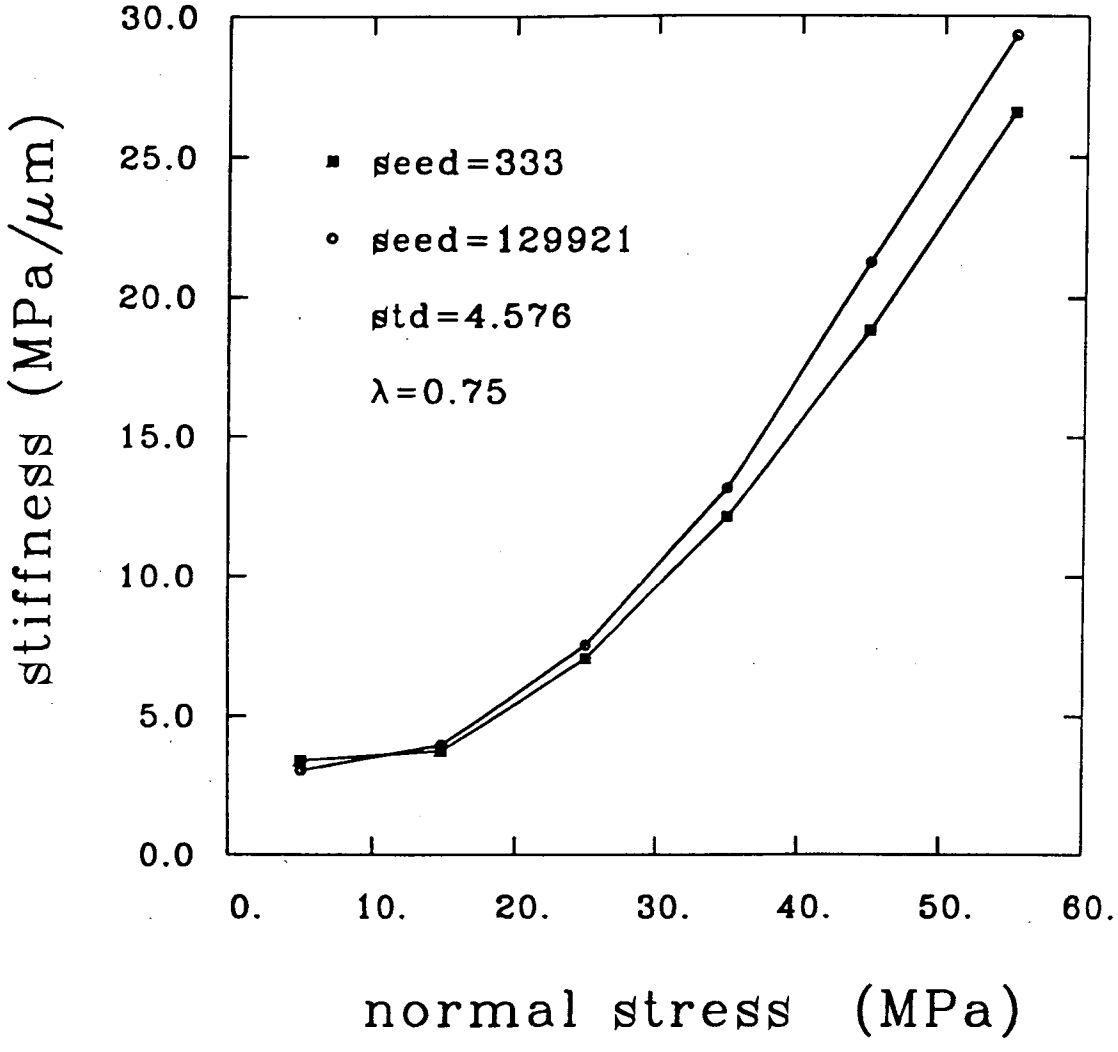

Figure 5-13 Stiffness as a function of normal stress, for two different realizations.

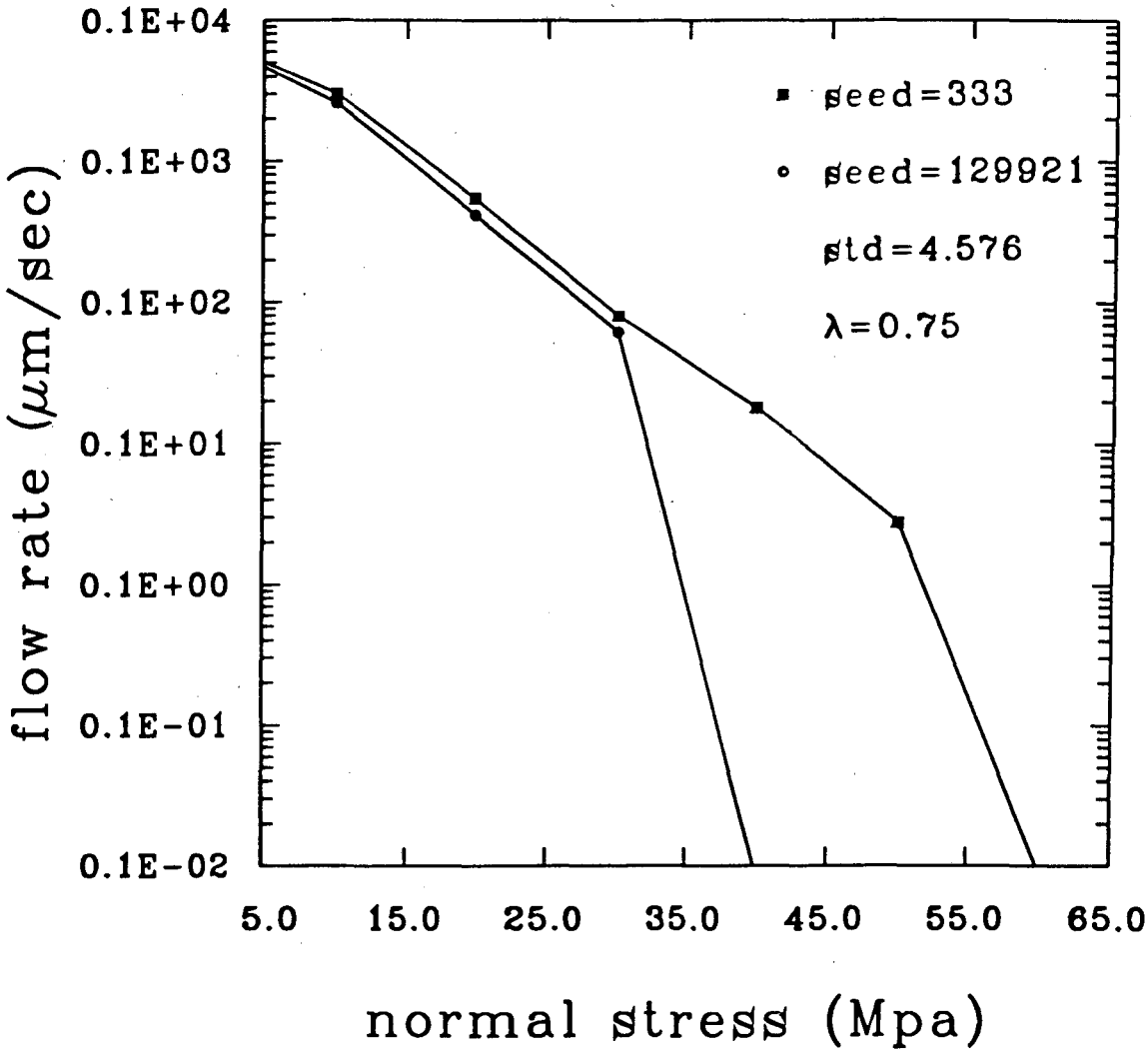

Figure 5-14 Flow rate under a unit pressure gradient, as a function of normal stress for two realizations.

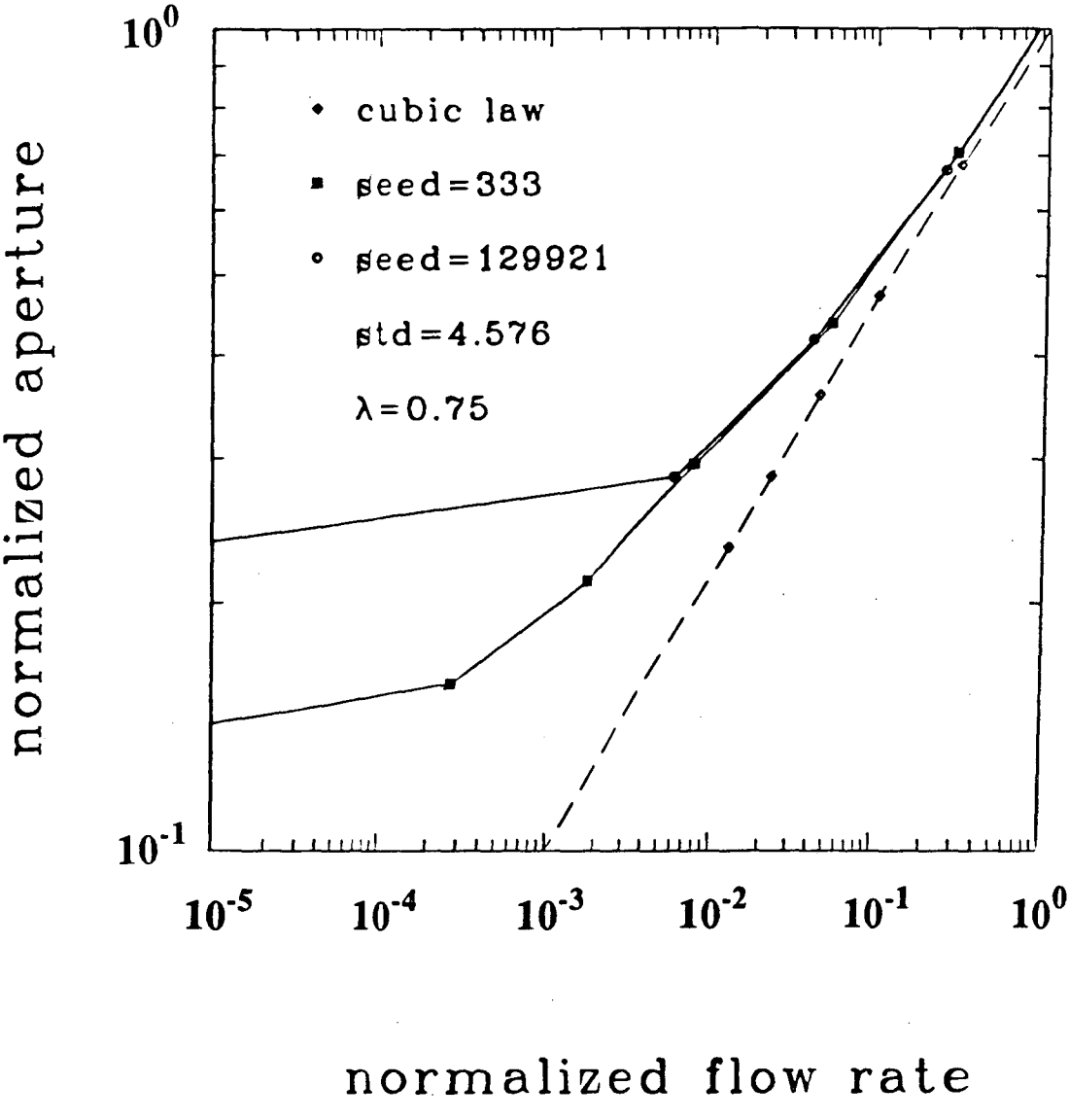

Figure 5-15 Permeability as a function of mean aperture for two realizations, and comparison with the 'cubic law'.

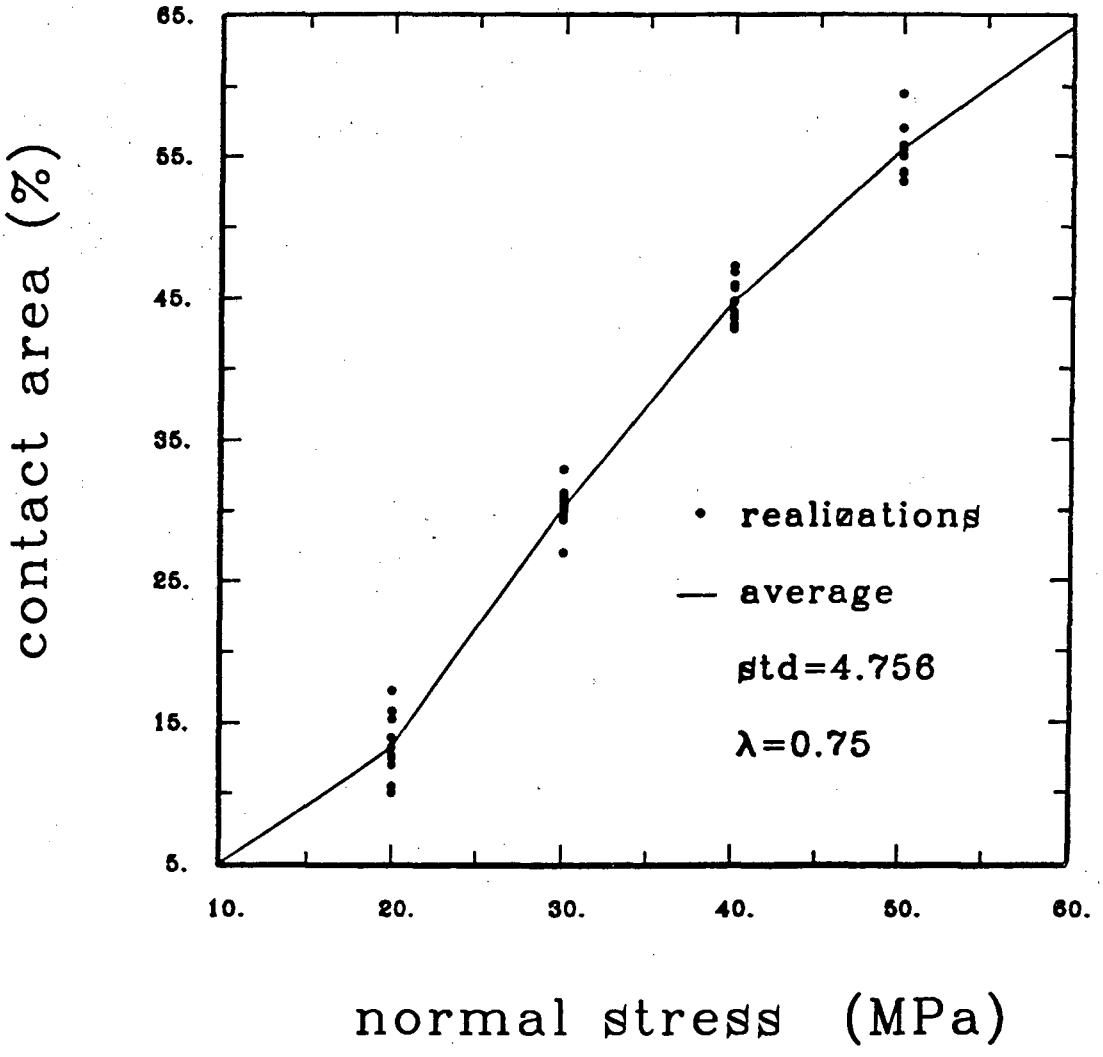

Figure 5-16 percent contact area as a function of normal stress, for ten different realizations.

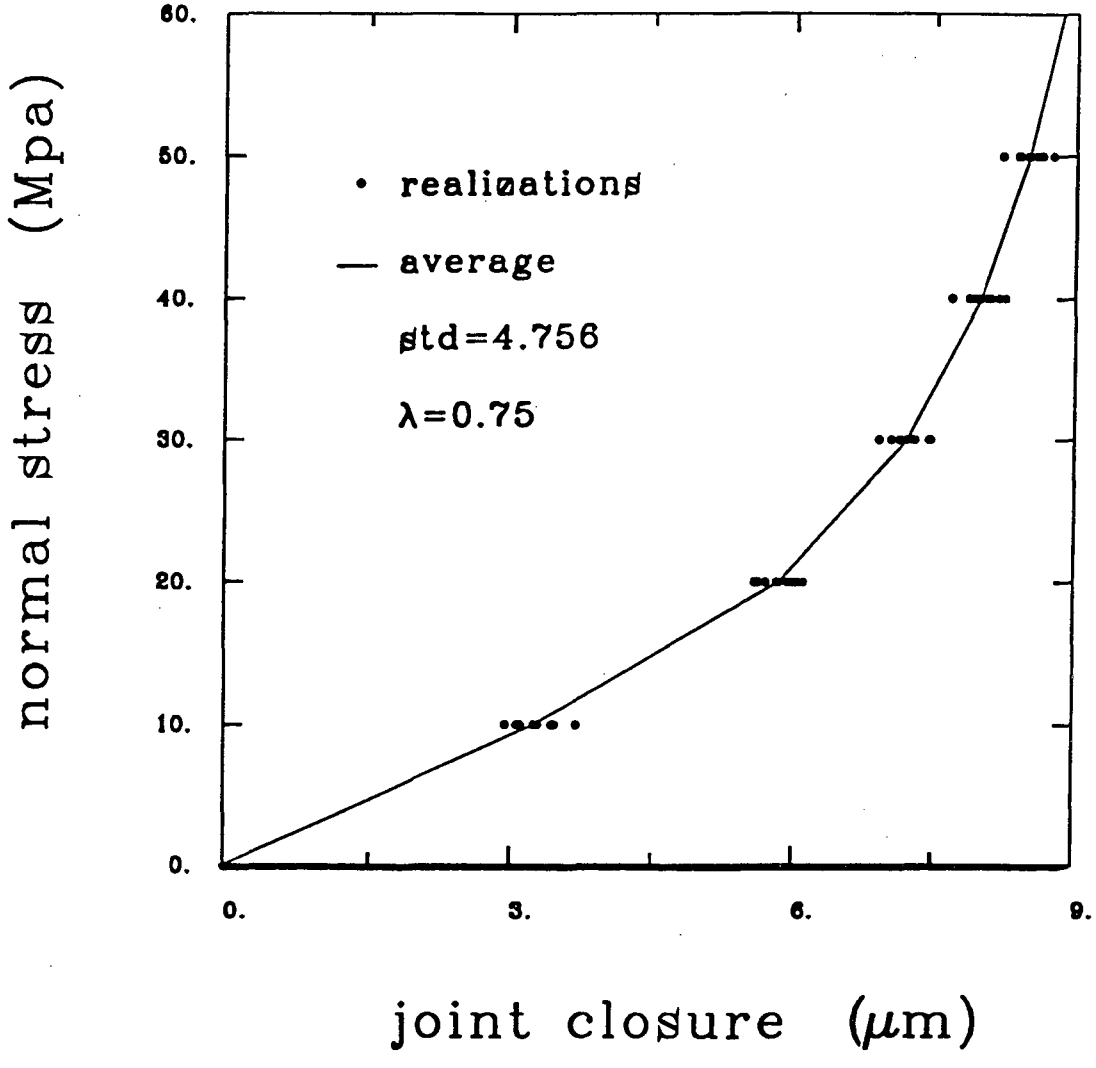

Figure 5-17 Joint closure as a function of normal stress, for ten different realizations.

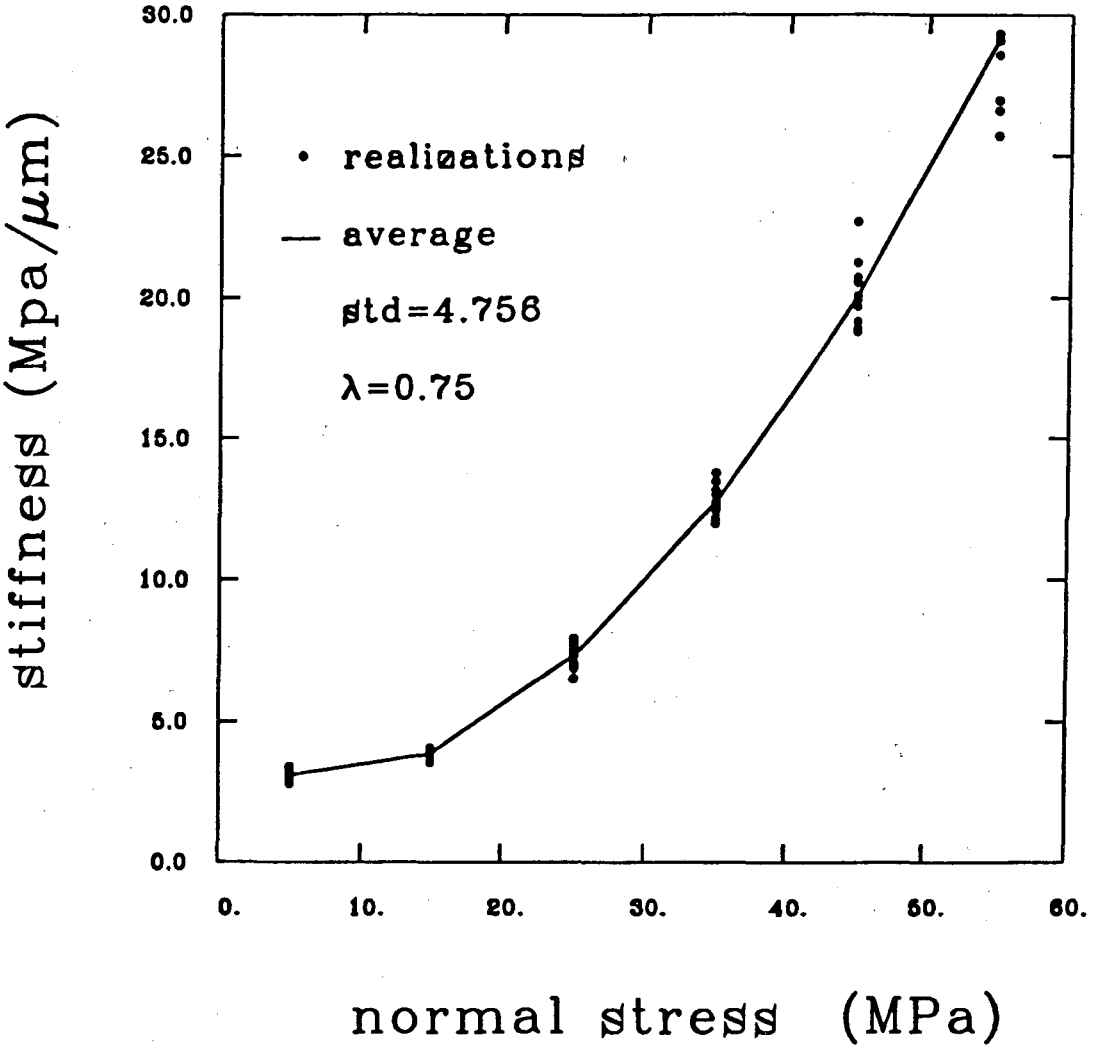

Figure 5-18 Stiffness as a function of normal stress, for ten different realizations.

Table 5-6a Results of parameters (λ and stdandard deviation) sensitivity study for the fracture with λ=0.75 and std.=2.926.

filter coeff. λ = 0.75, standard deviation=2.926						
normal stress	**contact area**	**average aperture**	**closure**	**stiffness**	**flux**	**flow rate**
MPa	%	μm	μm	*MPa*/μm	f/f_o	Q/Q_o
0	5.00	10.000	0.000	3.12	0.8688	0.8688
10	5.00	6.798	3.202	3.25	0.8688	0.2729
20	7.56	3.719	6.281	6.23	0.8006	0.0412
30	29.56	2.115	7.885	12.16	0.2912	0.0276
40	44.33	1.293	8.707	21.19	0.1643	0.0036
50	61.44	0.821	9.179	37.17	0.0522	0.0003
60	72.44	0.552	9.448			

Table 5-6b Results of parameters (λ and standard deviation) sensitivity study for the fracture with λ=0.75 and std.=4.576.

filter coeff. λ = 0.75, standard deviation=4.576						
normal stress	**contact area**	**average aperture**	**closure**	**stiffness**	**flux**	**flow rate**
MPa	%	μm	μm	*MPa*/μm	f/f_o	Q/Q_o
0	5.00	10.000	0.000	3.12	0.8688	0.8688
10	5.00	6.798	3.202	3.78	0.8688	0.2729
20	12.00	4.151	5.849	7.26	0.6316	0.0452
30	29.22	2.773	7.227	12.36	0.3356	0.0072
40	42.44	1.964	8.036	19.30	0.1154	0.00087
50	54.44	1.446	8.554	28.33	0.0441	0.00013
60	62.56	1.093	8.907			

Table 5-6c Results of parameters (λ and standard deviation) sensitivity study for the fracture with λ=0.75 and std.=7.089.

filter coeff. λ = 0.75, standard deviation=7.089						
normal stress	**contact area**	**average aperture**	**closure**	**stiffness**	**flux**	**flow rate**
MPa	%	μm	μm	*MPa*/μm	f/f_o	Q/Q_o
0	5.00	10.000	0.000	3.13	0.8688	0.8688
10	5.44	6.810	3.190	4.80	0.8596	0.2715
20	18.11	4.727	5.273	8.72	0.5446	0.0575
30	34.33	3.580	6.420	13.77	0.2200	0.01009
40	46.22	2.854	7.146	19.53	0.0849	0.00197
50	52.33	2.342	7.658	24.94	0.0717	0.00092
60	59.67	1.941	8.059			

Table 5-6d Results of parameters (λ and standard deviation) sensitivity study for the fracture with λ=1.5 and std.=2.934.

filter coeff. λ = 1.50, standard deviation=2.934						
normal stress	**contact area**	**average aperture**	**closure**	**stiffness**	**flux**	**flow rate**
MPa	%	μm	μm	*MPa*/μm	f/f_o	Q/Q_o
0	5.00	10.000	0.000	3.38	0.8482	0.8482
10	5.00	7.042	2.958	3.54	0.8482	0.2962
20	7.33	4.219	5.781	5.05	0.7895	0.0593
30	21.67	2.570	7.430	11.49	0.4266	0.00724
40	37.11	1.700	8.300	18.90	0.1749	0.00085
50	49.33	1.171	8.829	30.03	0.0519	0.00008
60	60.78	0.838	9.162			

Table 5-6e Results of parameters (λ and standard deviation) sensitivity study for the fracture with λ=1.5 and std.=4.576.

filter coeff. λ = 1.50, standard deviation=4.576						
normal stress	**contact area**	**average aperture**	**closure**	**stiffness**	**flux**	**flow rate**
MPa	%	μm	μm	*MPa*/μm	f/f_o	Q/Q_o
0	5.00	10.000	0.000	3.38	0.8482	0.8482
10	5.00	7.043	2.957	4.20	0.8482	0.2963
20	11.11	4.660	5.340	7.84	0.6720	0.0680
30	24.67	3.385	6.615	12.71	0.3528	0.0137
40	34.89	2.598	7.402	18.87	0.2076	0.0036
50	45.44	2.068	7.932	26.67	0.0418	0.0004
60	52.56	1.693	8.307			

Table 5-6f Results of parameters (λ and standard deviation) sensitivity study for the fracture with λ=1.5 and std.=7.090.

filter coeff. λ = 1.50, standard deviation=7.090						
normal stress	**contact area**	**average aperture**	**closure**	**stiffness**	**flux**	**flow rate**
MPa	%	μm	μm	*MPa*/μm	f/f_o	Q/Q_o
0	5.00	10.000	0.000	3.45	0.8482	0.84820
10	6.33	7.103	2.897	5.58	0.8156	0.29228
20	18.33	5.312	4.688	10.06	0.5064	0.07590
30	29.89	4.318	5.682	14.99	0.2611	0.02102
40	38.00	3.651	6.349	19.65	0.1416	0.00689
50	45.11	3.142	6.858	25.25		0.00001
60	51.56	2.746	7.254			

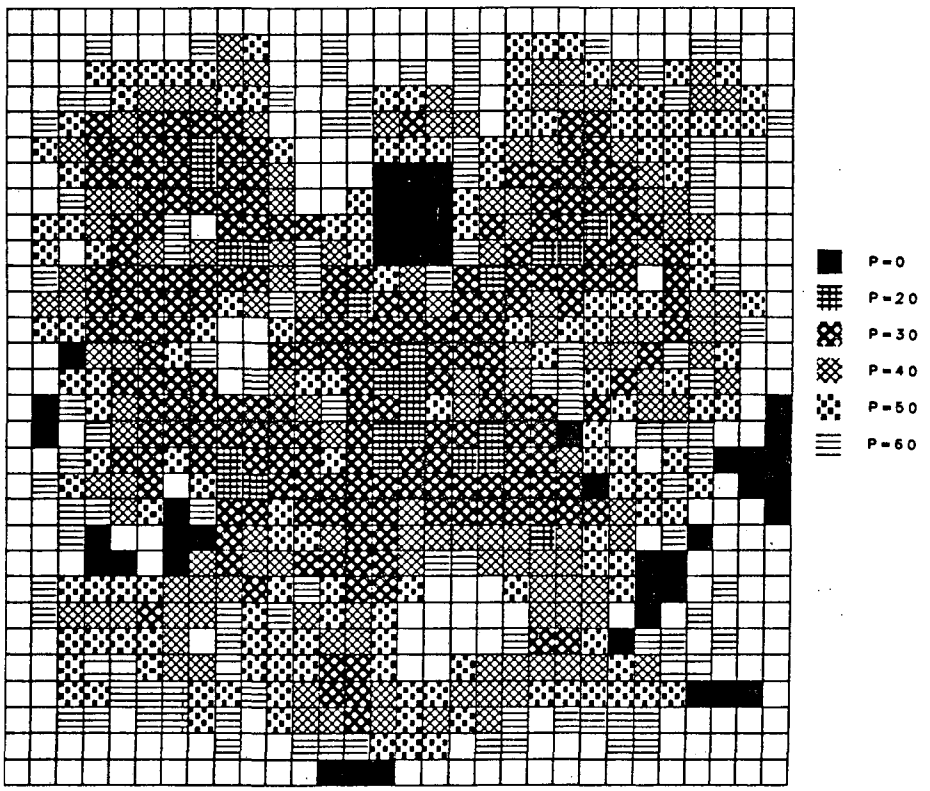

average aperture=10 μm

standard deviation=2.926

filter coefficient λ =0.75

Figure 5–19a Contact area as a function of normal stress for the fracture with λ=0.75 and std.=2.926 for parameter (λ, standard deviation) sensitivity study.

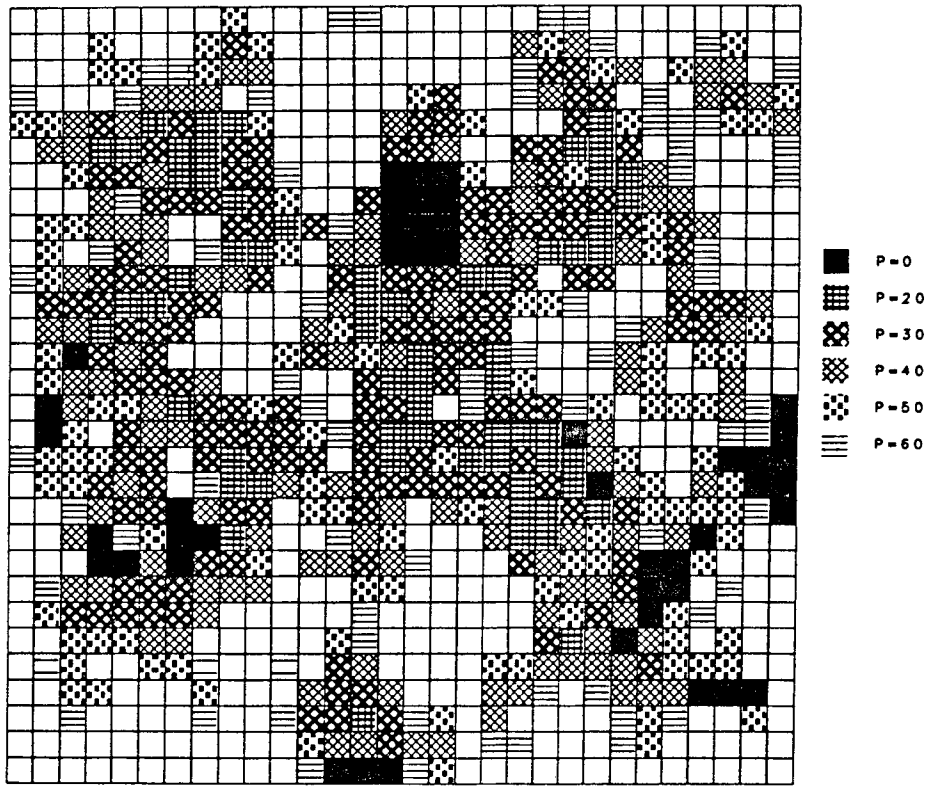

average aperture=10 μm

standard deviation=4.576

filter coefficient λ =0.75

Figure 5–19b Contact area as a function of normal stress for the fracture with λ=0.75 and std.=4.576 for parameter (λ, standard deviation) sensitivity study.

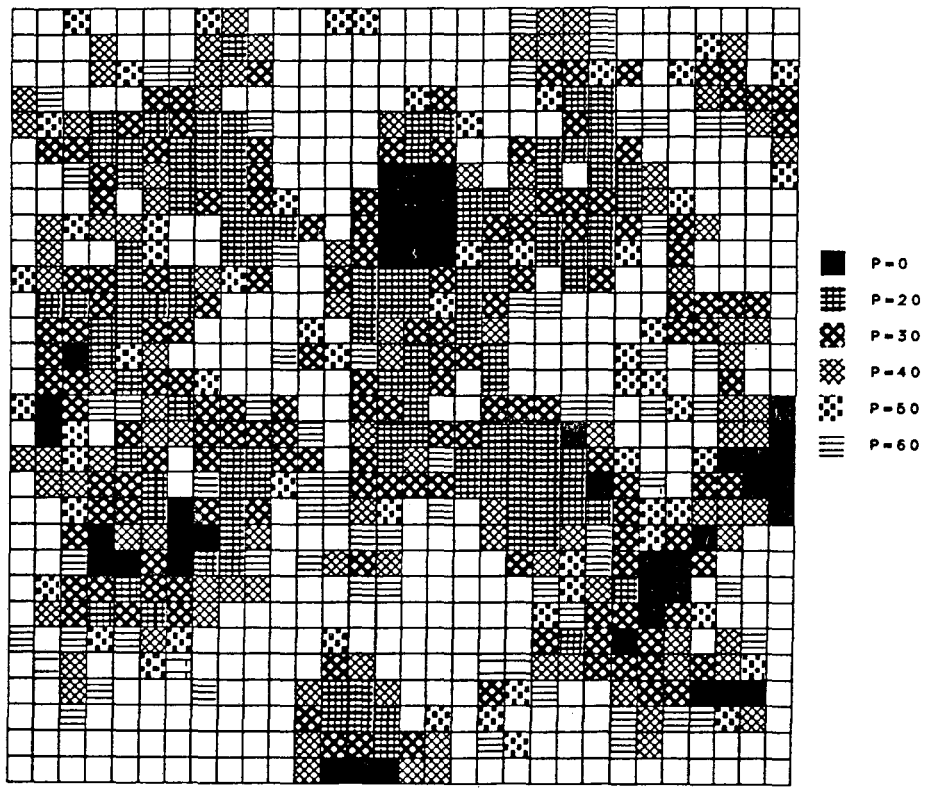

average aperture=10 μm

standard deviation=7.089

filter coefficient λ =0.75

Figure 5–19c Contact area as a function of normal stress for the fracture with λ=0.75 and std.=7.089 for parameter (λ, standard deviation) sensitivity study.

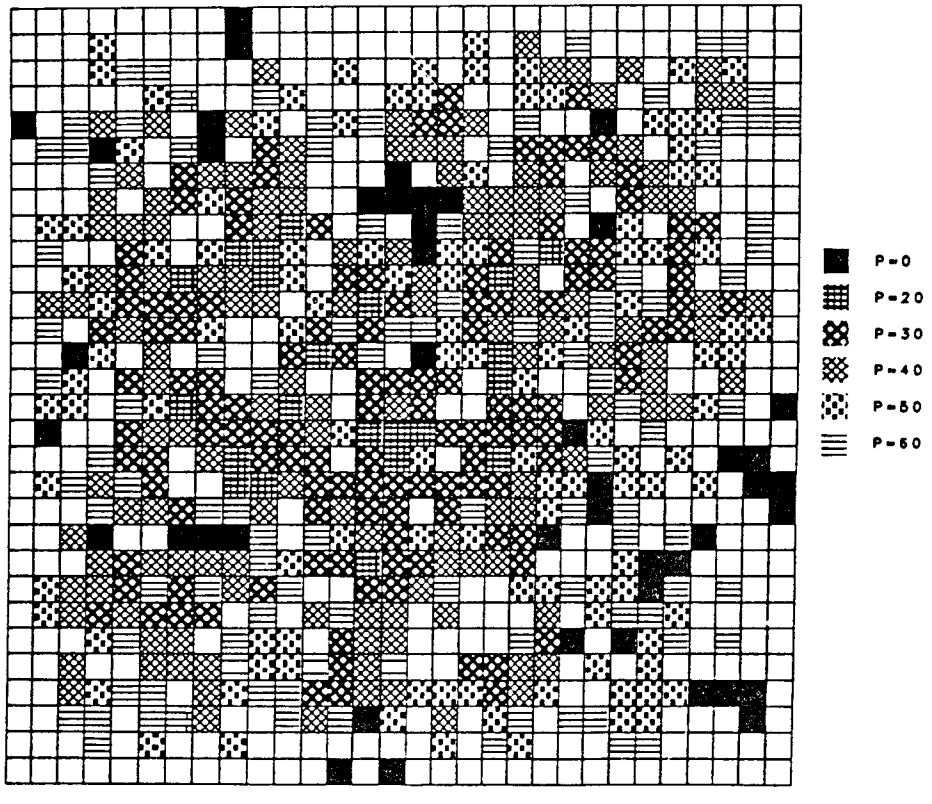

average aperture=10 μm

standard deviation=2.934

filter coefficient λ =1.50

Figure 5–19d Contact area as a function of normal stress for the fracture with λ=1.50 and std.=2.934 for parameter (λ, standard deviation) sensitivity study.

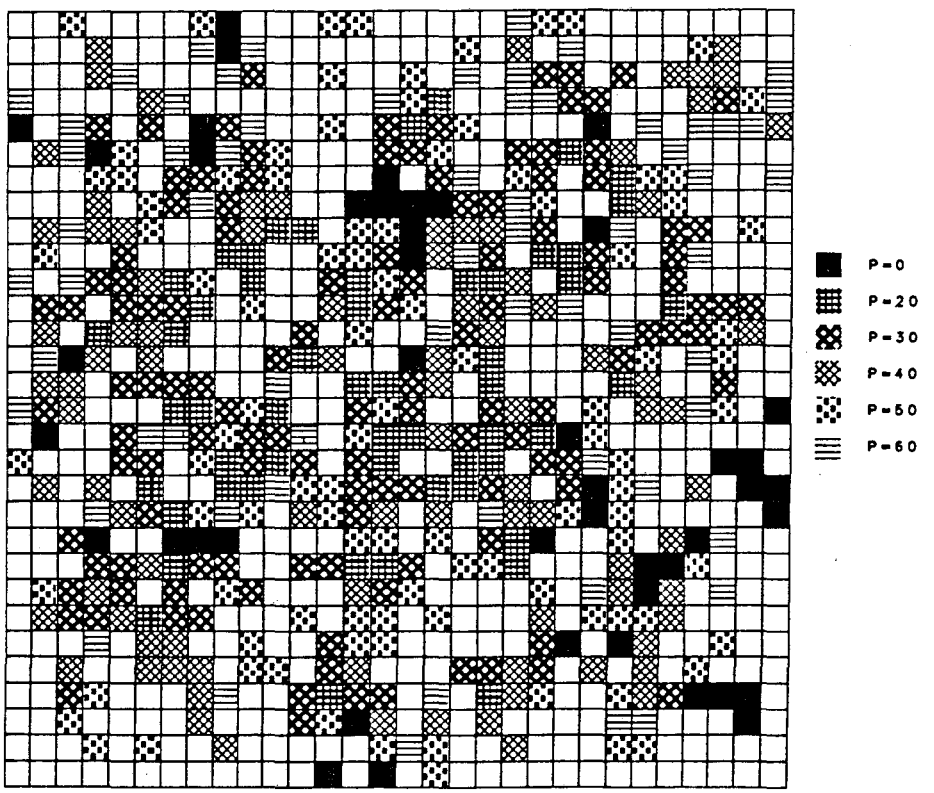

average aperture=10 μm

standard deviation=4.576

filter coefficient λ =1.50

Figure 5–19e Contact area as a function of normal stress for the fracture with λ=1.50 and std.=4.576 for parameter (λ, standard deviation) sensitivity study.

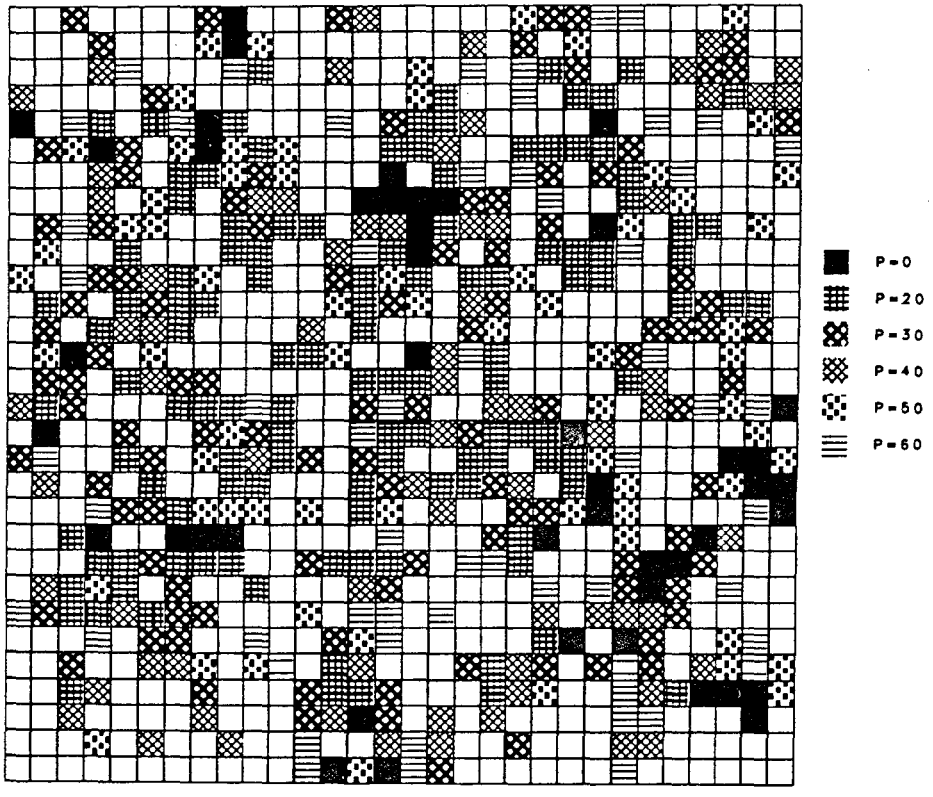

average aperture=10 μm

standard deviation=7.090

filter coefficient λ =1.50

Figure 5–19f Contact area as a function of normal stress for the fracture with λ=1.50 and std.=7.090 for parameter (λ, standard deviation) sensitivity study.

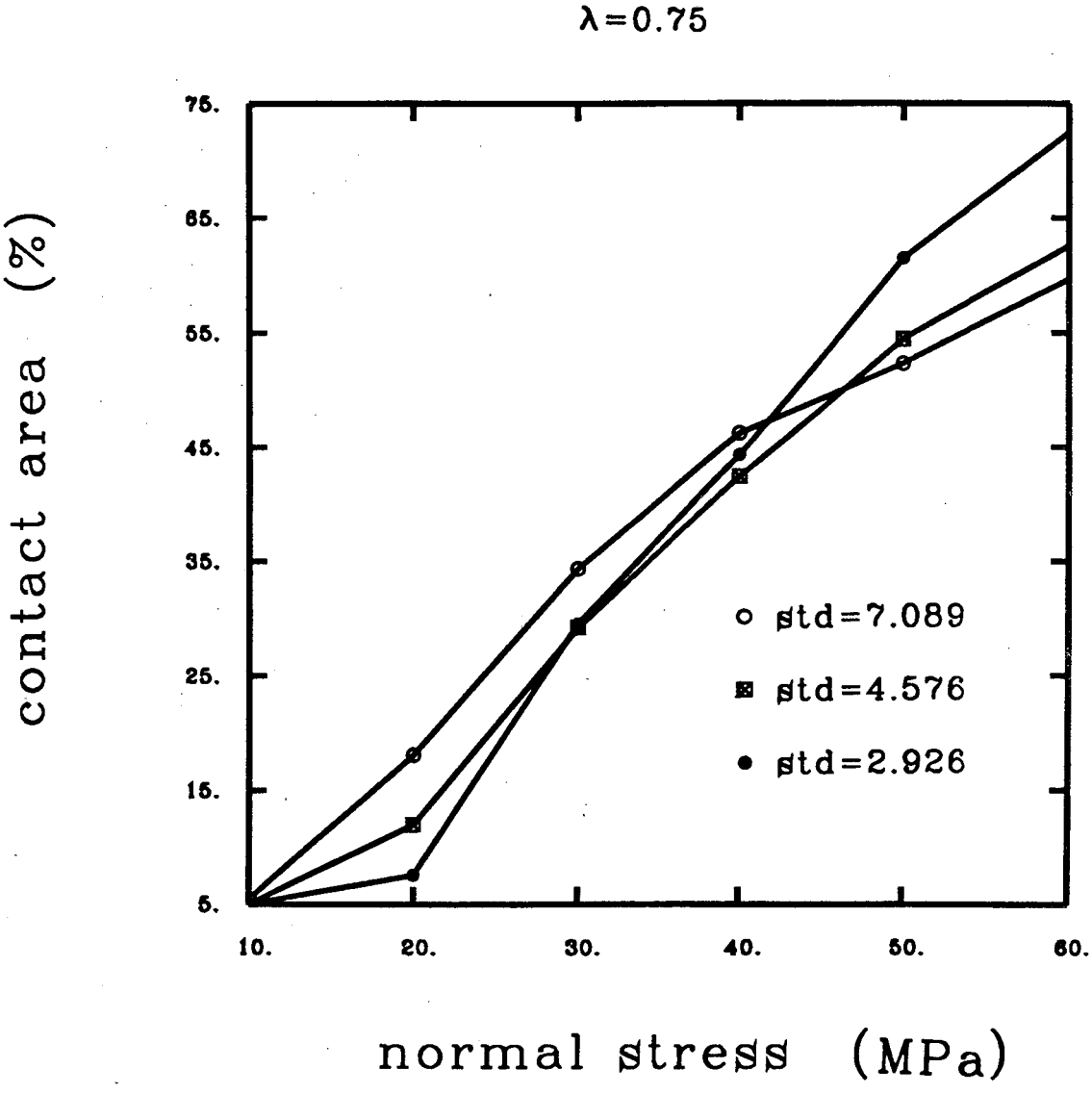

Figure 5–20–a contact area as a function of normal stress for fractures with λ=0.75, as standard deviation changes.

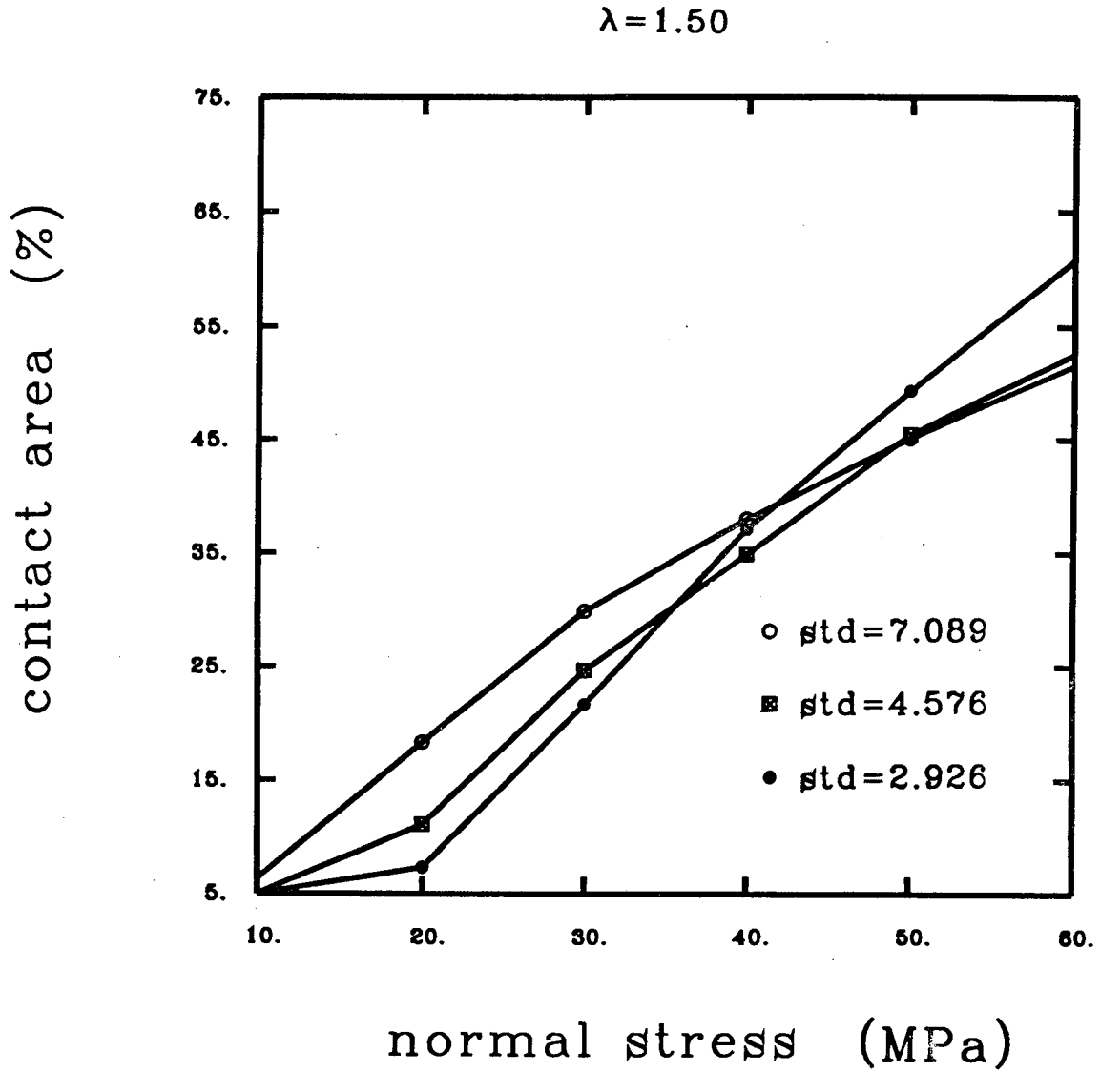

Figure 5–20–b contact area as a function of normal stress for fractures with λ=1.50, as standard deviation changes.

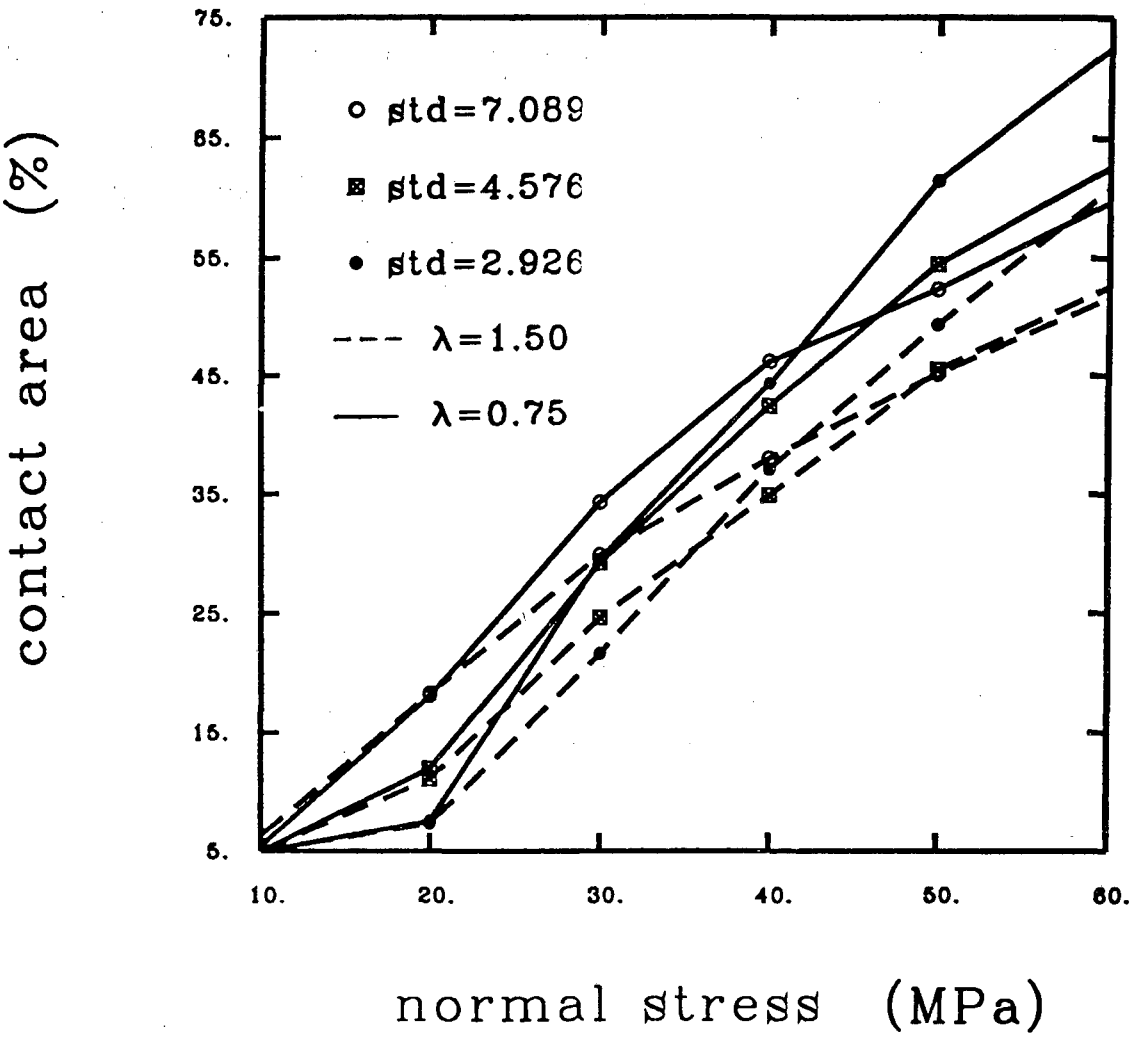

Figure 5–20–c contact area as a function of normal stress, as standard deviation and correlation factor λ change.

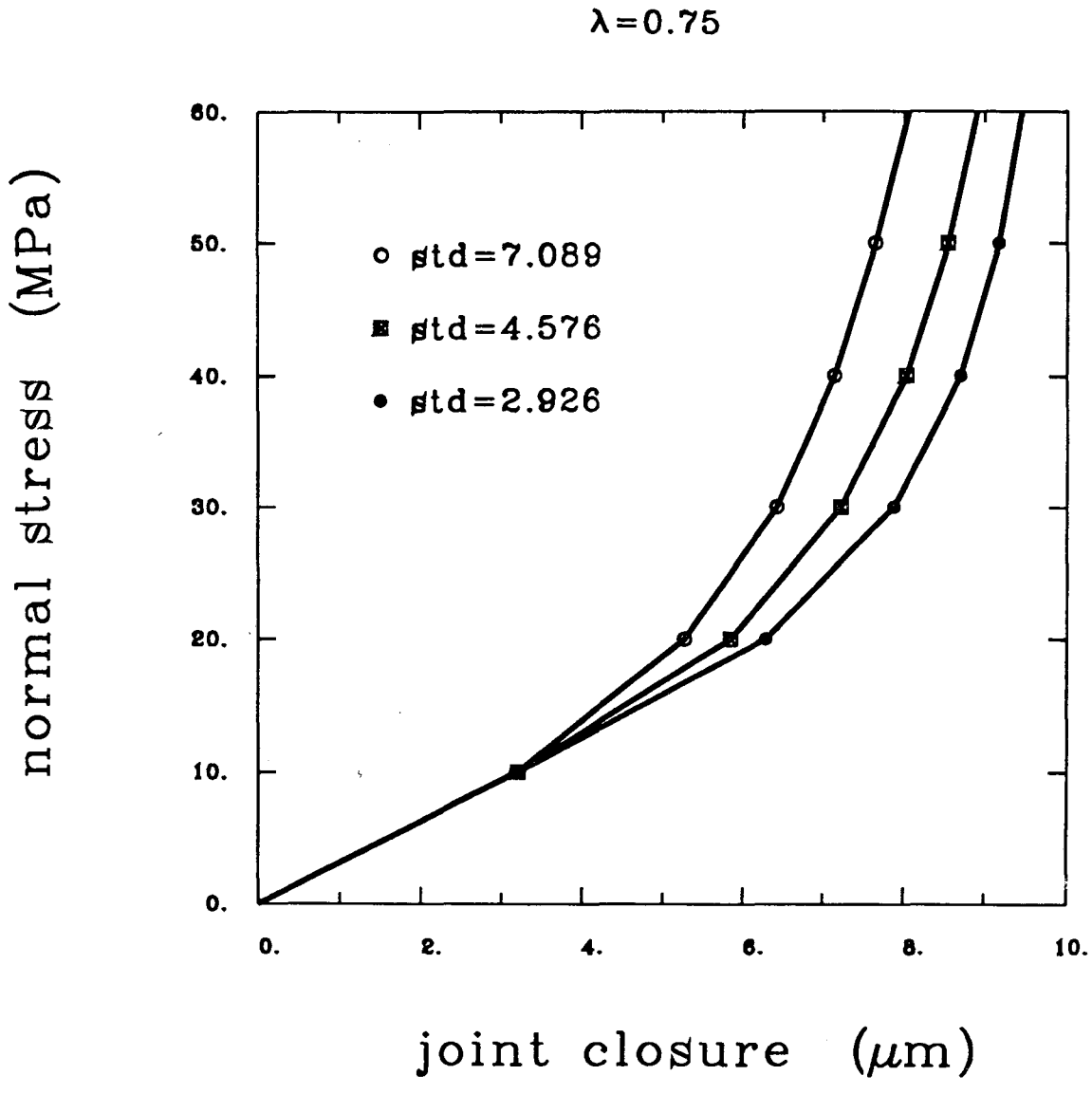

Figure 5–21–a Joint closure as a function of normal stress for fractures with λ=0.75, as standard deviation changes.

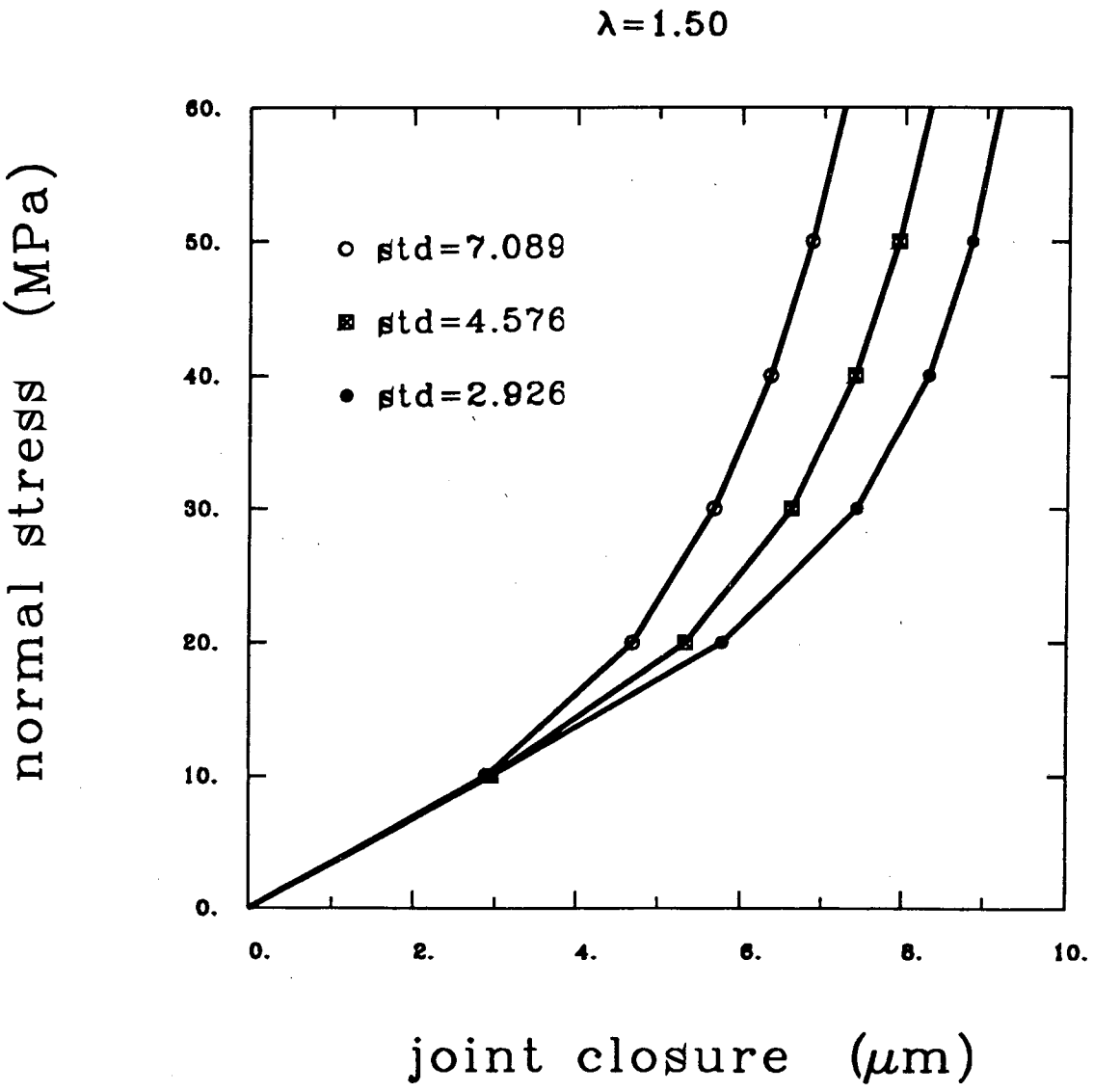

Figure 5–21–b Joint closure as a function of normal stress for fractures with λ=1.50, as standard deviation changes.

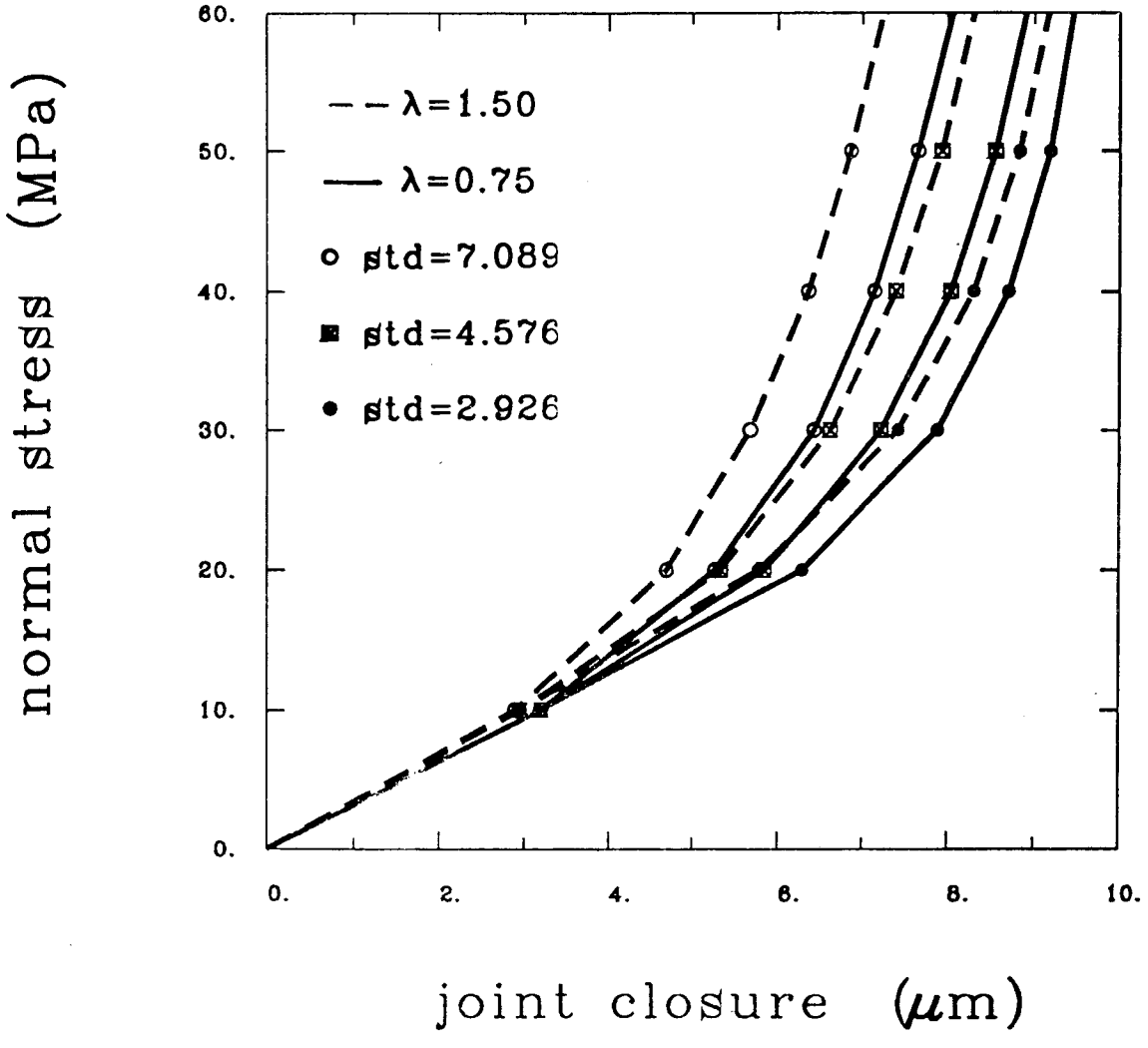

Figure 5–21–c Joint closure as a function of normal stress, as standard deviation and correlation factor λ change.

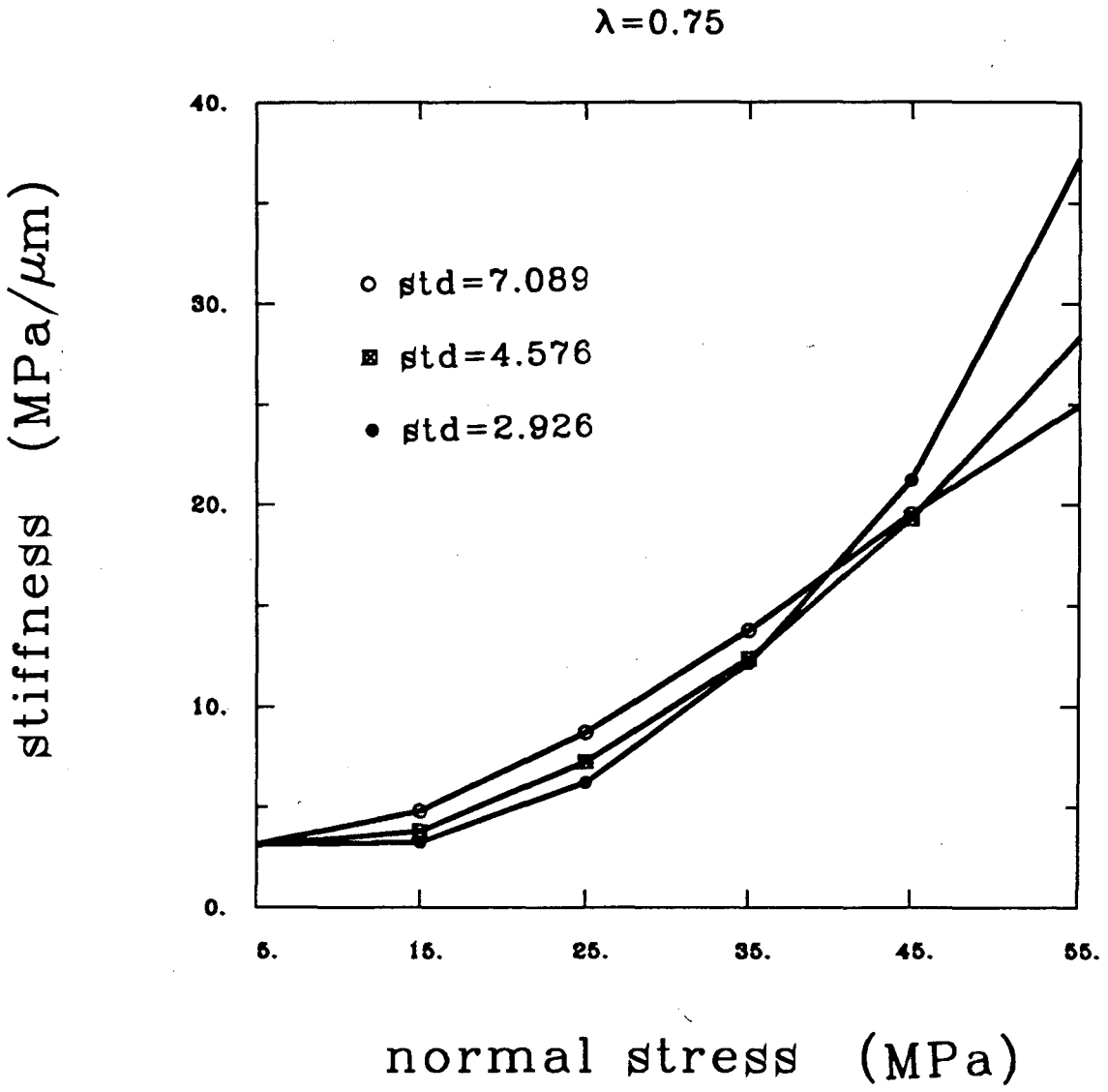

Figure 5–22–a Stiffness as a function of normal stress for fractures with λ=0.75, as standard deviation changes.

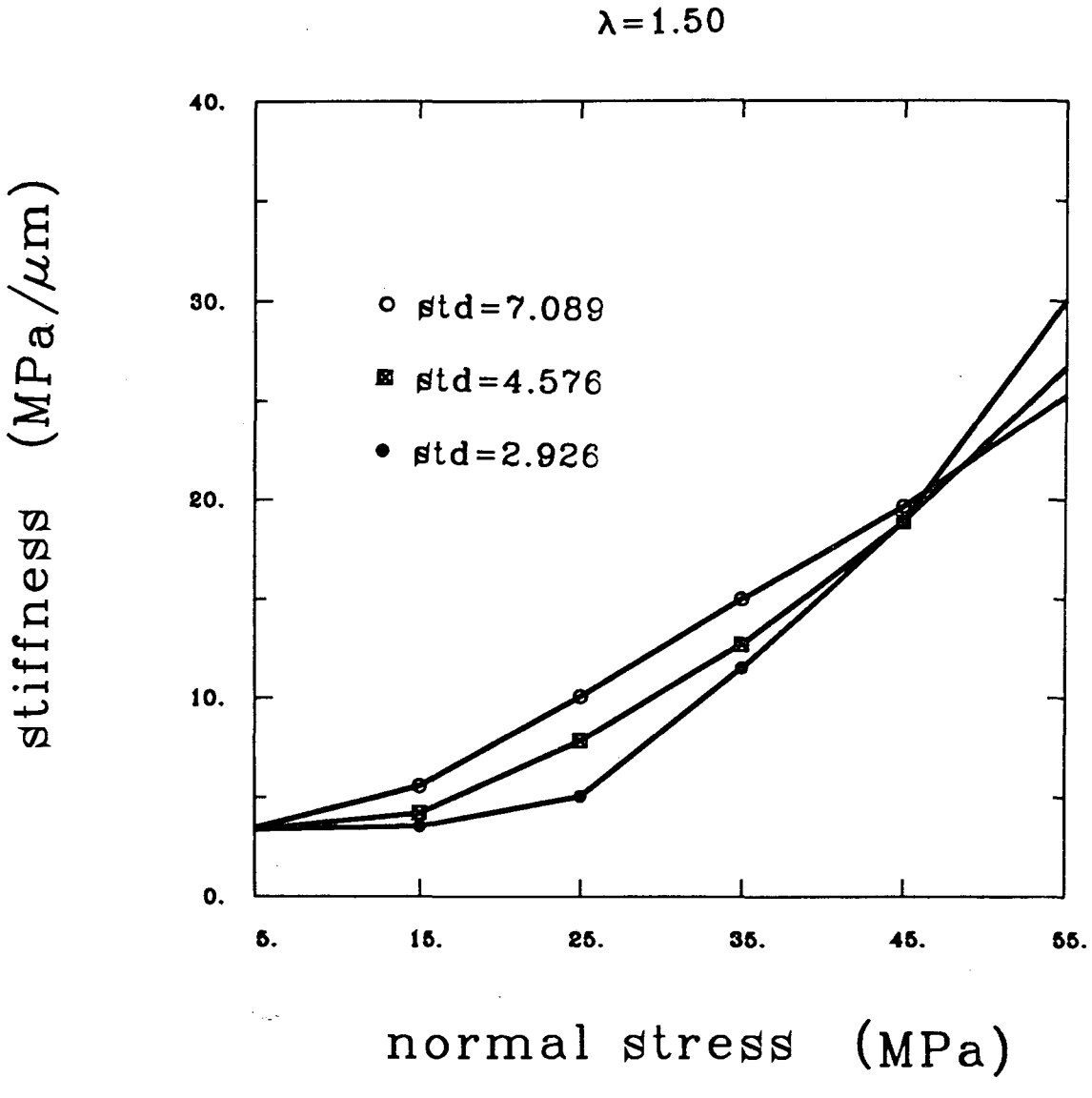

Figure 5–22–b Stiffness as a function of normal stress for fractures with λ=1.50, as standard deviation changes.

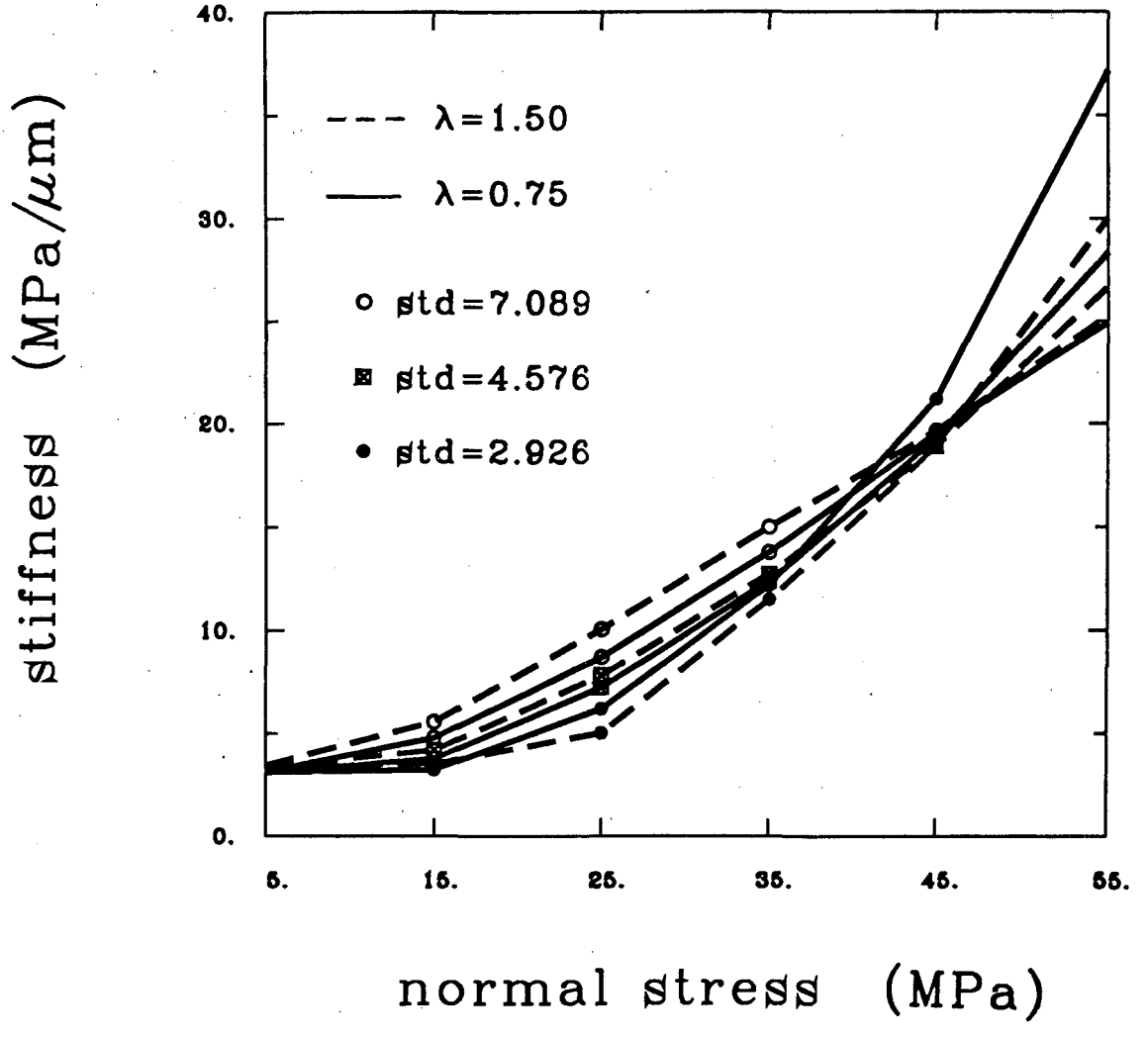

Figure 5–22–c Stiffness as a function of normal stress, as standard deviation and correlation factor λ change.

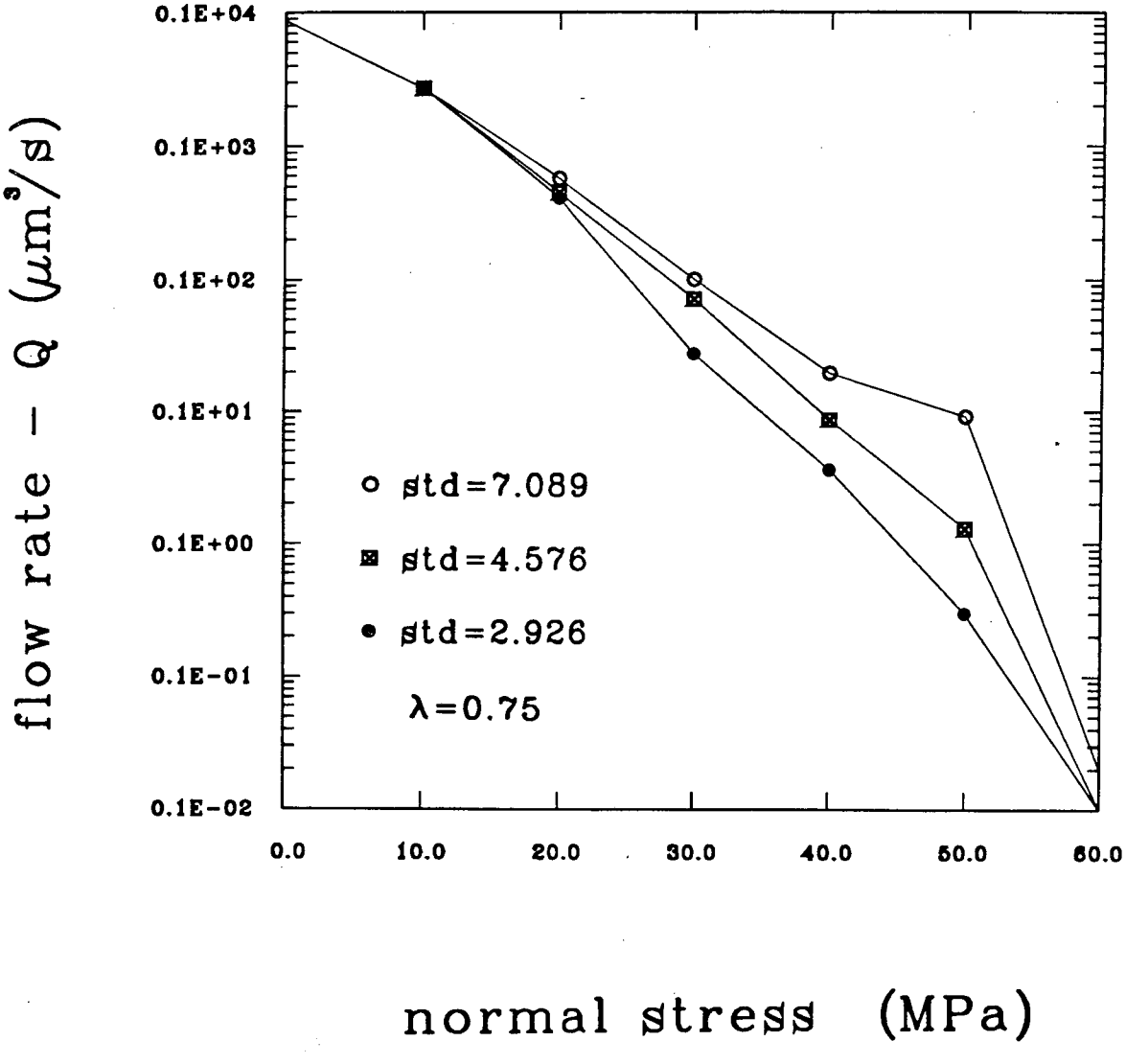

Figure 5–23–a Normalized flow rate as a function of normal stress for fractures with λ=0.75, as standard deviation changes.

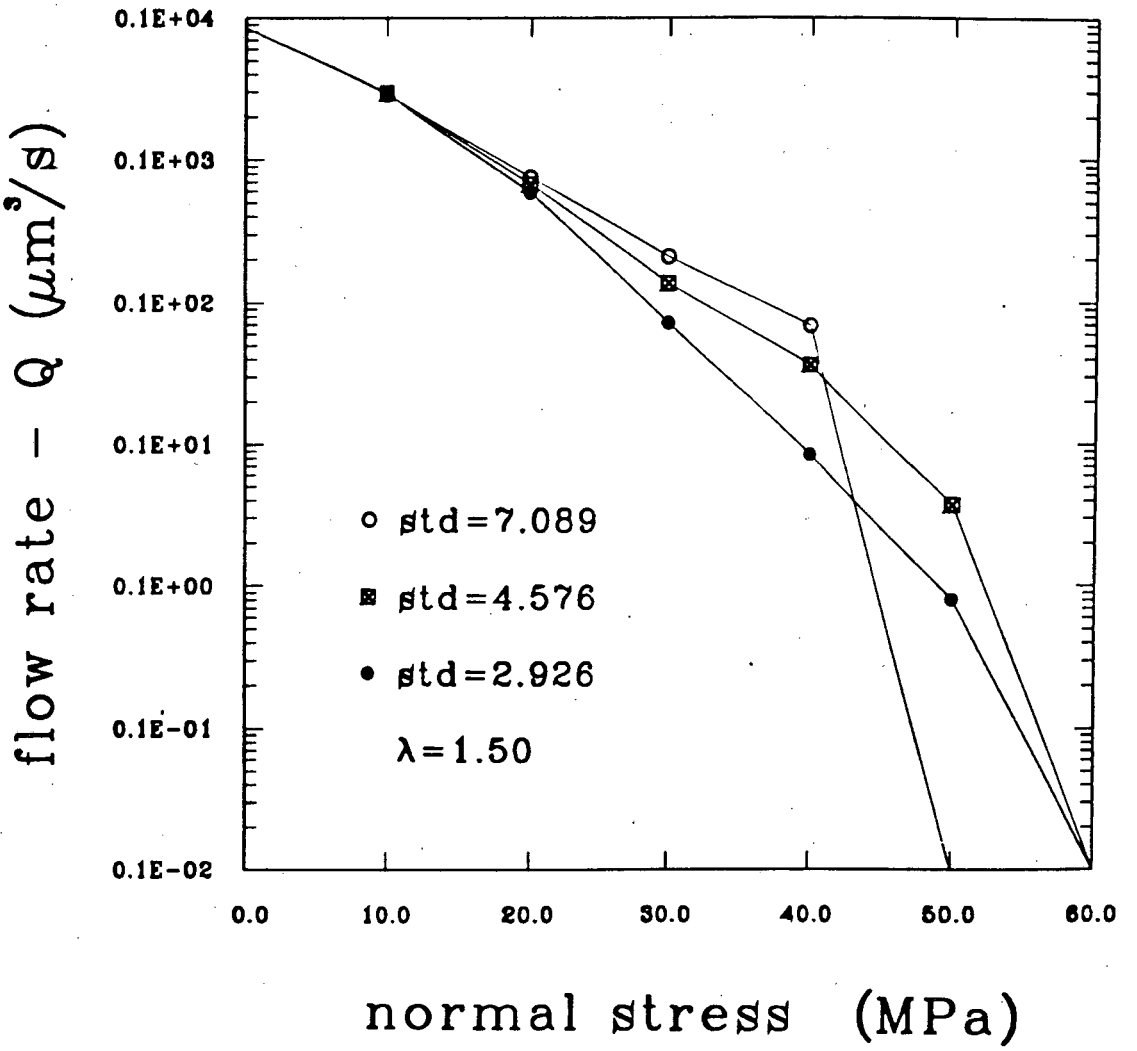

Figure 5–23–b Normalized flow rate as a function of normal stress for fractures with λ=1.50, as standard deviation changes.

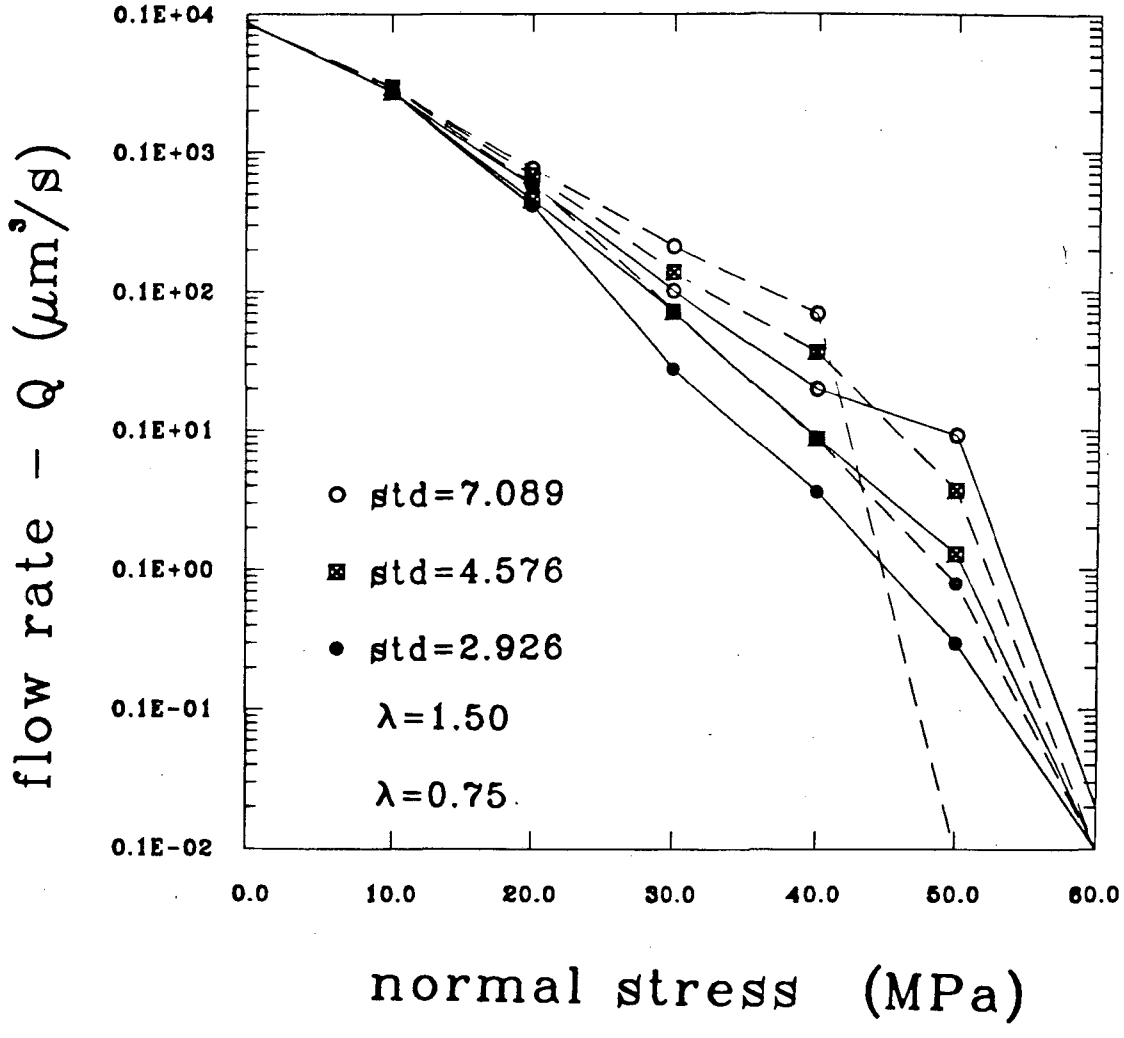

Figure 5–23–c Normalized flow rate as a function of normal stress, as standard deviation and correlation factor λ change.

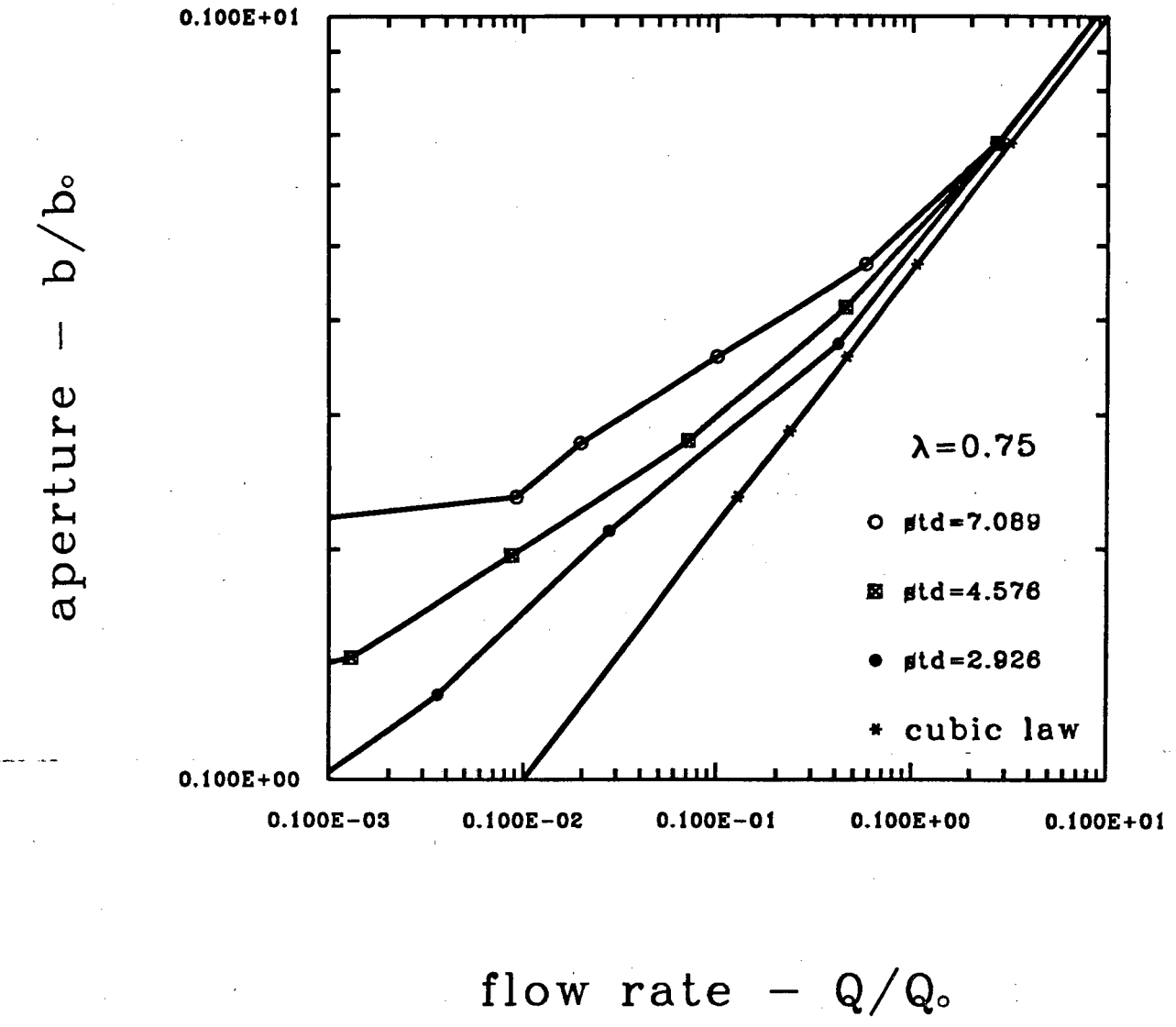

Figure 5–24–a Normalized flow rate as a function of mean aperture for fractures with λ=0.75 as standard deviation changes, and comparison with the 'cubic law'.

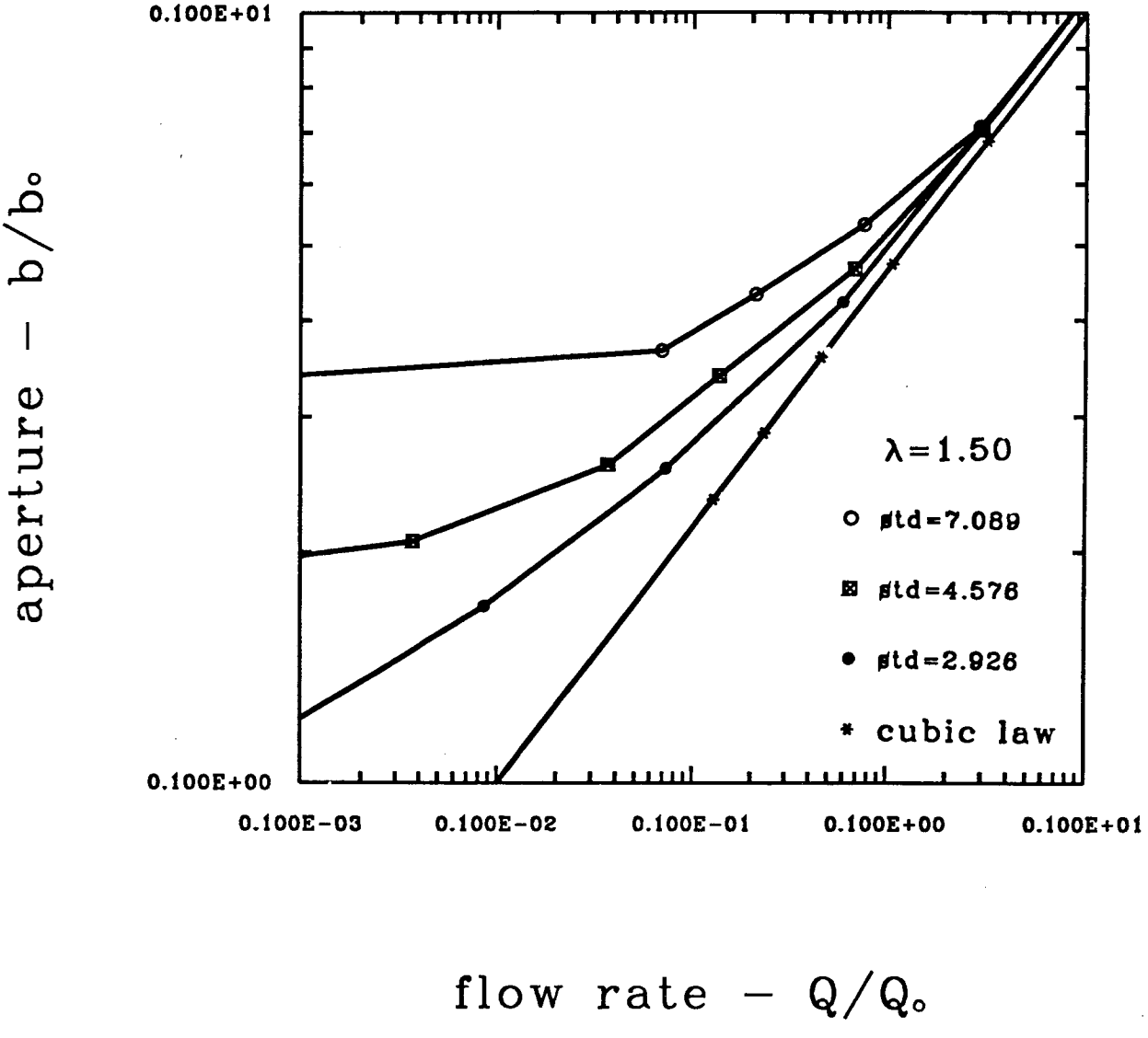

Figure 5–24–b Normalized flow rate as a function of mean aperture for fractures with λ=1.50 as standard deviation changes, and comparison with the 'cubic law'.

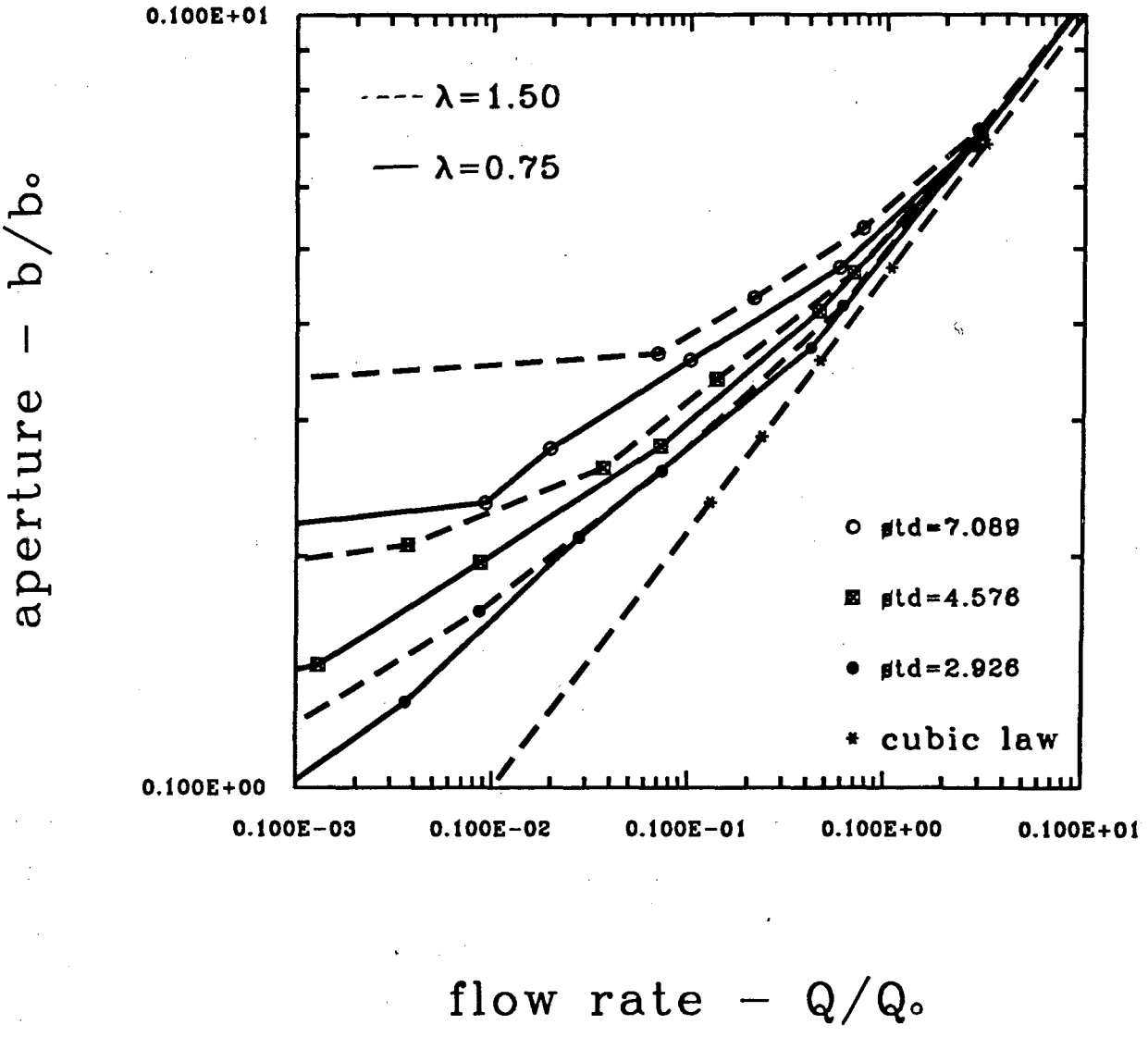

Figure 5–24–c Normalized flow rate as a function of mean aperture as standard deviation and correlation factor λ change, and comparison with the 'cubic law'.

Table 5-7a Results of parameter (mean aperture $\bar{h}$) sensitivity study for the fracture with λ=1.5 and std.=2.934.

filter coeff. λ = 1.50, standard deviation=2.934								
normal	normal case				apertures less than $0.2\bar{h}$ are closed			
stress	c.a.	$\bar{h}$	flux	flow rate	c.a.	$\bar{h}_c$	flux	flow rate
MPa	%	μm	f/f_o	Q/Q_o	%	μm	f/f_o	Q/Q_o
0	5.00	10.000	0.8482	0.8482	5.00	10.000	0.8482	0.8482
10	5.00	7.042	0.8482	0.2962	5.00	7.043	0.8482	0.2962
20	7.33	4.219	0.7895	0.0593	11.33	4.201	0.6613	0.04903
30	21.67	2.570	0.4266	0.00724	27.44	2.553	0.3067	0.00510
40	37.11	1.700	0.1749	0.00085	40.67	1.691	0.1535	0.00074
50	49.33	1.171	0.0519	0.00008	51.22	1.166	0.0495	0.00008
60	60.78	0.838			61.89	0.834		

Table 5-7b Results of parameter (mean aperture $\bar{h}$) sensitivity study for the fracture with λ=1.5 and std.=4.576.

filter coeff. λ = 1.50, standard deviation=4.576								
normal	normal case				apertures less than $\overline{0.2h}$ are closed			
stress	c.a.	$\bar{h}$	flux	flow rate	c.a.	$\bar{h}_c$	flux	flow rate
MPa	%	μm	f/f_o	Q/Q_o	%	μm	f/f_o	Q/Q_o
0	5.00	10.000	0.8482	0.8482	5.00	10.000	0.8482	0.8482
10	5.00	7.043	0.8482	0.2963	5.00	7.043	0.8482	0.2963
20	11.11	4.660	0.6720	0.0680	18.78	4.623	0.4567	0.0451
30	24.67	3.385	0.3528	0.0137	30.11	3.364	0.2998	0.0114
40	34.89	2.586	0.2076	0.0036	40.67	2.570	0.0595	0.0010
50	45.44	2.050	0.0418	0.0004	49.00	2.043	0.0360	0.0003
60	52.56	1.670			56.44	1.664		

Table 5-7d Results of parameter (mean aperture $\bar{h}$) sensitivity study for the fracture with λ=0.75 and std.=4.576.

λ = 0.75 standard deviation =4.576								
normal	normal case				apertures less than 0.2$\bar{h}$ are closed			
stress	c.a.	$\bar{h}$	flux	flow rate	c.a.	$\bar{h}_c$	flux	flow rate
MPa	%	μm	f/f_o	Q/Q_o	%	μm	f/f_o	Q/Q_o
0	5.00	10.000	0.8688	0.8688	5.00	10.000	0.8688	0.8688
10	5.00	6.798	0.8688	0.2729	5.00	6.798	0.8688	0.2729
20	12.00	4.151	0.6316	0.0452	20.89	4.113	0.4946	0.0344
30	29.22	2.773	0.3356	0.0072	35.67	2.752	0.1528	0.0032
40	42.44	1.962	0.1154	0.0009	47.56	1.950	0.0934	0.0007
50	54.44	1.440	0.0441	0.0001	57.22	1.436	0.0000	0.0000
60	62.56	1.086			64.00	1.084		

Table 5-7c Results of parameter (mean aperture $\bar{h}$) sensitivity study for the fracture with λ=1.5 and std.=7.090.

filter coeff. λ = 1.50, standard deviation=7.090								
normal	normal case				apertures less than 0.2$\bar{h}$ are closed			
stress	c.a.	$\bar{h}$	flux	flow rate	c.a.	$\bar{h}_c$	flux	flow rate
MPa	%	μm	f/f_o	Q/Q_o	%	μm	f/f_o	Q/Q_o
0	5.00	10.000	0.8482	0.84820	5.00	10.000	0.8482	0.84820
10	6.33	7.103	0.8156	0.29228	12.56	7.051	0.6539	0.22922
20	18.33	5.312	0.5064	0.07590	27.33	5.256	0.2988	0.04339
30	29.89	4.318	0.2611	0.02102	32.89	4.308	0.1714	0.01370
40	38.00	3.651	0.1416	0.00689	43.33	3.620		0.00001
50	45.11	3.142			50.22	3.109		
60	51.56	2.746			55.78	2.718		

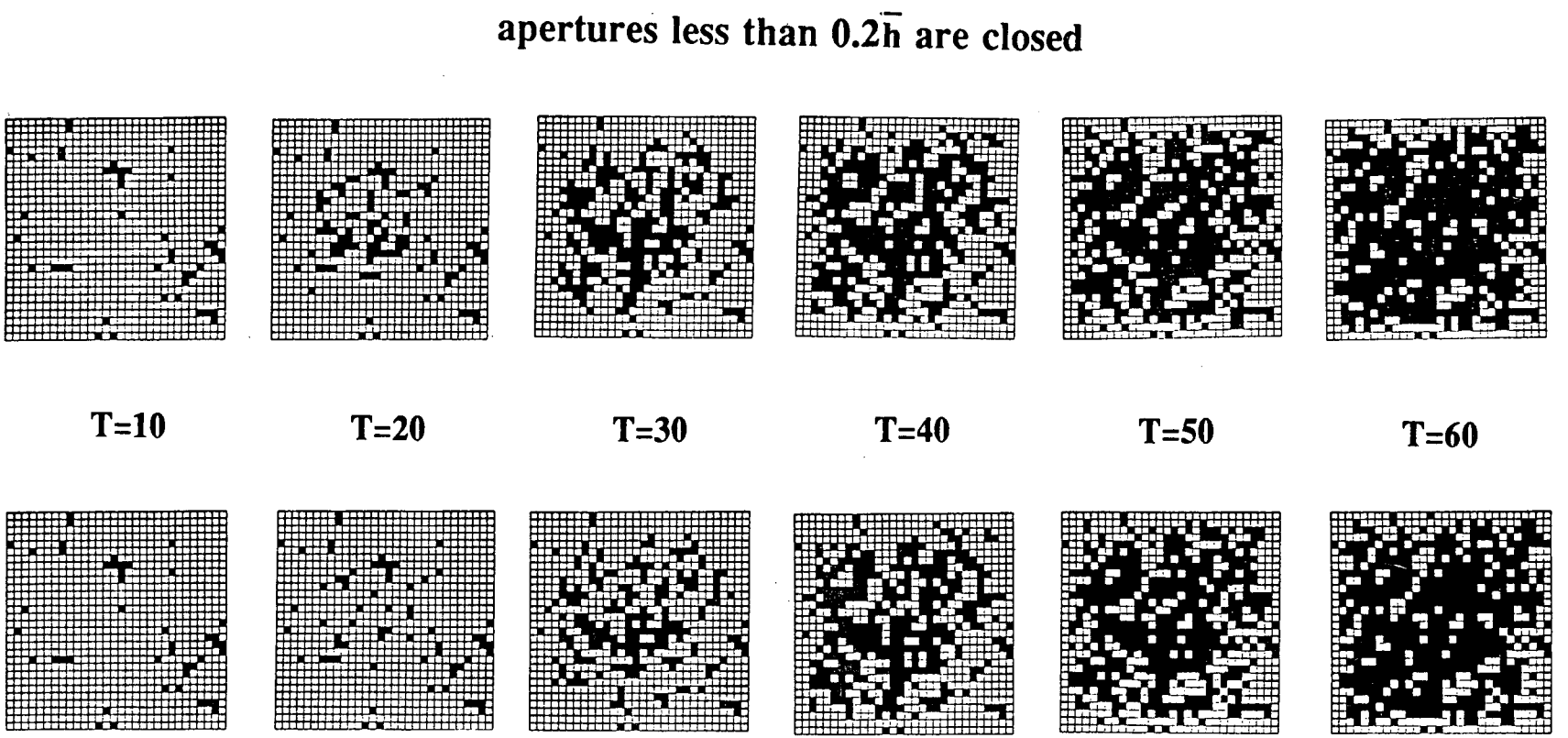

Figure 5-25a Contact area as a function of normal stress for the fracture with λ=1.5 and std.=2.934 for parameter (mean aperture) sensitivity study.

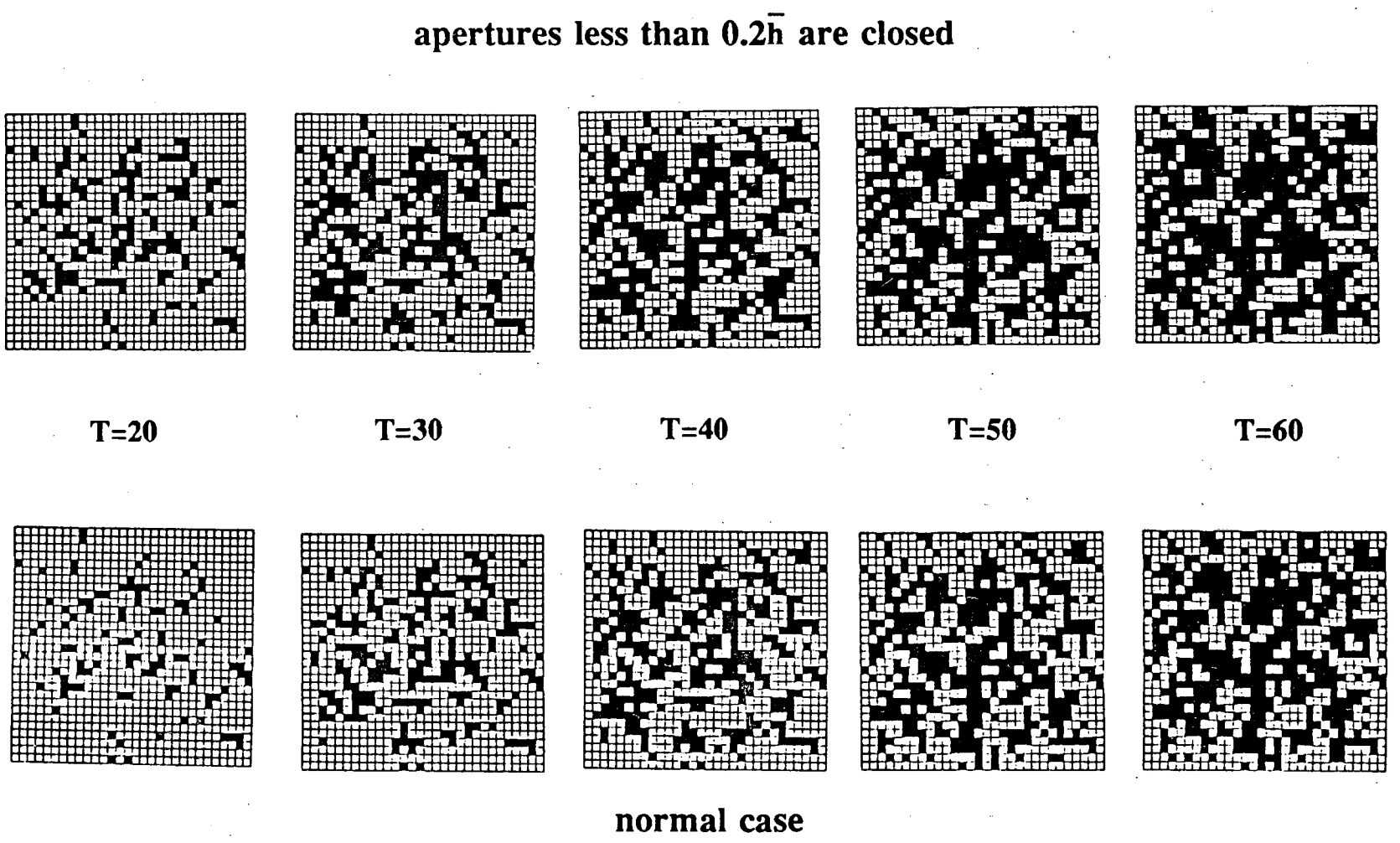

Figure 5-25b Contact area as a function of normal stress for the fracture with λ=1.5 and std.=4.576 for parameter (mean aperture) sensitivity study.

apertures less than $0.2\bar{h}$ are closed

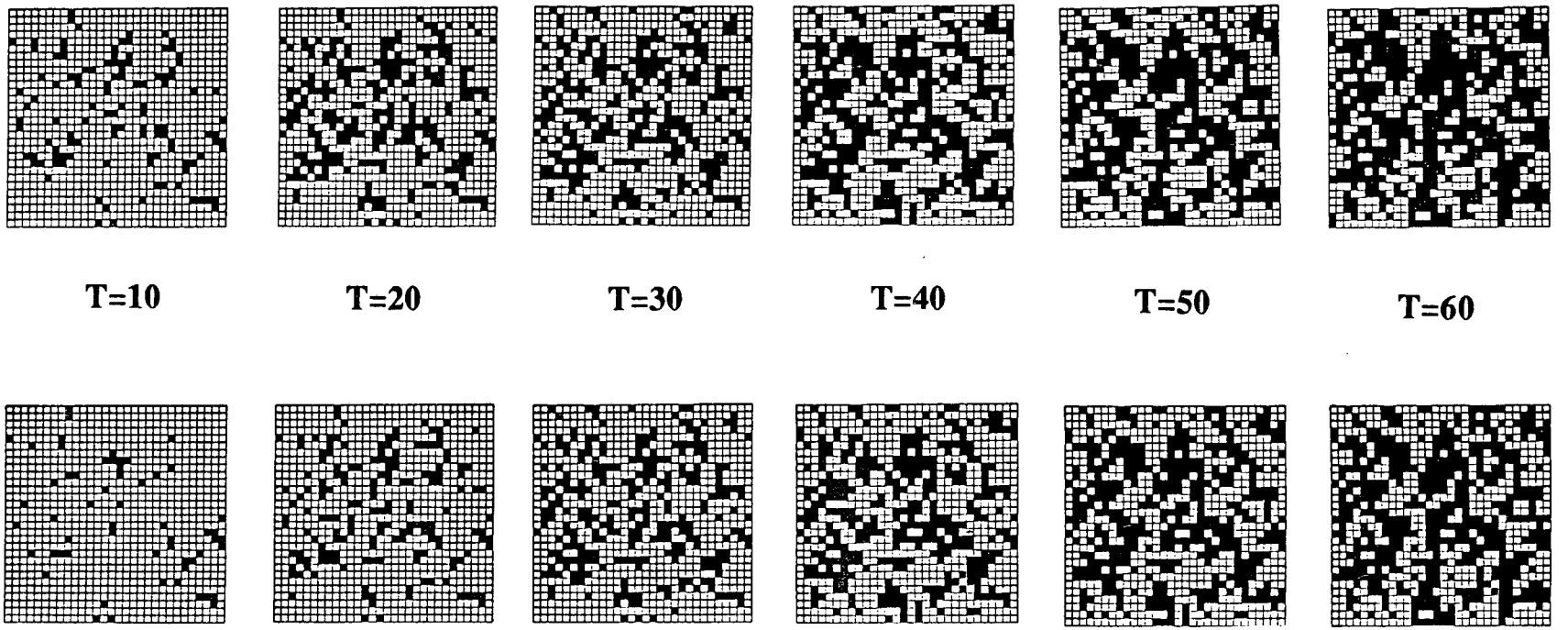

normal case

average aperture = 10 μm
standard deviation = 7.090
filter corfficient λ = 1.50

Figure 5-25c Contact area as a function of normal stress for the fracture with λ=1.5 and std.=7.090 for parameter (mean aperture) sensitivity study.

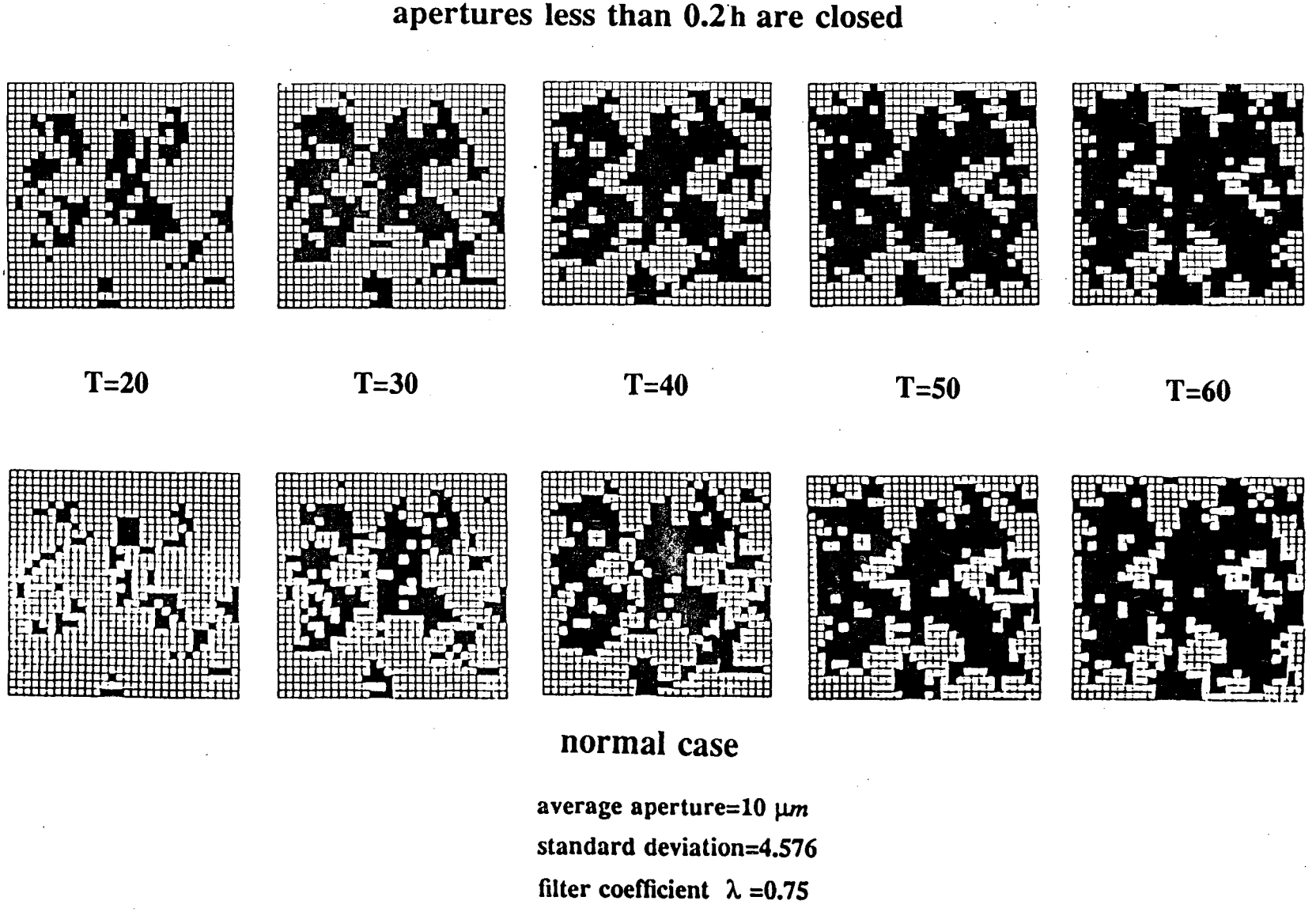

Figure 5-25d Contact area as a function of normal stress for the fracture with λ=0.75 and std.=4.576 for parameter (mean aperture) sensitivity study.

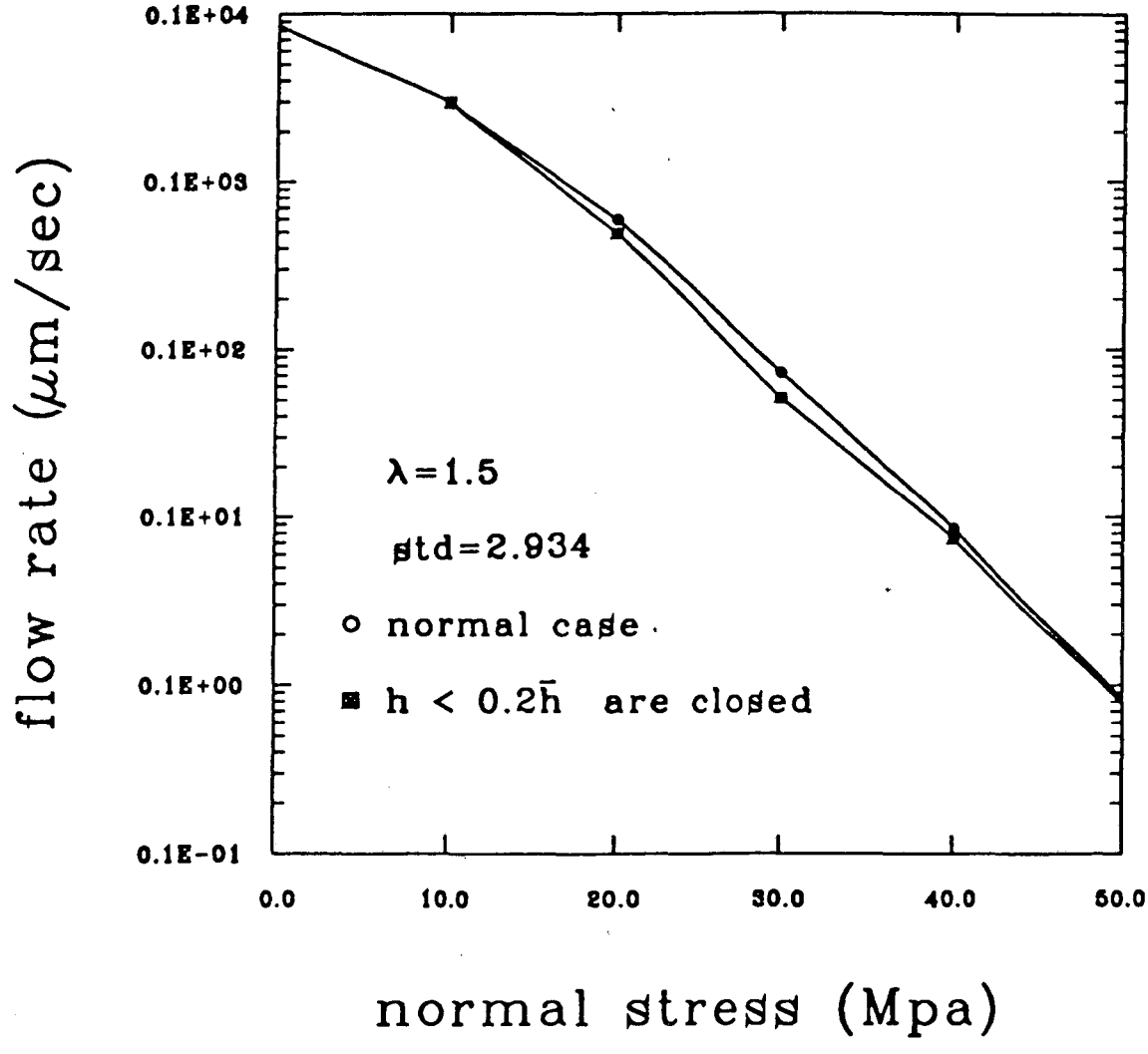

Figure 5-26a Flow rate as a function of normal stress for a fracture with λ=1.5 and std.=2.934 for mean aperture sensitivity study.

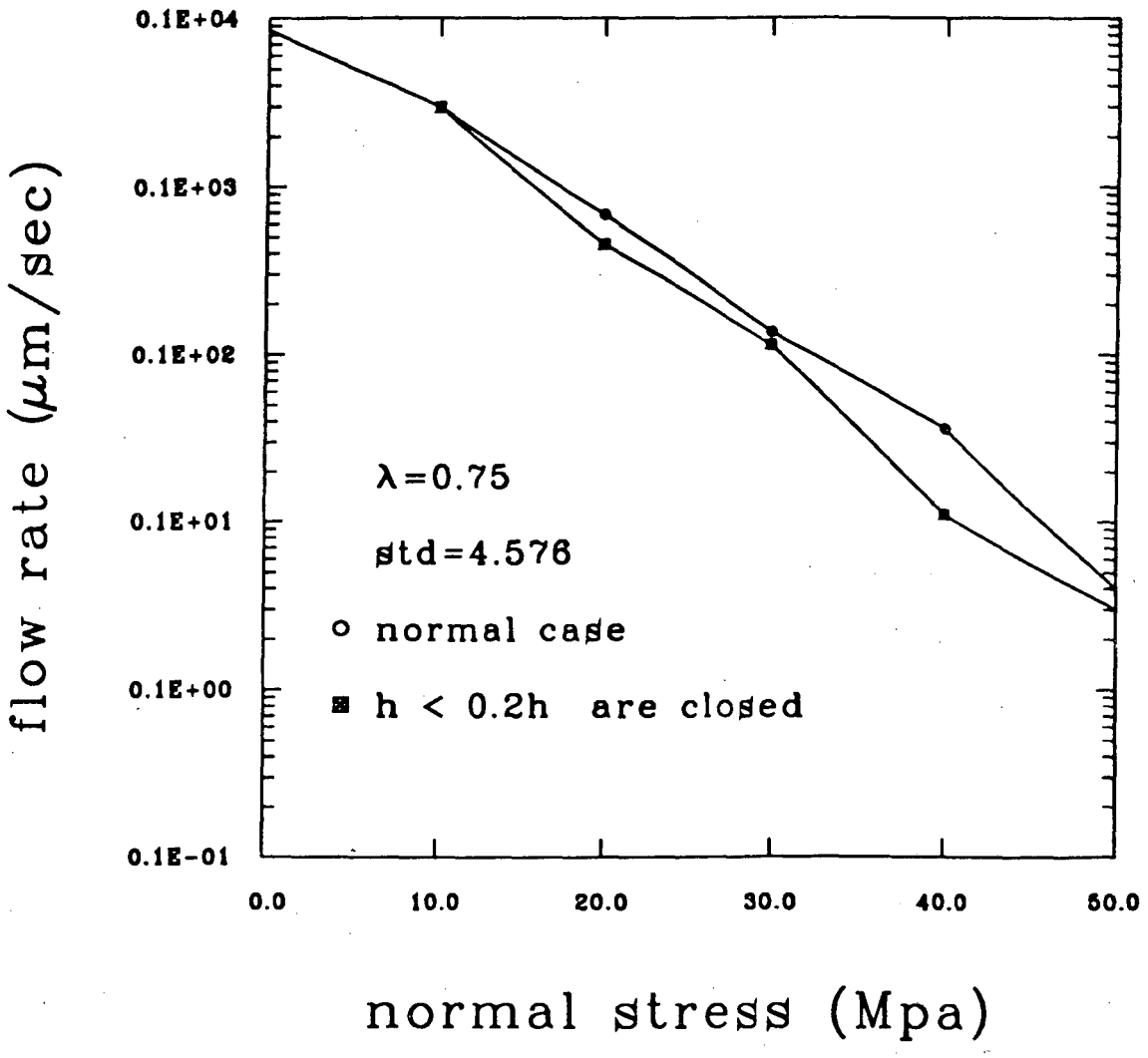

Figure 5-26b Flow rate as a function of normal stress for a fracture with λ=1.5 and std.=4.576 for mean aperture sensitivity study.

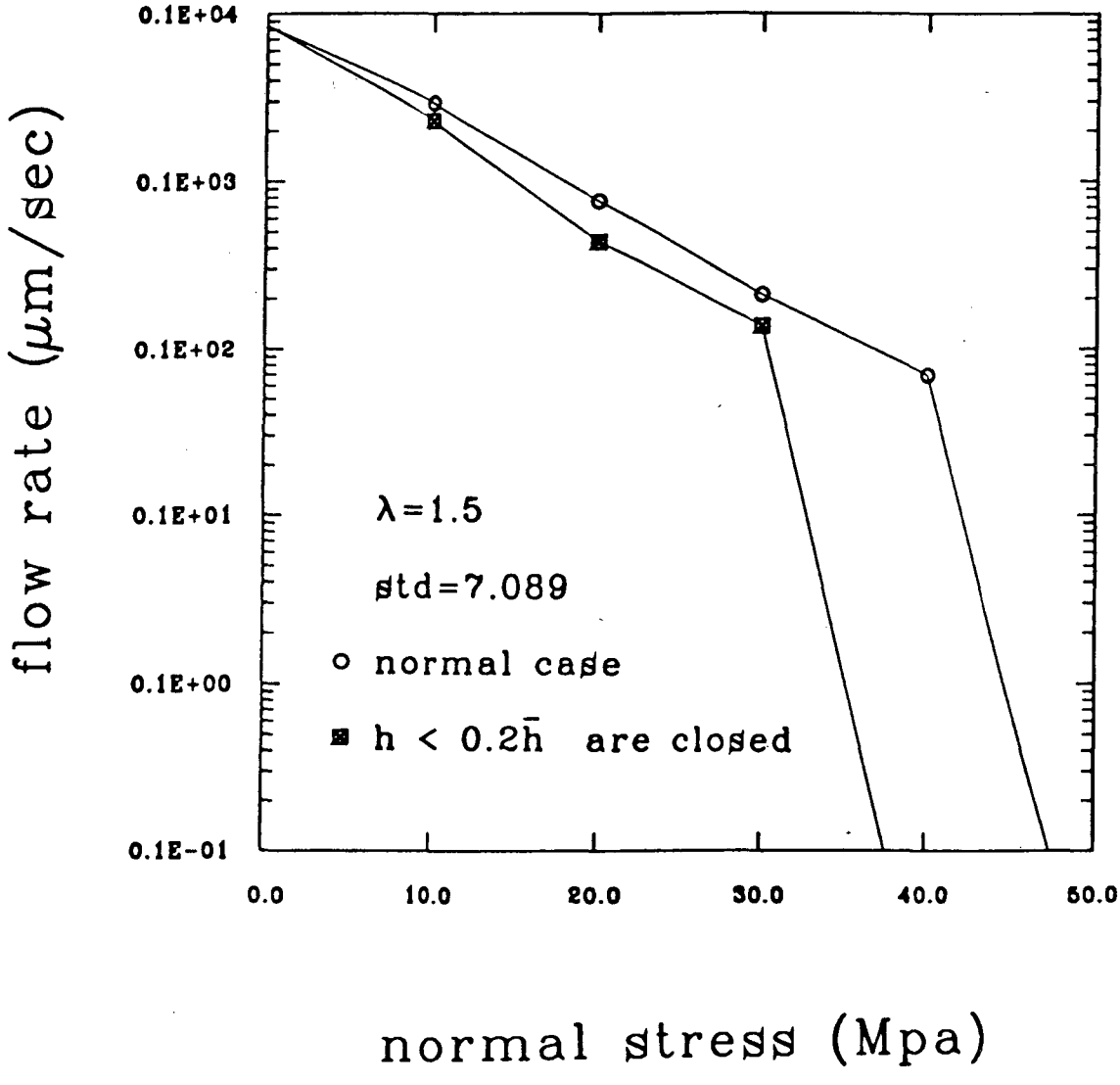

Figure 5-26c Flow rate as a function of normal stress for a fracture with λ=1.5 and std.=7.090 for mean aperture sensitivity study.

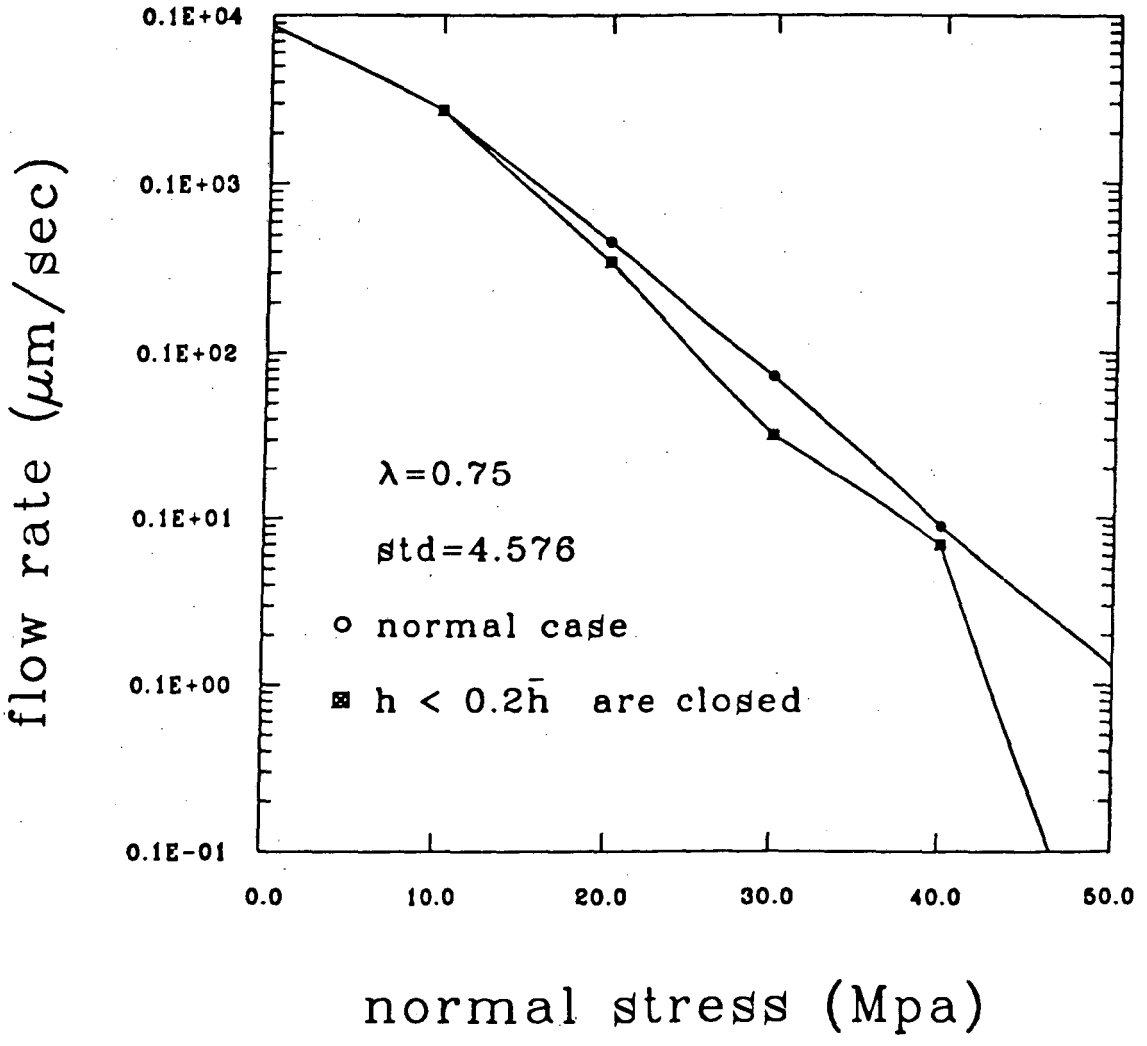

Figure 5-26d Flow rate as a function of normal stress for a fracture with λ=0.75 and std.=4.576 for mean aperture sensitivity study.

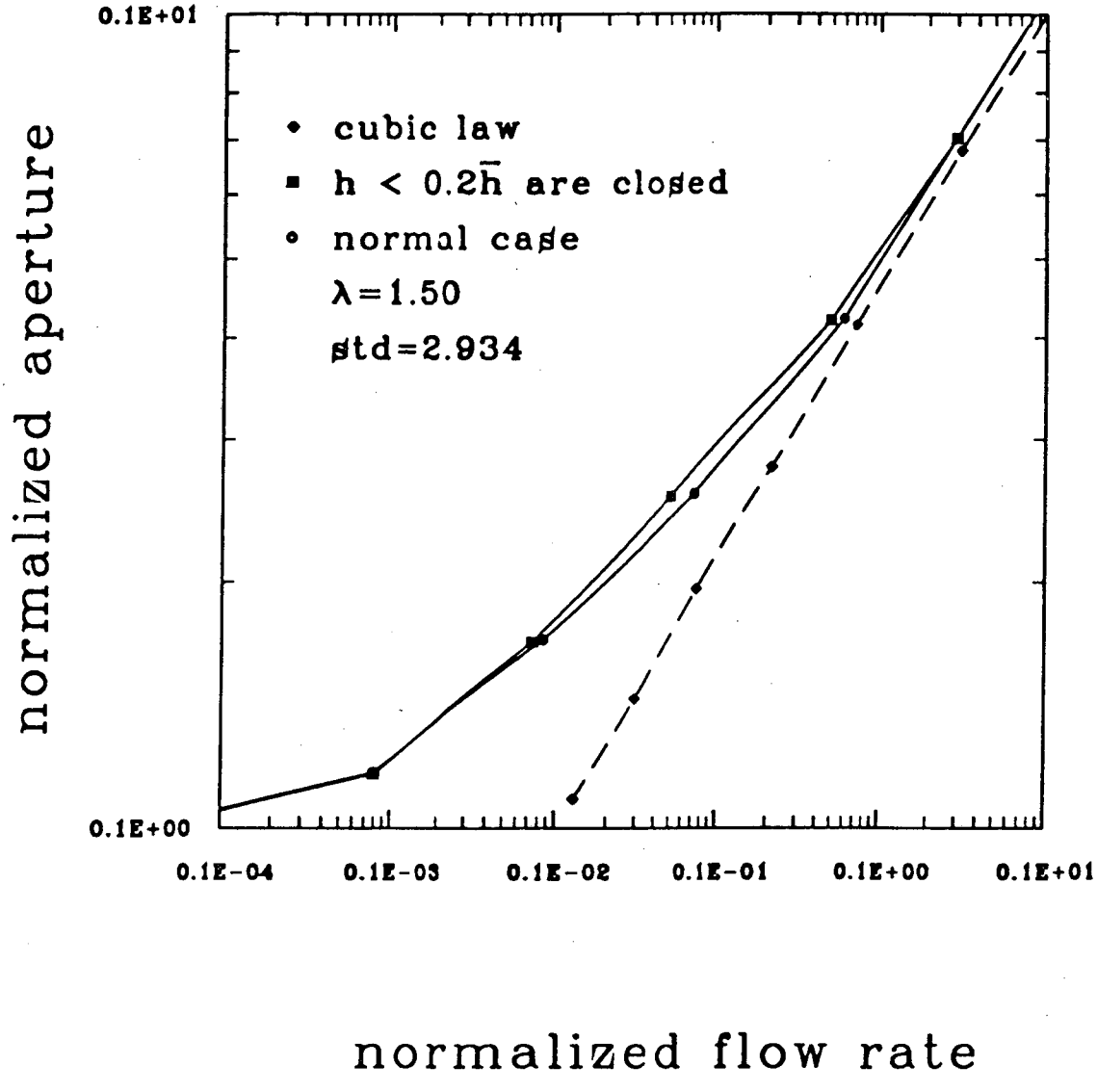

Figure 5-27a Flow rate as a function of mean aperture for a fracture with λ=1.5 and std.=2.934 and comparison with the "cubic law" for the mean aperture sensitivity study.

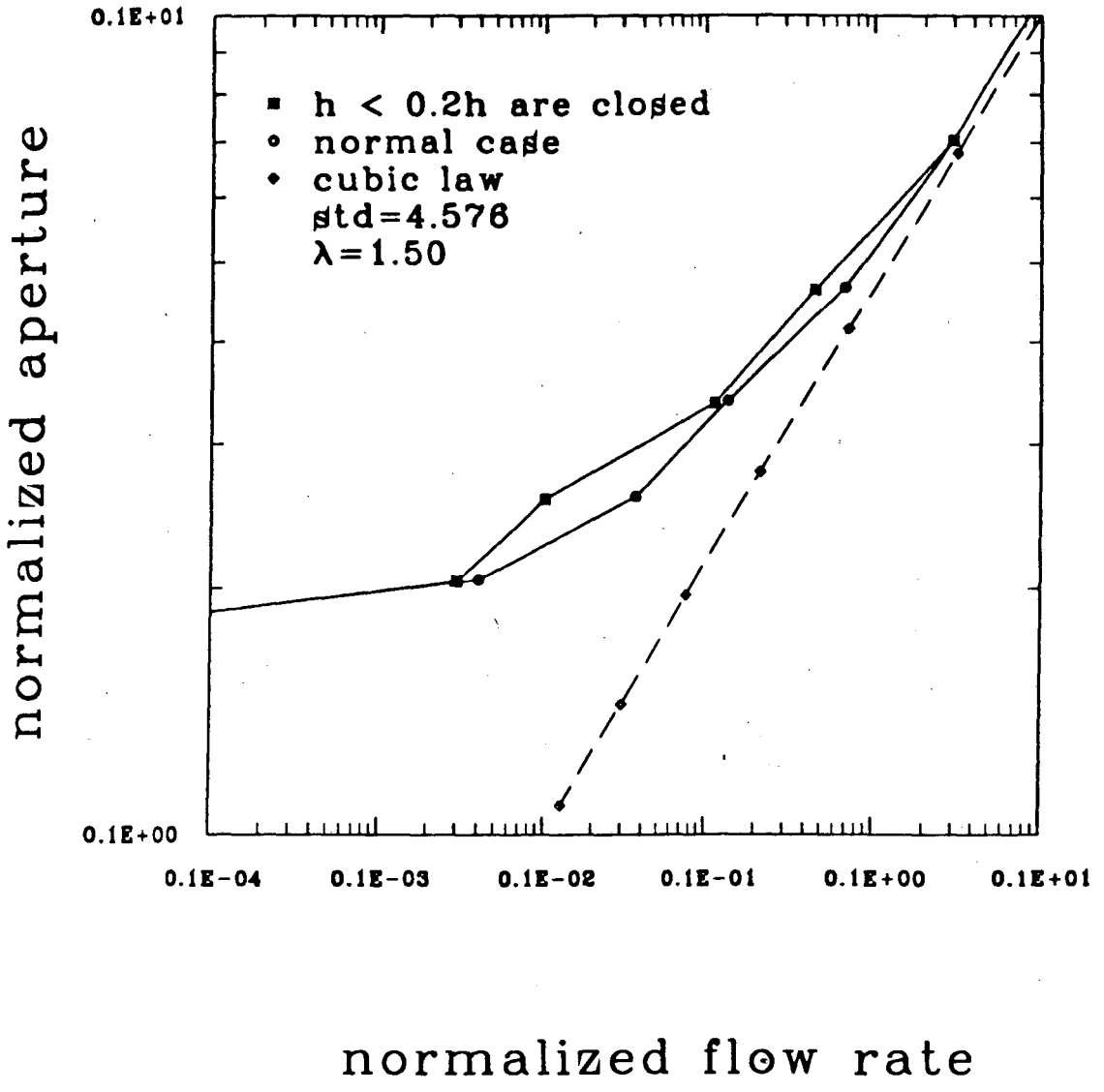

Figure 5-27b Flow rate as a function of mean aperture for a fracture with λ=1.5 and std.=4.576 and comparison with the "cubic law" for the mean aperture sensitivity study.

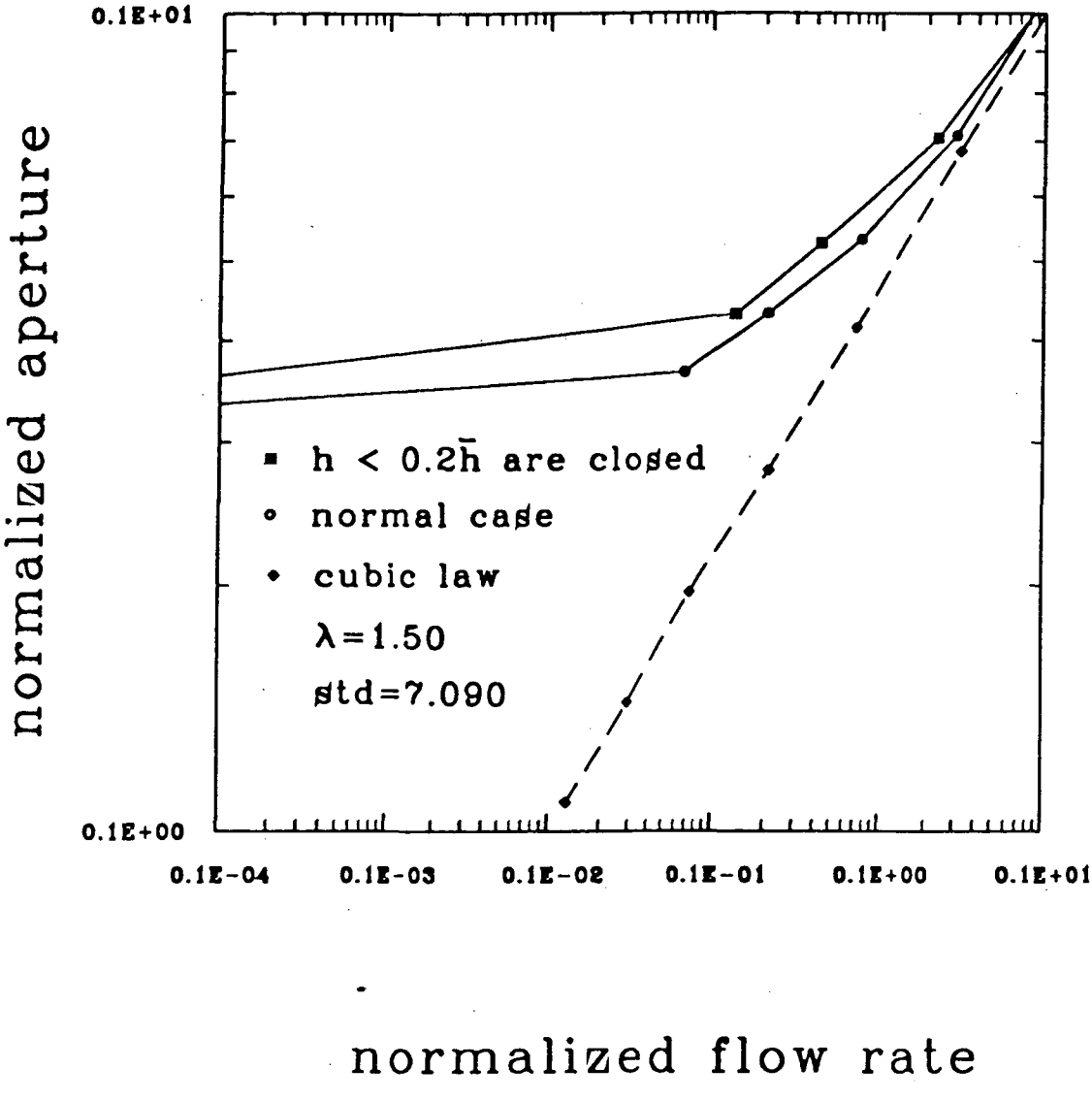

Figure 5-27c Flow rate as a function of mean aperture for a fracture with λ=1.5 and std.=7.090 and comparison with the "cubic law" for the mean aperture sensitivity study.

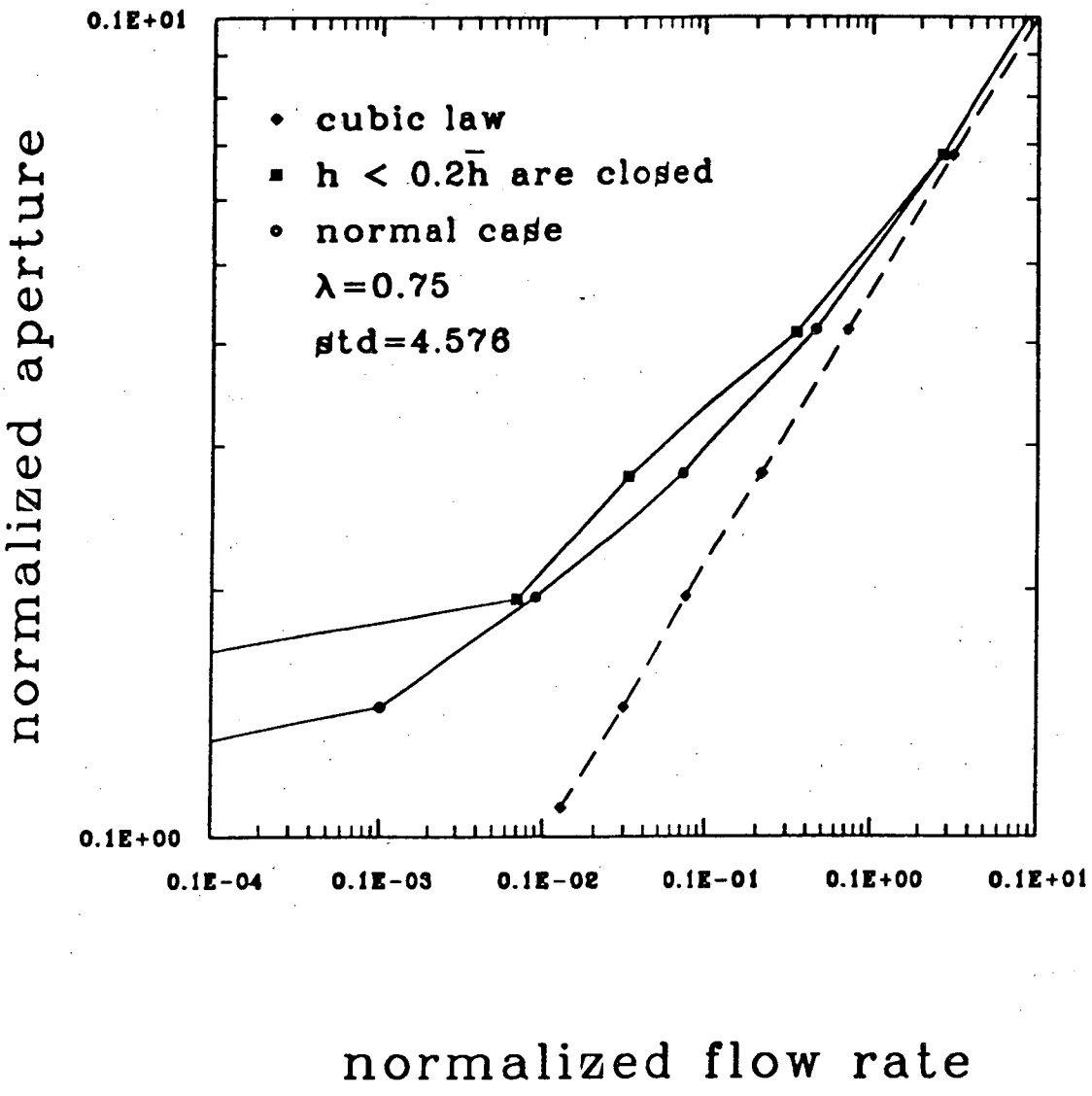

Figure 5-27d Flow rate as a function of mean aperture for a fracture with λ=0.75 and std.=4.576 and comparison with the "cubic law" for the mean aperture sensitivity study.

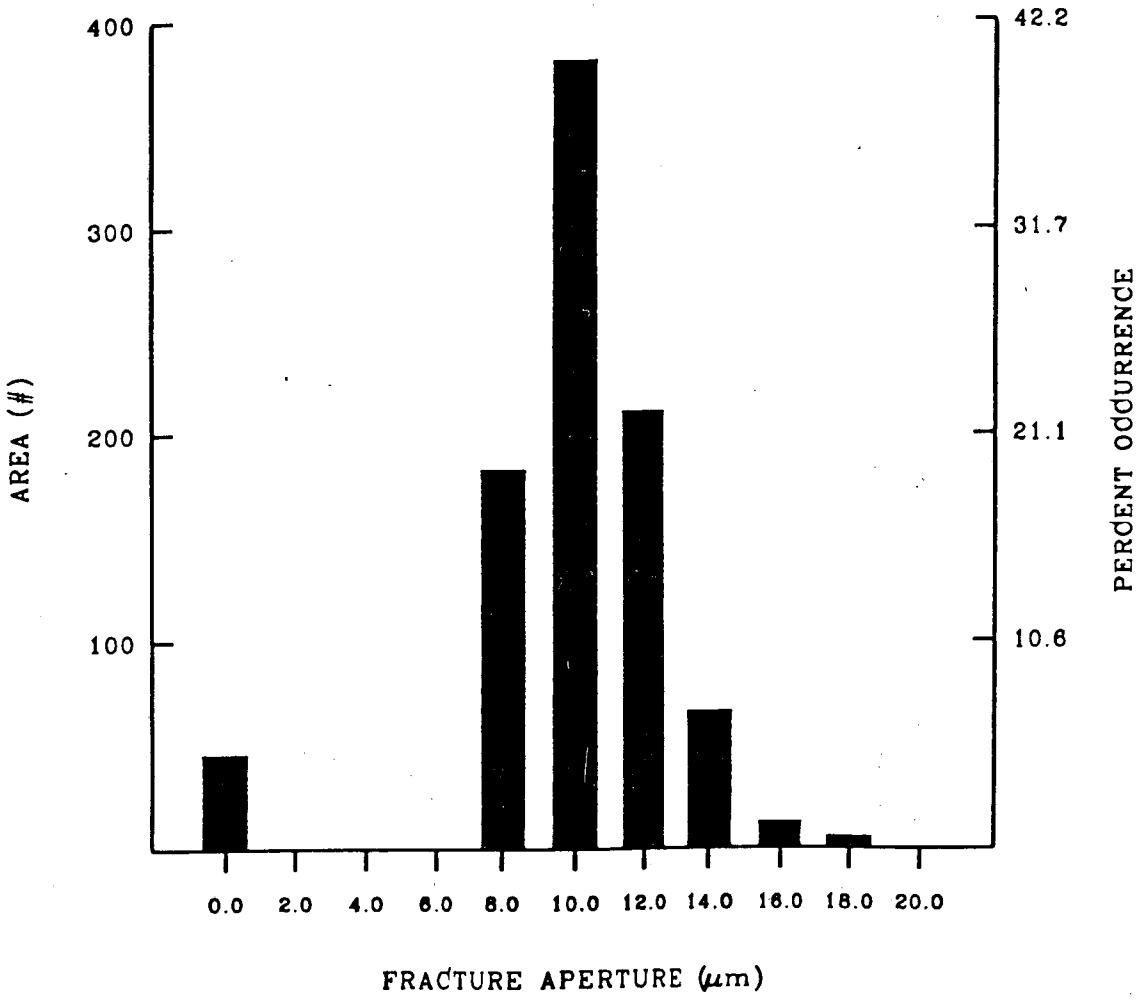

average aperture=10 μm

standard deviation=2.934

filter coefficient λ =1.50

Figure 5-28a Aperture density distribution for the fracture with s=2.934 and λ=1.5 at normal stress T=0.

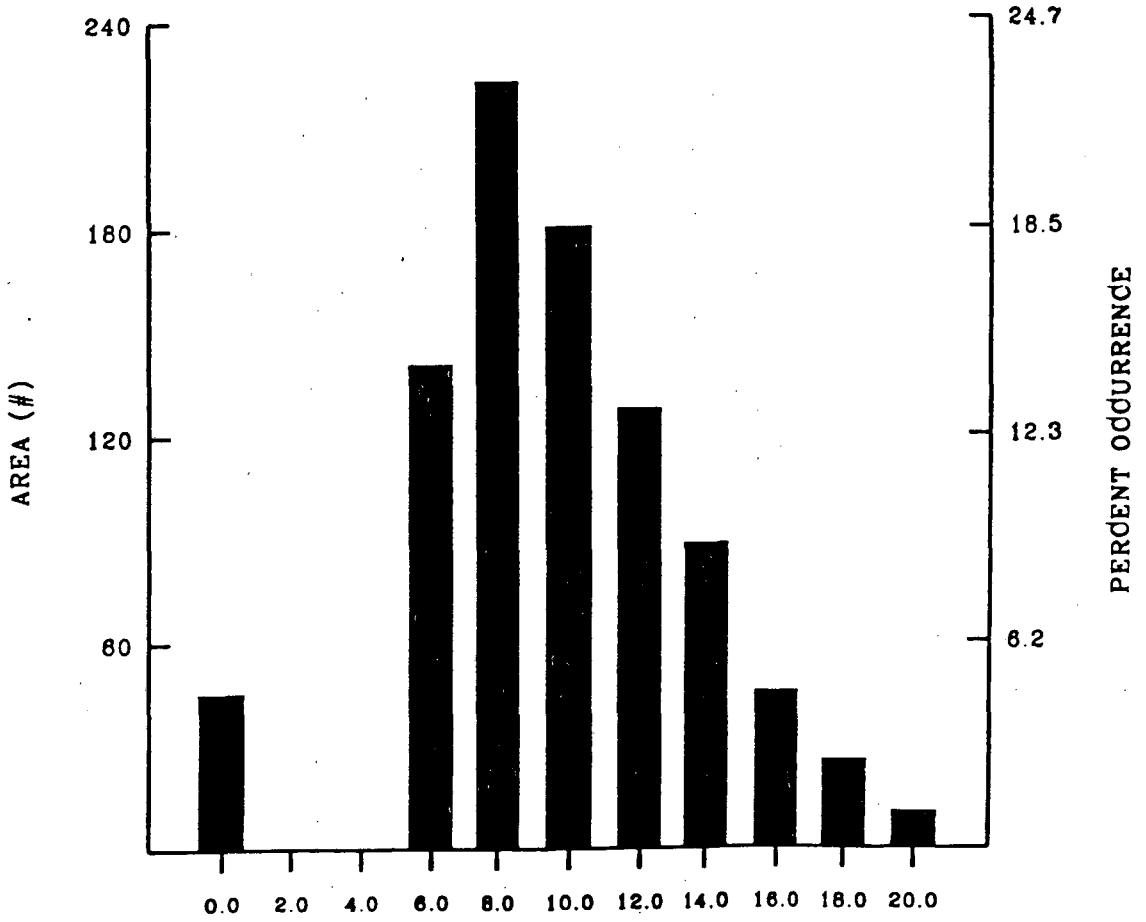

Figure 5-28b Aperture density distribution for the fracture with s=4.576 and λ=1.5 at normal stress T=0.

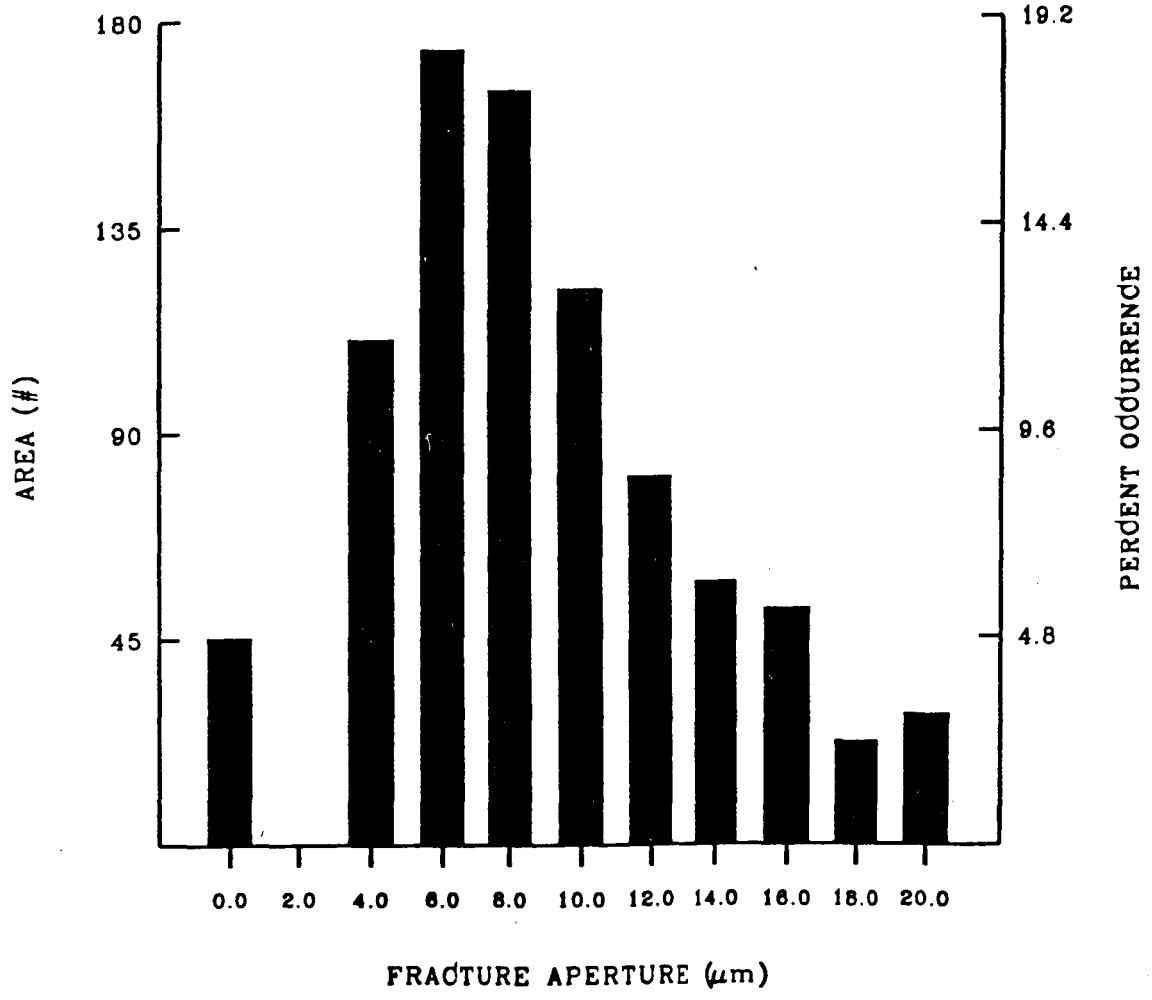

average aperture=10 μm

standard deviation=7.090

filter coefficient λ =1.50

Figure 5-28c Aperture density distribution for the fracture with s=7.090 and λ=1.5 at normal stress T=0.

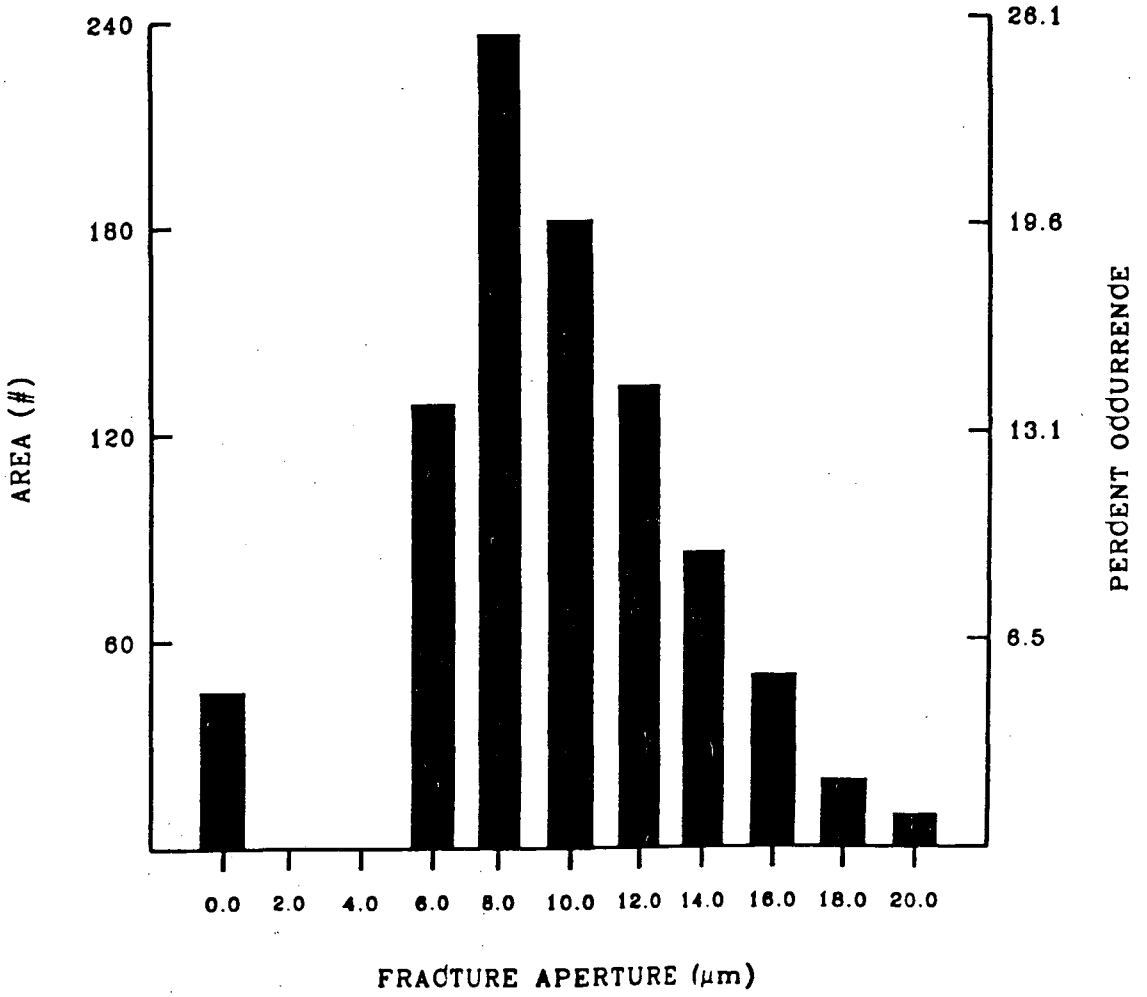

average aperture=10 μm

standard deviation=4.576

filter coefficient λ =0.75

Figure 5-28d Aperture density distribution for the fracture with s=4.576 and λ=0.75 at normal stress T=0.

Table 5-8 Calculation of $\Delta\bar{h}$, Δc, and ΔQ for the sensitivity study of mean aperture.

standard deviation=2.934, correlation factor λ= 1.50						
T *MPa*	$\bar{h}$ μm	$\bar{h}_c$ μm	$\Delta h/h$ %	Q $\mu m^3/s$	Q_ξ $\mu m^3/s$	$\Delta Q/Q$ %
20	4.219	4.201	0.43	0.0596	0.0490	17.73
30	2.570	2.553	0.66	0.00724	0.00510	29.56
40	1.700	1.691	0.53	0.00085	0.00074	12.94
50	1.171	1.166	0.43	0.00008	0.00006	
60	0.838	0.834	0.48			
standard deviation=4.576, correlation factor λ= 1.50						
T *MPa*	$\bar{h}$ μm	$\bar{h}_c$ μm	$\Delta h/h$ %	Q $\mu m^3/s$	Q_ξ $\mu m^3/s$	$\Delta Q/Q$ %
20	4.660	4.623	0.79	0.0680	0.0451	33.68
30	3.385	3.364	0.62	0.0137	0.0132	3.56
40	2.586	2.570	0.62	0.0036	0.0010	72.22
50	2.050	2.043	0.34	0.0004	0.0001	25.00
60	1.670	1.664	0.35			
standard deviation=7.090, correlation factor λ= 1.50						
T *MPa*	$\bar{h}$ μm	$\bar{h}_c$ μm	$\Delta h/h$ %	Q $\mu m^3/s$	Q_ξ $\mu m^3/s$	$\Delta Q/Q$ %
20	7.103	7.051	0.73	0.29228	0.22922	21.58
30	5.312	5.256	1.05	0.07590	0.04339	42.83
40	4.318	4.308	0.23	0.02102	0.01370	34.82
50	3.651	3.620	0.85	0.00689	0.00001	
60	3.142	3.109	1.05			
standard deviation=4.576, correlation factor λ= 0.75						
T *MPa*	$\bar{h}$ μm	$\bar{h}_c$ μm	$\Delta h/h$ %	Q $\mu m^3/s$	Q_ξ $\mu m^3/s$	$\Delta Q/Q$ %
20	4.151	4.113	0.92	0.0452	0.0344	23.89
30	2.773	2.752	0.76	0.0072	0.0032	55.56
40	1.962	1.950	0.61	0.0009	0.0007	22.22
50	1.440	1.436	0.28	0.0001		
60	1.086	1.084	0.18			

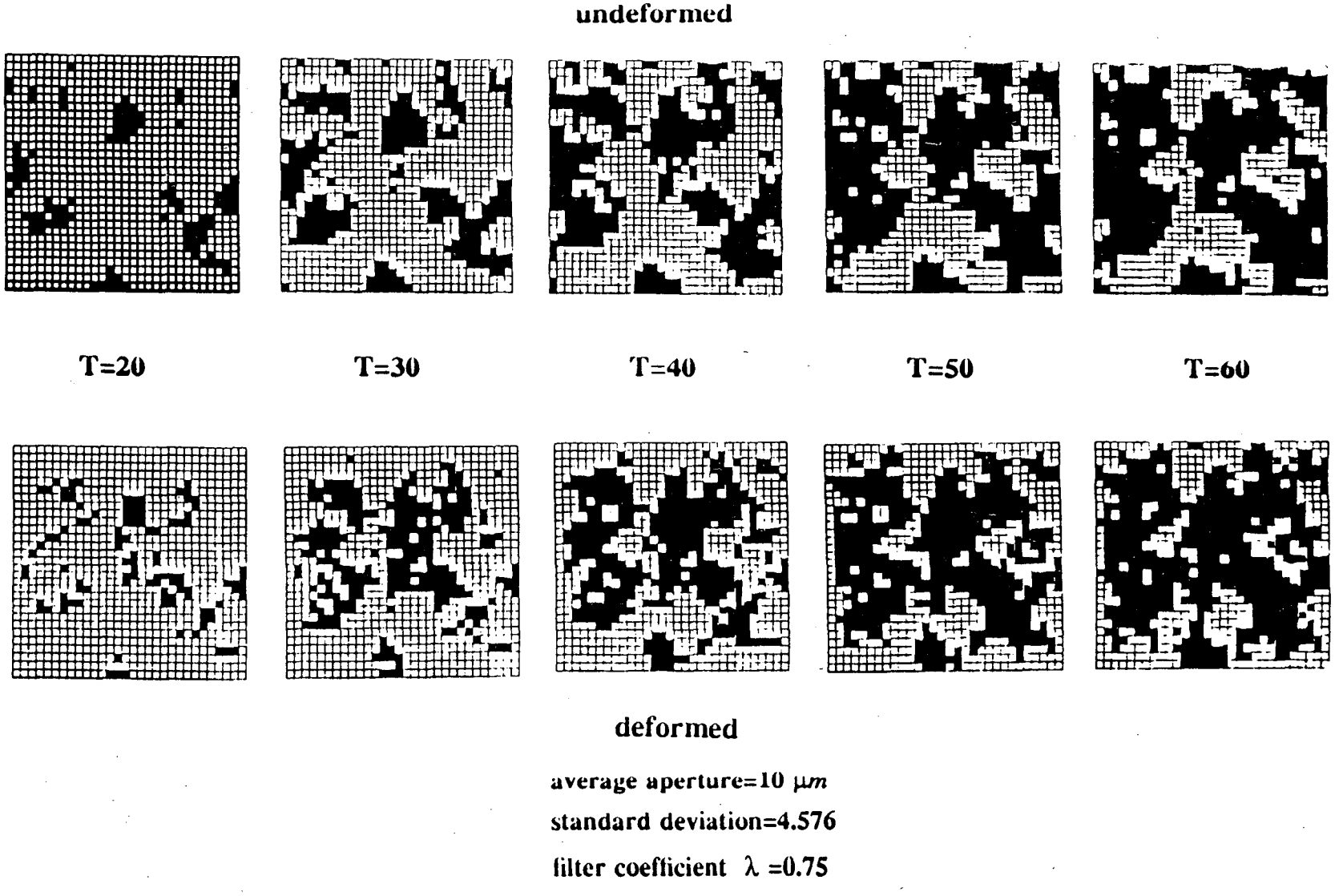

Figure 5-29a Comparison between contact area distributions of deformed and undeformed fracture with λ=0.75 and std.=4.576, keeping percent contact area constant at each stress level.

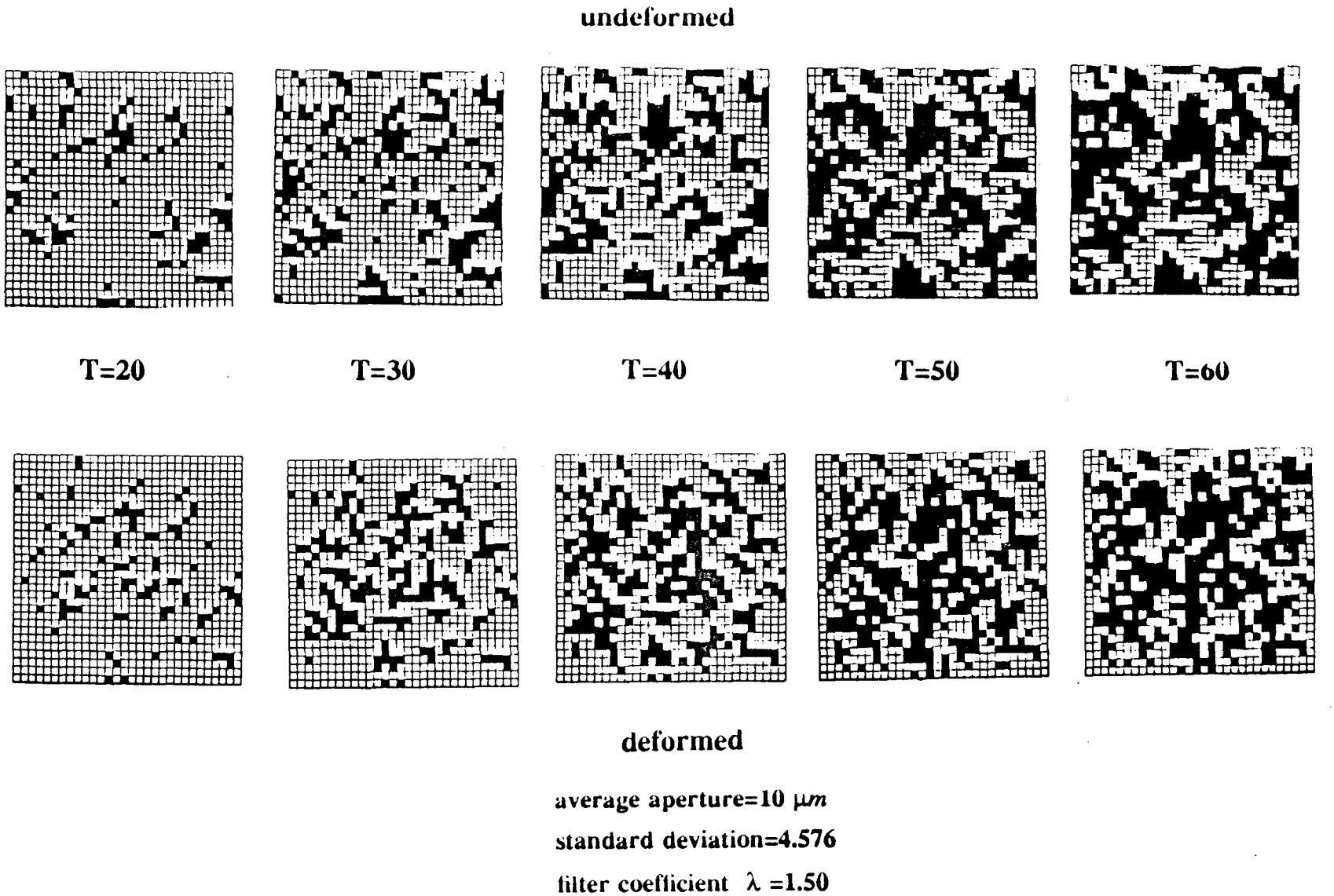

Figure 5-29b Comparison between contact area distributions of deformed and undeformed fracture with λ=1.50 and std.=4.576, keeping percent contact area constant at each stress level.

CHAPTER 6

CONCLUSION

Numerical analysis on statistically equivalent fractures, using boundary element methods, to account for the effects of contact areas and tortuosity of the flow path between two rough surfaces when an increment of normal stress is applied to the fracture, has been carried out. It is found that a cubic relationship between flow and mean aperture derived from the Reynolds equation for flow between nearly parallel plates does not fit the simulations of flow through a fracture in partial contact. The exponent of the aperture in the "cubic law" is greater than 3.0 at low stress. At some critical stress, typically on the order of 30-70 MPa, the percolation limit is reached (i.e. a connected pathway for fluid flow no longer exists), and the permeability drops precipitously. Simulations also show that fracture closure, fracture stiffness and fluid flow are highly non-linear functions of the effective normal stress applied across the fracture.

The compliance of fractures and fluid flow through a fracture depend primarily upon the amount and spatial arrangement of contact areas. Percent contact area is the sole parameter in Walsh's expression for predicting flow through a fracture with partial contact (2-35). The expression derived by Walsh (1981) using a Maxwell-type effective medium approximation for contact area fractions ranging from 0 to 0.25 is verified by the simulations and analogue measurements. Walsh's result has also been extended to the case, where instead of circular shapes, obstructions have elliptical shapes (Eq. 2-36) (see Chapter 4). For fracture stiffness or compressibility, dependence on contact area is examined in Chapter 4. Simulations there suggest that the values of fracture stiffnesses increase with linearly increasing percent contact area. For a

constant contact area percentage, a dispersed arrangement of contact areas forms a stiffer interface than a compacted arrangement of contact areas.

While fracture stiffness and flow through the fracture are controlled by the void space geometry (percent contact area, the distribution of contact area, local apertures, percolation limit), the void space geometry strongly depends on fracture deformation under stress and on the topographies of the two rough surfaces of the fracture, characterized by the standard deviation s in the lognormal aperture density distribution function and correlation factor λ. It reminds us that the effects of fracture deformation and the roughness of fracture surfaces must be included in the equation describing flow through a fracture.

The possibility now exists of simulating the mechanical and hydraulic behavior of real fractures, based on measured aperture distributions, and comparing the predictions with experimental results. The computer codes, ROUGH and FLOW, may be a powerful tool to select the optimum representive of fracture surface topograph from different variable aperture functions and fractal models by "inverse simulations". It is also interesting that ROUGH and FLOW may be used to predict the pressure distributions of fluid flow and flow channels, the preferred flow paths, along the fracture plane with the increment of normal stress.

REFERENCES

Bandis, S.C., Lumsden, A.C. & N.R. Barton. 1983. Fundamentals of rock joint deformation, *Int. J. Rock Mech. Min. Sci & Geomech. Abstr.*, 20:249.

Barton, N., Bandis, S. & K. Bakhtar. 1985. Srength, deformation and conductivity coupling of rock joints, *Int. J. Rock Mech. Min. Sci & Geomech. Abstr.*, 22:121.

Banerjee, P.k. & R. Butterfield. 1981. *Boundary Element Methods in Engineering Science*, London: McGraw-Hill.

Batchelor,G.K. 1967. *Introduction to Fluid Dynamics*, Cambridge: Cambridge University Press.

Brebbia, C.A. 1978. *The Boundary Element Method for Engineers*, London: Pentech Press.

Brown, S.R. 1987. Fluid flow through rock joints: The effect of surface roughness, *J. Geophys. Res.*, 92:1337.

Brown, S.R., Kranz, R.L. and B.P. Bonner. 1986. Correlation between the surfaces of natural rock joints, *J. Geophys. Res. Letts.*, 13:1430.

Brown, S.R., & C.H. Scholz. 1985a. Closure of random elasctic surfaces in contact, *Jour. Geophys. Res.*, 90:5531.

Brown, S.R., & C.H. Scholz. 1985b. Broad bandwidth study of the topography of natural rock surfaces, *J. Geophys. Res.*, 90:12575.

Brown, S.R., & C.H. Scholz. 1986. Closure of rock joints, *J. Geophys. Res.*, 91:4939.

Carslaw, H.S. & J.C. Jaeger. 1959. *Conduction of Heat in Solids*, Oxford: Oxford University Press

Chen, D.W., R.W. Zimmerman, & N.G.W. Cook. 1989. The effect of contact area on the permeability of fractures, Proceedings 30th Symp. Rock Mech., Rotterdam: Balkema, pp 81-88.

Coakley, K. 1989. *Spatial Statistics for Predicting Flow through a Single Rock Fracture*, Ph.D. thesis, Stanford University.

Cook, N.G.W. 1988. *Natural Joints in Rock: Mechanical, Hydraulic and Seismic Behavior and Properties under Normal Stress*, First Jaeger Memorial Lecture, 29th U.S. Symposium on Rock Mechanics, University of Minnesota.

Crouch, S.L. & A.M. Starfield. 1983. *Boundary Element Methods in Solid Mechanics*, London: George Allen & Unwin.

Engelder, T. and C.H. Scholz. 1981. Fluid flow along very smooth joints at effective pressures up to 200 megapascals, in *Mechanical Behavior of Crustal Rocks*, Amer. Geophys. Union Monograph, 24:147.

Gale, J.E. 1987. Comparison of Coupled Fracture Deformation and Fluid Flow Models with Direct Measurements of Fracture Pore Structure and Stress Flow Properties, In I.W. Farmer et al. (eds)., 28th US Symposium on Rock Mech. pp 1213-1222.

Goodman, R.E. 1976. *Method of Geological Engineering in Discontinuous Rocks*, New York: West Publishing, p172.

Greenwood, J.A. & J.B.P. Williamson. 1966. Contact of nominally flat surfaces, *Proc. Roy. Soc. London A*, 295.

Hopkins, D.L., N.G.W. Cook & L.R. Myer. 1987. Fracture stiffness and aperture as a function of applied stress and contact geometry. In I.W. Farmer et al. (eds.), Proc. 28th U.S. Symp. Rock Mech., pp. 673-680.

Iwai, K. 1976. *Fundamental studies of fluid flow through a single fracture*, Ph.D. thesis, University of California at Berkeley.

Kumar, S., R.W. Zimmerman & G.S. Bodvarsson. 1989. Permeability of a fracture with cylindrical asperities. Report LBL-27626, Lawrence Berkeley Laboratory.

Louis, C. 1976. *Introduction a l'hydraulique des roches*, Ph.D thesis, University of Paris.

Moreno, L., Y.W. Tsang, C.F. Tsang, F.V. Hale, and I. Neretnieks. 1988. Flow and Tracer Transport in a Single Fracture: A Stochastic Model and Its Relation to Some Field Observations, *Water Resour. Res.*, 24:2033.

Nolte, D.D., L.J. Pyrak-Nolte & N.G.W. Cook. 1988. Fluid percolation through single fractures, *J. Geophys. Res. Letts.*, 15: 1247-1250.

Pyrak-Nolte, L.J., L.R. Myer, N.G.W. Cook & P.A. Witherspoon. 1987. In G. Herget & S. Vongpaisal (eds), *Proc. 6th Int. Cong. Rock Mech.*, Rotterdam: Balkema, pp 225-231.

Raven, K.G. & J.E. Gale. 1985. Water flow in natural rock fractures as a function of stress and sample size, *Int. J. Rock Mech. Min. Sci & Geomech. Abstr.*, 22:251.

Rongved, L. 1957. Dislocation over a bounded plane area in an infinite solid. *J. Appl. Mech.*, 24: 252.

Schlichting, H. 1968. *Boundary-Layer Theory, 6th Ed.*, New York: McGraw-Hill.

Sinha, K.P. 1979. *Displacement discontinuity technique for analyzing stresses and displacements due to mining in seam deposits*, Ph.D. thesis, University of Minnesota.

Sokolnikoff, I.S. 1956. Mathematical Theory of Elasticity, 2nd ed., New York: McGraw-Hill.

Swan, G. 1983. Determination of stiffness and other joint properties from roughness measurements, *Rock Mech. & Rock Eng.*, 16:19.

Tsang, Y.W. & C.F. Tsang. 1987. Channel model of flow through fractured media, *Water Resour. Res.*, 23:467.

Tsang, Y.W. 1984. The effect of tortuosity on fluid flow through a single fracture, *Water Resour. Res.*, 20:1209.

Tsang, Y.W. & P.A. Witherspoon. 1981. Hydromechanical behavior of a deformable rock fracture subject to normal stress, *J. Geophys. Res.*, 86: 9287.

Walsh, J.B. 1981. The effect of pore pressure and confining pressure on fracture permeability, *Int. J. Rock Mech. Min. Sci & Geomech. Abstr.*, 18: 429.

Witherspoon, P.A., Y.W. Tsang, J.C.S. Long, & J. Noorishad. 1981. New approaches to problems of fluid flow in fractured rock masses, 22nd U.S. Symp. on Rock Mech., Massachusetts Institute of Technology.

Witherspoon, P.A., Wang, J.S.Y., Iwai, K, and J.E. Gale. 1980. Validity of cubic law for fluid flow in a deformable rock fracture, *Water Resour. Res.*, 16:1016.

Zimmerman, R.W. 1984. *The effect of Pore Structure on the Pore and Bulk Compressibilities of Consolidated Sandstones*, Ph.D. thesis, University of California at Berkeley.

Zimmerman, R.W., M.S. King & W.H. Somerton. 1986. Compressibility of porous rocks, *J. Geophys. Res.*, 91:12765.

APPENDIX A

ROUGH: A Computer Program for Evaluating Fracture Deformation

The program ROUGH evaluates the three-dimensional elastic deformation of a rough-walled fracture with normal stress across it, based on the mathematical formulations given in Chapter 3. ROUGH includes two simple subroutines (COEFF, OUTF). The main program controls the logic calling sequence of subroutines to read the input data, to initialize the parameters, to set up a system of linear algebraic equations, to solve for the unknown displacements and stresses at fracture plane by iteration method, and to write the output data. Subroutine COEFF evaluates the Equations given in section 3.2, and obtains the displacement and stress influence coefficients of the algebraic equations for both boundary elements and field points. Subroutine OUTF obtains the displacements and stresses at specified off-fracture locations in the infinite region.

The main input of ROUGH is a variable aperture function characterized by mean aperture $\bar{h}$, standard deviation s, and correlation factor λ. This function is generated by a computer program which is not listed here. The output of ROUGH obtains the closure and contact area distributions, percent contact area, mean aperture to characterize the deformed fracture. A description of input variables and formats for the program and a listing of the code are given below.

1. Description of ROUGH Input Variables

v	Poisson's ratio of fractured rock mass,
E	Young's modulus of fractured rock mass,

p1, p2, p3	primitive stress along x, y, and z axis respectively,
bw	side length of the square boundary element,
nrow	number of elements along x axis,
ncol	number of elements along y axis,
nelbw	number of elements along each side of any element,
nosp	number of off-fracture points at which displacements and stresses are to be computed,
xo, yo, zo	coordinates of the origin
orf	over relaxation factor,
itmax	maximum numbers of iterations specified,
nrun	iteration cycles were completed in previous runs,
xmean	mean aperture,
thick(i,j)	aperture located at jth row and ith colume.

2. ROUGH Input Variables and Formats

Variable	**Format**
title	free
v, E	(f8.2, e12.2)
p1, p2, p3	(3f10.0)
bw, nrow, ncol, nelbw, nosp	(f8.2, 4i8)
xo(1, 1), yo(1, 1), zo	(3f12.0)
orf, itmax, nrun	(f8.2, 2i8)
xmean	free

((thick(j,i), i=1,ncol), j=1,nrow) (9f8.3)

```
      common/rko/v,v1,v2,e,cons,cond,con
      common/rk1/dub(900),dvb(900),dwb(900),kode(30,30)
      common/rk3/nrow,ncol,nbxe,bw,hbw,zo
     .     ,xo(30,30),yo(30,30),zo1(30,30),thick(30,30),en(3,3)
      common/rk7/rw,cw,seg,cf01,cf02,cf03,cf04,cf05,cf06,
     .      cf07,cf08,cf09,cf10,cf11,cf12,cf13,cf14,cf15,
     .      cf16,cf17,cf18,cf19,zmn
      dimension s13u(900),s23u(900),s33u(900),s23v(900),s33v(900),
     .      s33w(900),cf(15)
      dimension d1u(900),d2u(900),d3u(900),d2v(900),d3v(900),
     .      d1w(900),d2w(900),d3w(900)
      dimension tuv1(900),tuv2(900),tuv3(900),the(30,30)
      data dub,dvb,dwb/900*0.0,900*0.0,900*0.0/
      data ncut,acc/40,.000000001/
      data pi/3.1415926535897/
      open (unit=1,file='inrough',status='old')
      open (unit=2,file='otrough',status='new')
      open (unit= 3,status='scratch',form='unformatted',
     .      access='direct',recl=3600)
      open (unit= 4,status='scratch',form='unformatted',
     .      access='direct',recl=3600)
      open (unit= 8,status='scratch',form='unformatted',
     .      access='direct',recl=3600)
      open (unit= 9,status='scratch',form='unformatted',
     .      access='direct',recl=3600)
      open (unit=10,status='scratch',form='unformatted',
     .      access='direct',recl=3600)
      open (unit=11,status='scratch',form='unformatted',
     .      access='direct',recl=3600)
      open (unit=12,status='scratch',form='unformatted',
     .      access='direct',recl=3600)
      open (unit=13,status='scratch',form='unformatted',
     .      access='direct',recl=3600)
      open (unit=14,status='scratch',form='unformatted',
     .      access='direct',recl=3600)
      open (unit=15,status='scratch',form='unformatted',
     .      access='direct',recl=3600)
      open (unit=16,status='scratch',form='unformatted',
     .      access='direct',recl=3600)
      open (unit=17,status='scratch',form='unformatted',
     .      access='direct',recl=3600)
      open (unit=18,status='scratch',form='unformatted',
     .      access='direct',recl=3600)
      open (unit=19,status='scratch',form='unformatted',
     .      access='direct',recl=3600)
      write(2, 5000)
      read(1,5001)
      write(2,5001)
      read(1,5005)v,e
      write(2,6001)v,e
      read (1,5009)p1,p2,p3
      read(1,5011)bw,nrow,ncol,nelbw,nosp
      write(2,6011) bw,nrow,ncol
      read(1,5013)xo(1,1),yo(1,1),zo
      write(2,5013)xo(1,1),yo(1,1),zo
      read(1,5023)orf,itmax,nrun
      write(2,6023)orf,itmax
      if(nrun-1)30,30,27
   27 write(2,6025)nrun
   30 continue
        read(1,*)xmean
      read(1,756)((thick(j,i),i=1,ncol),j=1,nrow)
  756 format(9f8.3)
c  756 format(12f6.3)
c       do 757 j=1,nrow
c       do 757 i=1,ncol
c  757 read(1,756)kode(j,i),thick(j,i)
c  756 format(6x,i3,e12.4)
      kcon1=0
      do 10 j=1,nrow
      do 10 i=1,ncol
      thick(j,i)=thick(j,i)*0.001
      kode(j,i)=1
      if(thick(j,i).le.0.)then
      thick(j,i)=0.
      kode(j,i)=3
      endif
      if(kode(j,i).eq.3.or.kode(j,i).eq.4)kcon1=kcon1+1
   10 continue
c
      fact=pi/180.
      v1=(1.-v)
      v2=(1.-2.*v)
      cons=e/(8.*pi*(1.-v*v))
      cond=1./(8.*pi*(1-v))
      con=-orf/cons
      con1=-orf/cond
      hbw=0.5*bw
      stfs=-e/(2.*(1+v))
      stfn=-e
      stifn=stfn/(xmean*cons)
      stifs=stfs/(xmean*cons)
c
      do 31 j=1,nrow
      do 31 i=1,ncol
      xo(j,i)=xo(1,1)+(j-1)*bw
      yo(j,i)=yo(1,1)+(i-1)*bw
   31 zo1(j,i)= 0.5*thick(j,i)
      call tract
      nn=0
      do 730 jp=1,nrow
      do 730 ip=1,ncol
      nn=nn+1
      xn=xo(jp,ip)
      yn=yo(jp,ip)
      z1n=zo1(jp,ip)
      z2n=-zo1(jp,ip)
      jb=jp-nelbw
      je=jp+nelbw
      if(jb.le.1)jb=1
      if(je.ge.nrow)je=nrow
      ib=ip-nelbw
      ie=ip+nelbw
      if(ib.le.1)ib=1
      if(ie.ge.ncol) ie=ncol
      lmn=(jp-jb)*(ie-ib+1)+ip-ib+1
      ll=0
      do 740 js=jb,je
      do 740 is=ib,ie
      ll=ll+1
      xm=xo(js,is)
      ym=yo(js,is)
      z1m= zo1(js,is)
      z2m=-zo1(js,is)
      seg=hbw
      rw=xm-xn
      cw=ym-yn
      zmn=z1m-z1n
```

```
      zmn2=z2m-z1n
      zt1=(xm-xn)*en(3,1)+(ym-yn)*en(3,2)+(z1m-z1n)*en(3,3)
      zt2=(xm-xn)*en(3,1)+(ym-yn)*en(3,2)+(z2m-z1n)*en(3,3)
      call coeff(zt1)
      if(zt.ne.0.and.zmn.eq.0)zt=0
      d1u(ll)=2.*v1*cf03-zt*cf04
      d2u(ll)=-zt*cf05
      d2v(ll)=2.*v1*cf03-zt*cf07
      d1w(ll)=-v2*cf01-zt*cf06
      d2w(ll)=-v2*cf02-zt*cf08
      d3u(ll)=v2*cf01-zt*cf06
      d3v(ll)=v2*cf02-zt*cf08
      d3w(ll)=2.*v1*cf03-zt*cf09
      s13u(ll)=v*cf04-v1*cf09+zt*cf12
      s23u(ll)=v*cf05+zt*cf14
      s23v(ll)=v*cf07-v1*cf09+zt*cf17
      s33u(ll)=zt*cf15
      s33v(ll)=zt*cf18
      s33w(ll)=zt*cf19-cf09
      if(ll.ne.lmn)go to 740
      tuv1(nn)=s13u(ll)
      tuv2(nn)=s23v(ll)
      tuv3(nn)=s33w(ll)
      if(kode(jp,ip).eq.3.or.kode(j,i).eq.4)then
      tuv1(nn)=s13u(ll)+stifs
      tuv2(nn)=s23v(ll)+stifs
      tuv3(nn)=s33w(ll)+stifn
      endif
  740 continue
      write( 3,rec=nn)s13u
      write( 4,rec=nn)s23u
      write( 8,rec=nn)s23v
      write( 9,rec=nn)s33u
      write(10,rec=nn)s33v
      write(11,rec=nn)s33w
      write(12,rec=nn)d1u
      write(13,rec=nn)d2u
      write(14,rec=nn)d3u
      write(15,rec=nn)d2v
      write(16,rec=nn)d3v
      write(17,rec=nn)d1w
      write(18,rec=nn)d2w
      write(19,rec=nn)d3w
  730 continue
      do 800 iter=1,itmax
      if(iter.gt.ncut) go to 810
      error=0.0
      ind1=0
      ind2=ind1
      ind3=ind2
      kcon=0
      do 450 j=1,nrow
      do 450 i=1,ncol
      nn=(j-1)*ncol+i
      s13pb=0.
      s23pb=0.
      s33pb=0.
      upb=0.
      vpb=0.
      wpb=0.
      jb=j-nelbw
      je=j+nelbw
      if(jb.le.1)jb=1
      if(je.ge.nrow)je=nrow
      ib=i-nelbw
      ie=i+nelbw
      if(ib.le.1)ib=1
      if(ie.ge.ncol) ie=ncol
      read( 3,rec=nn)s13u
      read( 4,rec=nn)s23u
      read( 8,rec=nn)s23v
      read( 9,rec=nn)s33u
      read(10,rec=nn)s33v
      read(11,rec=nn)s33w
      read(12,rec=nn)d1u
      read(13,rec=nn)d2u
      read(14,rec=nn)d3u
      read(15,rec=nn)d2v
      read(16,rec=nn)d3v
      read(17,rec=nn)d1w
      read(18,rec=nn)d2w
      read(19,rec=nn)d3w
      ll=0
      do 460 js=jb,je
      do 460 is=ib,ie
      ll=ll+1
      mm=(js-1)*ncol+is
      s13pb=s13pb+s13u(ll)*dub(mm)+s23u(ll)*dvb(mm)+s33u(ll)*dwb(mm)
      s23pb=s23pb+s23u(ll)*dub(mm)+s23v(ll)*dvb(mm)+s33v(ll)*dwb(mm)
      s33pb=s33pb+s33u(ll)*dub(mm)+s33v(ll)*dvb(mm)+s33w(ll)*dwb(mm)
      upb=upb+d1u(ll)*dub(mm)+d2u(ll)*dvb(mm)+d1w(ll)*dwb(mm)
      vpb=vpb+d2u(ll)*dub(mm)+d2v(ll)*dvb(mm)+d2w(ll)*dwb(mm)
      wpb=wpb+d3u(ll)*dub(mm)+d3v(ll)*dvb(mm)+d3w(ll)*dwb(mm)
  460 continue
      ss1=tuv1(nn)
      ss2=tuv2(nn)
      ss3=tuv3(nn)
      t1=s13pb*cons
      t2=s23pb*cons
      t3=s33pb*cons
      cf(1)=con/ss1
      cf(2)=con/ss2
      cf(3)=con/ss3
      if(kode(j,i).eq.3.or.kode(j,i).eq.4)go to 420
      s13=p1+t1
      s23=p2+t2
      s33=p3+t3
      go to 421
  420 s13=stfs*dub(nn)/xmean+t1
      s23=stfs*dvb(nn)/xmean+t2
      s33=stfn*dwb(nn)/xmean+t3
  421 delu=s13*cf(1)
      delv=s23*cf(2)
      delw=s33*cf(3)
      if(dwb(nn).ge.thick(j,i))then
      delw=thick(j,i)-dwb(nn)
      if(kode(j,i).eq.1)kode(j,i)=5
c      kode(j,i)=9
      endif
      if(kode(j,i).eq.5)kcon=kcon+1
      dub(nn)=dub(nn)+delu
      dvb(nn)=dvb(nn)+delv
      dwb(nn)=dwb(nn)+delw
      eror1=abs(delu)
      eror2=abs(delv)
      eror3=abs(delw)
      if(eror1.gt.acc) ind1=ind1+1
      if(eror2.gt.acc) ind2=ind2+1
```

```
      if(eror3.gt.acc) ind3=ind3+1
      error=amax1(error,eror1,eror2,eror3)
      jter=iter
      ind=ind1+ind2+ind3
  450 continue
      if(ind)810,810,800
  800 continue
      write(2,6040)jter
      write(2,6043) error
  810 if(ind.gt.0) write(2,6042)ind1,ind2,ind3
      write(2,6038)
      tho=0.
      thx=0.
      do 500 j=1,nrow
      do 500 i=1,ncol
      nn=(j-1)*ncol+i
      read( 3,rec=nn)s13u
      read( 4,rec=nn)s23u
      read( 8,rec=nn)s23v
      read( 9,rec=nn)s33u
      read(10,rec=nn)s33v
      read(11,rec=nn)s33w
      read(12,rec=nn)d1u
      read(13,rec=nn)d2u
      read(14,rec=nn)d3u
      read(15,rec=nn)d2v
      read(16,rec=nn)d3v
      read(17,rec=nn)d1w
      read(18,rec=nn)d2w
      read(19,rec=nn)d3w
      sg1=0
      sg2=0
      sg3=0
      upb=0.
      vpb=0.
      wpb=0.
      xn=xo(j,i)
      yn=yo(j,i)
      z1n=zol(j,i)
      z2n=-zol(j,i)
      jb=j-nelbw
      je=j+nelbw
      if(jb.le.1)jb=1
      if(je.ge.nrow)je=nrow
      ib=i-nelbw
      ie=i+nelbw
      if(ib.le.1)ib=1
      if(ie.ge.ncol) ie=ncol
      ll=0
      do 510 js=jb,je
      do 510 is=ib,ie
      ll=ll+1
      mm=(js-1)*ncol+is
      sg1=sg1+s13u(ll)*dub(mm)+s23u(ll)*dvb(mm)+s33u(ll)*dwb(mm)
      sg2=sg2+s23u(ll)*dub(mm)+s23v(ll)*dvb(mm)+s33v(ll)*dwb(mm)
      sg3=sg3+s33u(ll)*dub(mm)+s33v(ll)*dvb(mm)+s33w(ll)*dwb(mm)
      upb=upb+d1u(ll)*dub(mm)+d2u(ll)*dvb(mm)+d1w(ll)*dwb(mm)
      vpb=vpb+d2u(ll)*dub(mm)+d2v(ll)*dvb(mm)+d2w(ll)*dwb(mm)
      wpb=wpb+d3u(ll)*dub(mm)+d3v(ll)*dvb(mm)+d3w(ll)*dwb(mm)
  510 continue
      upos=upb*cond
      vpos=vpb*cond
      wpos=wpb*cond
      uneg=upos+dub(nn)
      vneg=vpos+dvb(nn)
      wneg=wpos+dwb(nn)
      t1=sg1*cons
      t2=sg2*cons
      t3=sg3*cons
      sig1=t1+po1
      sig2=t2+po2
      sig3=t3+po3
      the(j,i)=thick(j,i)-dwb(nn)
      thx=thx+thick(j,i)-dwb(nn)
      tho=tho+thick(j,i)
  500 write(2,6039)j,i,kode(j,i),the(j,i),thick(j,i),upos,vpos,wpos,
     .             dub(nn),dvb(nn),dwb(nn),sig1,sig2,sig3
      write(2,4002)kcon1
 4002 format( ' numbers of contact point before loading increases  = '
     .        ,i6)
      write(2,4003)kcon
 4003 format( ' increased numbers of contact point after loading  = '
     .        ,i6)
      nkc=ncol*nrow-kcon1-kcon
      thxo=(tho-thx)/(ncol*nrow-kcon1)
      if(nkc.eq.0)then
      ttt=0
      go to 501
      endif
      ttt=thx/nkc
  501 write(2,4001)thxo,ttt,tho,thx
 4001 format( '   average closure =    ',e16.6,/
     .        '   average aperture =   ',e16.6,/
     .        ' void volumn before loading =   ',e16.6,/
     .        ' void volumn after loading =   ',e16.6)
      xm1=tho/(ncol*nrow)
      xm2=thx/(ncol*nrow)
      st1=0
      st2=0
      do 505 j=1,nrow
      do 505 i=1,ncol
      st2=st2+(the(j,i)-xm2)**2
  505 st1=st1+(thick(j,i)-xm1)**2
      st1=sqrt(st1/(nrow*ncol-1))
      st2=sqrt(st2/(nrow*ncol-1))
      write(2,506)xm1,st1
  506 format(' xmean before loading =',f10.4,/,
     .       ' st.d. before loading =',f10.4)
      write(2,507)xm2,st2
  507 format(' xmean after loading =',f10.4,/,
     .       ' st.d. after loading =',f10.4)
      if(nosp.eq.0) go to 845
      write(2,6050) nosp
      call outf(nosp)
 5000 format(1h1)
 5001 format(80h
     .                                        )
 5005 format(f8.2,e12.2)
 5009 format(3f10.0)
 5011 format(f8.2,4i8)
 5013 format(3f12.0)
 5023 format(f8.2,4i8)
 6001 format(/'  poissons ratio of rock mass           -',f15.2
     .       /'   modulus of elasticity of rock mass    -',f15.2)
 6011 format( /'  width of blocks                      -',f8.2//
     .         '  no. of blocks along x1 axis          -',i8//
     .         '  no. of blocks along x2 axis          -',i8/)
 6023 format(//'  over relaxation factor                -',f8.2//
```

```
     .        'maximum no. of iterations specified    -',i8)
 6025 format(/'  this is computer run no.',i3,' for this problem,')
 6038 format(              /'  j  i cd      the      thick       disp-x
     .      disp-y     disp-z      ride-x       ride-y      closure    s
     .ig13 sig23 sig33'/)
c 6039 format(6e10.2,3f6.2)
c 6039 format(3i3,2f5.2,3e12.4,3f7.2)
c 6039 format(3i3,f6.3,6e12.4,3f8.3)
 6039 format(3i3,8e12.4,3f6.2)
 6040 format(/'  no. of iterations completed in all the runs   =',i8)
 6042 format(/'  insufficient accuracy -',i4,'  elements affected in ri
     .de along x1 axis'/'                        ',i4,'  elements affec
     .ted in ride along x2 axis'/'                        ',i4,'  eleme
     .nts affected in closure')
 6043 format(/'  maximum error in the ride and closure values  ',f10.7)
 6050 format(//'  displacements and stresses at off-seam elements.'//
     .'   total no. of off-seam planes      -',i4)
  845 nn=nrow*ncol
      do 16 j=1,nrow
16    write(2,18)(kode(j,i),i=1,ncol)
18    format(30i2)
      stop
      end
      subroutine coeff(zt)
      common/rk7/rw,cw,seg,cf01,cf02,cf03,cf04,cf05,cf06,
     . cf07,cf08,cf09,cf10,cf11,cf12,cf13,cf14,cf15,
     .  cf16,cf17,cf18,cf19,zmn
      data pi/3.1415926535897/
      f0(p,r)=alog(r-p)
      f1(p,q,r)=(p*q)/((r**2-q**2)*r)
      f2(p,q,r,t)=q*t*(p**2*(r**2+p**2)-zt**2*(r**2-p**2))
      f3(p,q,r,t)=p*q*zt*t*(3.*r**2-q**2)
      rw1=rw-seg
      rw2=rw+seg
      cw1=cw-seg
      cw2=cw+seg
      r1=sqrt(rw1**2+cw1**2+zt**2)
      r2=sqrt(rw2**2+cw2**2+zt**2)
      r3=sqrt(rw1**2+cw2**2+zt**2)
      r4=sqrt(rw2**2+cw1**2+zt**2)
      t1=1./((rw1**2+zt**2)**2*r1**3)
      t2=1./((rw2**2+zt**2)**2*r2**3)
      t3=1./((rw1**2+zt**2)**2*r3**3)
      t4=1./((rw2**2+zt**2)**2*r4**3)
      cf01=f0(cw2,r3)+f0(cw1,r4)-f0(cw1,r1)-f0(cw2,r2)
      cf02=f0(rw1,r3)+f0(rw2,r4)-f0(rw1,r1)-f0(rw2,r2)
      if(zt.ne.0) go to 145
      cf03=0.
      if(abs(rw).le.seg.and.abs(cw).le.seg)cf03=-2*pi
      go to 146
  145 cf03=atan(rw1*cw2/(r3*zt))+atan(rw2*cw1/(r4*zt))
     .     -atan(rw1*cw1/(r1*zt))-atan(rw2*cw2/(r2*zt))
      if(zmn.eq.0.)cf03=0
  146 cf04=f1(rw1,cw2,r3)+f1(rw2,cw1,r4)-f1(rw1,cw1,r1)-f1(rw2,cw2,r2)
      cf05=1./r1+1./r2-1./r3-1./r4
      cf06=f1(zt,cw2,r3)+f1(zt,cw1,r4)-f1(zt,cw1,r1)-f1(zt,cw2,r2)
      cf07=f1(cw2,rw1,r3)+f1(cw1,rw2,r4)-f1(cw1,rw1,r1)-f1(cw2,rw2,r2)
      cf08=f1(zt,rw1,r3)+f1(zt,rw2,r4)-f1(zt,rw1,r1)-f1(zt,rw2,r2)
      cf09=-cf04-cf07
      cf10=f2(rw1,cw1,r1,t1)+f2(rw2,cw2,r2,t2)-f2(rw1,cw2,r3,t3)
     .    -f2(rw2,cw1,r4,t4)
      cf11=rw1/r3**3+rw2/r4**3-rw1/r1**3-rw2/r2**3
      cf12=f3(rw1,cw1,r1,t1)+f3(rw2,cw2,r2,t2)-f3(rw1,cw2,r3,t3)
     .    -f3(rw2,cw1,r4,t4)
      cf13=cw2/r3**3+cw1/r4**3-cw1/r1**3-cw2/r2**3
      cf14=zt*(1./r3**3+1./r4**3-1./r1**3-1./r2**3)
      cf15=-cf10-cf13
      t1=1./((cw1**2+zt**2)**2*r1**3)
      t2=1./((cw2**2+zt**2)**2*r2**3)
      t3=1./((cw2**2+zt**2)**2*r3**3)
      t4=1./((cw1**2+zt**2)**2*r4**3)
      cf16=f2(cw1,rw1,r1,t1)+f2(cw2,rw2,r2,t2)-f2(cw2,rw1,r3,t3)
     .    -f2(cw1,rw2,r4,t4)
      cf17=f3(cw1,rw1,r1,t1)+f3(cw2,rw2,r2,t2)-f3(cw2,rw1,r3,t3)
     .    -f3(cw1,rw2,r4,t4)
      cf18=-cf16-cf11
      cf19=-cf12-cf17
      return
      end
      subroutine outf(nop)
      common/rk9/mate(9),os11u(37),os12u(37),os13u(37),
     . os22u(37),os23u(37),os33u(37),os11v(37),os12v(37),
     . os22v(37),os23v(37),os33v(37),os11w(37),os12w(37),
     .   os22w(37),os33w(37),od1u(37),od2u(37),od3u(37),
     . od2v(37),od3v(37),od1w(37),od2w(37),od3w(37)
      common/rko/v,v1,v2,e,cons,cond,con
      common/rk1/dub(1),dvb(1),dwb(1),kode(30,1)
      common/rk3/nrow,ncol,nbxe,bw,hbw,zo
     .     ,xo(30,1),yo(30,1),zol(30,1),thick(30,1),en(3,3)
      common/rk7/rw,cw,seg,cf01,cf02,cf03,cf04,cf05,cf06,
     . cf07,cf08,cf09,cf10,cf11,cf12,cf13,cf14,cf15,
     .  cf16,cf17,cf18,cf19
      do 350 np=1,nop
      read(1,5005)xop,yop,zop,b1,b2,n1,n2
      read(1,5006)en1x,en2x,en3x,en1y,en2y,en3y,en1z,en2z,en3z
      write(2,6007)np
      write(2,6008)xop,yop,zop,b1,b2,n1,n2
      write(2,6009)en1x,en2x,en3x,en1y,en2y,en3y,en1z,en2z,en3z
      write(2,6015)
      h1=b1/2.
      h2=b2/2.
      n12=n1*n2
      hrw1=h1*(en1x*en(1,1)+en1y*en(1,2)+en1z*en(1,3))
      hcw1=h1*(en1x*en(2,1)+en1y*en(2,2)+en1z*en(2,3))
      hzt1=h1*(en1x*en(3,1)+en1y*en(3,2)+en1z*en(3,3))
      hrw2=h2*(en2x*en(1,1)+en2y*en(1,2)+en2z*en(1,3))
      hcw2=h2*(en2x*en(2,1)+en2y*en(2,2)+en2z*en(2,3))
      hzt2=h2*(en2x*en(3,1)+en2y*en(3,2)+en2z*en(3,3))
      do 335 jp=1,n1
      ej=float(2*jp-1)
      do 335 ip=1,n2
      ei=float(2*ip-1)
      num=0
      mum=1
      x=xop-xo(1,1)
      y=yop-yo(1,1)
      z=zop-zo
c      z=zop-zo(1,1)
      rwp=x*en(1,1)+y*en(1,2)+z*en(1,3)+ej*hrw1+ei*hrw2
      cwp=x*en(2,1)+y*en(2,2)+z*en(2,3)+ej*hcw1+ei*hcw2
      ztp=x*en(3,1)+y*en(3,2)+z*en(3,3)+ej*hzt1+ei*hzt2
      zt=ztp
      s11pe=0.
      s12pe=0.
      s13pe=0.
      s22pe=0.
      s23pe=0.
      s33pe=0.
```

```
      upe=0.
      vpe=0.
      wpe=0.
      do 150 js=1,nrow
      rwb=rwp-2*(js-1)*hbw
      do 150 is=1,ncol
      cwb=cwp-2*(is-1)*hbw
      zt1=zt+0.5*thick(js,is)
      zt2=zt-0.5*thick(js,is)
      seg=hbw
      num=num+1
      call coeff(zt1)
      mum=mum+1
  142 os11u(num)=os11u(num)+zt*cf10-2.*cf06
      os12u(num)=os12u(num)+zt*cf11-v1*cf08
      os13u(num)=os13u(num)+v*cf04-v1*cf09+zt*cf12
      os22u(num)=os22u(num)+zt*cf13-2.*v*cf06
      os23u(num)=os23u(num)+v*cf05+zt*cf14
      os33u(num)=os33u(num)+zt*cf15
      os11v(num)=os11v(num)+zt*cf11-2.*v*cf08
      os12v(num)=os12v(num)+zt*cf13-v1*cf06
      os22v(num)=os22v(num)+zt*cf16-2.*cf08
      os23v(num)=os23v(num)+v*cf07-v1*cf09+zt*cf17
      os33v(num)=os33v(num)+zt*cf18
      os11w(num)=os11w(num)+v2*cf04-2.*v*cf09+zt*cf12
      os12w(num)=os12w(num)+v2*cf05+zt*cf14
      os22w(num)=os22w(num)+v2*cf07-2.*v*cf09+zt*cf17
      os33w(num)=os33w(num)-cf09+zt*cf19
c
      od1u(num)=od1u(num)+2.*v1*cf03-zt*cf04
      od2u(num)=od2u(num)-zt*cf05
      od3u(num)=od3u(num)+v2*cf01-zt*cf06
      od2v(num)=od2v(num)+2.*v1*cf03-zt*cf07
      od3v(num)=od3v(num)+v2*cf02-zt*cf08
      od1w(num)=od1w(num)-v2*cf01-zt*cf06
      od2w(num)=od2w(num)-v2*cf02-zt*cf08
      od3w(num)=od3w(num)+2.*v1*cf03-zt*cf09
      if(mum.ge.2)go to 141
      call coeff(zt2)
      mum=mum+1
      go to 142
  141 s11pe=s11pe+os11u(num)*dub(num)+os11v(num)*dvb(num)+
     .       os11w(num)*dwb(num)
      s12pe=s12pe+os12u(num)*dub(num)+os12v(num)*dvb(num)+
     .       os12w(num)*dwb(num)
      s13pe=s13pe+os13u(num)*dub(num)+os23u(num)*dvb(num)+
     .       os33u(num)*dwb(num)
      s22pe=s22pe+os22u(num)*dub(num)+os22v(num)*dvb(num)+
     .       os22w(num)*dwb(num)
      s23pe=s23pe+os23u(num)*dub(num)+os23v(num)*dvb(num)+
     .       os33v(num)*dwb(num)
      s33pe=s33pe+os33u(num)*dub(num)+os33v(num)*dvb(num)+
     .       os33w(num)*dwb(num)
      upe=upe+od1u(num)*dub(num)+od2u(num)*dvb(num)+
     .     od1w(num)*dwb(num)
      vpe=vpe+od2u(num)*dub(num)+od2v(num)*dvb(num)+
     .     od2w(num)*dwb(num)
      wpe=wpe+od3u(num)*dub(num)+od3v(num)*dvb(num)+
     .     od3w(num)*dwb(num)
  150 continue
      x=xop+ej*en1x*h1+ei*en2x*h2
      y=yop+ej*en1y*h1+ei*en2y*h2
      z=zop+ej*en1z*h1+ei*en2z*h2
      ux=(en(1,1)*upe+en(2,1)*vpe+en(3,1)*wpe)*cond
      vy=(en(1,2)*upe+en(2,2)*vpe+en(3,2)*wpe)*cond
      wz=(en(1,3)*upe+en(2,3)*vpe+en(3,3)*wpe)*cond
      sxx=(en(1,1)**2*s11pe+2.*en(1,1)*en(2,1)*s12pe+2.*en(1,1)*en(3,1)*
     .  s13pe+en(2,1)**2*s22pe+2.*en(2,1)*en(3,1)*s23pe+en(3,1)**2*s33pe
     .    )*cons+a11-b11*z
      sxy=(en(1,1)*en(1,2)*s11pe+(en(1,1)*en(2,2)+en(2,1)*en(1,2))*s12pe
     .  +(en(1,1)*en(3,2)+en(3,1)*en(1,2))*s13pe+en(2,1)*en(2,2)*s22pe+
     .   (en(2,1)*en(3,2)+en(3,1)*en(2,2))*s23pe+en(3,1)*en(3,2)*s33pe
     .    )*cons+a12-b12*z
      sxz=(en(1,1)*en(1,3)*s11pe+(en(1,1)*en(2,3)+en(2,1)*en(1,3))*s12pe
     .  +(en(1,1)*en(3,3)+en(3,1)*en(1,3))*s13pe+en(2,1)*en(2,3)*s22pe+
     .   (en(2,1)*en(3,3)+en(3,1)*en(2,3))*s23pe+en(3,1)*en(3,3)*s33pe
     .    )*cons+a13-b13*z
      syy=(en(1,2)**2*s11pe+2.*en(1,2)*en(2,2)*s12pe+2.*en(1,1)*en(3,2)*
     .  s13pe+en(2,2)**2*s22pe+2.*en(2,2)*en(3,2)*s23pe+en(3,2)**2*s33pe
     .    )*cons+a22-b22*z
      syz=(en(1,2)*en(1,3)*s11pe+(en(1,2)*en(2,3)+en(2,3)*en(1,3))*s12pe
     .  +(en(1,2)*en(3,3)+en(3,2)*en(1,3))*s13pe+en(2,2)*en(2,3)*s22pe+
     .   (en(2,2)*en(3,3)+en(3,2)*en(2,3))*s23pe+en(3,2)*en(3,3)*s33pe
     .    )*cons+a23-b23*z
      szz=(en(1,3)**2*s11pe+2.*en(1,3)*en(2,3)*s12pe+2.*en(1,3)*en(3,3)*
     .  s13pe+en(2,3)**2*s22pe+2.*en(2,3)*en(3,3)*s23pe+en(3,3)**2*s33pe
     .    )*cons+a33-b33*z
      write(2,6010)np,ip,jp,x,y,z,ux,vy,wz,sxx,sxy,sxz,syy,syz,szz
  335 continue
  350 continue
 5005 format(5f12.3,2i8)
 5006 format(9f8.5)
 6007 format(///'  off-seam plane no.                -',i4)
 6008 format(/'  location of local origin and grid-work details -'//
     . '              grid origin at                  block widths
     .  no. of blocks'/
     .,'         xop          yop          zop          b1          b2
     .        n1      n2',/5f12.3,2i8)
 6009 format(/'  orientation of the off-seam plane  -'///      en1x
     .       en2x         en3x         en1y         en2y         en3y
     .  en1z         en2z         en3z'/,9f12.5)
 6015 format(///'   n   j   i      x        y        z       ux        uy
     .        uz       sxx       sxy       sxz       syy       syz
     .    szz '/)
 6010 format(3i4,3f9.2,3f10.6,6f10.2)
      return
      end
```

APPENDIX B

FLOW: A Computer Program For Evaluating Flow Through A Fracture With Partial Contact

The program FLOW evaluates the flow of Newtonian fluid through a fracture containing contact areas of various shapes, based on the mathematical formulations given in Chapter 3. The main program controls the logic calling sequence of subroutines to read the input data, to initialize the parameters, to set up a system of linear algebraic equations, to solve for the unknown pressure P and fluid flux q at boundary elements by Gauss elimination method, and to write the output data. FLOW includes following subroutines,

INPUT	Reads the program input.
FMAT	Forms the two matrices H and G (Eq. 3-34) and rearranges them according to the boundary conditions to form the matrix A of Equation (Eq. 3-35).
SLNPD	Solves the system of equations by Gauss elimination.
INTER	Reorders the unknown P and q, and computers the values ot the pressure at the selected internal points (values of q are not computed here but could easily be included).
OUTPT	Outputs the results.

1. Description of FLOW Input Variables

bw — side length of the square boundary element.

nrow — number of elements along x axis.

ncol — number of elements along y axis.

l — number of internal points where the function is calculated.

id(i,j) — contact area index of the element located at ith row and jth column,

if id(i,j)=0 contact area,

if id(i,j) > = 0 void space.

ms — number of different contact area surfaces (archipelagoes).

mt — number of boundary elements of each archipelagoes.

idm(k) — number of boundary elements which coincide with those of outer boundary.

nkk, nii — identifiers of boundary element locations (row and column).

ndd — identifier of the side of the element which coincides with the outer boundary:

ndd=1 top side of the element coincides with the outer boundary,

ndd=2 right side of the element coincides with the outer boundary,

ndd=3 bottom side of the element coincides with the outer boundary,

ndd=4 left side of the element coincides with the outer boundary.

kode — identifer of boundary conditions:

kode=0 if essential boundary condition P=constant is prescribed.

kode=1 if natural boundary condition $q=\partial P/\partial n$ is prescribed.

fi — prescribed values of boundary conditions

nc(1) — number of elements included in the outer boundary.

2. ROUGH Input Variables and Formats

Variable	Format
title	free
nrow, ncol, L, bw	(3i5, f6.2)
(id(i,j), j=1,ncol)	(30i2), nrow cards need to be read.
ms	(i5)
mt, idm(i)	(2i10)
nkk, nii, (ndd(i), i=1,3)	(5i5)
(kode(i), fi(i), i=1,nc(1))	(8(i3,f6.0))

```
c     program flow.f
      common n,l,nc(100),m,nrow
      dimension x(701),y(701),xm(700),ym(700),fi(700),dfi(700)
      dimension g(700),h(700)
      dimension kode(700)
      dimension cx(36),cy(36),sol(36)
      open (unit=1,file='inflow',status='old')
      open (unit=2,file='otflow',status='new')
      open (unit=8,status='scratch',form='unformatted',access='direct',
     .      recl=2800)
      open (unit=9,status='scratch',form='unformatted',access='direct',
     .      recl=2800)
      call input(cx,cy,x,y,kode,fi)
      call fmat(x,y,xm,ym,g,h,fi,dfi,kode)
      call slnpd(dfi,n)
      call inter(fi,dfi,kode,cx,cy,x,y,sol)
      call output(xm,ym,fi,dfi,kode,cx,cy,sol)
      stop
      end
c
      subroutine input(cx,cy,x,y,kode,fi)
      common n,l,nc(100),m,nrow
      dimension x(701),y(701),fi(700),cy(36),cx(36),kode(700),idm(100)
      dimension title(18),id(32,32),ng(32,32),nk(100),ni(100),ndd(3)
      dimension xx(701),yy(701),xt(701),yt(701),xs(700),ys(700)
      dimension cangle(100)
      dimension ra(10),rb(10),centx(10),centy(10),iseg(50),ncl(100)
      write(2,100)
  100 format(' ',120('*'))
      read(1,150) title
  150 format(18a4)
      write(2,250)title
  250 format(25x,18a4)
      read(1,200)nrow,ncol,l,bw
      write(2,200)nrow,ncol,l,bw
  200 format(3i5,f6.2)
      mn=0
      do 31 i=1,ncol
      mn=mn+1
     * x(mn)=bw*(i-1)
   31 y(mn)=0.
      do 32 i=1,nrow
      mn=mn+1
      x(mn)=bw*ncol
   32 y(mn)=bw*(i-1)
      do 33 i=1,ncol
      mn=mn+1
      x(mn)=bw*(ncol-i+1)
   33 y(mn)=bw*nrow
      do 34 i=1,nrow
      mn=mn+1
      x(mn)=0.
   34 y(mn)=bw*(nrow-i+1)
      nc(1)=mn
c
      do 802 ims=1,nrow
      read (1,801)(id(ims,jms),jms=1,ncol)
  802 continue
  801 format(32i2)
      do 808 i=1,nrow
      do 808 j=1,ncol
  808 if(id(i,j).ge.3) id(i,j)=0.
      do 609 ims=1,nrow
      write (2,801)(id(ims,jms),jms=1,ncol)
  609 continue
      read(1,110)ixyz,iuv
  110 format(2i5)
c      if(ixyz.ne.0)go to 115
      m=1
      n=mn
c      go to 863
c  115 do 113 i=1,ixyz
c      read(1,112)iu,iv
c      id(iu,iv)=1
c      write(2,114)iu,iv,id(iu,iv)
c  113 continue
c      if(iuv.eq.0)go to 863
c  114 format('iu =',i5,'iv =',i5,'id(iu,iv)=',i5)
c  112 format(2i5)
      do 803 ii=1,nrow
      do 803 jj=1,ncol
      ng(ii,jj)=0
      if(id(ii,jj).ne.0)go to 803
      if(ii.eq.nrow)go to 804
      if(id(ii+1,jj).eq.0)ng(ii,jj)=ng(ii,jj)+1
  804 if(jj.eq.1)go to 805
      if(id(ii,jj-1).eq.0)ng(ii,jj)=ng(ii,jj)+1
  805 if(ii.eq.1)go to 806
      if(id(ii-1,jj).eq.0)ng(ii,jj)=ng(ii,jj)+1
  806 if(jj.eq.ncol)go to 803
      if(id(ii,jj+1).eq.0)ng(ii,jj)=ng(ii,jj)+1
  803 continue
c      write(2,777)((ng(ii,jj),jj=1,ncol),ii=1,nrow)
c  777 format(5i10)
      jk=0
      do 809 ii=1,nrow
      do 809 jj=1,ncol
      if(id(ii,jj).ne.0)go to 809
      if(ng(ii,jj).eq.0)then
      jk=jk+1
      nk(jk)=ii
      ni(jk)=jj
      endif
  809 continue
      nn=2*(nrow+ncol)
      na=0
      nx=nrow*4
      if(jk.eq.0)go to 807
      do 811 ijk=1,jk
      ncs=ni(ijk)
      nrt=nk(ijk)
      if(ncs.eq.1.and.nrt.eq.1)go to 62
      if(nrt.eq.1.and.ncs.eq.ncol)go to 63
      if(nrt.eq.nrow.and.ncs.eq.ncol)go to 64
      if(nrt.eq.nrow.and.ncs.eq.1)go to 65
      na=na+1
      idm(na)=0
      if(ncs.eq.1.or.ncs.eq.ncol)idm(na)=2
      if(nrt.eq.1.or.nrt.eq.nrow)idm(na)=2
      mn1=nn+4*(na-1)+1
      mn2=nn+4*(na-1)+2
      mn3=nn+4*(na-1)+3
      mn4=nn+4*(na-1)+4
      x(mn1)=(ncs-1)*bw
      y(mn1)=(nrt-1)*bw
      x(mn2)=(ncs-1)*bw
      y(mn2)=nrt*bw
      x(mn3)=ncs*bw
```

```
      y(mn3)=nrt*bw
      x(mn4)=ncs*bw
      y(mn4)=(nrt-1)*bw
      go to 811
   62 x(1)=ncs*bw
      y(1)=nrt*bw
      go to 811
   63 x(ncol+1)=(ncs-1)*bw
      y(ncol+1)=nrt*bw
      go to 811
   64 x(nrow+ncol+1)=(ncs-1)*bw
      y(nrow+ncol+1)=(nrt-1)*bw
      go to 811
   65 x(3*nrow+1)=ncs*bw
      y(3*nrow+1)=(nrt-1)*bw
  811 continue
      do 813 k=1,jk+1
      nc(1)=nx
  813 nc(k)=nc(1)+4*(k-1)
      n=4*(nrow+jk)
c      write(2,900)(x(i),y(i),i=nx+1,n)
c  900 format(2f16.2)
  807 m1=na
      nn1=nx+4*m1
      do 812 ii=1,nrow
      do 812 jj=1,ncol
      if(ng(ii,jj).eq.0)go to 812
      if(ng(ii,jj).gt.1)go to 812
      if(id(ii,jj).ne.0)go to 812
      nrr=ng(ii,jj)+ng(ii,jj+1)
      ncc=ng(ii,jj)+ng(ii+1,jj)
      if(nrr.eq.2)then
      id(ii,jj)=-1
      id(ii,jj+1)=-1
      if(ii.eq.1.and.jj.eq.1)then
      x(1)=jj*bw
      y(1)=ii*bw
      x(2)=(jj+1)*bw
      y(2)=ii*bw
      go to 812
      endif
      if(ii.eq.1.and.jj+1.eq.ncol)then
      x(ncol)=(jj-1)*bw
      y(ncol)=ii*bw
      x(ncol+1)=jj*bw
      y(ncol+1)=ii*bw
      go to 812
      endif
      if(ii.eq.nrow.and.jj.eq.1)then
      nabc=2*nrow+ncol
      x(nabc)=(jj+1)*bw
      y(nabc)=(ii-1)*bw
      x(nabc+1)=jj*bw
      y(nabc+1)=(ii-1)*bw
      go to 812
      endif
      if(ii.eq.nrow.and.jj+1.eq.ncol)then
      nabc=nrow+ncol
      x(nabc+1)=jj*bw
      y(nabc+1)=(ii-1)*bw
      x(nabc+2)=(jj-1)*bw
      y(nabc+2)=(ii-1)*bw
      go to 812
      endif
      na=na+1
      idm(na)=0
      if(ii.eq.1.or.ii.eq.nrow)idm(na)=3
      if(jj.eq.1.or.jj+1.eq.ncol)idm(na)=2
      mn1=nn1+6*(na-m1-1)+1
      mn2=nn1+6*(na-m1-1)+2
      mn3=nn1+6*(na-m1-1)+3
      mn4=nn1+6*(na-m1-1)+4
      mn5=nn1+6*(na-m1-1)+5
      mn6=nn1+6*(na-m1-1)+6
      x(mn1)=(jj-1)*bw
      y(mn1)=(ii-1)*bw
      x(mn2)=(jj-1)*bw
      y(mn2)=ii*bw
      x(mn3)=jj*bw
      y(mn3)=ii*bw
      x(mn4)=(jj+1)*bw
      y(mn4)=ii*bw
      x(mn5)=(jj+1)*bw
      y(mn5)=(ii-1)*bw
      x(mn6)=jj*bw
      y(mn6)=(ii-1)*bw
      go to 812
      endif
      if(ncc.eq.2)then
      id(ii,jj)=-1
      id(ii+1,jj)=-1
      if(ii.eq.1.and.jj.eq.1)then
      x(1)=jj*bw
      y(1)=ii*bw
      x(nx)=jj*bw
      y(nx)=(ii+1)*bw
      go to 812
      endif
      if(ii.eq.1.and.jj.eq.ncol)then
      x(ncol+1)=(jj-1)*bw
      y(ncol+1)=ii*bw
      x(ncol+2)=(jj-1)*bw
      y(ncol+2)=(ii+1)*bw
      go to 812
      endif
      if(ii+1.eq.nrow.and.jj.eq.1)then
      nabc=2*nrow+ncol
      x(nabc+1)=jj*bw
      y(nabc+1)=ii*bw
      x(nabc+2)=jj*bw
      y(nabc+2)=(ii-1)*bw
      go to 812
      endif
      if(ii+1.eq.nrow.and.jj.eq.ncol)then
      nabc=nrow+ncol
      x(nabc)=(jj-1)*bw
      y(nabc)=(ii-1)*bw
      x(nabc+1)=(jj-1)*bw
      y(nabc+1)=ii*bw
      go to 812
      endif
      na=na+1
      idm(na)=0
      if(jj.eq.1.or.jj.eq.ncol)idm(na)=3
      if(ii.eq.1.or.ii+1.eq.nrow)idm(na)=2
      mn1=nn1+6*(na-m1-1)+1
      mn2=nn1+6*(na-m1-1)+2
      mn3=nn1+6*(na-m1-1)+3
```

```
      mn4=nn1+6*(na-m1-1)+4
      mn5=nn1+6*(na-m1-1)+5
      mn6=nn1+6*(na-m1-1)+6
      x(mn1)=(jj-1)*bw
      y(mn1)=(ii-1)*bw
      x(mn2)=(jj-1)*bw
      y(mn2)=ii*bw
      x(mn3)=(jj-1)*bw
      y(mn3)=(ii+1)*bw
      x(mn4)=jj*bw
      y(mn4)=(ii+1)*bw
      x(mn5)=jj*bw
      y(mn5)=ii*bw
      x(mn6)=jj*bw
      y(mn6)=(ii-1)*bw
      endif
  812 continue
      m=na+1
      if(m.eq.1) go to 863
      do 37 i=1,m
      if(i.gt.m1+1)go to 42
      nc(i)=nc(1)+(i-1)*4
      go to 37
   42 nc(i)=nc(1)+m1*4+(i-m1-1)*6
   37 continue
  863 nq=nc(m)
      n=nq
c      write(2,998)m,(nc(k),k=1,m)
c  998 format(/2x,'number of different surfaces=',i3/2x,'last nodes in
c     .these surfaces',5(2x,i3))
      mp=0
      read (1,850)ms
  850 format(i5)
      do 864 i=1,ms
      read(1,851)mt,idm(m+i-1)
  851 format(2i10)
      nrmax=0
      nrmin=nrow
      ncmax=0
      ncmin=ncol
      do 860 j=1,mt
      read(1,861)nkk,nii,(ndd(is),is=1,3)
  861 format(5i5)
      if(nkk.ge.nrmax)nrmax=nkk
      if(nkk.le.nrmin)nrmin=nkk
      if(nii.ge.ncmax)ncmax=nii
      if(nii.le.ncmin)ncmin=nii
      do 860 ist=1,3
      if(ndd(ist).eq.0)go to 860
      if(ndd(ist).eq.1)then
      nq=nq+1
      mp=mp+1
      x(nq)=(nii-1)*bw
      y(nq)=nkk*bw
      go to 860
      endif
      if(ndd(ist).eq.2)then
      nq=nq+1
      mp=mp+1
      x(nq)=nii*bw
      y(nq)=nkk*bw
      go to 860
      endif
      if(ndd(ist).eq.3)then
      nq=nq+1
      mp=mp+1
      x(nq)=nii*bw
      y(nq)=(nkk-1)*bw
      go to 860
      endif
      if(ndd(ist).eq.4)then
      nq=nq+1
      mp=mp+1
      x(nq)=(nii-1)*bw
      y(nq)=(nkk-1)*bw
      endif
  860 continue
      nc(m+i)=nc(m)+mp
  864 continue
      n=nc(m+ms)
      m=m+ms
      go to 40
   40 do 49 i=1,n
      xt(i)=x(i)
   49 yt(i)=y(i)
      m2=m-1
      if (m.eq.1)go to 50
      do 70 k=1,m2
      nk2=nc(k+1)
      nk1=nc(k)+1
      mt=nk2-nc(k)-idm(k)
      mt1=mt+idm(k)
      if(k.eq.1)nkk=nc(1)
      do 73 is=1,mt1
      nks=nc(k)+is
      xs(is)=x(nks)
   73 ys(is)=y(nks)
      if(idm(k).eq.0)go to 70
      mm=0
      idp=0
      do 71 i=1,nkk
      mm=mm+1
      if(idm(k).le.2.or.k.eq.1)go to 77
   77 xx(mm)=x(i)
      yy(mm)=y(i)
      if(idp.eq.1)then
      xx(mm)=x(i+idm(k)-1)
      yy(mm)=y(i+idm(k)-1)
      endif
      if(idm(k).eq.0)go to 71
      do 74 it=1,mt1
      iss=it-idm(k)+1
      if(iss.le.0)iss=iss+mt1
      ixm=i+idm(k)-1
      if(ixm.gt.nkk)ixm=ixm-nkk
      if(xs(it).eq.x(i).and.xs(iss).eq.x(ixm).and.
     .   ys(it).eq.y(i).and.ys(iss).eq.y(ixm))goto 88
      go to 74
   88 if(idm(k).ge.3)then
      mt=mt+1
      idp=1
      endif
      do 72 j=1,mt
      mm=mm+1
      isj=it+j
      if(isj.gt.mt1)isj=isj-mt1
      xx(mm)=xs(isj)
      yy(mm)=ys(isj)
```

```
   72 continue
      if(idm(k).le.2)go to 71
   74 continue
   71 continue
      nkk=nkk+mt1-idm(k)-(idm(k)-2)
      do 78 i=1,nkk
      x(i)=xx(i)
   78 y(i)=yy(i)
   70 continue
      n6=nkk
      do 180 k=1,m-1
      if(idm(k).ne.0)go to 180
      mt1=nc(k+1)-nc(k)
      if(idm(k).eq.0)then
      do 181 j=1,mt1
      ncj=nc(k)+j
      n6=n6+1
      x(n6)=xt(ncj)
      y(n6)=yt(ncj)
  181 continue
      endif
  180 continue
      idd=1
      do 80 k=1,m-1
      mt1=nc(k+1)-nc(k)
      nc1(1)=nkk
      if(idm(k).eq.0)then
      idd=idd+1
      nc1(idd)=nc1(idd-1)+mt1
      endif
   80 continue
      m=idd
      do 182 k=1,m
  182 nc(k)=nc1(k)
      if(m)56,56,92
   92 write(2,99)m,(nc(k),k=1,m)
   99 format(/2x,'different surfaces=',i3/2x,'last nodes of
     .these surfaces',5(2x,i3))
      n=nc(m)
   50 if(m.eq.1)n=nc(1)
      nnn1=2*(nrow+ncol)+1
      nnn=0
      mr=(nrmax-nrmin+1)/2
      mr1=nrmin-mr-2
      mr2=nrmax+mr+2
      mc=(ncmax-ncmin+1)/2
      mc1=ncmin-mc-2
      mc2=ncmax+mc+2
   56 l=1
      cx(1)=9.0
      cy(1)=9.0
      write(2,300)n,l
  300 format(//'data'//2x,'number of boundary elements=',
     .i3/2x,'number of internal points where the function is calculated
     .=',i3)
c       write(2,500)
c  500 format(//2x,'coordinates of the extreme points of the boundary ele
c     .ments',//2x,'point',12x,'x',18x,'y')
        do 96 i=1,n
   96 write(2,97)i,x(i),y(i)
   97 format(i8,2f19.5)
c       write(2,800)
c  800 format(//2x,'boundary conditions'//5x,'node',6x,'code',
c     .5x,'prescribed value')
c       do 20 i=1,nc(1)
c       read(1,900) kode(i),fi(i)
c    20 write(2,950)i,kode(i),fi(i)
c    20 continue
      read(1,901) (kode(i),fi(i),i=1,nc(1))
      nc11=nc(1)+1
      do 21 i=nc11,n
      kode(i)=1
   21 fi(i)=0.
  901 format(8(i3,f6.0))
      return
      end
c
      subroutine fmat(x,y,xm,ym,g,h,fi,dfi,kode)
      common n,l,nc(100),m,nrow
      dimension x(1),y(1),xm(1),ym(1),fi(1),dfi(1)
      dimension g(700),h(700)
      dimension kode(1)
      x(n+1)=x(1)
      y(n+1)=y(1)
      do 10 i=1,n
      xm(i)=(x(i)+x(i+1))/2
   10 ym(i)=(y(i)+y(i+1))/2
      if(n-l)15,15,12
   12 xm(nc(1))=(x(nc(1))+x(1))/2
      ym(nc(1))=(y(nc(1))+y(1))/2
      do 13 k=2,m
      xm(nc(k))=(x(nc(k))+x(nc(k-1)+1))/2
   13 ym(nc(k))=(y(nc(k))+y(nc(k-1)+1))/2
c
   15 do 31 i=1,n
      do 30 j=1,n
      h(j)=0.
      g(j)=0.
      if(m-1)16,16,17
   17 if(j-nc(1))19,18,19
   18 kk=1
      go to 23
   19 do 22 k=2,m
      if(j-nc(k))22,21,22
   21 kk=nc(k-1)+1
      go to 23
   22 continue
   16 kk=j+1
   23 if(i-j)20,25,20
   20 call inte(xm(i),ym(i),x(j),y(j),x(kk),y(kk),h(j),g(j))
      go to 30
   25 call inlo(x(j),y(j),x(kk),y(kk),g(j))
      h(j)=3.1415926
   30 continue
      write(8,rec=i)g
      write(9,rec=i)h
   31 continue
c
      do 51 i=1,n
      read(8,rec=i)g
      read(9,rec=i)h
      do 50 j=1,n
      if(kode(j))50,50,40
   40 ch=g(j)
      g(j)=-h(j)
      h(j)=-ch
   50 continue
      write(8,rec=i)g
```

```
      write(9,rec=i)h
   51 continue
      do 60 i=1,n
      dfi(i)=0.
      read(9,rec=i)h
      do 60 j=1,n
      dfi(i)=dfi(i)+h(j)*fi(j)
   60 continue
      return
      end
c
      subroutine inte(xp,yp,x1,y1,x2,y2,h,g)
      dimension xco(4),yco(4),gi(4),ome(4)
      gi(1) =0.86113631
      gi(2) =-gi(1)
      gi(3) =0.33998104
      gi(4) =-gi(3)
      ome(1) =0.34785485
      ome(2) =ome(1)
      ome(3) =0.65214515
      ome(4) =ome(3)
      ax =(x2-x1)/2
      bx =(x2+x1)/2
      ay =(y2-y1)/2
      by =(y2+y1)/2
      if(ax)10,20,10
   10 ta=ay/ax
      dist=abs(ta*xp-yp+y1-ta*x1)/sqrt(ta**2+1)
      go to 30
   20 dist=abs(xp-x1)
   30 sig=(x1-xp)*(y2-yp)-(x2-xp)*(y1-yp)
      if(sig)31,32,32
   31 dist=-dist
   32 g=0.
      h=0.
      do 40 i=1,4
      xco(i)=ax*gi(i)+bx
      yco(i)=ay*gi(i)+by
      ra=sqrt((xp-xco(i))**2+(yp-yco(i))**2)
      g=g+alog(1/ra)*ome(i)*sqrt(ax**2+ay**2)
   40 h=h-(dist*ome(i)*sqrt(ax**2+ay**2)/ra**2)
      return
      end
c
      subroutine inlo(x1,y1,x2,y2,g)
      ax=(x2-x1)/2
      ay=(y2-y1)/2
      sr=sqrt(ax**2+ay**2)
      g=2*sr*(alog(1/sr)+1)
      return
      end
c
      subroutine inter(fi,dfi,kode,cx,cy,x,y,sol)
      common n,l,nc(100),m
      dimension x(1),y(1),fi(1),dfi(1),kode(1)
      dimension cx(1),cy(1),sol(1)
      do 20 i=1,n
      if(kode(i))20,20,10
   10 ch=fi(i)
      fi(i)=dfi(i)
      dfi(i)=ch
   20 continue
      do 40 k=1,l
      sol(k)=0.
      do 30 j=1,n
      if(m-1)28,28,22
   22 if(j-nc(1))24,23,24
   23 kk=1
      go to 29
   24 do 26 lk=2,m
      if(j-nc(lk))26,25,26
   25 kk=nc(lk-1)+1
      go to 29
   26 continue
   28 kk=j+1
   29 call inte(cx(k),cy(k),x(j),y(j),x(kk),y(kk),a,b)
   30 sol(k)=sol(k)+dfi(j)*b-fi(j)*a
   40 sol(k)=sol(k)/(2*3.1415926)
      return
      end
c
      subroutine output(xm,ym,fi,dfi,kode,cx,cy,sol)
      common n, l, nc(100), m, nrow
      dimension xm(1),ym(1),fi(1),dfi(1)
      dimension kode(1)
      dimension cx(1),cy(1),sol(1),aper(32),dkf(32)
      write(2,100)
  100 format(' ',120('*')//1x,'results'//2x,'boundary nodes'//9x,
     .'x',18x,'y',14x,'potential',5x,'potential derivative'/)
      nd=4*nrow+1
c      do 10 i=nd,n
      do 10 i=1,n
   10 write(2,200)xm(i),ym(i),fi(i),dfi(i)
  200 format(4(5x,e14.7))
      dff=0.
c      do 60 i=1,nrow
c      i2=2*nrow
c   60 dff=dff+dfi(i2+i)
c      dff=dff/nrow
      kd=0
      do 60 i=1,n
      if(kode(i).eq.0.and.fi(i).eq.0.)then
      dff=dff+dfi(i)
      kd=kd+1
      dkf(kd)=dfi(i)
      endif
   60 continue
      dff=dff/nrow
      write(2,80)dff
   80 format(' average out flux =',e14.7)
      do 61 i=1,kd
      read(1,62)aper(i)
   61 continue
   62 format(9x,e12.4)
c      read(1,66)(aper(i),i=1,kd)
c66     format(8f9.1)
c      do 67 i=1,kd
c67     aper(i)=aper(i)*0.001
      qq=0.
      do 64 i=1,kd
   64 qq=qq+aper(kd-i+1)*dkf(i)
      write(2,63)qq
   63 format(' total flow rate =',f10.6)
      write(2,300)
  300 format(//,2x,'internal points',//11x,'x',18x,'y',14x,
     .'potential',/)
      do 20 k=1,l
   20 write(2,400)cx(k),cy(k),sol(k)
```

```
  400 format(3(5x,e14.7))
c      write(2,500)
c  500 format(' ',120('*'))
      return
      end
c
      subroutine slnpd(b,n)
      dimension ai(700),ak(700),b(700)
      n1=n-1
      do 100 k=1,n1
      read(8,rec=k)(ak(m),m=1,n)
      k1=k+1
      c=ak(k)
      if(c.eq.0.)go to 100
      b(k)=b(k)/c
      do 9 j=k1,n
    9 ak(j)=ak(j)/c
      write(8,rec=k)(ak(m),m=1,n)
      do 10 i=k1,n
      read(8,rec=i)(ai(m),m=1,n)
      d=ai(k)
      do 11 j=k1,n
   11 ai(j)=ai(j)-d*ak(j)
      b(i)=b(i)-d*b(k)
      write(8,rec=i)(ai(m),m=1,n)
   10 continue
  100 continue
      read(8,rec=n)(ai(m),m=1,n)
      if(ai(n).eq.0.)go to 600
      b(n)=b(n)/ai(n)
  600 do 200 l=1,n1
      k=n-l
      read(8,rec=k)(ai(m),m=1,n)
      k1=k+1
      do 200 j=k1,n
      b(k)=b(k)-ai(j)*b(j)
  200 continue
      return
      end
```